ABSTRACT

Title of dissertation: A SCALABLE TIME-PARALLEL SOLUTION OF PERIODIC DYNAMICS FOR THREE-DIMENSIONAL ROTORCRAFT AEROMECHANICS

Mrinalgouda Patil
Doctor of Philosophy, 2022

Dissertation directed by: Professor Anubhav Datta
Department of Aerospace Engineering

The principal barrier of computational time for rotorcraft trim solution using high-fidelity three-dimensional (3D) structures on real rotor problems was overcome with parallel and scalable algorithms. These algorithms were devised by leveraging the modern supercomputer architecture. The resulting parallel X3D solver was used to investigate advanced coaxial rotors using a notional hingeless rotor test case, Metaltail. This investigation included rotor performance, blade airloads, vibratory hub loads, and three-dimensional stresses.

The technical approach consisted of first studying existing algorithms for periodic rotor dynamics — time marching, finite element in time (FET), and harmonic balance. The feasibility of these algorithms was studied for large-scale rotor structures, and drawbacks were identified. Modifications were then performed on the harmonic balance method to obtain a Modified Harmonic Balance (MHB) method. A parallel algorithm for skyline solver was devised on shared memory to obtain faster solutions to large linear system of equations. The MHB method was implemented on a hybrid distributed–shared memory architecture to allow for parallel computations of harmonics. These developed algorithms were then integrated into the X3D solver to

obtain a new parallel X3D.

The new parallel X3D was verified and validated in hover and forward flight conditions for both idealized and real rotor test cases. A total of four test cases were studied: 1) uniform beam, 2) Frank Harris rotor, 3) UH-60A-like Black Hawk rotor, and 4) NASA Tilt Rotor Aeroacoustic Model (TRAM). The predictions of tip displacements, airloads, and stress distributions from the MHB algorithm showed good agreement with the test data and time marching predictions. The key conclusion is that the new solver converges to the time marching solution 50-70 times faster and achieves a performance greater than 1 teraFLOPS.

The new parallel X3D solver opened the opportunity for modeling advanced rotor configurations. In this work, the coaxial rotor was the selected configuration. Two open access models were developed; 1) a notional hingeless coaxial rotor, and 2) a notional articulated UH-60A-like coaxial rotor. The aerodynamics, structural dynamics, and trim modules of X3D were expanded for coaxial modeling. The coaxial aerodynamics was validated with hover performance data from the U.S. Army model test. The coaxial solver was then used to study rotor aeromechanics in forward flight. The analysis was performed at a low-speed transition flight for which qualitative data is available for the Sikorsky S-97 Raider aircraft for comparison. The UH-60A coaxial airloads showed good agreement with the S-97 data as the twists are likely similar. However, the Metaltail model showed dissimilarities, and the cause was investigated to be its high twist. Vibratory hub loads with advance ratio were studied, and the maximum vibration occurred at the transition flight speed ($\mu = 0.1 - 0.15$), which was consistent with the S-97 data. The effect of the inter-rotor phase was examined for the reduction of vibratory hub loads. Three-dimensional stresses and strains were predicted and visualized for the first time on lift offset coaxial rotors in the blade and the hub.

A SCALABLE TIME-PARALLEL SOLUTION OF PERIODIC DYNAMICS FOR THREE-DIMENSIONAL ROTORCRAFT AEROMECHANICS

by

Mrinalgouda Patil

Dissertation submitted to the Faculty of the Graduate School of the
University of Maryland, College Park in partial fulfillment
of the requirements for the degree of
Doctor of Philosophy
2022

Advisory Committee:
Professor Anubhav Datta, Chair/Advisor
Professor Inderjit Chopra
Professor James Baeder
Professor Christoph Brehm
Professor Alan Sussman, Dean's Representative

Dedicated to my mother and my father for their sacrifices, and those whose ideas and attitude to life have inspired me:

A P J Abdul Kalam

Srinivasa Ramanujan

Rafael Nadal

Rahul Dravid

Acknowledgments

However your great dedication, you never win or achieve anything on your own. None of this would have been possible without the support of the wonderful people around me. A lot of people have contributed to this research both directly and indirectly. With great pleasure and deep gratitude, I take this opportunity to acknowledge the people who made this possible.

First and foremost, I would like to thank my advisor, Dr. Anubhav Datta. I am truly fortunate to have him as my advisor, who believed in me and gave me this opportunity of tackling an amazing research problem. I have immense respect and admiration for his commitment and patience, and over the years I have tried to imbibe some of it in my life. He has been a great research guide and has always provided time for me and listened to my questions even during his busiest hours, and space for allowing me to work with freedom. I thank him wholeheartedly for all the help, support, advice, and mentorship. His ability to mentor students and direct a research program is exemplary, which I hope to emulate one day.

Next, I would like to thank my thesis committee. I want to thank Dr. Chopra and Dr. Baeder for their advice and mentorship throughout these five years. Dr. Chopra has been a great inspiration, and I am indebted to all his support. The later part of my Ph.D. program had many interactions with Dr. Baeder on CFD coupling, and I benefited immensely from these discussions. I express my sincere gratitude to Dr. Sussman for his insightful comments on my work and being part of my committee despite his busy schedule. Most of my learning on high-performance parallel computing stems from his course, which significantly impacted my research. I would also like to thank Dr. Brehm for being part of my committee at short notice and providing feedback on my work.

The VLRCOE project I worked on allowed me to collaborate with some of the distinguished rotorcraft researchers in government and industry. Roger Strawn and

Andy Wissink from Army AFDD were two key people who always supported this project and our work. The thought-provoking discussions I had with them had a great impact on my research. I thank them wholeheartedly for their unwavering support and enthusiasm. I express my gratitude to Mahendra, Buvana, Rajneesh, and Moble for their constant support of my work whenever I met them during VLRCOE reviews and other events. I would also like to thank the UMD Deepthought2 staff (Thomas) for their help with my research.

My Ph.D. career would not have been the same without my time with the senior students and staff. I want to thank VT Nagaraj for his insightful comments on my research and for teaching me several aspects of the rotor design. I want to thank the two most important people of my early years at UMD – Ananth and Bharath, whom I fondly call sir. The first year was an important one for me where I had so many interactions with them that helped me with the rotorcraft introduction and shaped the rest of my Ph.D. Also, I thank them for always keeping in touch with me after they went from UMD, ensuring I am on the right track, for which I will always be indebted. I am also thankful to Daniel Escobar, Will Staruk, and Tyler Sinotte for all the engaging discussions regarding research. Special mention to my friend and colleague Wanyi, with whom I had the fortune of working on the fuel cell project. I had a great time and learned so many things from her, and I will always cherish that time.

The list is quite long; I hope I don't miss any of them. First, my labmates – Ravi, Abhishek, Shashank, Seyhan, Fred, Emily, James, Lex, and Paulo – thank you for being part of my journey and for your valuable friendships. Special mention to Ravi, my partner in crime for our VLRCOE project, who has greatly supported me and helped me calm my nerves during presentations and examinations on numerous occasions. Next, I want to thank my friends from other departments – Nikhil, Koushik, Animesh, Nishant, Hema, and many others with whom I had a great time these last five years. I have been housemates with Nikhil, Abhishek (five years), Shashank, Koushik, Animesh (three years) – who have tolerated my untidiness and disaster cooking yet still accepted me. Next, I want to thank my friends I met through tennis – Amit, Saptarshi, Sanchit, and Apoorva. Over the last few years, I had a great time playing tennis and having random conversations ranging from tennis to crypto to the U.S. economy and whatnot. Lastly, I want to mention my gratitude to Ericka, whose infectious smile has always put a smile on my face. I had a great time these last five years outside research – playing cricket, tennis, intramural sports, and all the hangouts; more importantly, each and everyone around me made me feel at home away from home, which I will never forget for the rest of my life.

Lastly, I want to thank the most important people – my family and close relatives for their constant support these last five years. I express gratitude to my grandparents, uncles, and aunts, who have always been my well-wishers throughout my career. Words won't do proper justice to my mother and father's contribution in my life. My mother is a true inspiration to me. She has undergone many sacrifices so that I can have a promising career in life. Nothing will repay that. I want to thank her for being the strongest person despite all the challenges. Her constant support in my life is the primary reason for what I am today. I will always be indebted to that. My father is the primary reason why I am into research or academics. He is a professor by profession, a strict one, and has instilled in me the right attitude to work with discipline and dedication. He was always proud of my accomplishments, and I am sure he will be happy to read my work. I will always be indebted for his contributions to my career. I want to thank my brother, who is pursuing a real doctorate, unlike me. He has been there for my mother at critical times when I was far away studying here, and I am forever grateful for that. I will always be indebted to him for his love for me and the things he has done for the family.

Table of Contents

List of Tables

List of Figures

List of Abbreviations

AFDD	(U.S. Army) Aeroflightdynamics Directorate
AGRC	Alfred Gessow Rotorcraft Center
ADD	(U.S. Army) Aviation Development Directorate
AHS	American Helicopter Society (renamed VFS since 2018)
BEMT	Blade element momentum theory
BERP	British Experimental Rotor Programme
CA	Comprehensive Analysis
CAD	Computer aided design
CAMRAD	Comprehensive Analytical Model of Rotor Aerodynamics and Dynamics
CATIA	Computer Aided Three-Dimensional Interactive Application
CFD	Computational Fluid Dynamics
CREATE	Computational Research and Engineering Acquisition Tools and Environments
CSD	Computational Structural Dynamics
DoD	(U.S.) Department of Defense
DOF	Degree(s) of freedom
FEA	Finite element analysis
FEM	Finite element method
FET	Finite element in time
FETI-DP	Finite element tearing and interconnecting - dual primal
FM	Figure of Merit
Garfield	GPU-Accelerated Rotor Flow Field (solver)
FVL	Future Vertical Lift
GPU	Graphics Processing Unit
Helios	Helicopter overset simulations
HPC	High performance computing
ID	Identifier, numerical tag
LCTR	Large Civil Tiltrotor
LO	Lift offset
MFW	Maryland Free Wake
MHB	Modified Harmonic Balance
MPI	Message Passing Interface
MUMPS	Multifrontal massively parallel sparse direct solver
NACA	National Advisory Committee for Aeronautics
NASA	National Aeronautics and Space Administration
OpenMP	Open Multi-Processing
RANS	Reynolds-Averaged Navier–Stokes
RCAS	Rotorcraft Comprehensive Analysis System
RPM	Revolutions per minute
SAM	Structural analysis model
SAR	Structural analysis representation
SMR	Single main rotor

STOL	Short take-off and landing
STOL	Short take-off and vertical landing
TRAM	Tilt Rotor Aeroacoustic Model
UMARC	University of Maryland Advanced Rotorcraft Code
UMD	University of Maryland
VFS	Vertical Flight Society (formerly AHS before 2018)
VLRCOE	Vertical Lift Research Center of Excellence
VTOL	Vertical take-off and landing
VVPM	Viscous vortex particle method
X3D	Experimental three-dimensional dynamic solver

Nomenclature

A	rotor disk area
a	speed of sound
C	damping matrix
C_{M_X}	hub roll moment coefficient
C_{M_Y}	hub pitch moment coefficient
C_Q	torque coefficient
C_T	thrust coefficient
C_T/σ	blade loading
C_P	power coefficient
C_X	propulsive force coefficient
c	blade chord
c_d	sectional drag coefficient
c_l	sectional lift coefficient
D	rotor diameter
F	nodal aerodynamic and internal force vector
F_0	0^{th} harmonic component of F
F_n	n^{th} harmonic complex Fourier coefficient of F
F_{nc}	n^{th} harmonic cosine component of F
F_{ns}	n^{th} harmonic sine component of F
F_X	hub longitudinal shear force
F_Y	hub lateral shear force
F_Z	hub vertical shear force
K	stiffness matrix
LO	lift offset
L/D_e	rotor lift-to-drag ratio
M	mass matrix
M_{tip}	tip Mach number $= V_{tip}/a_\infty$
M_X	hub roll moment
M_Y	hub pitch moment
M_Z	hub yaw moment
M^2c_n	sectional normal force normalized by $\frac{1}{2}\rho a^2 c$
N_b	number of rotor blades
q	nodal solution
q_0	0^{th} harmonic component of q
q_{nc}	n^{th} harmonic cosine component of q
q_{ns}	n^{th} harmonic sine component of q
q_n	n^{th} harmonic complex Fourier coefficient of q
R	rotor radius
Re	Reynolds Number
S	vector storing skyline entries of a matrix
T	time period

T	rotor thrust
Δt	time-step size
V_{tip}	rotor tip speed
z	inter-rotor separation distance
α	shaft tilt angle (positive into flow)
γ	Lock Number
ϵ_{11}	axial strain
ϵ_{13}	transverse shear strain
θ	blade pitch angle
θ_0	collective
θ_{1c}	lateral cyclic
θ_{1s}	longitudinal cyclic
μ	rotor tip speed ratio, aircraft speed $\div(\Omega R)$
ρ	air density
σ	rotor solidity, blade area $\div A$
σ_{11}	axial / bending stress
ψ	blade azimuth angle
Ω	rotor rotation speed

Superscripts

CCW	counter clockwise
CW	clockwise
L	lower rotor
U	upper rotor

All other symbols are defined where used.

Chapter 1: Introduction

This chapter introduces the topic of this dissertation. It covers motivation, a background on the past studies, objectives of this research, and a technical approach to accomplish them.

1.1 Motivation

Helicopters have become a vital means of transportation for their ability to vertically take off and land (VTOL), hover, and perform all-axes controlled flight. These attributes make them ideal candidates for critical missions such as emergency medical evacuation, disaster relief, search and rescue, fire-fighting, law enforcement support, etc. Moreover, they can operate in congested or isolated areas where fixed-wing aircraft and STOL (Short Takeoff and Landing) or STOVL (Short Takeoff and Vertical Landing) aircraft cannot perform due to lack of runways. Despite their utility, helicopters are limited by slow speeds and small ranges due to the poor cruise efficiency of the rotor in forward flight. A typical helicopter such as the Black Hawk UH-60 has a cruise speed of 152 knots (281 km/h). Several new configurations have emerged supported by new technologies to overcome the speed and range limitations inherent to a single rotor helicopter. Tilt rotors, coaxial rotors, and lift or thrust compounded rotors are some of the new configurations. Advanced geometry blades, modern hubs, variable speed engines, slowed rotors, and mission-adaptive morphing rotor blades are some of the new technologies. Behind the success of them all, lies modern aeromechanical analysis.

The design and development of a rotary-wing aircraft is intensive, expensive, and demanding. Moreover, it is an iterative process wherein the designers use computational tools of various fidelity (low to high) to calculate aircraft parameters as the basis to invent or modify a design until the desired level of performance with safety is met. For brand new designs, it is necessary to use high-fidelity tools and wind tunnel testing to achieve a high level of confidence. It takes time to insert new tools into an established industry workflow. The rotorcraft industry is still primarily inclined to use tools based on postdictive models developed years ago, which were calibrated, refined, and fine-tuned for existing aircraft from years of wind tunnel and flight testing. But they are not suitable for new aircraft development. Gordon Leishman emphasized in his book *The Helicopter: Thinking Forward, Looking Back* [1] that it is crucial to invest in new, truly-predictive, high-fidelity tools. With the advent of modern computing, there is little excuse not to do so. It is also economical as the price of the chip generally falls with time as opposed to parts and labor that always rise.

Consider the example of modern coaxial rotors and tilt rotors. The modern coaxial is designed for high speeds, around 250 knots. This is made possible by thrust compounding pusher-propellers and heavy hubs that carry high roll moments, allowing the individual rotors to produce high lift on their advancing sides. Figure 1.1(a) shows the Sikorsky-Boeing SB-1 Defiant aircraft in flight. The hub is large and heavy to carry these moments. These hubs increase the vehicle's weight and drag, which in turn cuts into the cruise performance. Accurate predictions of the stresses and strains are needed to minimize weight and drag. The modern tilt rotor is designed for even higher speeds, close to 300 knots. Figure 1.1(b) shows the Bell V-280 Valor aircraft in flight. Current tilt rotors have heavy proprotor blades and hubs. The weight of these components is driven by the critical stresses experienced due to high unsteady aerodynamic loads. A heavy rotor makes the wing thick (up to 23% chord) to prevent whirl flutter instability, which in turn cuts into the cruise performance. Again, accurate predictions of the stresses and strains are needed to minimize weight and drag.

(a) Sikorsky Boeing SB-1 Defiant Coaxial Rotor

(b) Bell V-280 Valor Tilt Rotor

Figure 1.1: Future Vertical Lift (FVL) configurations; (a) Coaxial rotor, and (b) Tilt rotor.

The state-of-the-art rotorcraft computational analysis is the coupled CFD/CA methodology [2]. Computational Fluid Dynamics (CFD) uses three-dimensional (3D) Reynolds Averaged Navier Stokes (RANS) based solvers for modeling rotor aerodynamics. Comprehensive Analysis (CA) uses computational structural dynamics (CSD) coupled with lifting-line aerodynamics, wake models, and flight dynamics and controls.

Computational structural dynamics in rotors use Euler-Bernoulli beam-based models, wherein the rotor blade is modeled as a slender one-dimensional (1D) beam with two-dimensional (2D) sectional analysis to calculate the spanwise structural properties of the blade. Although accurate and efficient for many applications, this approach faces several limitations, such as its inability to accurately model the non-slender three-dimensional (3D) hub components of advanced rotors. Advanced blade tips, cross-section deformations, discontinuities, damage, and cut-outs such as flaps all break the beam assumption. Constant iteration to extract properties and back transform stresses with design changes is also antithetical to the concept of modern CAD-based digital design and manufacture. Presently they almost always rely on priori measurements to derive equivalent root springs and couplings.

In 2008, Johnson and Datta [3] identified 3D structures as a requirement for future comprehensive analysis. The X3D [4] solver attempts to fill this requirement. Before this thesis, the major limitation of 3D structures was its high computational time. It is the principal barrier to the application of 3D finite elements on helicopter rotors. This then, is the central task of this thesis. The intricacies of the rotor structural dynamics pose unique challenges to this task. Its low damped modes, modes near resonance, complex load paths, joints and bearings, control inputs, and poorly conditioned matrices make it complicated but also interesting. These complications must be addressed efficiently for a structural model to be admissible for rotor aeromechanics analysis.

1.2 Rotorcraft Aeromechanics

Aeromechanics is the branch of aeronautics that deals with motion and control of elastic aircraft in air. It involves study of multiple disciplines covering aerodynamics, structural dynamics, stability, and control. For a helicopter, the aeromechanics is dominated by its main rotor. Computational aeromechanics predicts performance, loads, vibration, and stability mathematically. Without predictions, designers are forced to rely on expensive wind tunnel tests or flight tests.

The availability of digital computers during the 1960s and 70s had a critical impact on the growth of aeromechanics. A review of rotorcraft aeromechanics can be found in the Nikolsky paper [5] by Johnson. The following two sections will describe the disciplines of aerodynamics and structural dynamics, which are relevant to 3D rotor structural modeling.

1.2.1 Aerodynamics

The analysis of rotor aerodynamics can be divided into two problems: outer and inner. The outer problem calculates rotor inflow. The inner problem calculates the blade airloads. Inflow affects the blade angle of attack, and blade lift generates circulation that produces inflow. Hence the problems are inter-connected. A lifting-line model connects these inner and outer problems by ensuring lift, inflow, and angle of attack are all consistent with one another.

Rotor aerodynamics modeling began with Glauert [6] who extended the momentum theory for hover first developed by Rankine (1865) to edgewise flight. These models assume uniform inflow throughout the rotor disk. Gustafson and Gessow proposed the Blade Element Momentum Theory (BEMT) in 1946 [7] for non-uniform inflow in hover. The inflow varies along the radius and includes Prandtl correction to capture the tip-loss effects.

To predict non-uniform inflow in forward flight, the rotor wake must be calculated precisely. Since the wake is dominated by tip vortices, vortex theory is widely used to calculate the wake. The tip vortex model can either be un-distorted (rigid or prescribed wake) or free to distort with time (free-wake). The important contributions to prescribed wake models were from Piziali and DuWaldt [8], and Landgrebe [9–11]. The important contributions to the free-wake models were from Scully [12, 13], Miller and Bliss [14], Johnson [15], Bagai and Leishman [16], and Bhagwat and Leishman [17, 18]. Since 1970s wake models are matured by including empirical models of vortex core size, core growth with time, roll-up, and efficient and effective numerical schemes for trim and transient flight. The work by Bagai and Leishman [16] on pseudo-implicit predictor-corrector (PIPC) scheme developed into the Maryland Free Wake (MFW). This was later upgraded by Bhagwat and Leishman [17, 18] with a predictor-corrector second-order backward (PC2B) scheme for application in both trim and transient flight. Recently Shastry [19] updated the azimuthal discretization with time discretization to allow transient and stopped rotor RPM. The free-wake models are vital for capturing vibratory airloads, without which vibrations cannot be predicted.

For aircraft stability analysis, the wake models are not suitable unless brought to a state-space form. This has been hard. Typically, dynamic inflow models are used instead. Dynamic inflow is an extension of momentum theory with variation in time. These methods represent the inflow using an assumed distribution over the disk as a Fourier series whose coefficients are related to the net rotor thrust and moments. The steady component is the momentum theory solution. The important contributions were from Mangler and Squire [20], Joglekar and Loewy [21], and Pitt and Peters [22, 23]. These models do not calculate individual tip vortices and are therefore inadequate for rotor vibration analysis.

The flow experienced by blades in the inner problem is highly complex due to excitation from blade motions. However, sectional unsteady thin airfoil theory can still be used for first-order predictions of airloads. The sectional angles of attack are calculated from blade motions at three-quarter chord consistent with Weissinger's L theory. The airfoil coefficients are obtained from 2D CFD look-up tables or wind-tunnel tests. The quasi-static airloads are then corrected using 2D unsteady aerodynamic theory. Unsteady theory correct for shed wake. Thus the outer and inner problems formally separate the wake into trailed and shed wake. Corrections are possible in frequency or time domains. The frequency-domain corrections range from the classical Theodorsen and Sears theory to the more accurate Lowey theory for rotors. These ignore compressibility and dynamic stall. Time-domain corrections range from classical Kissner and Wagner to modern semi-empirical models with compressibility and dynamic stall. The popular semi-empirical models are Leishman and Beddoes [24, 25], and the ONERA [26, 27].

Instead of using a lifting-line model that deals with the inner and outer problems, computational fluid dynamics (CFD) can be used to solve the flow directly. Typically unsteady Reynolds-Averaged Navier-Stokes (RANS) equations are solved with turbulence models. Thus airloads and wake are solved all at once, eliminating the need for inner and outer problems. But with that goes the ability to predict induced losses of the rotor. Nevertheless, RANS is essential for capturing the 3D unsteady transonic effects near the blade tip and the dynamic stall inboard. With the advancement of computer power, enough resolution is possible today to capture the wake precisely. For a review of CFD methods in rotorcraft, see Strawn, Caradonna, Duque [28]. For a review of CFD methods in rotorcraft coupled to structures, see Datta, Nixon, Chopra [29].

1.2.2 Structures

In 1958, Houbolt and Brooks gave the linear theory for elastic rotor blades [30]. In 1974, Hodges and Dowell gave the non-linear beam theory retaining up to second order terms for elastic rotor blades [31]. Subsequent years saw many related and independent efforts such as Hodges, Ormiston, and Peters [32], Kvaternik [33], Rosen and Friedmann [34], Johnson [35], Bauchau and Hong [36], Smith and Chopra [37], and Bauchau and Kang [38] to expand the analysis to composites and multibody dynamics. These have now become essential parts of rotor beam modeling. Thus 3D models must retain these capabilities. Multibody dynamics uses joints undergoing arbitrary rotations connecting flexible components. This enables analysis of modern rotor hubs built up from many components, each with its own role. Parallel efforts have focused on improving the calculations of 2D cross-sectional properties [39].

There has been work on analyzing rotor structural dynamics with higher dimensional models but not in helicopter rotors. See Datta and Johnson [40] review for other applications. All these applications have either insignificant centrifugal effect (wind turbines) or no blade motions (turbo-machinery), and none deal with integrated aeromechanics.

In summary, one-dimensional beam models have remained the dominant state of the art in rotor structural dynamics. It may be fair to say that aerodynamics has gone far ahead to harness the explosion in computer power by effective RANS solutions to replace lifting-line aerodynamics. It is time to do the same in the structural domain by developing three-dimensional finite element solutions to replace beams.

1.3 The X3D Solver

In 2006, the U.S. Department of Defense (DoD) High Performance Computing Modernization Program (HPCMP) Computational Research and Engineering Acquisition Tools and Environments (CREATE) program was launched to develop and deploy set of multi-physics high performance computing (HPC) software tools to aid the DoD acquisition community (government and industry) develop innovative military air vehicles [41]. The program consisted of several domain-specific software products. One of them was HI-ARMS which produced the software Helios dedicated to the high-fidelity analysis and design of rotary-wing aircraft. Initially, it focused only on CFD. During that time, the NASA survey in 2008 identified 3D structures as one of the essential requirements for next-generation comprehensive analysis [3]. This led to the development of X3D [4].

X3D is an experimental (X) three-dimensional (3D) dynamic analysis software for rotors. It is a departure from current 1D beam-based comprehensive codes as well as commercially available finite element analysis. The flexible parts of a structure are modeled using 3D solid finite elements, which are 27 noded hexahedral bricks. Euler joints with 6 degrees of freedom (3 displacements and 3 rotations) are used to model hinges, bolts, and bearings. The finite element analysis was formulated carefully with emphasis on non-linear strains, inertial couplings, trim controls, and aerodynamics crucial for the analysis of rotating structures. X3D has a built-in lifting-line aerodynamic model and an interface to couple with external CFD software.

Over the years, there have been significant developments to the X3D solver. The timeline for these developments can be broadly divided into three phases. The first phase corresponded to the years between 2008 and 2014. The main goal in this phase was to demonstrate the basic capability of 3D FEA on rotors [42, 43]. Idealized rotor geometries and meshes were used. Once the basic capability of 3D

FEA was demonstrated, an integrated 3D CFD/CA aeromechanics solution for an idealized UH-60A-like rotor was performed in Helios [43]. This initial capability demonstration identified two significant barriers: the lack of 3D modeling tools for geometry and meshing, and the high computational cost, making parallelization in time and space an urgent imperative.

The second phase was during 2014 and 2018. In this phase, the first barrier was resolved. UMD developed 3D geometry and meshing tools for generic rotor blades. This effort was supported by the CAD-based Modeling of Rotary-Wing Structures (CMARS) program of the U.S. Army. NASA Ames Research Center – Aeromechanics Branch specially released the Tilt Rotor Aeroacoustic Model (TRAM) – a 1/4-scaled model of V-22 Osprey tilt rotor to develop and demonstrate integrated-3D (I3D) analysis [44–46]. The UH-60A rotor was modified with extension-torsion coupling to demonstrate self-twist, and increased rotor lift-to-drag ratio for 15% rotor speed reduction at high speeds [47, 48]. The Mars helicopter Ingenuity was stress-tested for adequate safety of flight [unpublished].

The third phase was during 2018 and 2022. In this phase, the second barrier was resolved. The governing equations are now efficiently solved in a parallel and scalable manner in both time and space. This thesis is on time. A contemporary thesis is on space.

1. **Time:** This is the topic of present dissertation. Several papers were published to document the work in progress of this research effort [49–53] culminating in this thesis.

2. **Space:** This is a topic of contemporary thesis. Several papers were published to document the work in progress [54–56].

Parallelization in time allowed the modeling of modern coaxial rotors [52, 53]. These are part of the present dissertation. It also opened the door for other contemporary research at UMD, from the study of double anhedral blades [57] to the design of next-generation Mars helicopter [58, 59]. To understand parallelization in time, a background is needed on Periodic Rotor Dynamics, and why it is particularly difficult in rotors.

1.4 Periodic Rotor Dynamics

The linearized governing equations obtained from a finite element model (FEM) of a structure has the well known form,

$$M\ddot{q} + C\dot{q} + Kq = F \tag{1.1}$$

where M, C, and K are the mass, damping and stiffness matrices respectively. F is the nodal force vector from aerodynamic and internal forces (for nonlinear). The vector q is the nodal solution. Several unique conditions make it difficult to solve this equation to find the periodic solution q in response to a periodic forcing F. These are:

1. low (or zero) damping in many modes (especially lag), makes marching in time to reach periodic solution very inefficient,
2. presence of near (or at) resonance modes (particularly for teetering/gimballed or articulated rotors), makes direct extraction of periodic solution to periodic forcing ill-conditioned,
3. numerical linearization of a large-scale problem into sensitivities typical of beam-based comprehensive codes,

$$F = A_0 + A_1 q + A_2 \dot{q} + A_3 \ddot{q} \tag{1.2}$$

to extract aerodynamic damping is impractical, and

4. numerically stiff problems having a large mass (M) and stiffness (K) matrix typically result in high condition numbers (ratio of highest and lowest frequencies), particularly in presence of joints connecting the finite element structures.

The first two conditions are generic to all rotor models regardless of large– or small– scale, whereas the next two are unique to large-scale structures. Thus, trim solution in rotorcraft with a large-scale structural model is challenging and a fertile ground for innovative parallel and scalable algorithms in time.

Periodic dynamics is a vast area with important applications in a variety of fields, from crystallography [60] to circuit analysis [61], to orbital mechanics [62]. Within mechanics, rotary-wing aeroelasticity has been a key area of application for many years. The commonly used approaches for solving periodic dynamics are broadly classified into: periodic shooting, finite elements in time, time-spectral and harmonic balance methods.

Periodic shooting methods are a variation of time marching methods and simply involve iterations to find the right initial conditions. The main drawback of the shooting methods is stability. In addition, every iteration for initial condition will require many rotor revolutions to attain periodicity (due to condition 1). The initial conditions can also be found by the Floquet transition matrix [63], a method more robust but also more expensive.

Direct extraction of periodicity without time marching can be carried out using finite elements in time, time-spectral methods, and harmonic balance methods. The first two are formulated in the time domain and the latter is formulated in the frequency domain.

Finite elements in time (FET) is a widely used method. This method uses local time shape functions and is well suited for capturing local gradients. It can be traced back to the 1960s when Argyris [64] introduced the method in nuclear engineering.

Borri [65], and Peters and Hou [66] first applied it in rotorcraft to study a flapping rotor. The work was extended by Panda and Chopra [67], and Dull and Chopra [68] to flap, lag, and torsion. The main advantage of FET is that it can capture high-frequency response with a relatively few time elements. These formulations are typically used in conjunction with numerical linearization of forcing to extract aerodynamic damping, thereby overcoming condition 2. However, for large-scale structures, this linearization is impractical, as noted in condition 3.

The time-spectral method uses global time shape functions. It is unsuitable for capturing local gradients. It is also prone to aliasing errors. It is rarely used in structures, but have been used with computational fluid dynamics (CFD) for analysis of helicopter rotor flows [69]. These methods might be suitable for fluids but lead to matrices of overwhelming size in structures with no apparent benefit.

Harmonic balance is a frequency-domain method. It uses Fourier expansions as shape functions. It is a global method and also unsuitable for local gradients. But it has no aliasing errors, and for elliptic problems such as structures where the solution is guaranteed to be smooth, as many harmonics as needed can be introduced to resolve the solution. Several other frequency-domain methods have been explored in large-scale fluid flows from systems including variable time periods [70] to occasional helicopter rotor flows [71], but none of these methods are suitable for near resonance low damped structural dynamics characterized by the four unique conditions given earlier. In rotors, harmonic balance is used routinely since the early work of Peters and Ormiston in the 1970s [72]. It will be shown later that this standard harmonic balance is not scalable to large problems due to matrix structure.

Historically, most efforts to parallelize the numerical solution of partial differential equations focus on the spatial discretization of the problem. In dynamic problems, time adds a new dimension, and when periodic solution is desired, particularly in a low damped near resonance system like the rotor, time becomes a critical bottleneck to scalability. A class of algorithms called Parallel in Time Algorithms (PITA) have been studied since 2001 for dynamic problems [73] and have found applications in various areas, from chemical kinetics [74] to power systems [75]. However, they can fail with second order systems of linear oscillators due to stability problems of near resonance modes (condition 2).

Time is fundamentally a serial concept. It has no boundaries, hence cannot be partitioned and parallelized in the same manner as space. For periodic systems, a transformation to frequency domain can be utilized to solve in parallel. But in addition to this transformation, other modifications are needed to account for the unique conditions 1 to 4 encountered in rotorcraft. These are the principal objectives of this work.

1.5 Coaxial Helicopters

Coaxial helicopters consist of two rotors mounted one above the other on concentric shafts, with the same axis of rotation but turning in opposite directions (counter-rotating). This gives them the natural ability to balance torque. The earliest examples of coaxial rotors were mainly toys and devices used for flight demonstration – Mikhail Lomonosov's clock-spring driven device (Russia, 1754), Launoy and Bienvenu's bow-string driven device (France, 1784), and Gustave de Ponton D'Amécourt's device (France, 1863) from which the helicopter derives its name were all coaxial and used the natural torque balance. The first controlled forward flight by Breguet and Dorand (France, 1935) was a coaxial helicopter. The first helicopter to demonstrate cyclic controls and autorotation was also a coaxial design by Raul Pateras Pescara (Argentina/France, 1923). Today, Kamov (Russia) and Sikorsky (U.S.), design and develop various coaxial rotors. The tiny Mars helicopter Ingenuity was also a coaxial design.

Achieving high speed without compromising hover efficiency has been an enduring quest for rotary-wing aircraft. In hover, the coaxial rotors have a slight aerodynamic advantage – an 8-10% reduction in induced power for the same total thrust than a single rotor with the same number of blades. Moreover, the lack of tail rotor saves power and makes it compact. During the 1970s, Sikorsky found that coaxial rotors can be used to prevent edgewise rotors from running out of lift by allowing roll moments on each rotor. This was later demonstrated by the XH-59A aircraft. Since both rotors have equal and opposite moments, the net is still zero. The roll moment is characterized by lift offset, which is simply the offset of the thrust from the center of rotation. But the roll moments must be absorbed somehow, either by motions or structure. Allow too much motion, and there is a danger of blade strike, preventing which requires greater inter-rotor separation, hence more drag. Have more structure, and the weight increases, which cuts into the payload.

1.6 Articulated Coaxial Helicopters

An articulated coaxial rotor consists of articulated hubs. This is the Kamov (Russia) helicopter. The articulated rotors allow high blade flapping. A large vertical separation is needed to prevent blade strike. Figure 1.2 shows some of the Kamov coaxial rotors. The compact design finds application for shipboard use (Ka-27). They are also used for various Army missions (Ka-50).

For articulated coaxial rotors, the upper rotor and lower rotor collectives θ_o^U, θ_o^L solve for vertical force balance (thrust) and yaw moment balance (torque). The roll and pitch moment equations are solved with a single lateral ($\theta_{1c} = \theta_{1c}^U = \theta_{1c}^L$) and longitudinal ($\theta_{1s} = \theta_{1s}^U = \theta_{1s}^L$) cyclic control, respectively. These coaxial rotors have the same cyclic given to both rotors through two swashplates that are mechanically linked. The inputs control flapping which tilts the thrust vector. This solution is acceptable because the hub moments are not a concern for these rotors. The body pitch and roll angles are found from propulsive force and side force balance.

(a) Kamov Ka-27

(b) Kamov Ka-50

(c) Kamov Ka-226

Figure 1.2: Examples of classical coaxial rotors; (a) Kamov Ka-27, (b) Kamov Ka-50, and (c) Kamov Ka-226.

1.7 Hingeless Coaxial Helicopters

A hingeless coaxial rotor consists of hingeless hubs. They restrict blade flapping, hence a small vertical separation can suffice. But the hub moments are very high and must be absorbed by heavier structure. The hub roll moments are quantified as a lift offset from the hub. It is defined as,

$$\mathrm{LO} = \frac{|C_{M_X}^U| + |C_{M_X}^L|}{C_T^U + C_T^L} \tag{1.3}$$

where $|C_{M_X}^U|$ and $|C_{M_X}^L|$ are the hub roll moment magnitudes of the upper and lower rotors respectively, and C_T^U, C_T^L are thrust coefficients. The magnitude of the roll moment is taken since their signs are opposite. The lift offset (LO) has a dimension of length and is typically represented as a fraction of the rotor radius. Higher the speed, greater the LO, hence higher the loads. Absorbing higher loads with less blade motion needs more stiffness, leading to greater stress and more weight.

Similar to articulated rotors, the collectives of upper and lower rotors solve for the total thrust and yaw moment balance (torque). However, the cyclic controls are solved differently. For rotors with high flap frequency, the longitudinal cyclic (θ_{1c}) primarily produces the roll moment, and lateral cyclic (θ_{1c}) produces the pitch moment. The lateral cyclic is kept same for both upper and lower rotors ($\theta_{1c}^U = \theta_{1c}^L = \theta_{1c}$) and this value along with the two longitudinal ($\theta_{1s}^U, \theta_{1s}^L$) cyclics are solved for a specified lift offset and net roll and pitch moments. The body pitch and roll angles are found from propulsive force and side force balance.

Figure 1.3: Sikorsky XH-59A flight demonstrator of the Advance Blade Concept (ABC) Rotor.

In the 1970s, Sikorsky introduced the Advancing Blade Concept (ABC) for coaxial rotors [76]. The experimental XH-59A (Figure 1.3) flight demonstration program was setup in collaboration with US Army and NASA [77, 78] to demonstrate the basic viability of this concept. While proving the basic viability of the concept, the XH-59A was compromised by many aerodynamic and structural dynamic factors, from heavy hub to high vibration which led to lower speeds than initially intended. During the 2000s, Sikorsky revisited the ABC rotor concept intending to resolve problems of XH-59A. They carried out flight tests of what was now called the X2 Technology Demonstrator (Figure 1.4(a)) [79–82]. The X2-TD is a 6,000 lbs aircraft which recorded a 250 knots steady-level flight in 2010. This led to the development of a larger 11,000 lbs S-97 Raider aircraft (Figure 1.4(b)). Since 2014, Sikorsky has conducted several tests of the S-97 Raider – model-scale tests at the National Full-scale Aerodynamics Complex 40 by 80 ft wind-tunnel at Ames Research Center [83], and flight tests [84–86]. In 2019, Sikorsky introduced the Raider X configuration for the Future Attack Reconnaissance Aircraft (FARA) program.

In late 2013, the Sikorsky-Boeing team entered the Joint Multi-Role Technology Demonstration (JMR-TD) program that marked the beginning of the even larger

30,000 lbs Sikorsky-Boeing SB-1 Defiant aircraft (Figure 1.4(c)). The first flight was in 2019, and several more have occurred since then. In 2020, SB-1 Defiant was shortlisted for the Future Long-Range Assault Aircraft (FLRAA) program alongside the Bell V-280 Valor tilt rotor aircraft. The FLRAA program was initiated by the U.S. Army to develop a successor to the Sikorsky UH-60 Black Hawk utility helicopter as part of the Future Vertical Lift (FVL) program. The SB-1 aircraft has undergone several flight tests and has demonstrated flight with speeds above 200 knots with the ultimate goal to reach 250 knots. Sikorsky has also announced to build an intermediate version of S-97 and SB-1 aircraft by 2034, weighing around 20,000 lbs, which is considered as the FVL medium aircraft. It can be clearly seen that the relative hub sizes increase with weight. Hence understanding and predicting the stresses of blades and hub components is critical for designing a low-weight modern coaxial rotor.

(a) Sikorsky X2, W = 6,000 lbs

(b) Sikorsky S-97 Raider, W = 11,000 lbs

(c) Sikorsky-Boeing SB-1 Defiant, W = 30,000 lbs

Figure 1.4: Examples of modern high-speed coaxial rotors; (a) Sikorsky X2, (b) Sikorsky S-97 Raider, and (c) Sikorsky-Boeing SB-1 Defiant.

1.8 Coaxial Rotor Analysis

It is more challenging and computationally intensive to model the aeromechanics of a coaxial rotor than a single main rotor. These challenges primarily arise from the inter-rotor aerodynamic interactions, stiff hingeless rotors, and the impact of lift offset on trimmed flight. The size of the problem is also doubled. There is a vast literature on modeling coaxial helicopters, but few are validated, and none use 3D structures capable of predicting accurate hub stresses.

An authoritative review of the principal works on coaxial rotors was given by Coleman in 1997 [87]. Escobar et al. in 2021 [88] provides a review of the work performed since. Coaxial rotor analysis can be classified into four categories: 1) isolated momentum and vortex theories, 2) isolated CFD with Reynolds Averaged Navier-Stokes (RANS) modeling, 3) lifting-line aerodynamic models coupled with beam finite elements and rotor trim – the typical comprehensive analysis (CA), and 4) CFD coupled with CA (CFD/CA coupling). The following sections review each category.

1.8.1 Isolated Momentum and Vortex Theory

The classic textbook analysis of a coaxial rotor in hover uses momentum theory. It can be found in any modern text [89]. Leishman and Ananthan [90] gave the blade element momentum theory (BEMT) analysis for coaxial rotors. These analysis are useful when the lower rotor is operating in the fully contracted wake of the upper rotor. For arbitrary inter-rotor separations, vortex theory is desired. Some of the relatively recent work are from Bagai and Leishman [91], Brown 2000 [92], Lim, McAlister, and Johnson 2009 [93], Syal and Leishman 2012 [94], and Singh and Friedmann 2018 [95, 96].

1.8.2 Isolated CFD Analysis

CFD captures the large impulsive blade passage airloads and the inter-rotor interactions from the first principles. The earliest work can be traced to Ruzicka and Strawn [97], and Lakshminarayanan and Baeder [98]. They provided insight into spanwise and azimuthal variations in coaxial airloads, which have been impossible to measure, and established that accurate wake modeling was necessary even for reasonable performance predictions. Juhasz et al. [99] compared results from CFD with blade element momentum theory (BEMT) and free-wake analysis for the old Harrington data [100]. Free-wake and CFD were needed to capture the inflow distribution, near the tip. Reed and Egolf studied the full X2-TD aircraft including the rotor, fuselage, and stabilizers [101]. Bowles et al. [102] studied the same for S-97 Raider aircraft.

Isolated CFD can be adequate for hover performance predictions, but it is insufficient in forward flight, where coupling with structural dynamics and trim solution is essential.

1.8.3 Comprehensive Analysis

The majority of analyses on coaxial rotors use comprehensive analysis. Proper analysis of hingeless coaxial rotors began with Johnson [103], which first quantified the lift offset parameter. This was further extended by Johnson, Moodie, and Yeo [104], confirming the benefits of lift offset with predictions of power and rotor lift to drag, and by Yeo and Johnson [105] to prove that lift offset allowed rotors to break past the McHugh stall boundary. These work were performed using RCAS and CAMRAD II comprehensive analysis, which were validated earlier with the XH-59A data.

Coaxial data obtained from the UT Austin – University of Maryland (UTA-

UMD) wind tunnel tests were used to validate and refine the University of Maryland Advanced Rotorcraft Code (UMARC) by Schmaus and Chopra [106, 107]. Similar validation was repeated with CAMRAD II by Feil et al. [108, 109]. The validated UMARC later formed the basis for Mars aeromechanics studies by Escobar [88, 110].

1.8.4 CFD/CA Coupled Analysis

Several studies have applied CFD/CA coupling on coaxial rotors. The UTA-UMD coaxial test data was analyzed using CFD/CA coupling by Singh, Kang and Sirohi [111] and Singh et al. [112]. Passe et al. [113, 114] carried out the CFD/CA analysis of X2-TD-like aircraft with rotor and fuselage, and this work was further extended by Klimchenko and Baeder [115] by adding the pusher propeller. These studies found strong interactions between the rotor, fuselage, and pusher propeller components. However, there was no available data for validation. Recently, Sikorsky published CFD/CA analysis for S-97 Raider aircraft [84–86]. The analysis was performed using Helios for CFD with RCAS for CA and S-97 flight test data was shown without any units. These studies appeared to capture the harmonic content of the airloads distribution at low and high-speed flights. The aircraft showed high vibrations at low-speed transition flight where the inter-rotor interactions are maximum.

1.9 Objectives of this Thesis

None of the methodologies so far could ultimately predict the 3D stresses and strains on the blades and hub of a coaxial rotor. The current work advances the state of the art by using 3D FEA-based structural models instead of 1D beams. This advancement is enabled and driven by the parallel solver. The aerodynamics uses a lifting-line model with free-wake. There is also a need for an open-source coaxial model instead of proprietary rotors. This open-source model can be a basis for academia, industry, and government joint action to understand the 3D vibratory stress patterns at the hub.

So the objectives of this dissertation are to develop parallel algorithms for 3D structures and bring it to bear on a modern coaxial rotor. The technical approach to meet these objectives is given below.

Part I

1. Study existing periodic solution algorithms used for 1D beams and test their feasibility for 3D structures.
2. Develop a new approach for 3D structures.
3. Integrate the new approach into X3D.
4. Validate new X3D with UH-60A flight test and NASA TRAM tunnel test data.
5. Measure the parallel performance of new X3D.

Part II

1. Develop an open-source notional 3D coaxial rotor model.
2. Refine the X3D for analyzing coaxial rotors.
3. Validate the refined X3D with U.S. Army coaxial test data.
4. Perform 3D comprehensive analysis.
5. Study vibratory loads and stresses versus lift offset and phasing.

1.10 Organization of the Dissertation

The dissertation is organized into nine chapters. Following this introduction chapter, Chapters 2 to 5 cover part I, and Chapters 6 to 8 cover part II. Chapter 2 discusses the existing solution algorithms for periodic dynamics. The feasibility of these algorithms for 3D structures is studied, and key drawbacks are identified. Chapter 3 introduces the new Modified Harmonic Balance (MHB) algorithm. Its development and integration into the X3D solver are described. Chapter 4 verifies and validates the MHB algorithm. The verification is performed on an idealized rotor, and validation on the UH-60A Black Hawk and NASA TRAM test cases. Chapter 5 studies and quantifies the new algorithms' parallel performance using metrics such as parallel speedup, FLOPS, and scalability. Chapter 6 describes the development of notional 3D coaxial models. Two models are reported; one is called the Metaltail – a notional hingeless rotor and the other is an artificially made-up articulated coaxial with two UH-60A-like rotors. Chapter 7 describes the coaxial-related refinements of the X3D solver and its validation with coaxial hover performance data. Chapter 8 performs a 3D comprehensive analysis of the two coaxial models. The predictions are compared with the S-97 published data at low-speed flight. The fundamental understanding of airloads, vibratory loads, and 3D stresses is studied. Finally, Chapter 9 ends with conclusions.

Chapter 2: Three-Dimensional Periodic Rotor Dynamics

This chapter discusses the existing methods to extract periodic rotor dynamics – time marching, finite element in time (FET), and harmonic balance. The feasibility, scalability, and scope of parallelization of these algorithms for three-dimensional large-scale structures are studied, and key drawbacks are identified.

2.1 Finite Element Analysis

The Finite Element Analysis (FEA) used in in the development of X3D solver is based on the established methods by Bathe 1982 [116] and Zienkiewicz and Taylor 2006 [117]. A total Lagrangian weak formulation with Green-Lagrange strains and second Piola-Kirchhoff stresses is used. The details of the theory and formulation can be found in Reference [118]. The material constitutive laws are linear with no yield or fracture.

X3D solver uses 27 noded hexahedral brick elements for the finite element analysis. Figure 2.1 shows a iso-parametric brick element in physical and natural coordinates. It consists of 8 vertex nodes and 19 internal nodes – 12 edge nodes, 6 face nodes, and 1 volume node. It uses iso-parametric formulation with quadratic Lagrangian shape functions.

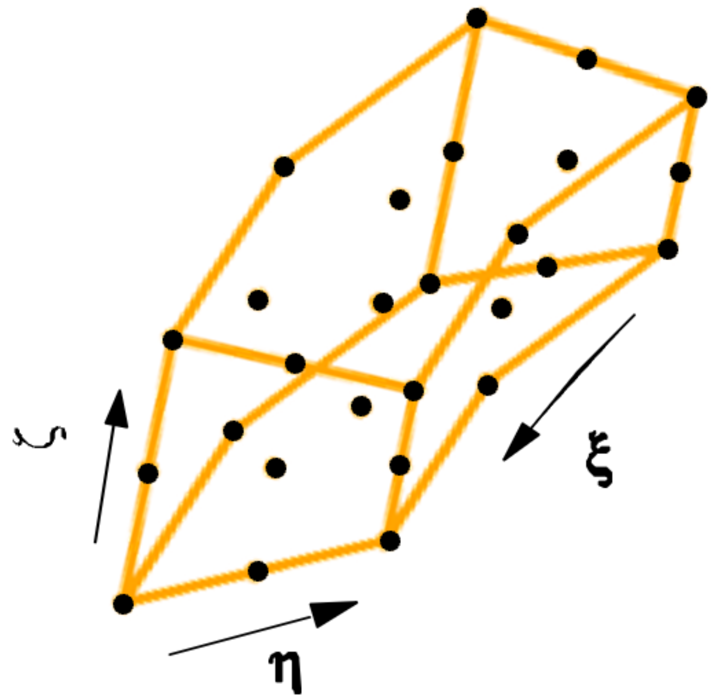

(a) Brick element in physical coordinates

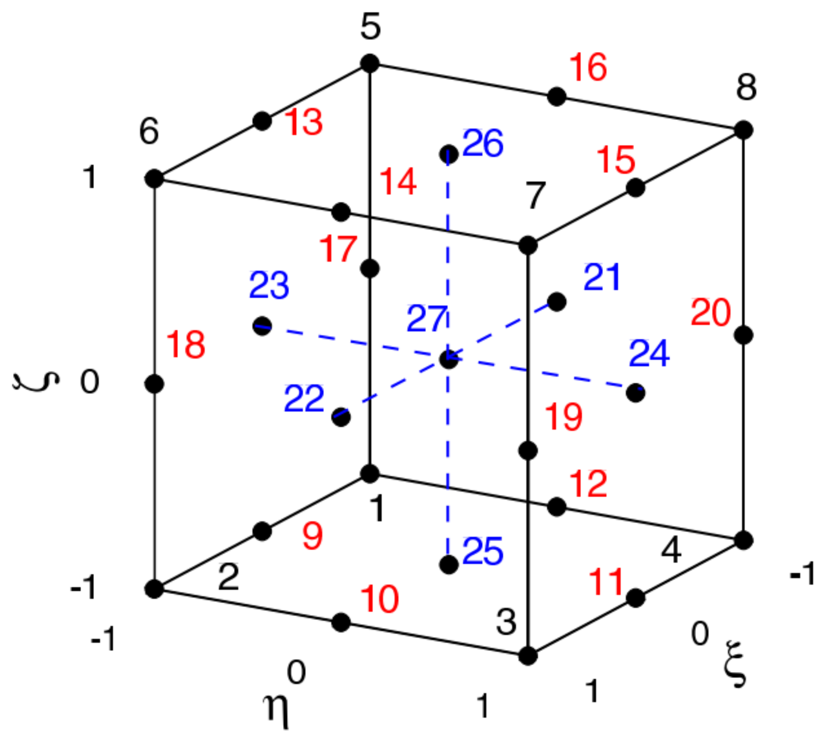

(b) Brick element in natural coordinates

Figure 2.1: 27-node isoparametric, hexahedral brick element in physical and natural coordinates.

The final governing equations for rotor structural dynamics are obtained by substituting the variational energies in to the Hamilton's principle. The linearized governing equations obtained has the well-known form,

$$M\ddot{q} + C\dot{q} + Kq = F \tag{2.1}$$

where M is the mass matrix, C is the damping matrix, K is the stiffness matrix, F is the nodal force vector from aerodynamic and internal forces (nonlinear), and q is the nodal solution vector for all the degrees of freedom.

2.2 Multibody Joints

The 3D FEA in X3D is unified with multibody dynamics to handle joint displacements and rotations. Mulitbody joints are essential to model the connections between parts in a complex structure such as of rotor blade. The X3D solver models joint rotations with Euler angles. The joint degrees of freedom are three displacements and three rotations. They can be free, locked (no motion), commanded (prescribed motion) or actuated (prescribed forcing). They can be assigned mass, stiffness and damping values. The joint degrees of freedom can also be used as load sensors – the joint motions will yield the loads transmitted by the joint as long as they are not locked.

The details of joint formulation can be found in Reference 118. The formulation preserves exact kinematics between the connected parts and allows arbitrary rotation relative to each other up to 90° per limitation of the Euler angles. The algebraic constraints are eliminated to ensure the resulting system of equations are ordinary differential equations. Only holonomic constraints are modeled where the deformation on either side of the joint are related by an explicit closed form relation. Non-holonomic constraints such as contact and friction cannot be modeled.

2.3 Time Marching

Direct time integration methods or time marching have been used to solve the ordinary differential equations since a long time. These methods carry both the transient as well as the forced response, as part of the total solution. In this approach, the governing equation (Eq. 2.1) is integrated over time to calculate the solution at new time step q_{t+1} from the solution at old time step q_t. In discrete time, the integration is reduced to summations which are performed using discretization schemes. Several schemes are available in the literature for second-order dynamic systems. A few popular ones are the Three-point Backward Euler, Trapezoidal, Newmark-beta, Generalized-α, etc., schemes. The details of these schemes can be found in Reference 118.

For rotors, one is interested in the periodic response. The time marching method provides it but one has to wait for the transients to decay. A typical transient rotor response using time marching solution procedure is shown in Figure 2.2. Flap, lag, and torsion degrees of freedom are shown. As expected, time marching requires many rotor revolutions before periodicity is attained particularly in lag, which has little aerodynamic damping. This is a significant barrier for rotorcraft trim solution, which makes them less suitable for large-scale problems.

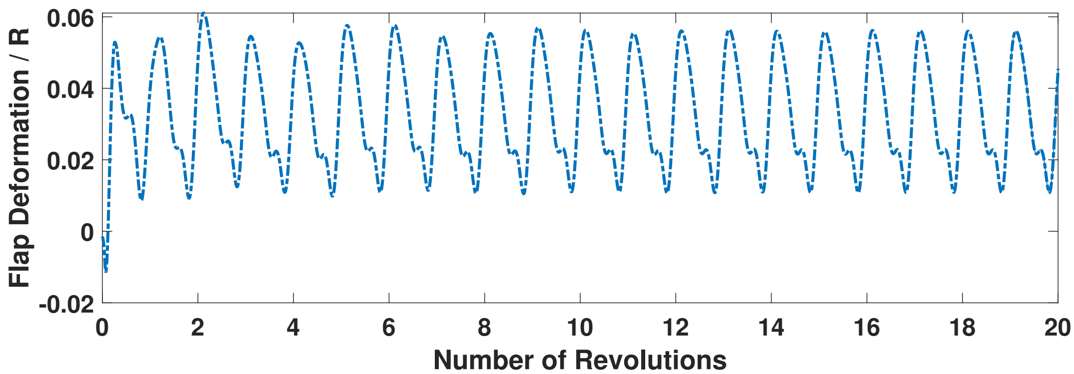

(a) Flap deformation

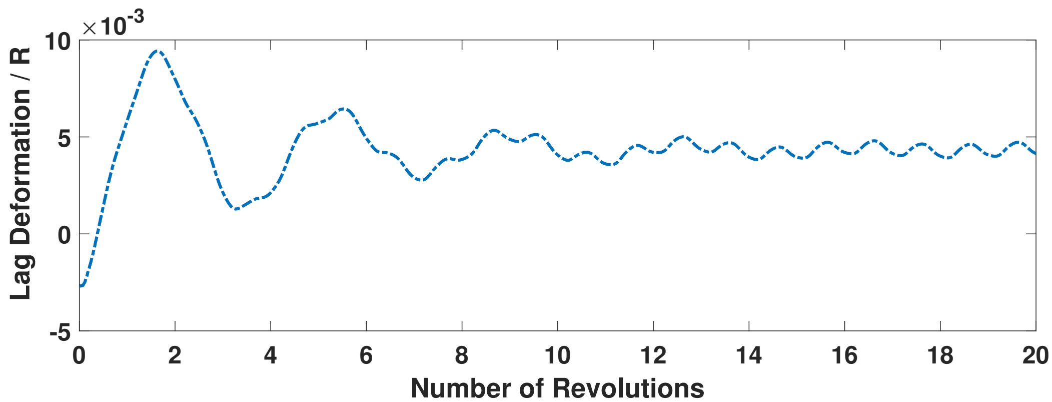

(b) Lag deformation

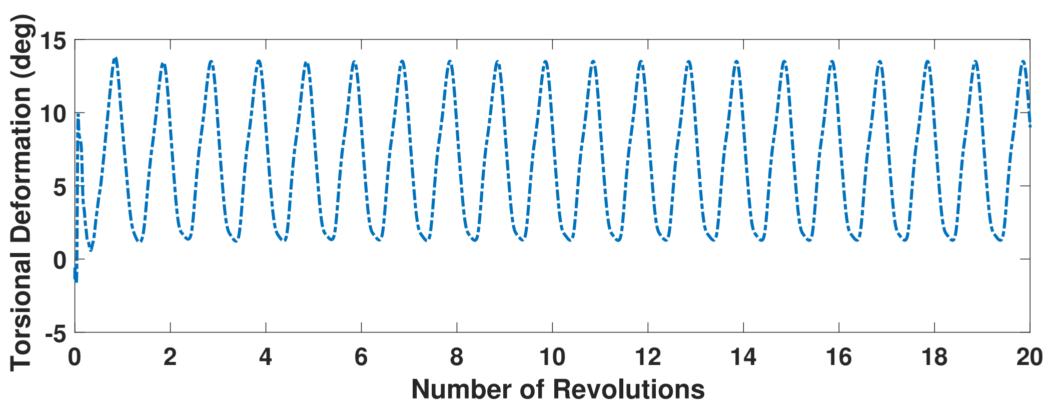

(c) Torsion deformation

Figure 2.2: Time-history of flap, lag and torsional deformation at tip of UH-60A-like rotor in forward flight.

2.4 Finite Element in Time

Finite Element in Time (FET) is used to calculate the forced response of a periodic system directly without initial transients. It is a widely used method in rotorcraft. The overall methodology is similar to that of the finite element method in space, except that the discretization is now performed in the time domain and the boundary condition is periodic.

Consider the governing equation obtained from FEM formulation in Eq. 2.1. For rotors, the forcing vector (F) is a function of both space and time. In time, the forcing is periodic.

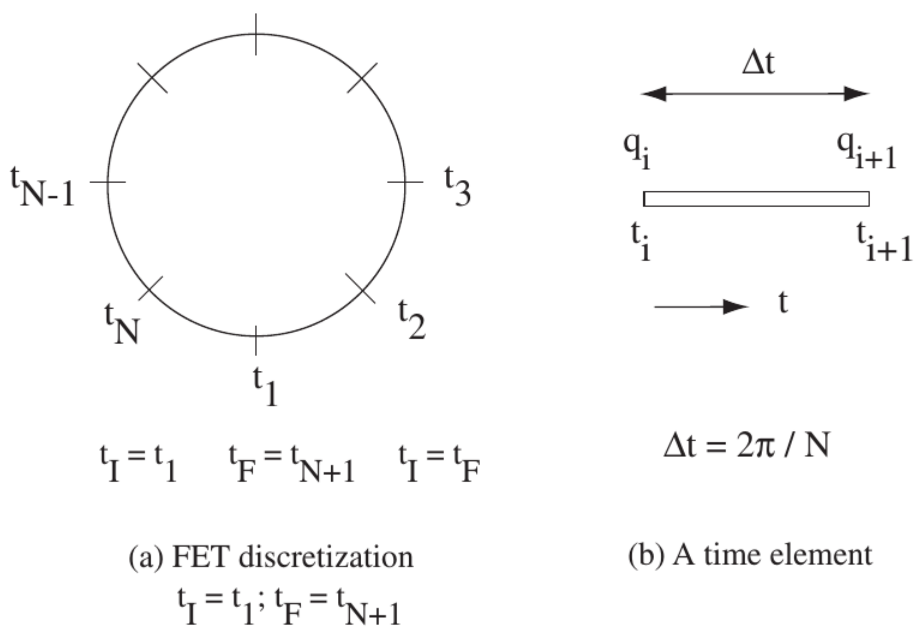

Figure 2.3: Finite Element in Time (FET) discretization of a period of oscillatory motion.

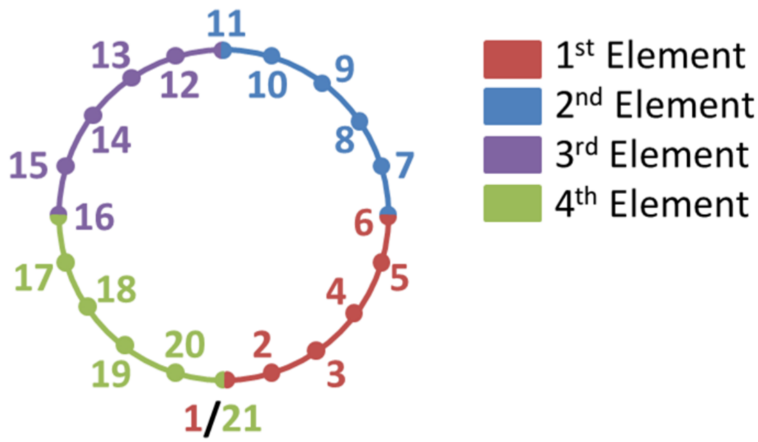

Figure 2.4: Distribution of 4 time elements and time nodes for a rotor periodic system. Each element is shown in a different color. The internal nodes to each element are used to carry the higher order interpolation (5^{th} order in this case).

In FET, the time domain $[0,\ T]$ is discretized into N time elements of length T/N, where $T = 2\pi$ is the period, as shown in Figure 2.3. The initial and final times are the same ($t_1 = t_{N+1}$). In each time element, the degree of freedom q is allowed to vary as a polynomial expressed as a linear combination of shape functions weighted by the value of q at the nodes (shown in Figure 2.4). This assumed variation could be of any order. A 5^{th} order Lagrangian time shape functions is used here. The use of Lagrangian shape functions enforces continuity of q. This is shown in Eq. 2.2 where $H_1, H_2, H_3, H_4, H_5, H_6$ are Lagrangian time shape functions.

$$q(t) = H_1(t)q_1 + H_2(t)q_2 + H_3(t)q_3 + H_4(t)q_4 + H_5(t)q_5 + H_6(t)q_6 \quad t \in [t_1,\ t_2] \tag{2.2}$$

In order to enforce continuity in q and $\dot{q}$, Hermite polynomials can be used. In this case, the velocity ($\dot{q}$) is obtained as follows.

$$\dot{q(t)} = \dot{H_1}(t)q_1 + \dot{H_2}(t)q_2 + \dot{H_3}(t)q_3 + \dot{H_4}(t)q_4 + \dot{H_5}(t)q_5 + \dot{H_6}(t)q_6 \tag{2.3}$$

The solution procedure of FET begins by transforming the governing equations into a variational form. The primary assumption in the FET formulation is that the mass matrix is void of any time-periodic terms. The above-defined shape functions are substituted to obtain the time elemental matrices for each of the elements. The final equation for the elemental time stiffness matrix, A_e, and the forcing vector, Q_e are given below.

$$A_e = \int_{t_1}^{t_2} [-\dot{H}^T M \dot{H} + H^T C \dot{H} + H^T K H] dt \tag{2.4}$$

$$Q_e = \int_{t_1}^{t_2} H^T F dt \tag{2.5}$$

where, M, K and C are mass, stiffness and damping matrices respectively. In the above equations, H is a matrix of the temporal shape functions defined by

$$H = [H_1 I_{N_{dof}} \; H_2 I_{N_{dof}} \; .... \; H_6 I_{N_{dof}}] \tag{2.6}$$

with $I_{N_{dof}}$ being an identity matrix of size N_{dof} by N_{dof} so that the temporal shape function matrix, H, is of size N_{dof} by $6 \times N_{dof}$.

Each time element shares its first and last node with neighboring elements. The elemental matrices are assembled in to a large linear system of equations, given by,

$$A\eta = Q \tag{2.7}$$

where A is global time stiffness matrix, η is the solution vector comprising of displacement at spatial nodes and time nodes, and Q is the global forcing vector.

The global time stiffness matrix, A, is a square matrix of size $N \times (N_{dt} - 1) \times N_{dof}$ by $N \times (N_{dt} - 1) \times N_{dof}$. The global time forcing vector, Q, is a vector of size $N \times (N_{dt} - 1) \times N_{dof}$. Here, N is the number of time elements, N_{dof} is the number of degrees of freedom in space, and N_{dt} is the number of internal nodes within each time element ($N_{dt} = 6$ for the example in Figure 2.4). It is very important to understand the organization of η vector. The first N_{dof} degrees of freedom in η corresponds to the solution q at time $t = 0$. Similarly, the next N_{dof} correspond to the solution q at the second node of the first time element. Hence, the vector is organized by first looping through all space degrees of freedom and then through the time degrees of freedom.

The FET method directly provides the periodic rotor solution, although sometimes iterations are required as the forcing vector depends on the blade deformations. The FET implementation requires the extraction of aerodynamic damping and stiffness terms from the right-hand side forcing vector. This is performed using the classical perturbation approach or by using the exact expressions of aerodynamic forcing. The perturbation approach is a bottleneck for large number of degrees of freedom and the use of exact expressions is cumbersome to account for all the aerodynamic effects. Note that, without the aerodynamic damping on the left-hand side, the FET solution does not converge.

Figure 2.5(a) shows the structure of the three-dimensional Finite Element Model (FEM) stiffness matrix of the UH-60A rotor blade. Figure 2.5(b) is the matrix obtained using Finite Element in Time (FET) with 10 time elements and 5^{th} order shape functions. The structure in both matrices resembles a skyline where only the entries below the stepped line are non-zero. Skyline representation is a form of sparse matrix storage widely used in structural mechanics, where only the entries below the skyline are stored. More details on skyline representation and skyline solver is provided later in Chapter 3. The FEM matrix has a size of around 17,000, but it is tiny compared to the size of the FET matrix. The size of the FET matrix is around 850,000. This makes it impractical for storage. The high ending columns are due to the periodic boundary condition. It also has a higher bandwidth due to the periodic boundary condition. It is seen later in Chapter 5 that the high bandwidth kills the efficiency of the linear system solver. Due to these reasons, the FET is infeasible for a large-scale structural problem.

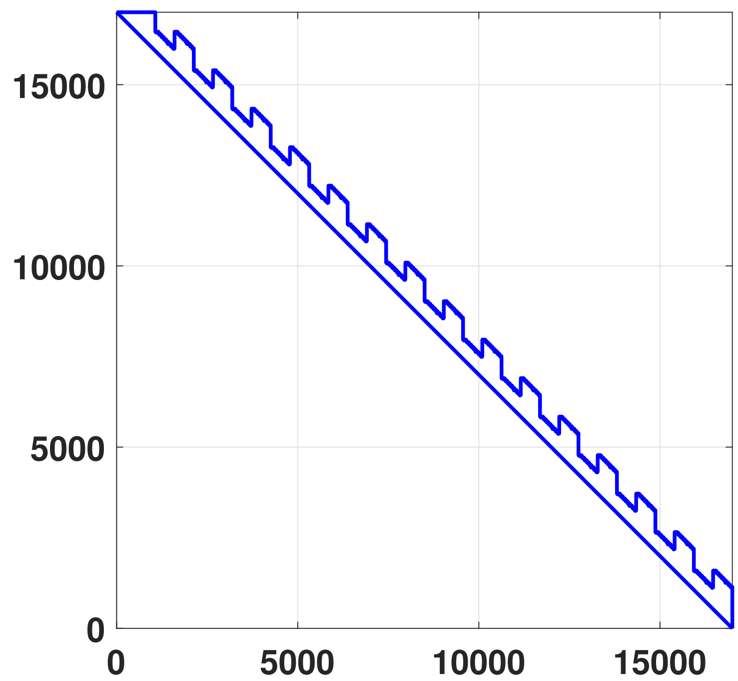

(a) FEM skyline

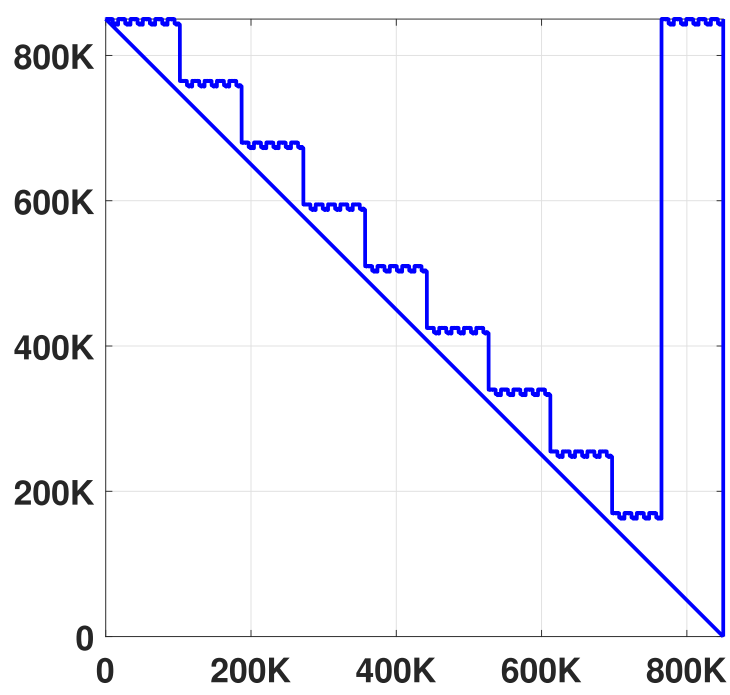

(b) FET skyline

Figure 2.5: . Structure of FEM and FET matrices; (a) FEM skyline, and (b) FET skyline.

Two types of partitions were considered to examine whether the FET matrix can be partitioned. One is a ring-wise partition shown in Figure 2.6(a) and another is a pie-wise partition shown in Figure 2.6(b). A ring-wise partition requires the blade to be also partitioned in space. It was found that this approach was not feasible. This is because the resulting FET matrix structure for each ring does not align with the required matrix structure for applying domain decomposition algorithms on a spatially partitioned blade. A pie-wise partition avoids spatial partitioning. This approach was found feasible. However, the scalability payoff is not significant. This is because a problem is expected to have more partitions in the space domain than in the time domain (a few time elements is sufficient to capture a smooth solution). Thus, even if the memory overhead, high-bandwidth skyline, and pie-wise partition were to be implemented, the potential scalability was expected to be poor.

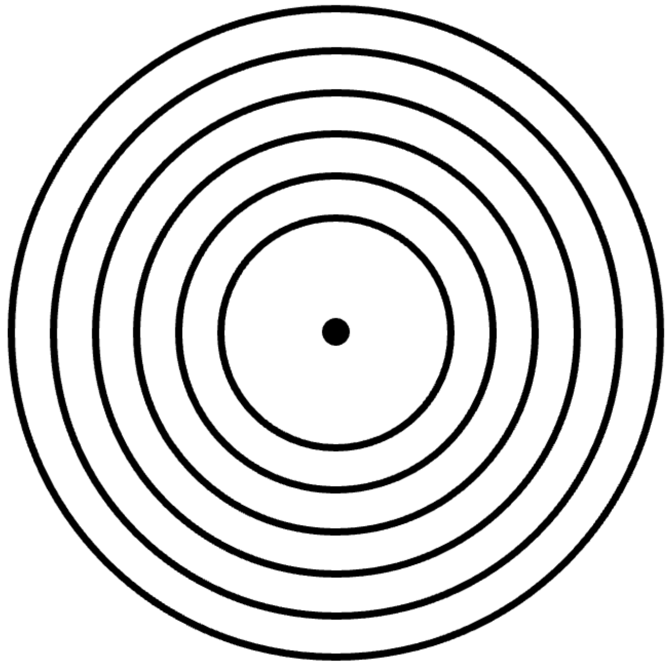

(a) Ring-wise partition

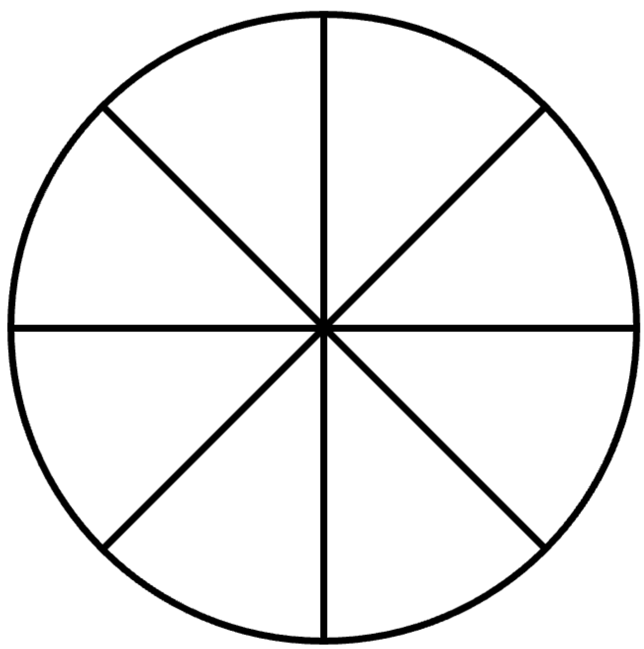

(b) Pie-wise partition

Figure 2.6: Illustration of ring-wise and pie-wise partitioning of FET matrix.

2.5 Harmonic Balance

Harmonic Balance is a method that uses Fourier series approximation to obtain direct periodic solution of the differential equations. Consider the discrete linearized governing equations of the finite element model (FEM) given in Eq. 2.1. In harmonic balance, the solution and the forcing are expanded as equations 2.8 and 2.9 respectively. A total of N harmonics is assumed with a fundamental time period T. For a rotor, $T = 2\pi/\Omega$, where Ω is the rotor speed in rad/sec. The assumption is M, C, K are time invariant, and the time varying quantities are all on the right hand side of Eq. 2.1. For example, if $K = K_0 + \sum_{n=1}^{N} K_{nc} \cos(n\Omega t) + \sum_{n=1}^{N} K_{ns} \sin(n\Omega t)$, then only K_0 is kept on the left hand side, the time-varying part is moved to the right. The right hand side can then be iterated. In rotors, the dominant non-linearity originates from rotation as mentioned earlier. Hence, the stiffness matrix (K_0) is calculated about a rotor solution in vacuum.

$$q = q_0 + \sum_{n=1}^{N} q_{nc} \cos(n\Omega t) + \sum_{n=1}^{N} q_{ns} \sin(n\Omega t) \tag{2.8}$$

$$F = F_0 + \sum_{n=1}^{N} F_{nc} \cos(n\Omega t) + \sum_{n=1}^{N} F_{ns} \sin(n\Omega t) \tag{2.9}$$

To solve for the harmonic coefficients $q_0, q_{1c}, q_{1s}, ..., q_{nc}, q_{ns}$, one can use different approaches. Some of them are mentioned here.

Substituting the assumed solution (Eq. 2.8) and forcing (Eq. 2.9) in the governing equation (Eq. 2.1), and equating the coefficients from left and right-hand sides yields Eq. 2.10.

$$\begin{bmatrix} (K - n^2\Omega^2 M) & n\Omega C \\ -n\Omega C & (K - n^2\Omega^2 M) \end{bmatrix} \begin{pmatrix} q_{nc} \\ q_{ns} \end{pmatrix} = \begin{bmatrix} F_{nc} \\ F_{ns} \end{bmatrix} \tag{2.10}$$

This is the essence of the standard harmonic balance method; the amplitude of Fourier components is balanced frequency by frequency such that the governing equation is satisfied. The accuracy of the solution improves with the number of harmonics, N. The system of equations in Eq. 2.10 is a barrier for large-scale structures as the matrix skyline is broken, it is no longer symmetric, and the sine and cosine components are coupled.

To overcome this problem, Hall et al. [119] developed many variations of the standard method in the context of time periodic fluid flows. These include the standard method with pseudo time marching, the nonlinear frequency domain method, and the time spectral method.

The pseudo time marching introduces a pseudo time τ that is used to iteratively drive the solution residuals to zero. Equation 2.11 is marched in τ using conventional time marching methods. This explicit pseudo time stepping avoids the inversion of a large matrix. This works well for fluid problems, however, when applied to rotors, the number of pseudo time steps required for convergence is large, defeating the purpose of direct periodic solution.

$$\frac{d}{d\tau}\begin{pmatrix} q_{nc} \\ q_{ns} \end{pmatrix} + \begin{bmatrix} (K - n^2\Omega^2 M) & n\Omega C \\ -n\Omega C & (K - n^2\Omega^2 M) \end{bmatrix} \begin{pmatrix} q_{nc} \\ q_{ns} \end{pmatrix} = \begin{bmatrix} F_{nc} \\ F_{ns} \end{bmatrix} \tag{2.11}$$

Time-spectral and nonlinear frequency domain forms of the standard method are essentially identical because one is a similarity transformation of the other. In time spectral form, instead of storing the Fourier coefficients denoted by $\tilde{q} = \{q_0, q_{1c}, q_{1s}, \ldots, q_{nc}, q_{ns}\}$, and $\tilde{F} = \{F_0, F_{1c}, F_{1s}, \ldots, F_{nc}, F_{ns}\}$ as working variables, the solution at a number of time levels equally distributed over one time period are stored. These time level solutions, denoted by q^* for solution, and F^* for forcing, are related to the Fourier coefficients $\tilde{q}$ by a discrete Fourier transform given in Eq. 2.12.

$$
\begin{aligned}
q^* = E\tilde{q} \quad \tilde{q} = E^{-1}q^* \\
F^* = E\tilde{F} \quad \tilde{F} = E^{-1}F^*
\end{aligned}
\tag{2.12}
$$

Substituting Eq. 2.12 in Eq. 2.10 and pre-multiplying the result by E yields,

$$
Dq^* = F^* \tag{2.13}
$$

where D is given by,

$$
D = EA^*E^{-1} \tag{2.14}
$$

In Eq. 2.14, D is circulant and skew symmetric matrix, and A^* is the block matrix constructed by contributions from harmonics 0 to N given in Eq. 2.15.

$$
A^* = \left[\begin{array}{ccccccc}
K & 0 & 0 \ \dots & 0 & 0 & 0 \ \dots & 0 \\
\hline
0 & (K - \Omega^2 M) & 0 \ \dots & 0 & \Omega C & 0 \ \dots & 0 \\
\vdots & \vdots & \vdots \ \ddots & \vdots & \vdots & \vdots \ \ddots & \vdots \\
0 & 0 & 0 \ \dots & (K - n^2\Omega^2 M) & 0 & 0 \ \dots & n\Omega C \\
\hline
0 & -\Omega C & 0 \ \dots & 0 & (K - \Omega^2 M) & 0 \ \dots & 0 \\
\vdots & \vdots & \vdots \ \ddots & \vdots & \vdots & \vdots \ \ddots & \vdots \\
0 & 0 & 0 \ \dots & -n\Omega C & 0 & 0 \ \dots & (K - n^2\Omega^2 M)
\end{array}\right]
\tag{2.15}
$$

The time spectral approach solves the equations in frequency domain using only the time domain variables. This approach is straightforward to work for codes with time domain solvers where little changes are necessary for the implementation. However, for large-scale structure, this approach breaks the system's skyline structure, hence unscalable.

In total, the size of the system and the skyline structure are two important entities that need to be preserved for efficient storage and performance of large scale structures. How this can be accomplished is described in the next chapter.

2.6 Summary and Conclusions

The existing methods to extract periodic dynamics – time marching, finite element in time (FET), and harmonic balance were studied and their feasibility for application to large-scale rotor structures is discussed. Based on this chapter, the following conclusions are drawn.

1. Time marching methods carry both the transient as well as the forced response as part of the total solution. As a result, one has to wait for the transients to decay to obtain the periodic solution. For rotors, this is around 20-25 revolutions in time, which makes it less practical for large-scale rotor applications.

2. The Finite Element in Time (FET) formulation for large-scale rotor structures results in a large matrix size which makes it impractical for storage. It also has a high bandwidth due to the periodic boundary conditions that kills the efficiency of the solver. For these reasons, it is infeasible.

3. The FET matrix was examined for feasibility of its partitioning. Two types of partitions were considered: ring-wise and pie-wise. A ring-wise partition requires the blade to be partitioned in space and is infeasible. A pie-wise partition avoids spatial partitioning and is feasible. However, the scalability payoff with pie-wise partitioning is not significant. Hence, even if implemented the potential scalability is expected to be poor.

4. The system of equations encountered in harmonic balance solution procedure is a barrier for large-scale structures as the matrix skyline is broken, it is no

longer symmetric, and the sine and cosine components are coupled. Hence, the classical harmonic balance cannot be directly applied for large-scale rotor problems. However, modifications to the harmonic balance are possible that circumvent these problems.

Chapter 3: Modified Harmonic Balance (MHB)

This chapter describes a new Modified Harmonic Balance (MHB) algorithm developed for solving large-scale periodic rotor dynamics. A parallel skyline solver forms the core of this algorithm. The rotor solution procedure and its integration in the X3D solver is described. The result of this integration is a new parallel X3D. The pseudo codes for the algorithms developed are provided wherever necessary.

3.1 Modified Harmonic Balance

In the modified harmonic balance method, the solution and the forcing are still expanded as Fourier series, but the solution procedure is modified. Consider again the linearized governing equations obtained from a finite element model.

$$M\ddot{q} + C\dot{q} + Kq = F \tag{3.1}$$

Substituting an assumed solution (Eq. 3.2) and forcing (Eq. 3.3) in the governing equation (Eq. 3.1), and equating the coefficients from left and right-hand sides yields $Kq_0 = F_0$ for zeroth harmonic and Eq. 3.4 for the non-zero harmonics.

$$q = q_0 + \sum_{n=1}^{N} q_{nc} \cos(n\Omega t) + \sum_{n=1}^{N} q_{ns} \sin(n\Omega t) \tag{3.2}$$

$$F = F_0 + \sum_{n=1}^{N} F_{nc} \cos(n\Omega t) + \sum_{n=1}^{N} F_{ns} \sin(n\Omega t) \tag{3.3}$$

$$\begin{bmatrix} (K - n^2\Omega^2 M) & n\Omega C \\ -n\Omega C & (K - n^2\Omega^2 M) \end{bmatrix} \begin{pmatrix} q_{nc} \\ q_{ns} \end{pmatrix} = \begin{bmatrix} F_{nc} \\ F_{ns} \end{bmatrix} \tag{3.4}$$

The system of equations in Eq. 3.4 is a barrier for large-scale structures as the matrix skyline was broken, it is no longer symmetric, and the sine and cosine components are coupled. Two modifications are performed to retain the skyline, bring back a symmetric structure, while still keeping the sine and cosine components uncoupled.

The first modification recovers the symmetric form. This is performed by multiplying the transpose of the left-hand side matrix of Eq. 3.4 on both sides to produce Eq. 3.5.

$$\begin{aligned} \begin{bmatrix} (K - n^2 M)^2 + (nC)^2 & 0 \\ 0 & (K - n^2 M)^2 + (nC)^2 \end{bmatrix} \begin{pmatrix} q_{nc} \\ q_{ns} \end{pmatrix} \\ = \begin{bmatrix} (K - n^2 M)F_{nc} - nCF_{ns} \\ (K - n^2 M)F_{ns} + nCF_{nc} \end{bmatrix} \end{aligned} \tag{3.5}$$

The resulting system is symmetric and keeps the sine and cosine components uncoupled. The problem is that it breaks the original skyline and increases it significantly. The skyline structure of K^2 is different from K, and in general denser.

The second modification recovers the original skyline structure. The matrix $(K - n^2\Omega^2 M)^2 + (n\Omega C)^2$ in Eq. 3.5 has a new and deeper skyline. Figure 3.1(a) shows the skyline of $K - n^2\Omega^2 M$ for the UH-60A-like rotor, whereas Figure 3.1(b) shows the skyline of $(K - n^2\Omega^2 M)^2$. A larger skyline is unacceptable for two reasons: 1) it increases memory requirements for storage; and 2) it increases the computational cost making it an expensive step. This problem is solved by expressing the squared matrix as a product of two complex matrices (Eq. 3.6).

$$\begin{aligned}
&[(K - n^2\Omega^2 M)^2 + (n\Omega C)^2]\ \ q_{nc} \\
&= [(K - n^2\Omega^2 M) + i(n\Omega C)] \times [(K - n^2\Omega^2 M) - i(n\Omega C)]\ \ q_{nc} \\
&= [(K - n^2\Omega^2 M) + i(n\Omega C)]\ \ \hat{q}_{nc}
\end{aligned} \tag{3.6}$$

Equation 3.6 assumes C to be a diagonal matrix where i is the imaginary unit, $i = \sqrt{-1}$. Now two linear solves are performed for each harmonic as shown in equations 3.7 and 3.8.

$$[(K - n^2\Omega^2 M) + i(n\Omega C)]\, \hat{q}_{nc} = (K - n^2\Omega^2 M)F_{nc} - n\Omega C F_{ns} \tag{3.7}$$

$$[(K - n^2\Omega^2 M) - in\Omega C]\ \ q_{nc} = \hat{q}_{nc} \tag{3.8}$$

First, an intermediate solution $\hat{q}_{nc}$ is obtained from Eq. 3.7. Then, the final solution q_{nc} is obtained from Eq. 3.8. The price to pay is two linear solves instead of one. This is acceptable provided there is an efficient and parallel way to solve the system of equations, which is discussed in the later sections.

An alternative approach is to express the solution and forcing in the complex-exponential form directly using equations 3.9 and 3.10 respectively. Here q_n and F_n are the complex n^{th} harmonic Fourier coefficients of the solution and forcing,

$$q = \sum_{n=-N}^{N} q_n\, e^{in\Omega t} \tag{3.9}$$

$$F = \sum_{n=-N}^{N} F_n\, e^{in\Omega t} \tag{3.10}$$

Substitution in the governing equation yields Eq. 3.11. This complex-exponential representation avoids the formation of non-symmetric system in the first place. Moreover, the equation corresponding to each harmonic retains the original skyline.

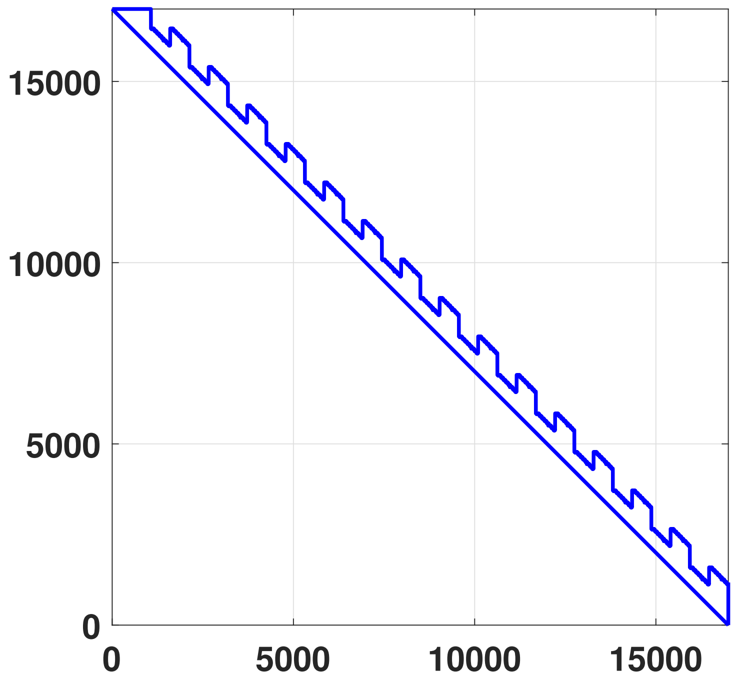

(a) Original skyline

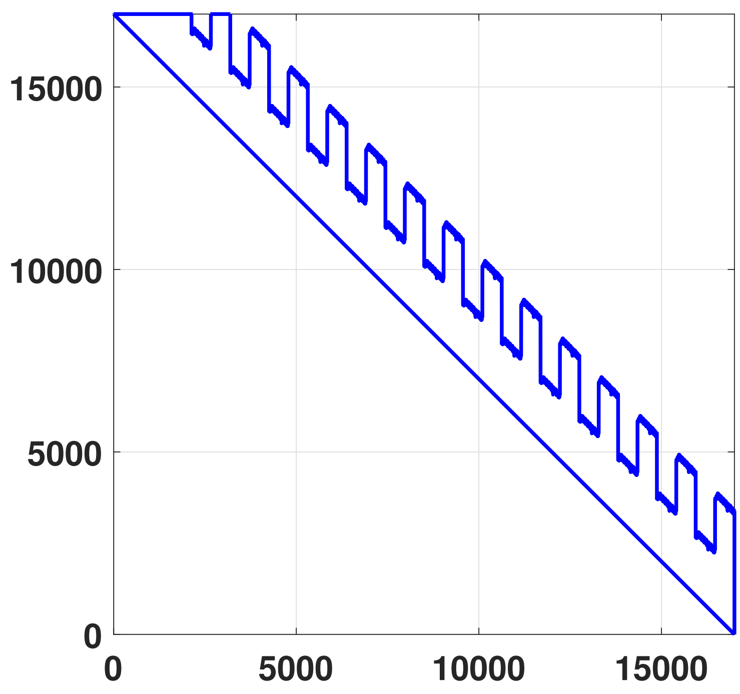

(b) Modified skyline

Figure 3.1: Comparison of original and modified skyline; squaring a matrix alters the structure of its original skyline.

However, it comes at the cost of storage, a complex variable requires twice the storage of a real variable.

$$[(K - n^2\Omega^2 M) + i(n\Omega C)]\ q_n = F_n \tag{3.11}$$

Expressing the solution in complex domain requires necessary transformations between complex and real domain. Equation 3.12 performs the conversion from complex to real, and Eq. 3.13 from real to complex.

$$q_{nc} = 2\ \mathrm{Re}\{q_n\}; \quad q_{ns} = -2\ \mathrm{Im}\{q_n\} \tag{3.12}$$

$$q_n = \frac{1}{2}(q_{nc} - iq_{ns}) \tag{3.13}$$

The real coefficients of the solution (q_{nc}, q_{ns}) are the deflections, which are used to calculate airloads. The real coefficients of airloads (F_{nc}, F_{ns}) are then converted to the complex coefficient F_n, which is used to solve Eq. 3.11. Thus, the harmonic solution q_n is obtained in the complex domain.

Of course, both the formulations produce the same solution. The second approach in complex domain uses one skyline solve per harmonic, making it faster than the first approach when implemented in serial. When implemented in parallel, both approaches yield the solution at the same time as the cosine and sine harmonics are uncoupled. Thus, solving Equations 3.7, and 3.8 (first approach) or Eq. 3.11 (second approach) now lies at the heart of the algorithm. This is described in the next section.

3.2 Linear Algebraic Solvers

To solve a large-system of linear equations $Ax = b$, many types of solvers are available. These are broadly classified into direct and iterative solvers.

1. Direct Solvers: These solvers provide direct (exact) solution by factorizing the matrix A. The factorization can be performed using LU or LDL^T decomposition. These solvers are needed for high condition number problems where exact solution is desired for accuracy as the iterative solvers fail to converge. Various storage techniques can be used for the matrix A. The solvers are often named after these techniques.

   (a) Banded Solver: This is the oldest solver of all the available ones. In a banded solver, the bandwidth of the problem is minimized by rearranging the nodes internally to cluster more non-zero terms near the diagonal. This process of rearrangement can take significant time in a large model. After rearrangement, only N terms are stored for each row, where N is the largest bandwidth. The largest bandwidth is the largest number of entries starting with the diagonal term up to the last non-zero term in any row. These solvers require a modest amount of memory for storage. They are typically the slowest.

   (b) Sparse Solver: In a sparse solver, the nodes are left as they are; instead only the nonzero terms are stored (hence the term "Sparse"). It does not zeros if they are within the bandwidth. However, indexing variables are required to store the locations. Thus, a sparse solver may require more memory than the banded. The sparse solver can provide the fastest solution for problems that have no structure at all by sparse (typically mid-size to large-sized problems).

   (c) Skyline Solver: In a skyline solver, the diagonal and each column above the diagonal is stored. The column height forms a skyline just like in buildings. Zero entries are stored if they are within the skyline. For a typical finite element system, there are not many of them. The exact details of this storage are described later. A skyline solver generally requires less memory than the banded solver. For finite element matrices with a skyline structure, they provide the fastest solution.

2. Iterative Solvers : These solvers provide an approximate solution that converges to the exact solution with proper preconditioning. Thus, the user must specify a convergence criteria. Unlike direct solvers, the number of iterations and floating point operations vary from problem to problem, and with initial conditions. For the right initial conditions and with good preconditioners, iterative solvers can provide the fastest solution. These solvers perform poorly for ill-conditioned problems.

The FEM matrices in structural dynamics and in particularly rotors have high condition numbers which favor a direct solver. It is reliable and guaranteed to converge with a fixed number of floating point operations regardless of the matrix entries. The skyline storage was the best choice for our matrices.

3.3 The Skyline Solver

Finite element matrices have a structure that resembles a skyline. A typical matrix structure for a 3D finite element rotor analysis is shown in Figs. 3.2(a) and 3.2(b). Figure 3.2(a) corresponds to UH-60A-like rotor blade, and Figure 3.2(b) to the NASA TRAM rotor blade. More details on these rotor blades are given in Chapter 4. The presence of multi-body joints can lead to spikes in the skyline structure as seen in the TRAM rotor test case. This increases the bandwidth of the matrix. Moreover, the FEM matrices have high condition numbers $\sim 10^{12}$ or higher (ratio of largest to lowest eigenvalues) and are stiff systems.

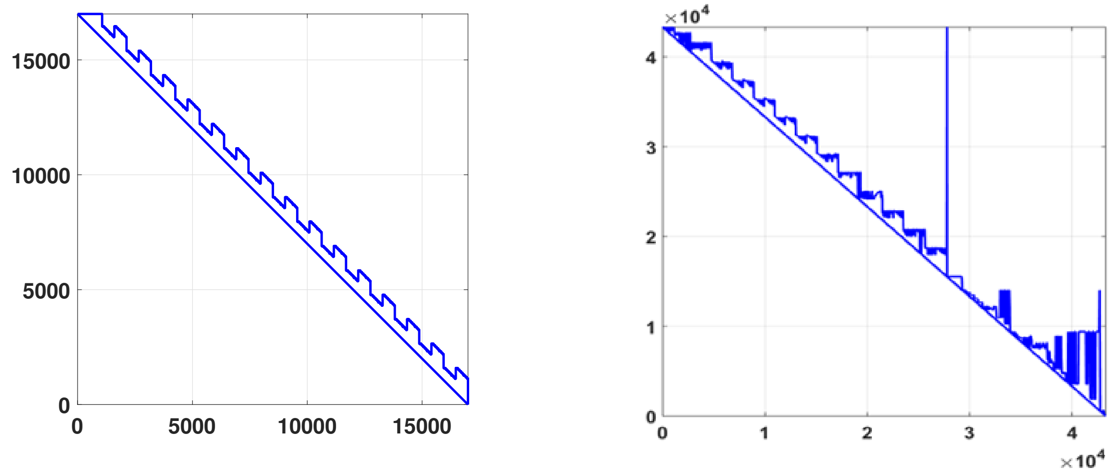

(a) UH-60A skyline

(b) TRAM skyline

Figure 3.2: Skyline structure of the finite element matrices; (a) UH-60A skyline with a single joint; (b) TRAM skyline with 6 joints.

A skyline solver uses direct factorization to solve a system of algebraic equations:

$$Ax = b \implies (LDL^T)x = b, \tag{3.14}$$

where A is a square symmetric matrix, and L and D are lower triangular and diagonal matrices respectively. The solution x can then be found by two triangular solves – a forward substitution $LDy = b$ and a backward substitution $L^T x = y$. The skyline is preserved, which means all the entries that might change from zero to a non-zero value during the factorization (also called as fill-ins) are guaranteed to fall within the skyline; so no entry outside the skyline is ever used or populated. The LDL^T factorization is the intricate and expensive stage.

3.4 Serial Skyline Factorization

Skyline solvers are routine in finite elements, its parallelization is what is novel in this work. But in order to understand the parallel algorithm, it is useful to review the serial algorithm first.

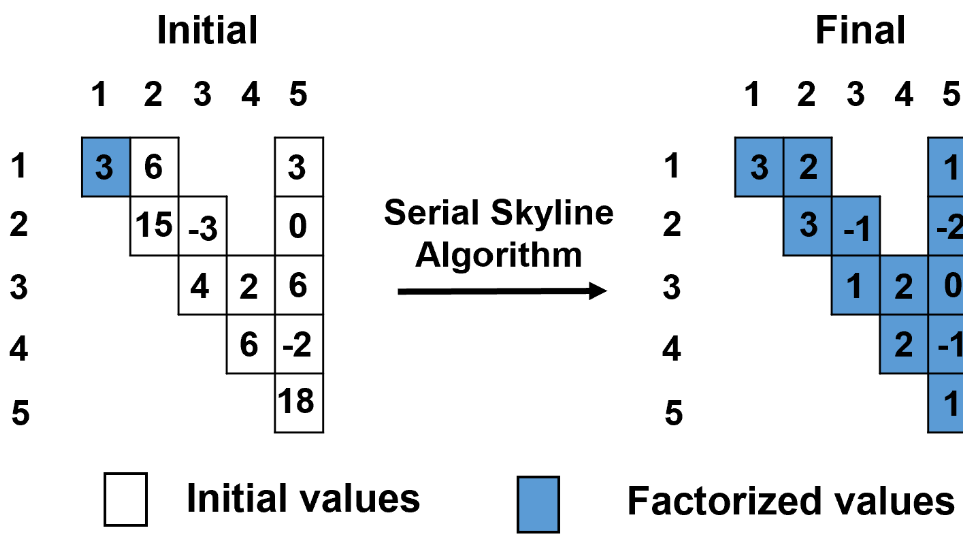

Figure 3.3: Skyline of a matrix in its initial and final states.

Suppose there is a square symmetric matrix A of size (5×5) with a skyline structure as shown in Figure 3.3. It is symmetric, so only the diagonal and upper triangular part is shown. The matrix A is stored as a vector S containing only the skyline entries. Another vector of row pointers r contains the indices of the diagonal positions of each column. In Figure 3.3, S and r are,

$$S = (3, 6, 15, -3, 4, 2, 6, 3, 0, 6, -2, 18)$$
$$r = (1, 3, 5, 7, 12) \tag{3.15}$$

The skyline format stores the entries of the matrix column by column, starting from the first to the last column. Within each column, the entries are stored from the first non-zero row to the diagonal element. The size of the vector r is equal to size of the matrix. The height (h_j) of each column j is,

$$h_j = r_j - r_{j-1} \quad \text{for} \quad j > 1 \tag{3.16}$$

An entry of the original matrix can be found from the skyline vector as,

$$A_{ij} = S(r_j - j + i) \quad \text{for} \quad j \geq i \tag{3.17}$$

In Figure 3.3, the white entries are the initial matrix values, while the shaded entries are the final factorized values. The starting entry will remain the same, hence it is already shaded. After the factorization is completed, S will automatically contain the solution L^T at the non-diagonal positions, and D at the diagonal positions. For our simple example,

$$\text{Factorized } S = (3, 2, 3, -1, 1, 2, 2, 1, -2, 0, -1, 1) \tag{3.18}$$

The factorization of any non-diagonal element at row i and column j is given by Eq. 3.19, and that of any diagonal element in column j is given by Eq. 3.20, where A^{fact} is the final factorized entry and A^{orig} is the original matrix entry. In Eq. 3.19, m_i and m_j correspond to the row number of first element in column i and column j respectively.

$$A_{ij}^{\text{fact}} = \frac{1}{A_{ii}} \left(A_{ij}^{\text{orig}} - \sum_{l=MAX(m_i,m_j)}^{i-1} A_{li}\, A_{lj} \right) \tag{3.19}$$

$$A_{jj}^{\text{fact}} = A_{jj}^{\text{orig}} - \sum_{i=m_j}^{j-1} A_{ij}^2\, A_{ii} \tag{3.20}$$

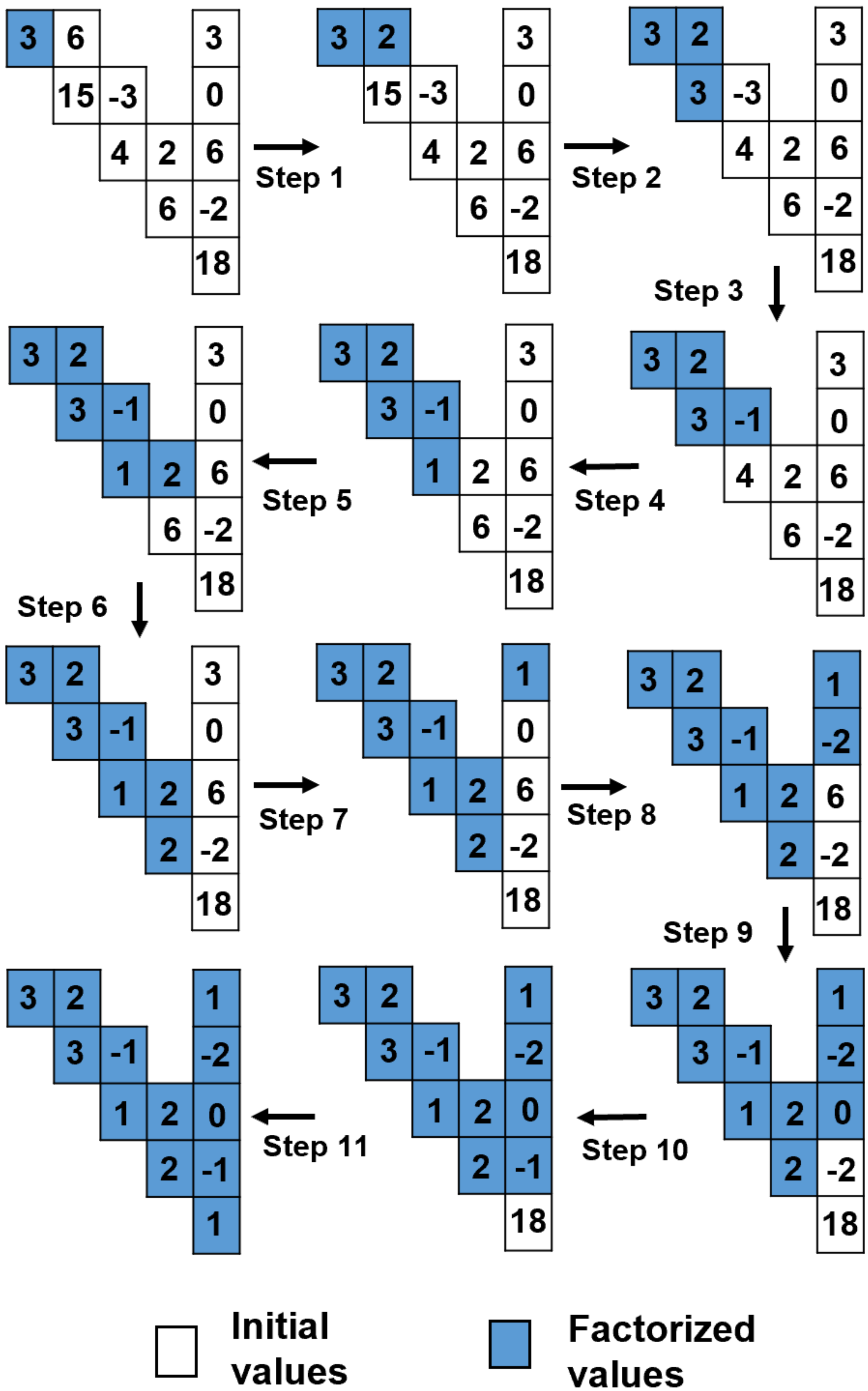

Figure 3.4: Step by step execution of the parallel skyline algorithm.

The factorization is performed each element at a time, in the ascending order of the columns. This process is depicted in Figure 3.4. To compute an element at row i and column j, the following are required:

1. all elements above (i, j) in column j, and
2. all elements up to column i.

Figure 3.5 depicts the operation pictorially. For example, to compute the entry (3,5), information from all the shaded elements is needed. This means all the shaded elements must be factorized before the entry (3,5). Observe, the elements from column 4 are not needed. The parallel algorithm is built to take advantage of this observation.

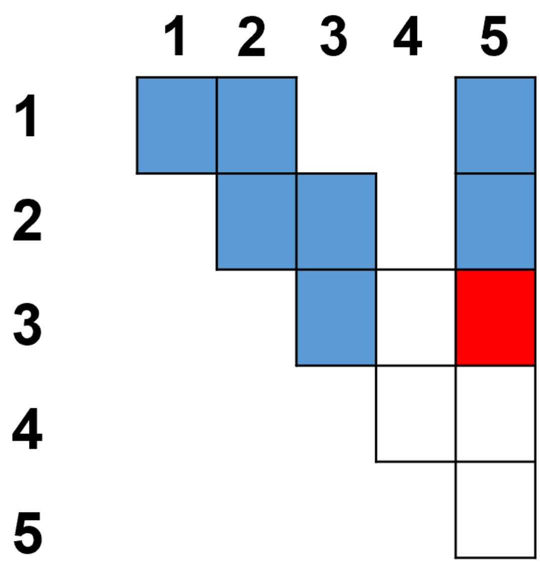

Figure 3.5: Skyline solver algorithm — to compute entry (3,5), all the shaded entries are needed.

3.5 Parallel Skyline Factorization

The parallel algorithm is built for speed, hence involves a large number of communications. Historically these communications were a barrier but with shared memory architectures this barrier can be overcome. Shared memory architectures are best suited because of guaranteed data locality. For purposes of illustration, consider 4 processors, namely $\mathbf{P_0}, \mathbf{P_1}, \mathbf{P_2}$ and $\mathbf{P_3}$. Each processor is assigned a column as shown in Figure 3.6.

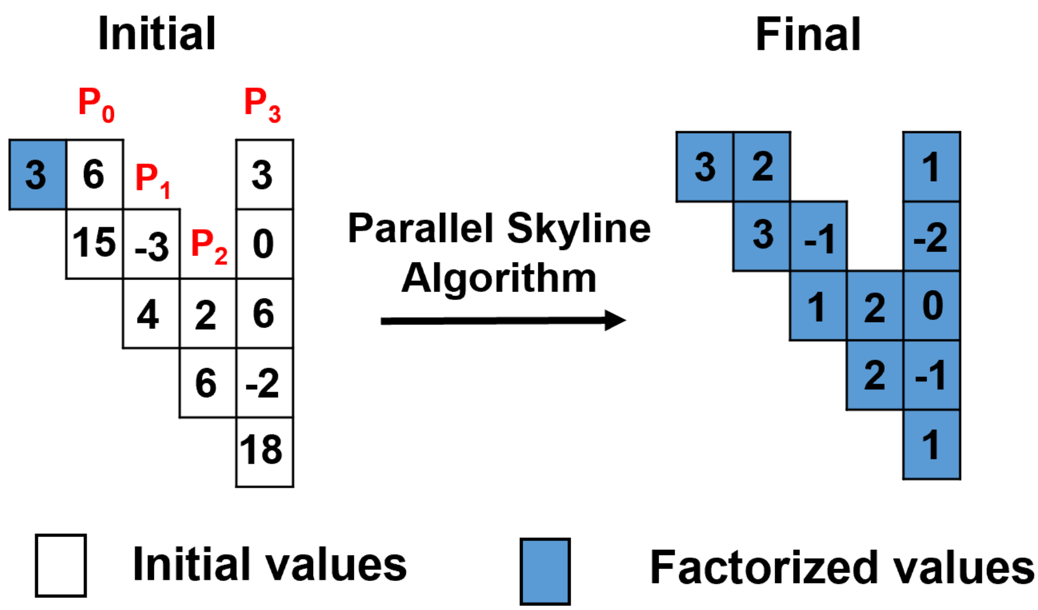

Figure 3.6: Assignment of processors to different columns of skyline.

Each processor is instructed to complete the computations in its column and then proceed to the next available column. In the first step, the processors $\mathbf{P_0}$ and $\mathbf{P_3}$ can compute the first elements of their respective columns. This is because all the elements needed are available. In the next step, only $\mathbf{P_0}$ can compute the next element. Once $\mathbf{P_0}$ has completed the column it was assigned, it can move on to the next available column. Note that, at each step, only the processors which have the required entries available can compute, others have to wait. Figure 3.7 shows a step by step depiction of the parallel execution. The fact that it is stored within the skyline makes it complicated for implementation, but possible, as shown here.

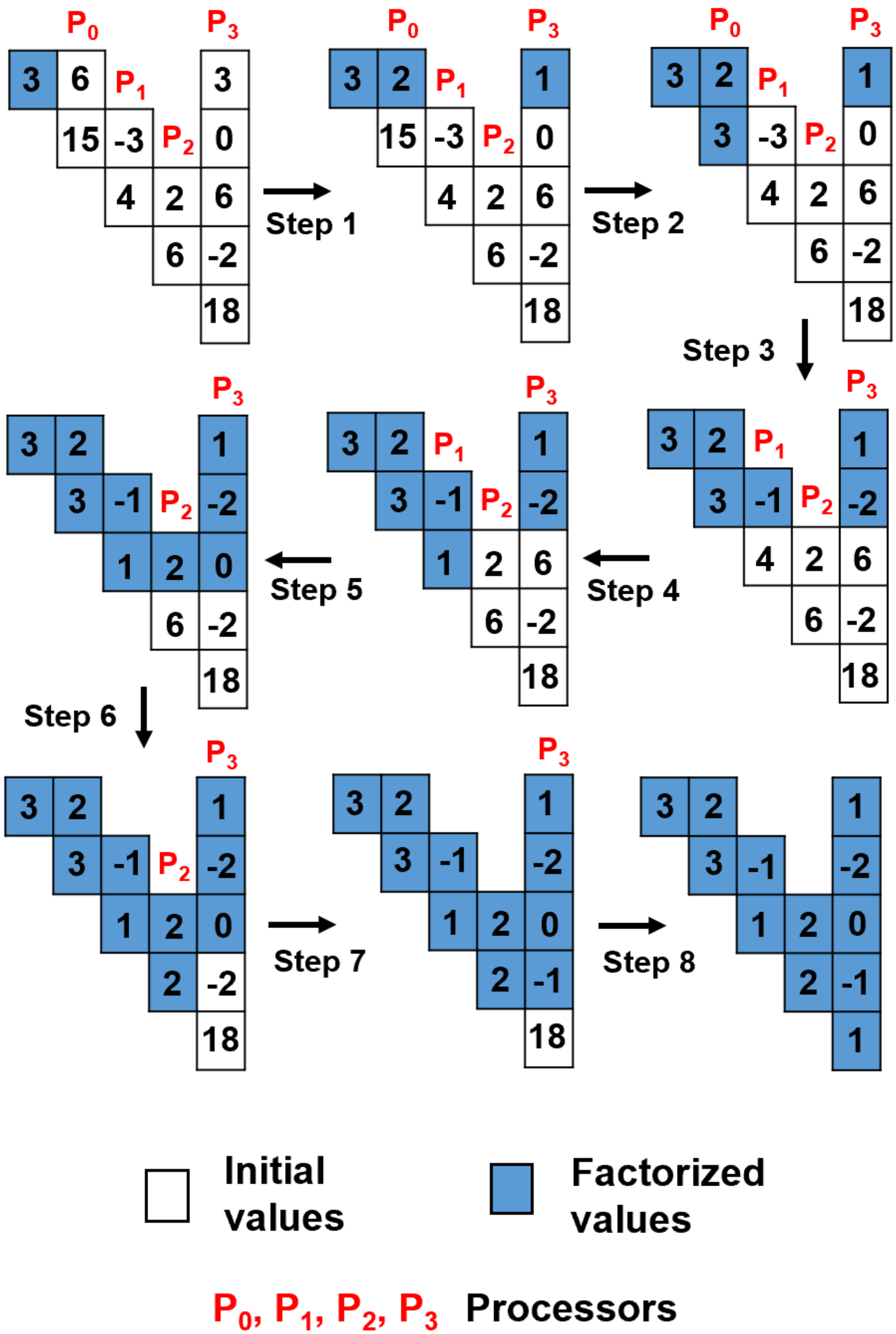

Figure 3.7: Step by step execution of the parallel skyline algorithm.

The pseudo-code of the parallel algorithm of skyline solver is given in Algorithm 1. The algorithm is implemented using OpenMP, which is an API that supports shared-memory programming. The algorithm begins by assigning shared variables: the skyline vector S, and row pointer vector r. Next, private variables are assigned to each processor: namely, the processor number id, the column number j, the position of an element inside the column k, the most recent factorized column number jp, and the most recent factorized diagonal position kp.

The outer loop executes until all the columns are factorized (While loop in line 3). The first step is to assign each processor a column j. Both jp and kp are set to 1 because the first column is already factorized. Each processor cycles over every element k in its column until all are factorized. This is the inner loop (While loop in line 7).

Within the inner loop, line 8 of the algorithm keeps the values of jp and kp current using the OpenMP command FLUSH. The FLUSH command ensures that each processor knows the current values of jp and kp of other processors. The processor assigned to the second column ($j = 2$) can factorize the entire column as the first column ($j = 1$) is already factorized. In general, all the elements of column j can be factorized if column $j - 1$ is available in factorized form (If condition in line 9). If, however, column $j - 1$ is not available, then column j can only be factorized partially (Else condition in line 11) only for entries for which both the conditions mentioned in Figure 3.5 are met (If condition in line 12). For the example shown in Figure 3.7, in step 1 processor $\mathbf{P_3}$ could factorize the first element of its column whereas, processors $\mathbf{P_1}$, $\mathbf{P_2}$ must wait until $\mathbf{P_0}$ completes its column (Wait condition in line 15).

Each processor updates jp and kp once the column assigned to it is factorized entirely (line 20, 21). This step is performed in serial using the OpenMP command CRITICAL, to avoid date races across processors. For the example shown in Figure

Algorithm 1: Parallel Skyline Solver

OMP SHARED (....S, r,....) ▷ Assign shared variables
OMP PRIVATE (....id, j, k, jp, kp,....) ▷ Assign private variables
while {All columns are factorized} **do**
  Assign next available column j to processor id
  jp = Most recent factorized column number ▷ Start with $jp = 1$
  kp = Most recent factorized diagonal position ▷ Start with $kp = 1$
  while {Each element k of column j is factorized} **do**
    OMP FLUSH (jp, kp) ▷ Updates jp, kp on that processor to the most recent written value
    if {Column $(j-1)$ is factorized} **then** ▷ Complete factorization of the column
      Factorize all elements of column j
    else ▷ Partial factorization of the column
      if {Conditions 1 and 2 for each k in column j} **then**
        Factorize each k inside column j that satisfies both conditions
      else
        Wait till the conditions are satisfied
      end if
    end if
    if {Column j is factorized} **then**
      OMP CRITICAL ▷ Performed by one processor at a time
      Update $jp = j$
      Update $kp = r_j$
    end if
  end while
end while

3.7, at the end of second step, processor $\mathbf{P_0}$ updates jp to 2 and kp to 3. The updated jp and kp are flushed across other processors. With the completion of its column, a processor is assigned to the next available column, and the process repeats.

The wait times encountered by the processors during the execution of the algorithm do not affect the solver performance adversely. When a processor is assigned a new column, it immediately begins to factorize what it can. During this time, the conditions necessary for complete factorization are often fulfilled. So the process proceeds to completion. Hence for a problem with many degrees of freedom, it is found that the wait times become negligible as the factorization proceeds.

3.6 Rotor Solution Procedure

The solution procedure for helicopter rotors call for an additional modification. This is generic to all models, large or small scale. But in large scale, the typical linearization to extract aerodynamic damping is no longer practical. Yet, damping is even more crucial in large-scale due to the richer frequency content.

$$M\ddot{q}_k + C_a\dot{q}_k + C\dot{q}_k + Kq_k = F + C_a\dot{q}_{k-1} \tag{3.21}$$

The solution is relatively simple: an artificial diagonal damping C_a is added to the left and removed from the right through iterations. Thus, even at flapping frequency 1/rev, the problem remains well posed. The original Eq. 3.1 is modified to Eq. 3.21. The subscript k refers to the iteration number. A relaxation factor can be used for faster convergence.

The modified harmonic balance is designed for implementation on a large-scale computer architecture typical of a supercomputer consisting of both shared and distributed memory. A detailed description on the specifics of supercomputer architecture is provided in Chapter 5. As stated earlier, the solution of the governing equation is expanded as the sum of harmonics (Eq. 3.2). Since these harmonics can be solved independent of one another, they are computed in parallel using distributed memory architecture (MPI). A total of $N+1$ MPI tasks are assigned for obtaining solution with N harmonics $(0, 1, 2, ..., N)$. Each MPI task is assigned with 10 shared memory processors (OpenMP programming). Overall, hybrid MPI-OpenMP parallelism involving a total of $10 \times (N+1)$ processors is used. Note that the shared memory processors are only spawned when necessary. Figure 3.8 shows the schematic representation of the employment of shared and distributed memory processors in implementing the modified harmonic balance. This hybrid parallelism improves performance dramatically while reducing memory requirements for each processor.

Algorithm 2: Periodic Rotor Response

Start with assumed solution in frequency domain (q_0, q_{nc}, q_{ns})
Assign each harmonic to a MPI task
while {solution q is converged} **do**
    Obtain the mass (M), stiffness (K) and damping (C) matrices ▷ Performed in parallel using OpenMP
    Obtain the nodal solution, velocities in time using Eq. 3.2 $(q, \dot{q}, \ddot{q})$
    Obtain airloads at all azimuths
    Assemble airloads and internal forces to get F ▷ Performed in parallel by each MPI task internally using OpenMP
    Artificial Damping: $F = F + C_a\dot{q}$
    Fourier decomposition of F in complex domain (F_n) ▷ Performed in parallel using OpenMP
    Skyline solve of each harmonic (Eq. 3.11) ▷ Performed in parallel by each MPI task internally using OpenMP
    Convert complex solution q_n to real (q_0, q_{nc}, q_{ns})
end while

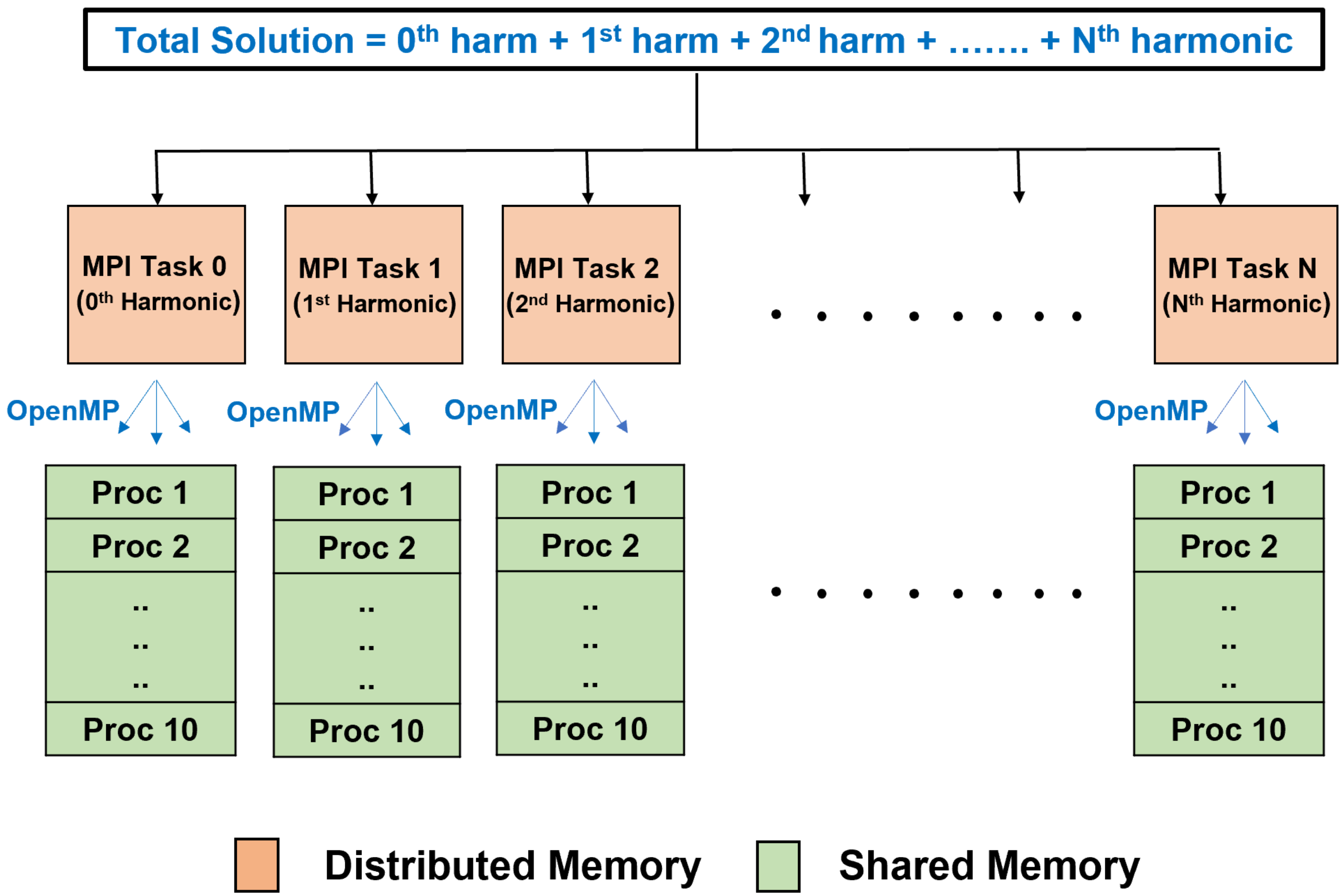

Figure 3.8: Implementation of modified harmonic balance using shared and distributed memory architecture.

A pseudo-code is shown in Algorithm 2. The algorithm begins with an assumed solution in frequency domain (q_0, q_{nc}, q_{ns}) and assigns each harmonic to a separate MPI task. The harmonics are solved iteratively till the solution is converged (line 3). The first step in the iteration is to obtain the mass (M), stiffness (K), and damping (C) matrices. This is followed by computing the nodal solution (q) and velocities ($\dot{q}$) in the time domain using Eq. 3.2 (line 5). These are used to calculate the aerodynamic forcing at all azimuths. The aerodynamic forcing obtained is now assembled as a force vector F using the finite element model at all azimuths (line 7). The next step adds the artificial damping to F and computes F_n (line 8 and 9). The final step solves the system of equations in Eq. 3.11 for each harmonic (line 10) in complex domain (q_n) which is in turn converted to the real domain (q_0, q_{nc}, q_{ns}) for starting the next iteration. The skyline solves of each harmonic are performed in parallel by each MPI task. Within each MPI task the parallel skyline solver is employed across shared memory processors.

3.7 New Parallel X3D

A new parallel in time X3D was developed by integrating the parallel algorithms into the old serial solver. The solver alone was not sufficient to achieve complete speedup. For large-scale non-linear structures with joints, the construction of matrices and forcing vectors at all azimuths contributes significantly to the total solution time. These steps must often be repeated for trim solution. Figure 3.9 shows the pie-chart representing distribution of total computation time for a trim solution. These numbers correspond to the UH-60A-like rotor test case. As expected, the periodic solution procedure is the computationally most expensive operation. The aerodynamics module uses lifting-line free-wake model and has the lowest contribution to the total solution time. The model construction takes around 28% of the total computation time. The model construction workload is distributed across MPI tasks and are internally parallelized using OpenMP. In summary, all the modules of X3D were parallelized to obtain the new parallel X3D. Only the aerodynamics module, inputs, and outputs were left serial. The rationale was aerodynamics will eventually be replaced with CFD which will have its own parallel implementation. The lower order aerodynamics required for that coupling do not produce a significant overhead.

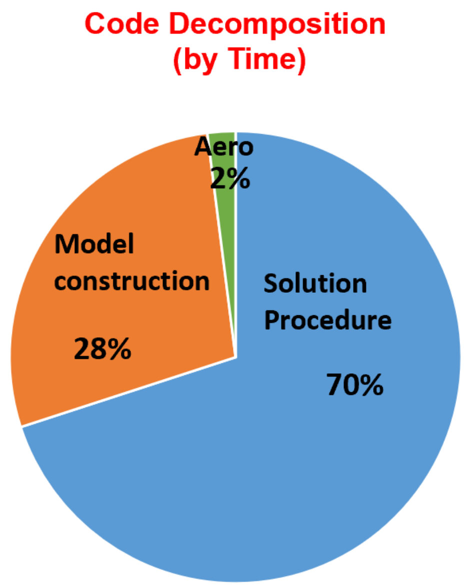

Figure 3.9: Pie chart showing distribution of computation time required for different pieces of X3D solver for UH-60A rotor trim solution.

3.8 Summary and Conclusions

In this chapter, a Modified Harmonic Balance (MHB) method was developed for large-scale structures tailored to the unique requirements of rotary-wing dynamics. The modified method is formulated in the complex domain and built upon a scalable skyline solver and implemented on hybrid shared and distributed memory architecture. The algorithm is integrated into the X3D solver. Based on this work, the following conclusions are drawn.

1. A Modified Harmonic Balance (MHB) algorithm formulated in the complex domain can help retain the original size and skyline of the large-scale 3D finite

element problem.

2. The harmonics of the rotor solution can be solved independently on a distributed memory architecture. This helps to reduce the memory requirements needed when the problem is solved in serial. Inter-harmonic couplings feedback through iterations.

3. Skyline solver can be be parallelized efficiently by taking advantage of data locality of the shared memory architecture.

4. For large-scale finite element structures with multi-body joints, the computation time for model construction (FEM matrices and forcing vectors) can significantly contribute to the overall time, hence parallelization of their construction is crucial, though a trivial task in comparison to the solver.

Chapter 4: Verification and Validation of MHB

Having completed the development of modified harmonic balance algorithm in the previous chapter, the next step is to validate the algorithm. The validation is performed on two different rotor models. But first, a verification test case is considered. The verification rotor is an idealized rotor which is analyzed for tip loading and prescribed aerodynamics. This is followed by the UH-60A Black Hawk single main rotor model, which is studied at hover and forward flight conditions. Finally, the validation is performed on the NASA Tilt-Rotor Aeroacoustic Model (TRAM) at low-speed forward flight with moderate and high thrust conditions. Throughout this chapter, all the predictions from modified harmonic balance are also verified with time marching predictions.

4.1 Idealized Rotor

The idealized rotor model begins with a uniform three-dimensional beam-like structure. This model provides the flexibility of uniform meshing with arbitrary number of finite element bricks. Figure 4.1 shows an idealized beam meshed with 10 $\times$ 1 $\times$ 1 hexahedral brick elements. Two test cases are studied.

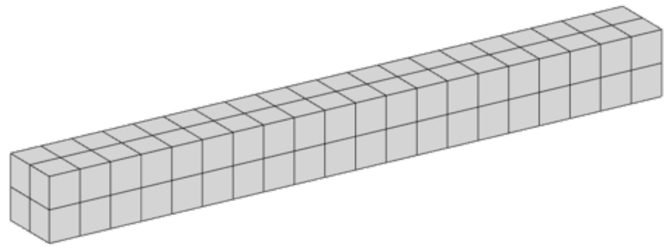

Figure 4.1: Idealized beam meshed with 10 × 1 × 1 brick elements.

The first test case is elementary: a non-rotating beam with a tip force. The force is either kept constant or harmonically varying in time. The tip displacement is verified with the analytical solution. For constant tip force, the solution procedure is a single skyline solve for constant q_0. This test case is ideal to compute the algorithmic performance of the parallel skyline solver (Chapter 5). With harmonic tip force, the solution procedure computes all harmonics. Since the forcing is prescribed and not deflection dependent, this test case is ideal to benchmark the total floating point operations. Details are given later in Chapter 5.

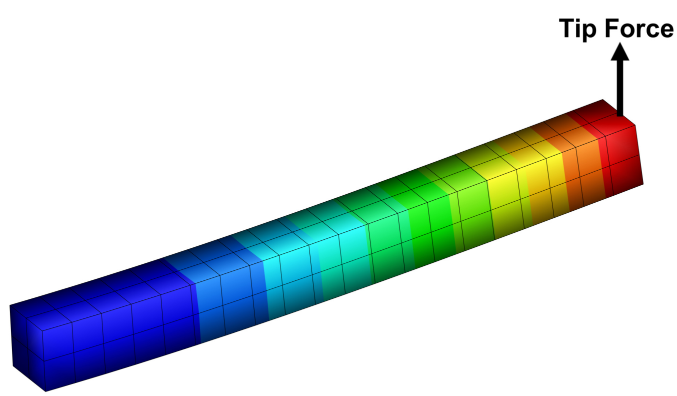

Figure 4.2: Deformation of a 3D cantilevered beam with a tip force; test case used for performance study of skyline solver.

Inclusion of aerodynamics leads to the Frank Harris test case (Reference 120). The test case was developed in 1990s for validating 1D beam bending moments in forward flight. Here it is extended to 3D structures.

The test case was constructed by using the fourth-order flap bending equation. Reference 120 provides the details. A representative beam deflection (z/R) is obtained from curve-fitting experimental data of a particular flight condition. This deflection is substituted in the governing flap equation to obtain the forcing function. The flight condition used here corresponds to an advance ratio $\mu = 0.287$. The blade deflection z/R and forcing dF/dr are analytical expressions consisting of six harmonics. The model parameters are tabulated in Table 4.1.

Table 4.1: Model parameters for Frank Harris test case.

Property	Value
Radius	8.53 m (28 ft)
Rotor speed	221.67 RPM (23.214 rad/s)
Lock number	8
Advance ratio, μ	0.287
Flap Stiffness, EI	5,255,337 Nm^2 (109,760 lb-ft^2)
Mass, m	9.518 kg/m (0.0.1988 slug/ft)

The rotor model is articulated at the root. A mesh size of $10 \times 1 \times 1$, and 567 degrees of freedom is used. The analytical forcing is applied to the degrees of freedom in the vertical (z) direction.

Figure 4.3 shows the tip displacement calculated using various methods and verified with analytical solution. The number of degrees of freedom was deliberately kept small so that finite element in time could also be employed. The implementation of finite element in time uses the formulation mentioned earlier in Chapter 2. Figure 4.3 verifies all three numerical methods provide the same solution and all match the analytical solution. The time marching solution was obtained for different azimuth-steps ranging from 10° to 1°. The solution achieves 5% accuracy with $\Delta\psi = 10°$, 2% with $\Delta\psi = 5°$, 0.5% with $\Delta\psi = 1°$, and 0.1% with $\Delta\psi = 0.5°$. The solution for $\Delta\psi = 0.5°$ is shown in Figure 4.3.

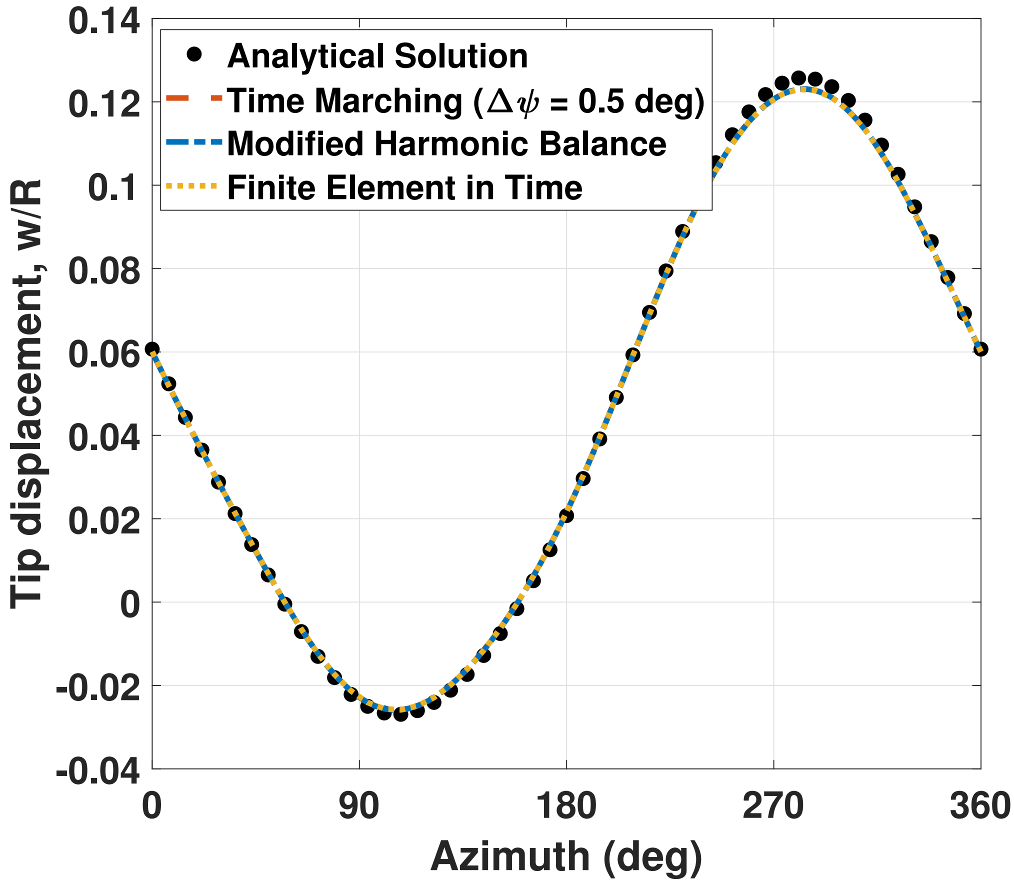

Figure 4.3: Tip displacement obtained using different solution procedures for the analytical rotor flap bending case.

4.2 The UH-60A-like Rotor

A representative 3D model of the UH-60A Black Hawk articulated rotor is used for validation. The internal structure is an idealization (see Figure 4.4), reverse engineered to reproduce similar fan plot as the real rotor. The true internal structure is not available in public domain. The external geometry and aerodynamic description including airfoil decks are nearly exact and follows the Army-NASA Database. Only the trim tab is neglected. The same model has been studied with slowed rotor tests by Ward et al. in Reference [47].

The control inputs are provided through joint commands at the pitch bearing.

The pitch bearing is coincident with the flap and lag hinge co-located at 4.66%R so a single joint is sufficient. The bearing also includes a linear lag damper. The actual damper properties and connection to the blade are complications deemed unnecessary for this validation study. Figure 4.5 shows the 3D model. There are 592 hexahedral bricks with 27–nodes each, a total of 17,523 degrees of freedom. Further details of the 3D model can be found in Reference 43.

The UH-60A rotor model is tested on three cases. The first two cases are made-up test cases used for verifying certain features of the solver and the third test case is a real flight test case used for validating the solver.

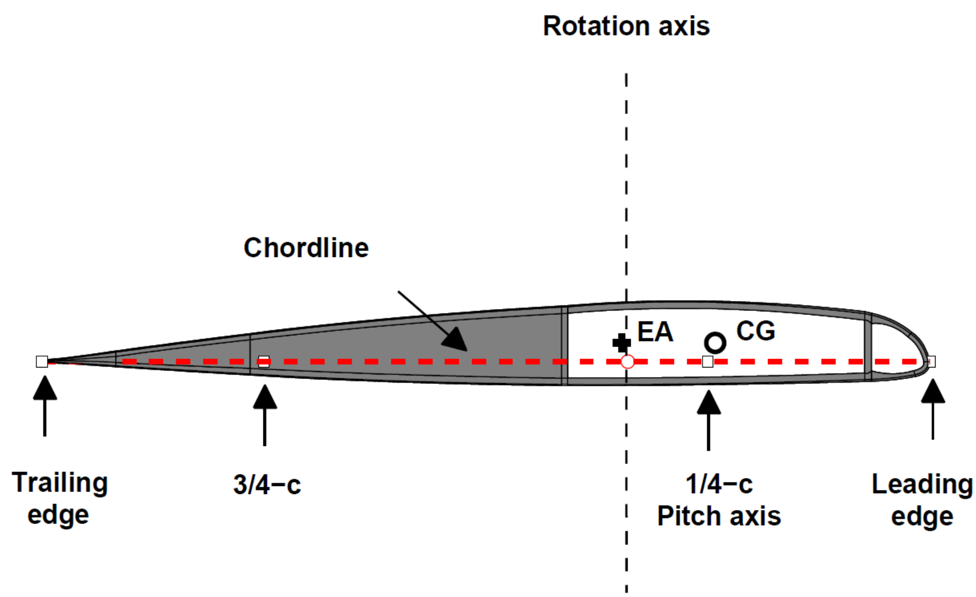

Figure 4.4: Idealized internal structure of a UH-60A-like articulated rotor.

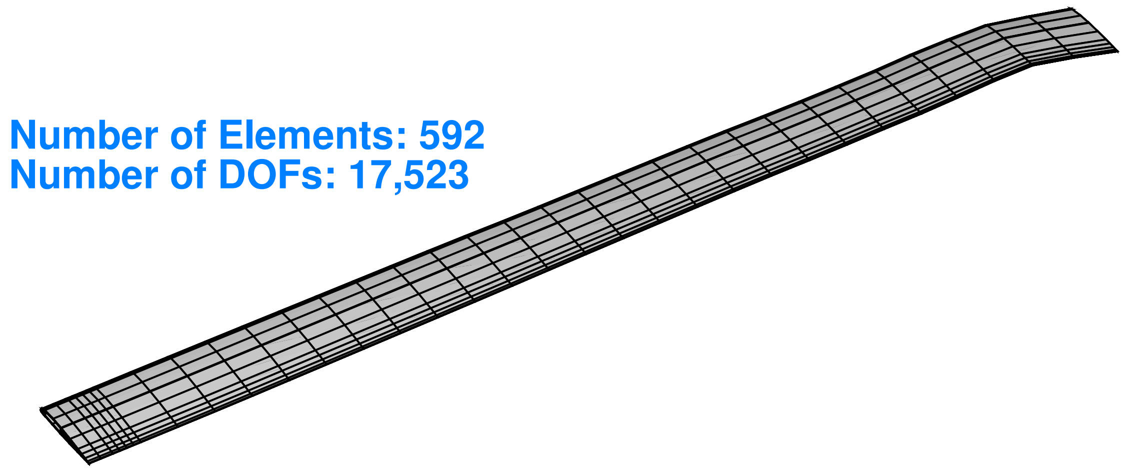

Figure 4.5: Three-dimensional brick mesh of an UH-60A-like articulated rotor; lifting-line geometry and aerodynamic definitions are exact (based on Ames database); the flap, lag, and torsion bearing are at 4.66% R.

4.2.1 Hover with higher harmonic pitch inputs

First, ideal hover flight is simulated with arbitrary higher harmonic pitch inputs. The pitch angle is given by Eq. 4.1, where Ω is the rotor speed and t is the time.

$$\theta = 10^\circ + 3^\circ \cos(\Omega t) - 5^\circ \sin(\Omega t) + 3^\circ \sin(2\Omega t) + 3^\circ \sin(4\Omega t) + 2^\circ \sin(6\Omega t) \quad (4.1)$$

There is no inter-harmonic coupling in hover, only harmonics of excitation are expected in the solution. The solution was obtained with 8 and 12 harmonics. Even though only 6 harmonics are expected in the solution, higher harmonics were solved to confirm they were indeed numerically zero. Figures 4.6(a) and 4.6(b) compare the flap and lag deformations (at tip 1/4 chord). A converged time marching solution obtained with Newmark scheme with $\Delta\psi = 1^\circ$ is also shown. Uniform inflow model was used to avoid harmonics from wake. The harmonic breakdown in Figures 4.6(c) and 4.6(d) show, as expected, only steady, 1, 2, 4, and 6 /rev harmonics are present in the solution. The small steady error in lag is likely a numerical artifact from the time marching solution. The lag is in general too small in this case. The phase error

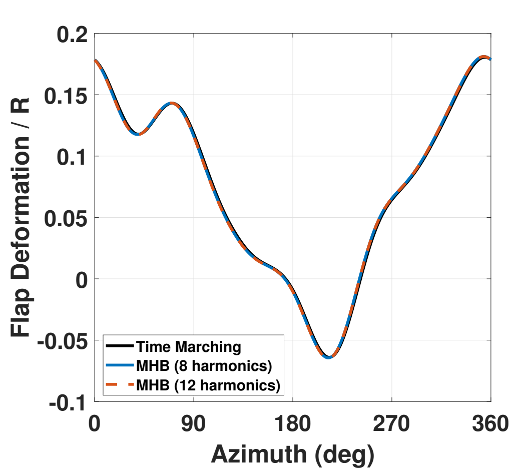

(a) Flap deformation

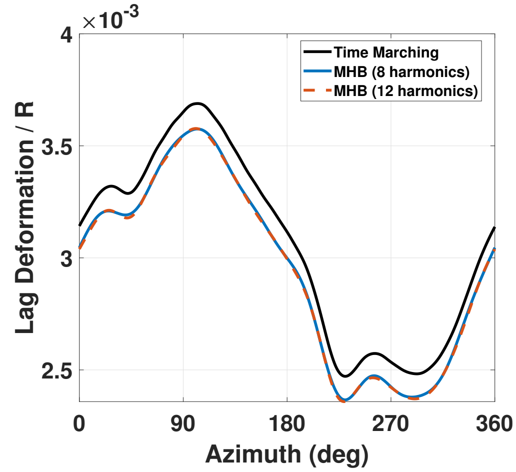

(b) Lag deformation

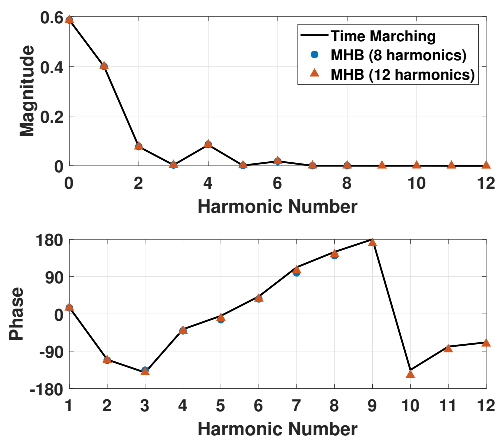

(c) Flap deformation

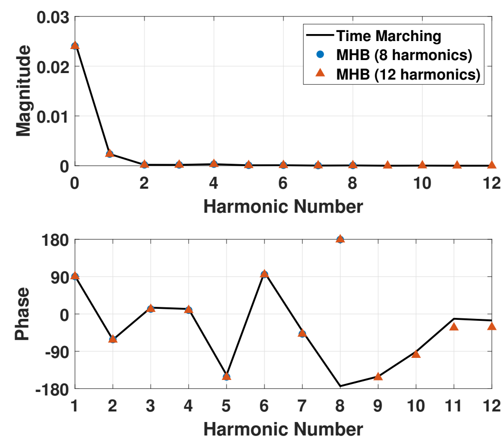

(d) Lag harmonics

Figure 4.6: Comparison of flap and lag deformations at the tip for hover with higher harmonic inputs; (a) flap deformation; (b) lag deformation; (c) flap harmonics; and (d) lag harmonics.

for harmonic 8 is merely a 360° wrap around.

4.2.2 Forward flight with fixed pitch inputs

Next, forward flight at advance ratio $\mu = 0.37$ is simulated with arbitrary 1/rev pitch inputs. The pitch angle is given by Eq. 4.2, where Ω is the rotor speed and t is the time.

$$\theta = 10^\circ + 3^\circ \cos(\Omega t) - 5^\circ \sin(\Omega t) \tag{4.2}$$

In forward flight, the inter-harmonic couplings are introduced naturally due to asymmetry in the flow. The high-speed case was chosen for maximum asymmetry. The solution was again obtained with 8 and 12 harmonics. Figures 4.7(a) and 4.7(b) compare the flap and lag deformations (at tip 1/4 chord) with a converged time marching solution. Linear inflow model was used to avoid harmonics from wake. The harmonic breakdown in Figures 4.7(c) and 4.7(d) show minor differences in the phase of higher harmonics. Overall, the results verify the accuracy of the Modified Harmonic Balance.

4.2.3 Forward flight with trim

The final test case is a full trim solution at low-speed transition flight. The pitch inputs are calculated from the trim solution by targeting rotor thrust and zero hub moments. The aircraft pitch is fixed at the measured value. The conditions are: $C_T/\sigma = 0.076$, $\mu = 0.15$, α_s = -3.75°. This is the same condition previously studied in the Black Hawk Loads workshop (Reference 29).

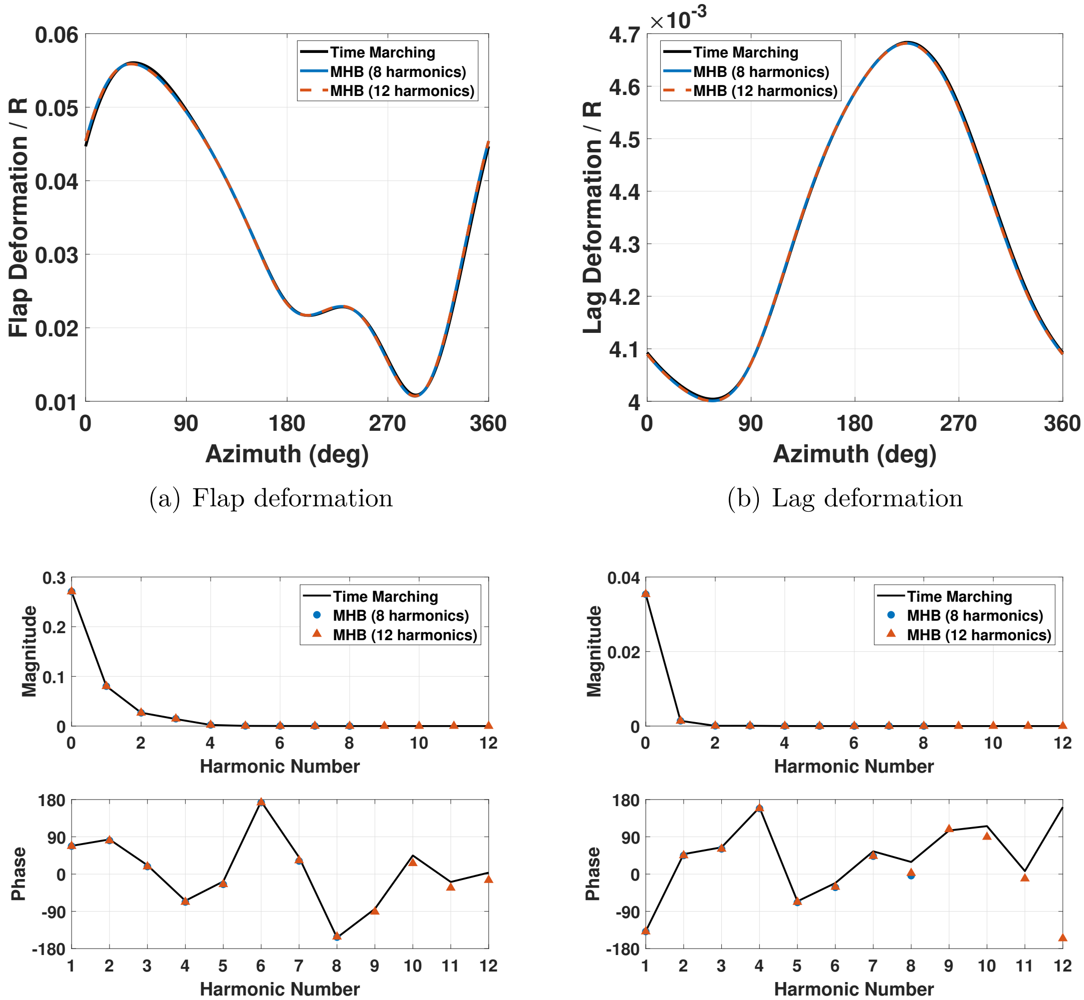

(a) Flap deformation

(b) Lag deformation

(c) Flap deformation

(d) Lag harmonics

Figure 4.7: Comparison of flap and lag deformations at the tip in forward flight with fixed control inputs; (a) flap deformation; (b) lag deformation; (c) flap harmonics; and (d) lag harmonics.

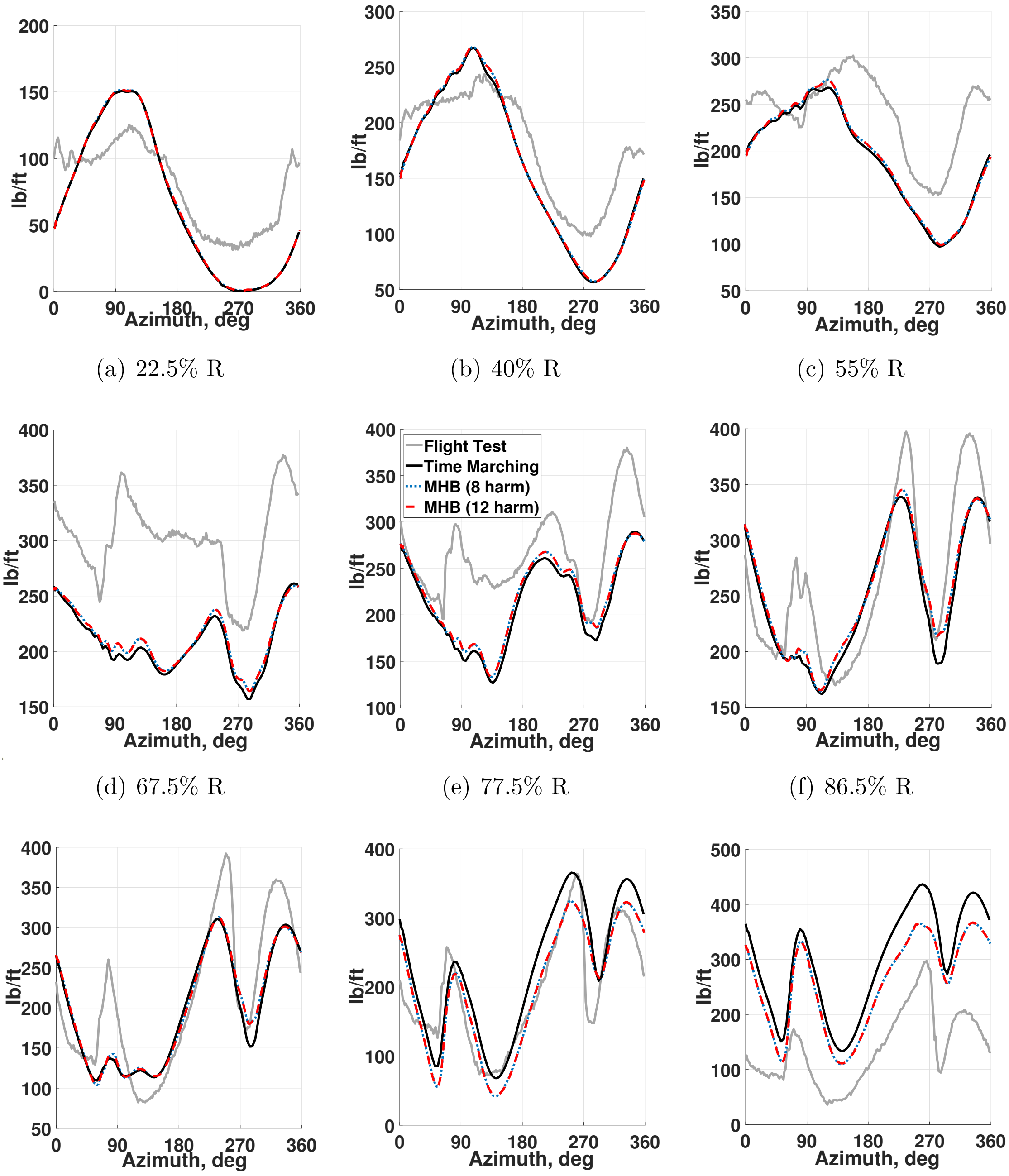

(a) 22.5% R (b) 40% R (c) 55% R

(d) 67.5% R (e) 77.5% R (f) 86.5% R

(g) 92% R (h) 96.5% R (i) 98.9% R

Figure 4.8: Normal force from modified harmonic balance method using 8 and 12 harmonics at different radial stations; predictions compared with time marching solution and measured UH-60A airloads.

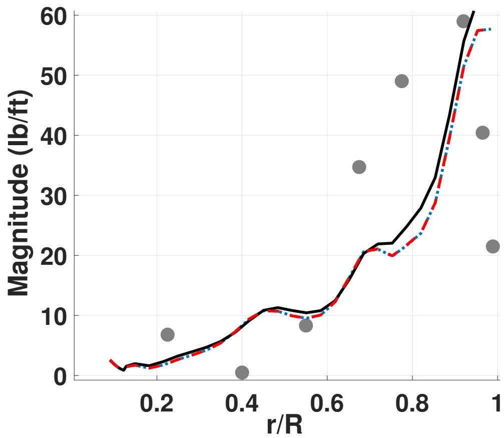

(a) 3/rev magnitude

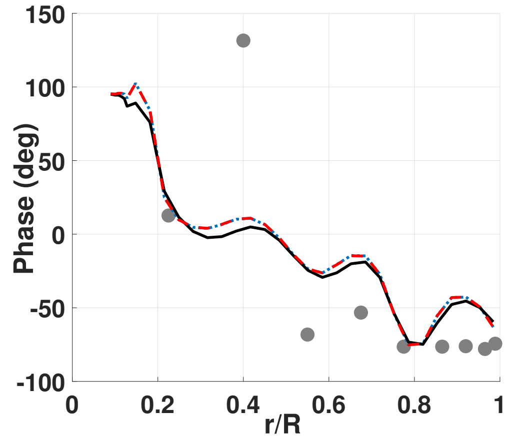

(b) 3/rev phase

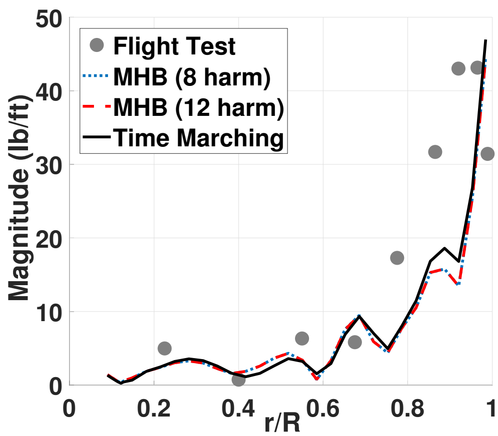

(c) 4/rev magnitude

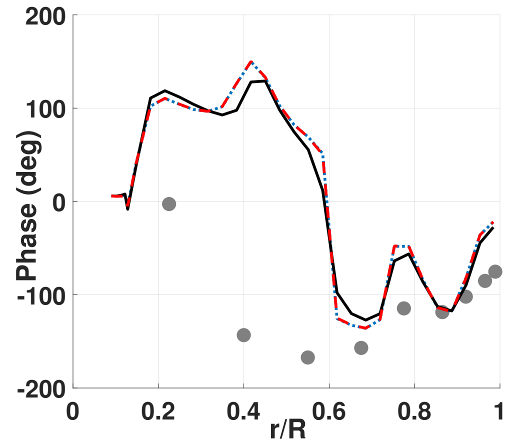

(d) 4/rev phase

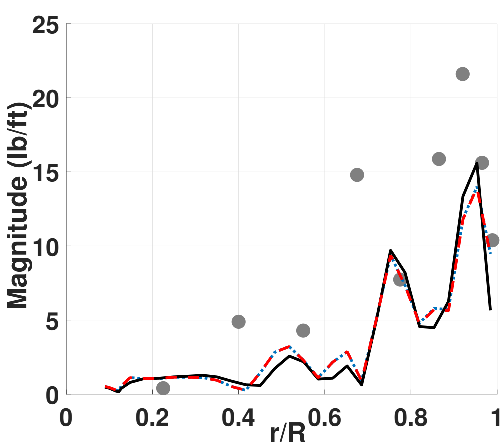

(e) 5/rev magnitude

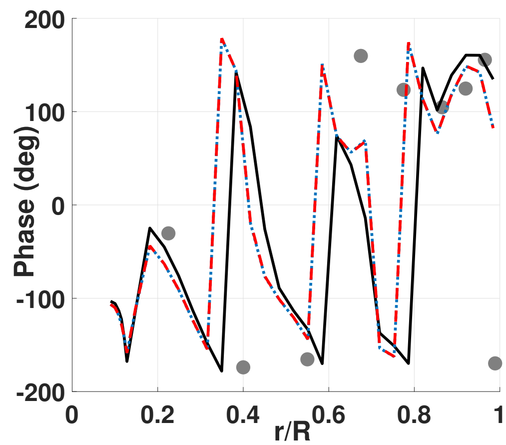

(f) 5/rev phase

Figure 4.9: Normal force vibratory harmonics (3,4,5 /rev) from modified harmonic balance using 8 and 12 harmonics; predictions compared with UH-60A airloads for qualitative comparison.

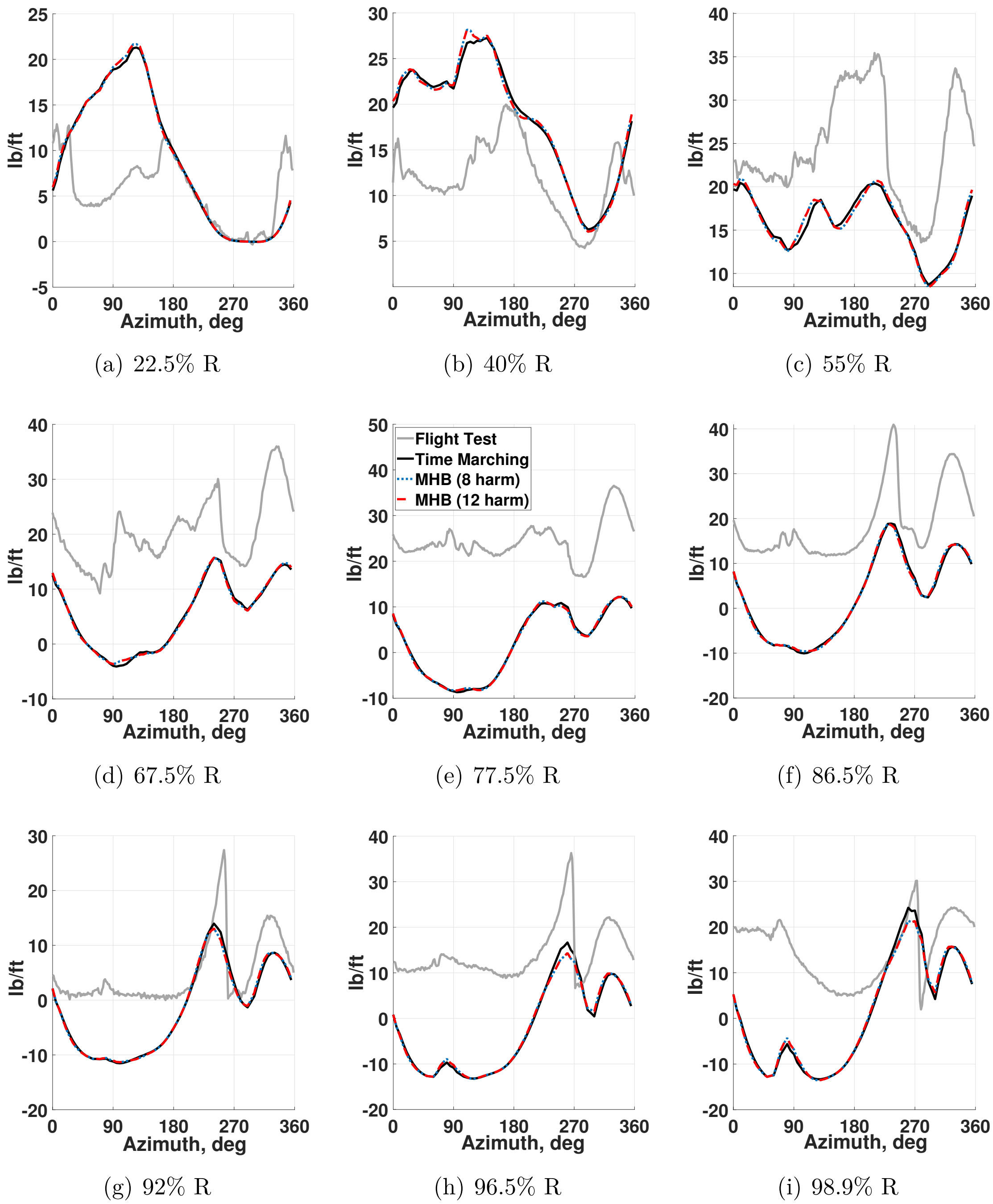

(a) 22.5% R

(b) 40% R

(c) 55% R

(d) 67.5% R

(e) 77.5% R

(f) 86.5% R

(g) 92% R

(h) 96.5% R

(i) 98.9% R

Figure 4.10: Chord force from modified harmonic balance method using 8 and 12 harmonics at different radial stations; predictions compared with time marching solution and measured UH-60A airloads.

The wake roll up and intertwining effects dominate the airloads at this condition and cause high vibratory loads. The rich harmonic content in airloads makes this an ideal case for validation. The free-wake model is a fully rolled-up single-tip vortex model with no inboard wake. Figure 4.8 shows the measured and predicted normal forces at different radial stations along the azimuth. Figure 4.9 shows the vibratory harmonics (3,4,5 /rev) versus span. This level of accuracy is generally the state of the art with lifting-line free-wake models. However, search for accuracy is not the objective here. The key conclusion is that the modified harmonic balance produces the same results as time marching. A converged time marching solution with $\Delta\psi = 5°$ is used for the assessment of convergence. The small differences at the tip are an artifact of using a finer time-step in time marching. Figure 4.10 shows the measured and predicted chord forces at different radial stations along the azimuth. The chord forces are usually difficult to predict with lifting-line models. Note that the measured data only includes the pressure drag, whereas the model contains both pressure and skin friction, with no mechanism to separate them.

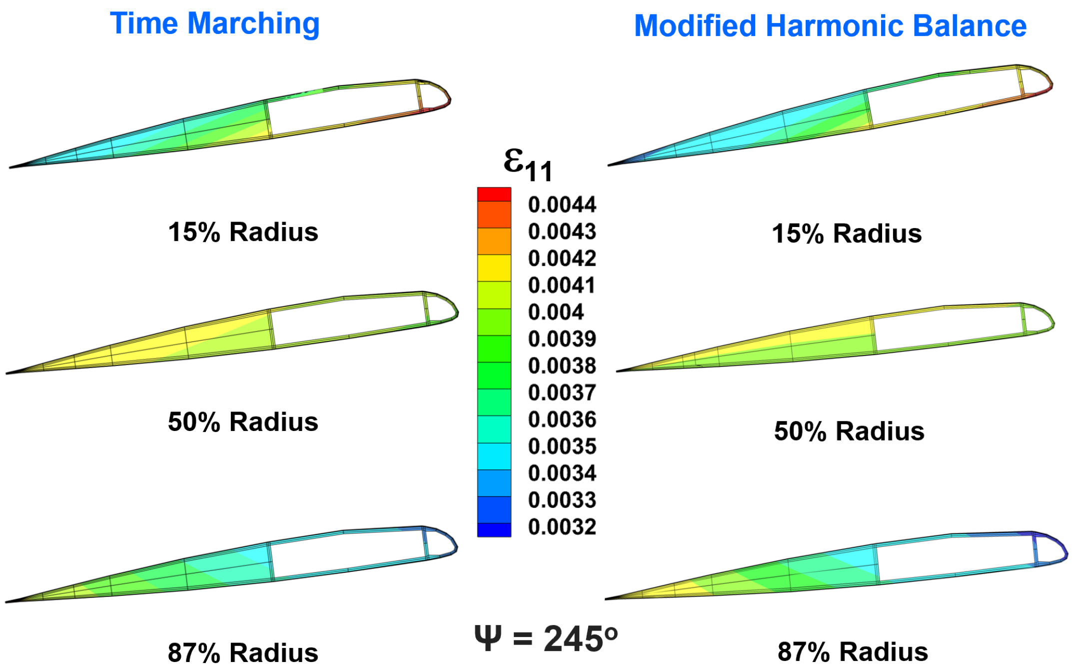

Figure 4.11: Distribution of axial strain obtained using time marching and modified harmonic balance methods for different radial stations at $\psi = 245°$.

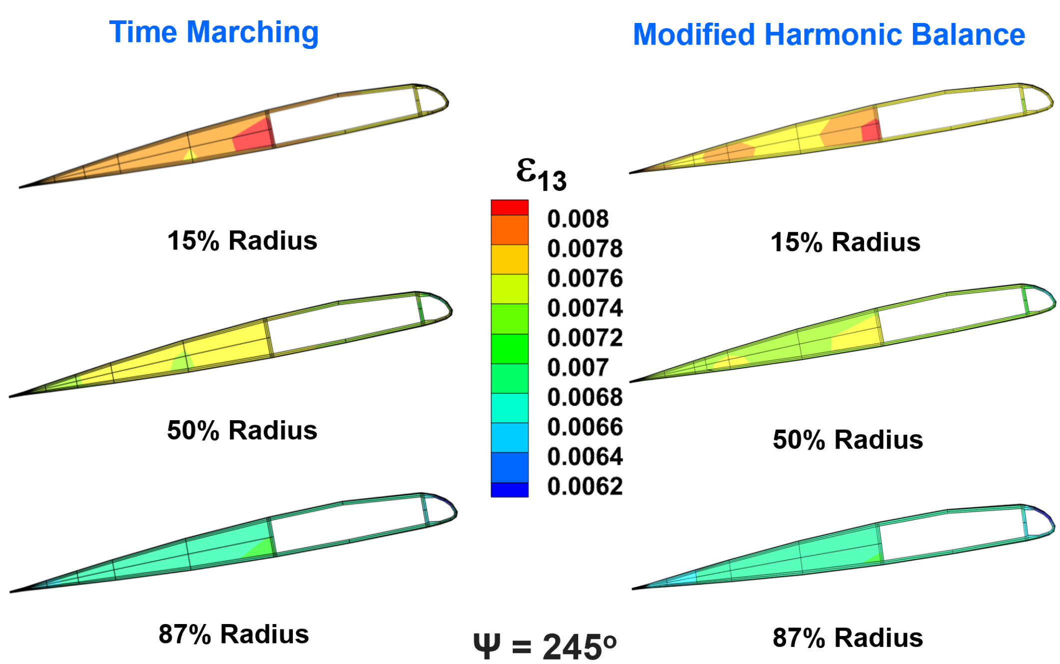

Figure 4.12: Distribution of transverse shear strain in vertical direction obtained using time marching and modified harmonic balance methods for different radial stations at $\psi = 245°$.

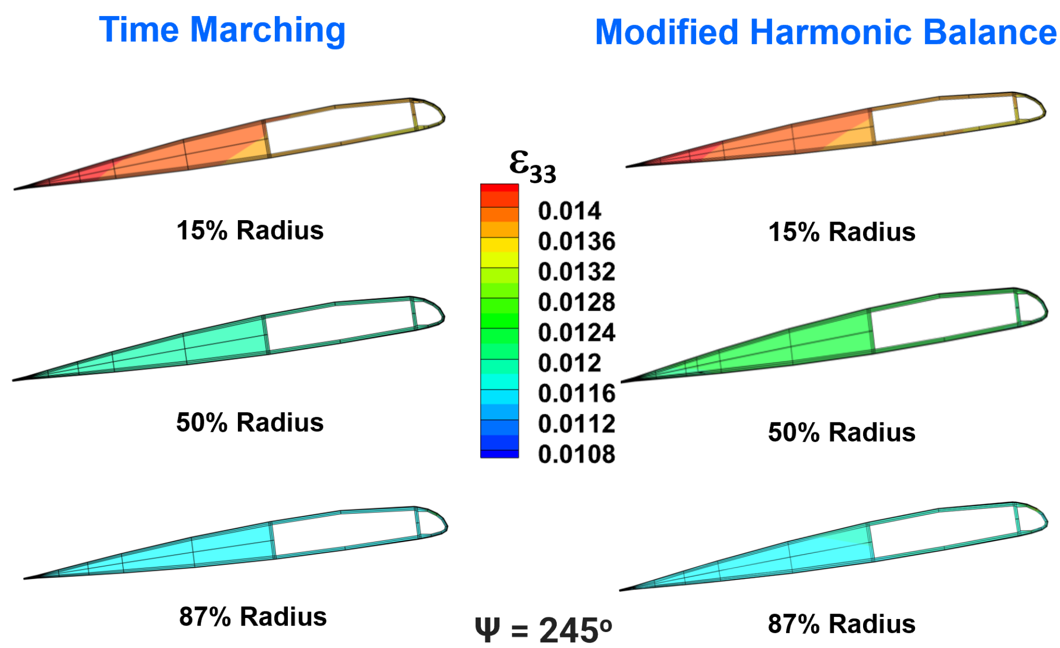

Figure 4.13: Distribution of inter-laminar strain in vertical direction obtained using time marching and modified harmonic balance methods for different radial stations at $\psi = 245°$.

The distribution of axial and transverse shear strain in vertical direction obtained at the azimuth, $\psi = 245°$ are shown in Figures 4.11 and 4.12. The harmonic balance solver appears to capture all the localized strain patterns of the internal structure with a similar accuracy as time marching. The differences (between MHB and time marching) observed in the foam behind spar account to around 1% and are considered negligible. The inter-laminar strain distribution is shown in Figure 4.13, which can be only predicted using 3D modeling. Here also both the solution procedures show good agreement with each other.

The total wall clock time for a trim solution of the UH-60A rotor using MHB is 2 minutes using 8 harmonics and 90 processors as opposed to 100 minutes using the time marching procedure. These and other computational specifics are provided in Chapter 5.

4.3 The NASA TRAM

The Tilt-Rotor Aeroacoustic Model (TRAM) is a 1/4-scale model of the V-22 tiltrotor. The structural model developed in Reference 46 is used here. The model consists of five flexible parts – blade, flexbeam, pitchcase, pitch horn, and pitch link. It includes a total of eight joints which model the bolts between the pitch case and the blade, the outboard and inboard bearings, gimbal at the hub, and pitch link connections. The assembled mesh of the model is shown in Figure 4.14. The total problem size is 43,305 degrees of freedom: 1709 elements, 8 joints, and 13 different materials.

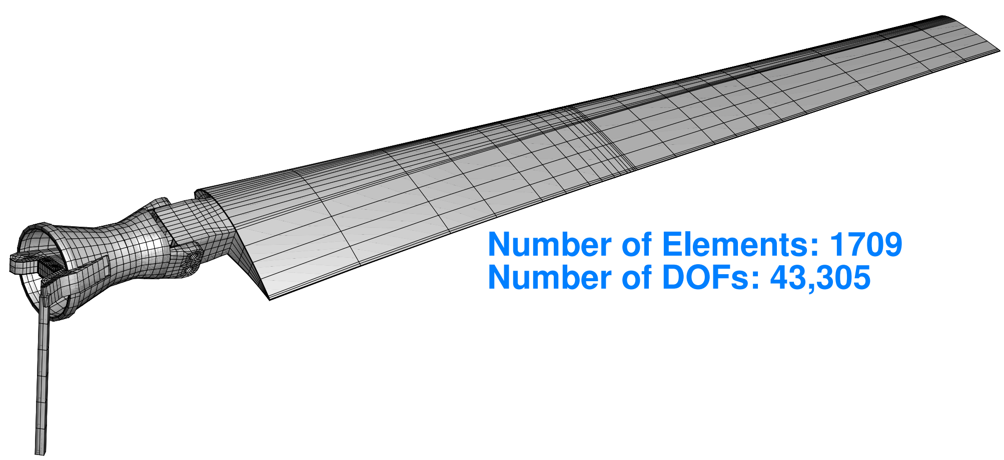

Figure 4.14: Three-dimensional brick mesh of the TRAM blade consisting of five flexible components, eight joints and 13 different composite materials.

The airfoils developed for the NASA large civil tiltrotor (LCTR) project were provided by NASA for the analysis (Reference 121). Trim is controlled via collective and cyclic inputs at the bottom of the pitch link. The free-wake model used here employs a single-tip vortex and no inboard wake. The predictions are compared to experimental test data for TRAM in the DNW wind tunnel (Reference 122). The results are for low-speed edgewise flight: advance ratio μ = 0.15, and shaft angle α_s = -2.97°. The thrust condtions are: moderate thrust ($C_T/\sigma = 0.089$) and high thrust ($C_T/\sigma = 0.128$). The trim targets are thrust and zero first harmonic flapping.

4.3.1 Forward flight at moderate thrust

Figures 4.15 and 4.16 shows the normal force predictions in the time and frequency domain at two radial stations (72%R and 90%R) for moderate thrust condition. The flight conditions are: $C_T/\sigma = 0.089$, α_s = -2.97°, $\mu = 0.15$. The trim targets are thrust and zero first harmonic flapping.

The single tip vortex free-wake model performs poorly in capturing the shape of the wake impulses, which is consistent with the state-of-the-art. Multiple trailers are needed to approach test data, or better still, coupling with CFD. The predictions are particularly poor near the front of the rotor disk. It is known that proprotor roll-up is difficult to capture without CFD (Reference 46). The purpose here is to validate the general trends, and verify the harmonics are consistent with time marching solution, for the same level of fidelity in aerodynamics.

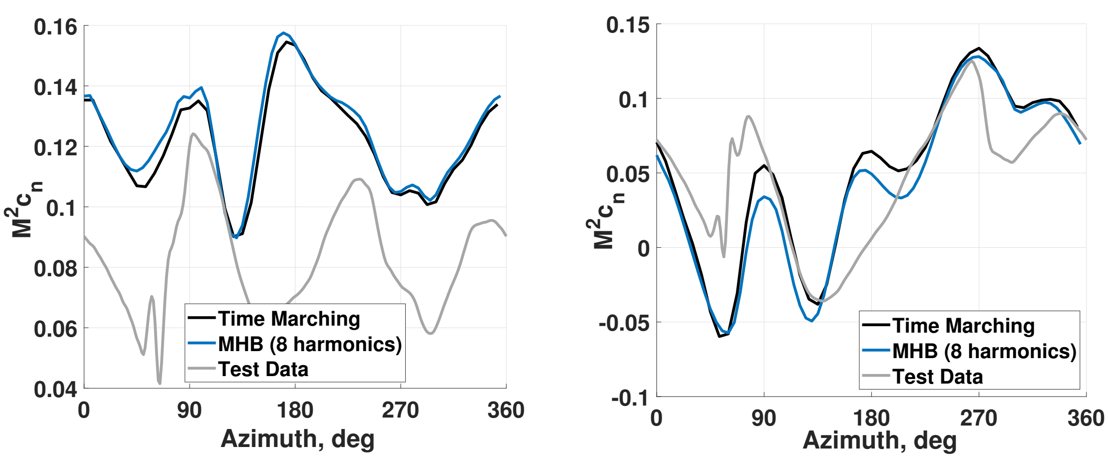

(a) Normal force at 72% radial location

(b) Normal force at 90% radial location

Figure 4.15: Predictions of normal force compared to wind-tunnel test data; $C_T/\sigma = 0.089$, α_s = -2.97°, $\mu = 0.15$; (a) r = 72% R; (b) r = 90.7% R .

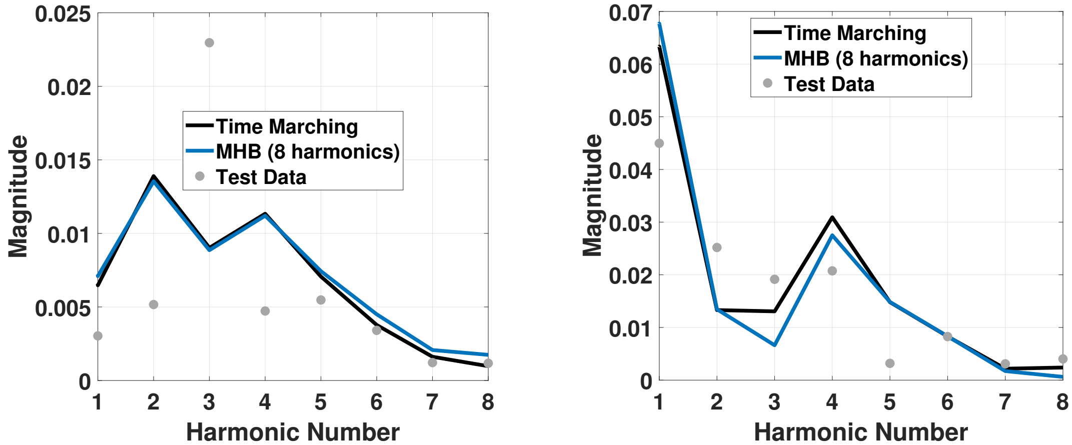

(a) Normal force harmonics at 72% radial location (b) Normal force harmonics at 90% radial location

Figure 4.16: Predictions of normal force harmonics compared to wind-tunnel test data; $C_T/\sigma = 0.089$, α_s = -2.97°, $\mu = 0.15$; (a) r = 72% R; (b) r = 90.7% R .

4.3.2 Forward flight at high thrust

Figures 4.17 and 4.18 shows the normal force predictions in the time and frequency domain at two radial stations ($72\%R$ and $90\%R$) for high thrust condition. The flight conditions are: $C_T/\sigma = 0.128$, α_s = -2.97°, $\mu = 0.15$. The trim targets are thrust and zero first harmonic flapping.

A dominant 4/rev is seen at the tip normal force distribution and overall similar trends are observed as the moderate thrust case.

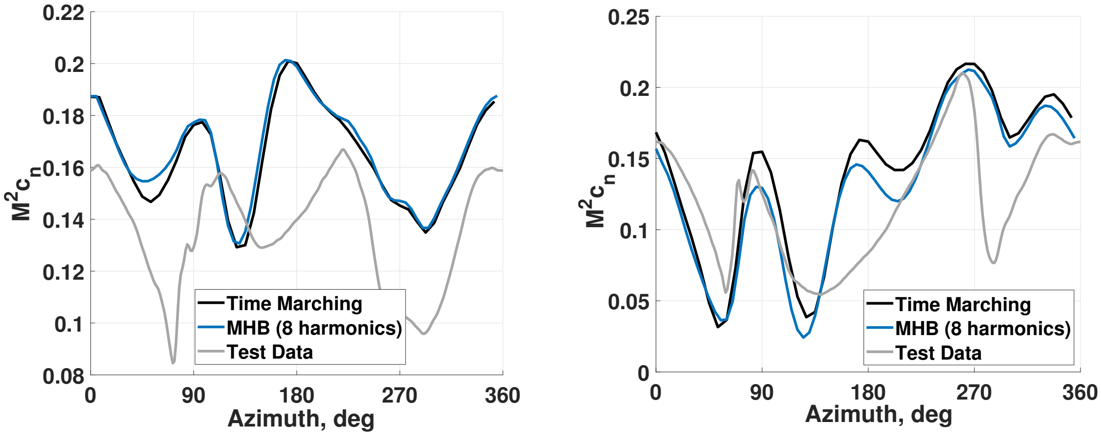

(a) Normal force at 72% radial location (b) Normal force at 90% radial location

Figure 4.17: Predictions of normal force compared to wind-tunnel test data; C_T/σ = 0.128, α_s = -2.97°, μ = 0.15; (a) r = 72% R; (b) r = 90.7% R .

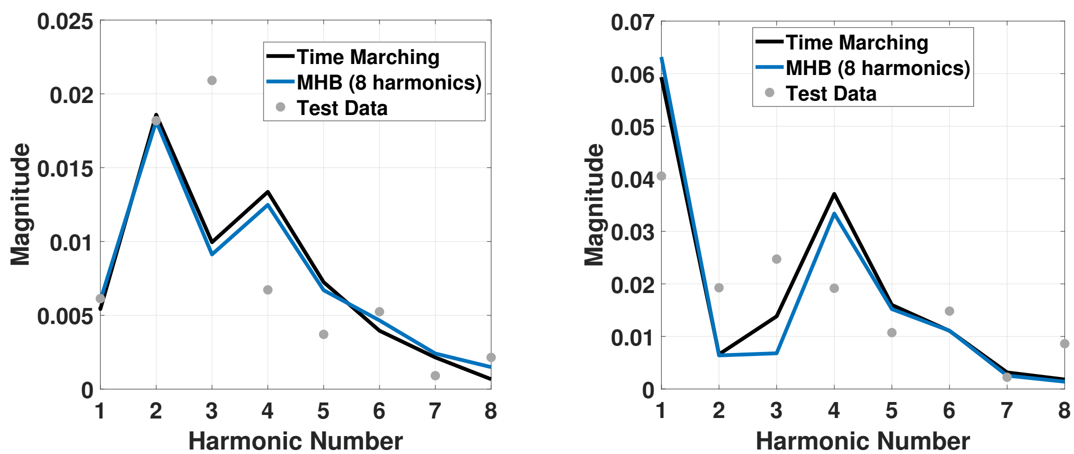

(a) Normal force harmonics at 72% radial location (b) Normal force harmonics at 90% radial location

Figure 4.18: Predictions of normal force harmonics compared to wind-tunnel test data; C_T/σ = 0.128, α_s = -2.97°, μ = 0.15; (a) r = 72% R; (b) r = 90.7% R .

The total wall clock time for a trim solution of the TRAM rotor using MHB is 8 minutes using 8 harmonics and 90 processors as opposed to 9 hours using the time marching procedure. These and other computational specifics are provided in Chapter 5.

4.4 Summary and Conclusions

The Modified Harmonic Balance (MHB) algorithm was verified with the Frank Harris analytical solution and validated with UH-60A rotor and NASA TRAM test cases in forward flight. Predictions of tip displacements, normal and chord forces, and stress distributions were studied. Based on this chapter, the following key conclusions are drawn.

1. The converged Modified Harmonic Balance (MHB) solution for the Frank Harris test case is identical to the converged time marching and finite element in time solution. This verifies the accuracy of the new algorithm.

2. The MHB method performs well in capturing the higher harmonic trends exhibited in the normal force distributions at low-speed wake-dominated flight.

3. Eight harmonics are sufficient to capture the impulsive wake-induced loading in the first and fourth quadrant for UH-60A and TRAM test cases.

4. The time marching procedure requires a low azimuth-step ($d\psi$) to achieve a converged solution that is of similar accuracy as the converged MHB solution. This requirement of a small time-step leads to huge computational time, especially for large-scale structures.

5. The total wall clock time for a trim solution of the UH-60A rotor using MHB is 2 minutes using 8 harmonics and 90 processors as opposed to 100 minutes using the time marching procedure.

6. The total wall clock time for a trim solution of the TRAM rotor using MHB is 8 minutes using 8 harmonics and 90 processors as opposed to 9 hours using the time marching procedure.

Chapter 5: Parallel Performance of Algorithms

Having verified and validated the new X3D solver for real rotor cases, this chapter studies its parallel performance. The first part introduces the specifics of computer architecture relevant to this work, parallel computing, and the components present in a typical supercomputer cluster. The second part discusses parallel performance of skyline solver and modified harmonic balance algorithms.

5.1 Computer Architecture

A computer is a machine that accepts data (input), processes it, and produces outputs. A mouse and a microphone are examples of input devices. A monitor and a speaker are examples of output devices. The processing element is called a processor or a Central Processing Unit (CPU). The core components of any computer are the following.

1. Motherboard

The motherboard is the computer's main circuit board. All components of a computer communicate through this circuit board. It houses the CPU, memory, and other units, such as connectors for the hard drive and connections to the external ports like the Universal Serial Bus (USB) ports.

2. Processor (CPU)

The CPU performs basic arithmetic, logic, and input/output operations and issues command for other components. Code written in high-level languages like C, Fortran, etc., is converted to assembly language for execution by the CPU. The CPU is housed in a microprocessor that contains other peripheral units.

The essential elements of a CPU include the arithmetic logic unit (ALU), the floating-point unit (FPU), registers, and cache memory. The four primary functions of a CPU are to fetch, decode, execute and write. Fetch is the operation that receives instructions from the Random Access Memory (RAM). Decode is where the instruction is converted to assembly language for execution. Execute is where the operation is performed. Finally, the output is written to a file.

3. Memory and Storage

There are two types of memory: primary and secondary. The term memory is often used as a synonym for primary memory or as an abbreviation for the Random Access Memory (RAM). In the primary memory, the data is stored only for a short time. It is volatile, meaning it is deleted when the computer is turned off. The term storage refers to secondary memory. An example of storage is a hard drive or a hard disk drive (HDD). It is nonvolatile, meaning the information is retained even after the computer is turned off.

Overall there are four major storage locations arranged hierarchically as depicted in Figure 5.1. The first two – registers and cache are internal to the CPU. A processor register is the fastest accessible memory location. The time taken to access it is around 1 CPU cycle, and it can store only a few thousand bytes. A cache is a larger, slower than register, and farther memory but still embedded on the CPU and stores copies of data from RAM that is frequently used. It helps to reduce the average time to access data from the RAM. Most processors have a hierarchy of multiple cache levels (L1, L2, and L3). L1 is the fastest and the smallest, and L3 is the slowest and largest. The cache size of modern processors is in the order of kilobytes, and access speed is around 100-700 Gigabytes per second.

The third hierarchy is the Random Access Memory (RAM), which allows information to be stored and retrieved on a computer. All requests, whether instructions or data, go to the random access memory. Its size is in the order of Gigabytes, and the access speed is around 1-10 Gigabytes per second. The last hierarchy is the hard disk and solid-state drive storage, which are terabytes in size and access speeds of thousand megabytes per second.

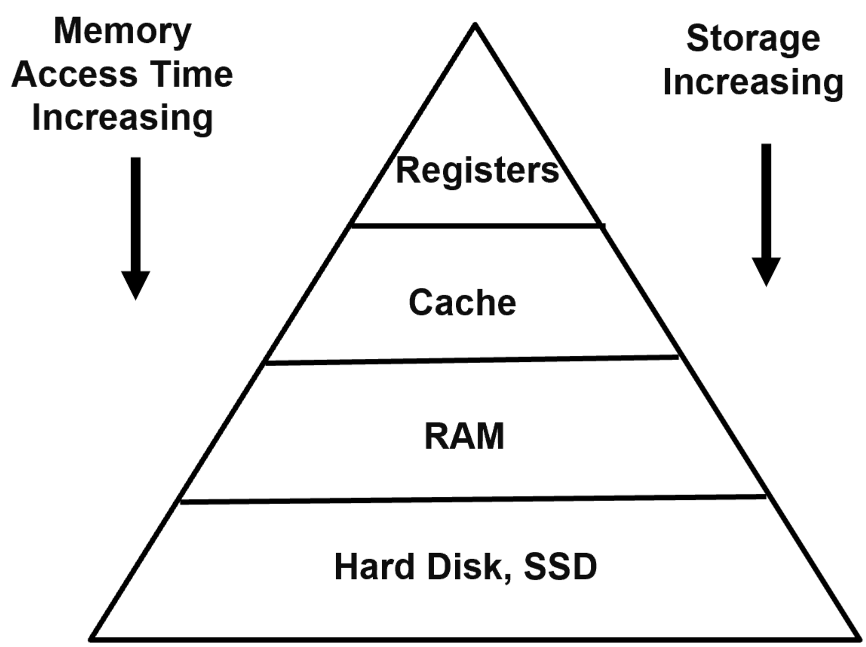

Figure 5.1: Memory hierarchy triangle

5.2 Shared Memory Architecture

In shared-memory architecture, the entire memory, i.e., main memory and disks, is shared by all processors. Shared memory parallel computers vary widely but generally have the ability for all processors to access all memory as global address space. The changes in a memory location affected by one processor are visible to all other processors. Based on the memory access times, shared memory machines are classified into two types:

1. **Uniform Memory Access (UMA):** This type is represented by Symmetric Multiprocessor (SMP) machines (Figure 5.2(a)). SMP machine involves an architecture where two or more identical processors are connected to a single, shared main memory. As the name suggests, all processors have equal access and access times to memory. It is also called CC-UMA - Cache Coherent UMA. Cache coherent means if one processor updates a location in shared memory, all the other processors know about the update. Cache coherency is accomplished at the hardware level.

2. **Non-Uniform Memory Access (NUMA):** These are constructed by linking two or more SMP machines (Figure 5.2(b)). As the name suggests, not all processors have equal access time to all memories. One SMP can directly access the memory of another SMP. However, memory access across links is slower. If cache coherency is maintained, it is called CC-NUMA (Cache Coherent NUMA).

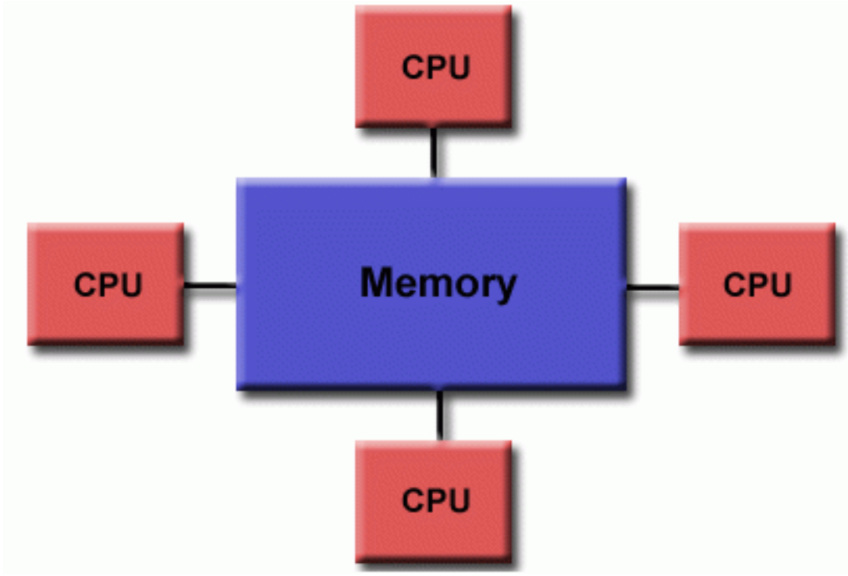

(a) UMA shared memory machine

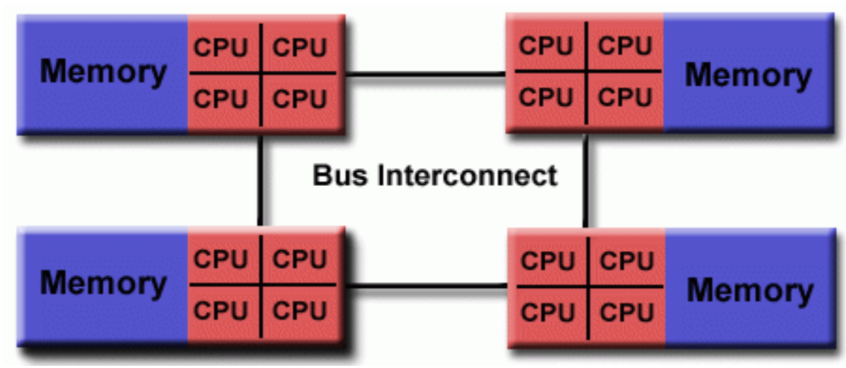

(b) NUMA shared memory machine

Figure 5.2: Illustration of UMA and NUMA shared memory machines.

The advantages and disadvantages of shared memory architectures are as follows.

Advantages

1. The data sharing between tasks is fast and uniform due to the proximity of memory to CPUs.

2. The presence of global address space makes it easy to write software.

Disadvantages

1. The primary disadvantage is the lack of scalability between memory and CPUs. Adding more CPUs can geometrically increase traffic on the shared memory-CPU path.

2. The performance might degrade when multiple processors try to access the shared memory simultaneously (contention problem). A typical design might use caches to solve the contention problem.

3. Having multiple copies of data spread throughout the caches might lead to a coherence problem. The cache copies are coherent if they are all equal to the same value. However, if one of the processors updates the copy, it becomes inconsistent because it no longer equals the value of the other copies.

4. It is difficult to ensure correct access of global memory and synchronization for the programmer.

Shared memory architectures are best suited to achieve fine-grained parallelism because they support fast communication. In fine-grained parallelism, a program is broken down into many small tasks. These tasks are assigned individually to many processors. The amount of work associated with each task is low, and the work is evenly distributed among the processors. Hence, fine-grained parallelism facilitates load balancing. As each task processes less data, the total number of processors required is high, leading to increased communication and synchronization overhead. Shared memory architecture with a low communication overhead is most suitable for fine-grained parallelism.

5.3 Distributed Memory Architecture

Distributed memory refers to a multiprocessor computer system in which each processor has its own private memory. Each processor has its own local memory.

It requires a communication network to connect inter-processor memory. These systems are also called message-passing systems. The network fabric used for data transfer varies widely, though it can be as simple as Ethernet. Memory addresses in one processor do not map to another processor, so there is no concept of global address space across all processors. Any changes made to its local memory do not affect the memory of other processors. Hence, the concept of cache coherency does not apply.

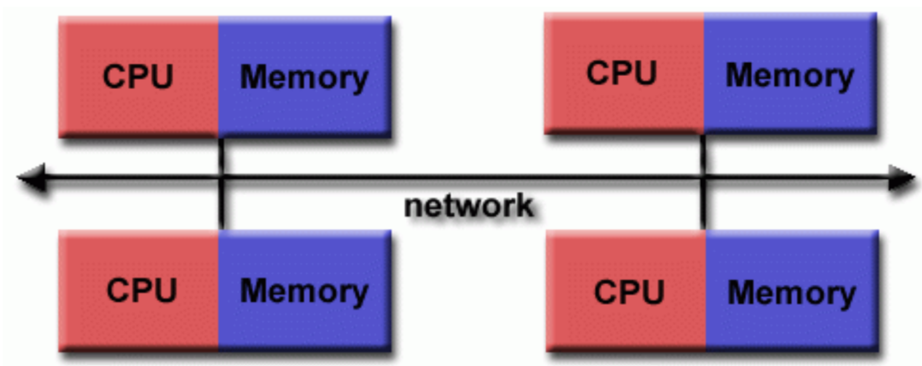

Figure 5.3: Illustration of distributed memory architecture.

The programmer ensures synchronization between tasks and handles communications between processors. Communications in message-passing systems are performed via send and receive operations. The advantages and disadvantages of distributed memory architecture are listed below.

Advantages

1. Memory is scalable with the number of processors. Increase the number of processors, and the size of memory increases proportionately.

2. Each processor can rapidly access its memory without interference and without the overhead incurred with trying to maintain global cache coherency.

Disadvantages

1. Non-uniform memory access times - data present on a remote node takes longer to access than local node data.

2. The programmer is responsible for details associated with data communication between processors.

Distributed memory architecture takes a long time to communicate data among processes, making it suitable for coarse-grained parallelism. In coarse-grained parallelism, a program is split into large tasks. Due to this, a large amount of computation takes place in each processor, resulting in load imbalance, wherein certain tasks require more time while others take less time. The advantage of this type of parallelism is low communication and synchronization overhead.

5.4 UMD Deepthought2

The largest and fastest computers in the world today are clusters employing both shared and distributed memory architectures. The University of Maryland's cluster is named Deepthought2.

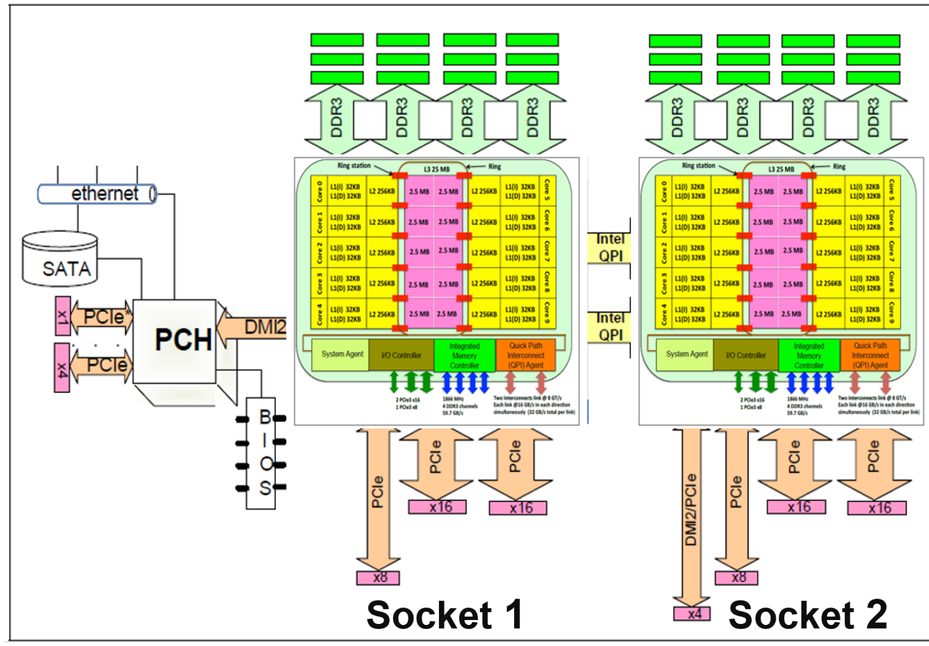

Figure 5.4: Schematics of a node encompassing shared memory architecture in the cluster Deepthought2.

The cluster consists of 480 nodes with a dual socket on each node. A node is a collection of processors with shared memory architecture. Figure 5.4 shows the picture of a node of the Deepthought2 cluster. It has two sockets with ten Intel Ivy Bridge E5-2680v2 processors running at 2.8 GHz on each. So a total of 20 processors are available on each node. Each of these processors has a separate L1 cache (64 KB), a separate L2 cache (256 KB), a shared L3 cache (25 MB), and a total shared memory of 128 GB. The arrangement of the processors on each socket is shown in Figure 5.5.

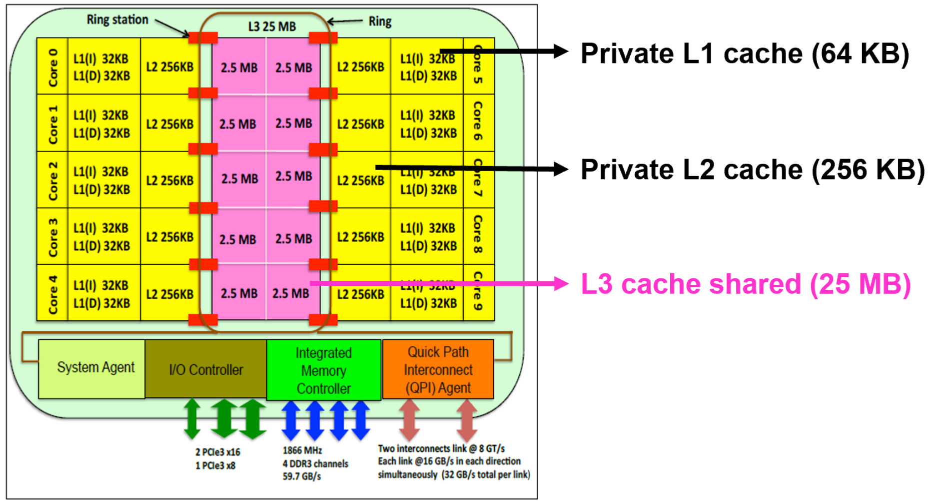

Figure 5.5: Schematics of arrangement of processors on each socket of a node in the cluster Deepthought2.

A collection of the nodes described above form a distributed memory architecture. This is represented in Figure 5.6. The memory is only shared internally and not between each node. This overall architecture represents a hybrid distributed and shared memory architecture. Note that all the processors internal to a node can also be used as distributed memory for programming purposes.

5.5 Parallel Computing

In simple terms, parallel computing is the simultaneous use of multiple computing resources to solve a computational problem. A problem is broken into discrete parts that can be solved concurrently on many processors. The problem's partitioning into discrete parts depends on the algorithm, and the distribution across the processors depends on the parallel computer architecture described above.

Parallel computing is critical to the understanding of complex real-world phenomena. During the past 20-30 years, significant advancements have been made in computer architectures and parallel programming modules that have made parallelism ubiquitous. Exascale (10^{18} calculations per second) computing is an

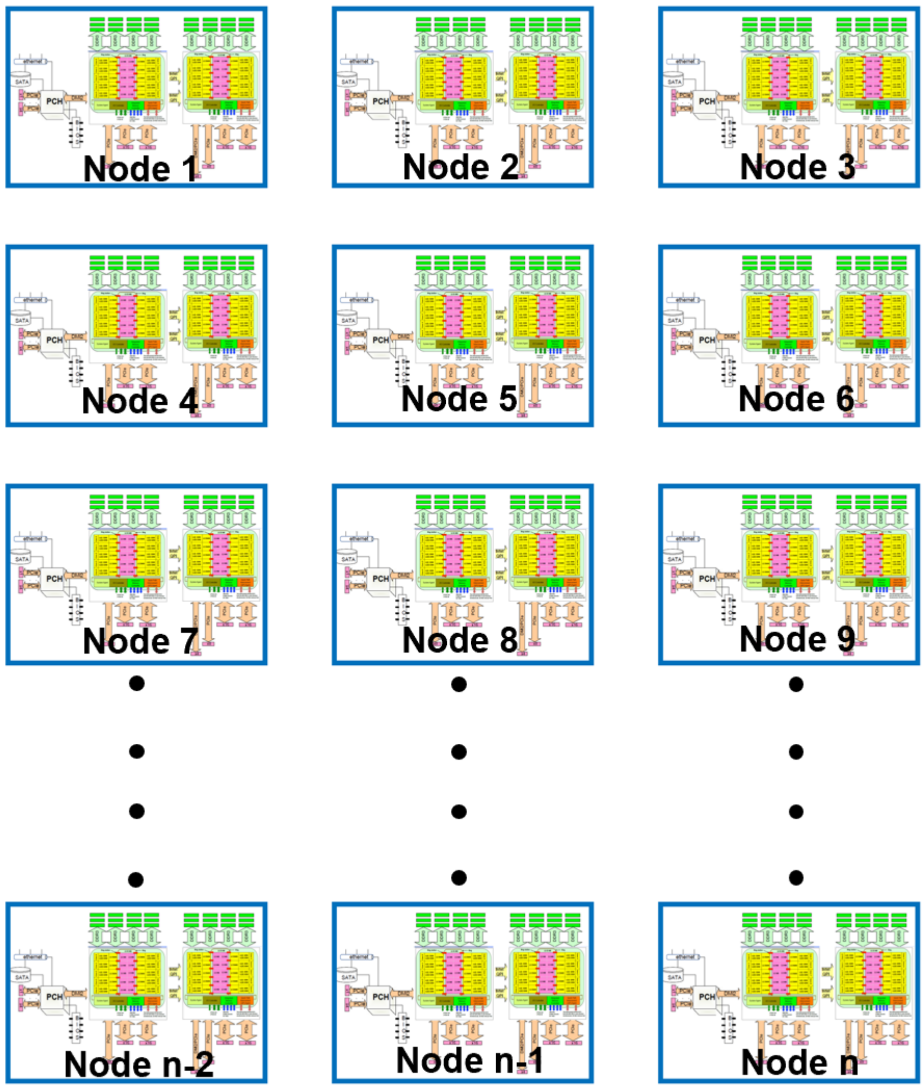

Figure 5.6: Hybrid Distributed Shared memory.

aspirational target for parallel computing.

In this section, some important terms of parallel computing are defined that are useful for understanding the results.

1. Speedup: Parallel speedup of a code that has been parallelized is defined as,

$$\text{Speedup} = \frac{\text{wall-clock time of serial execution}}{\text{wall-clock time of parallel execution}} \tag{5.1}$$

   One of the most widely used indicators for a parallel algorithm's performance.

2. Scalability: It refers to the ability to demonstrate a proportionate increase in parallel speedup with the addition of more resources. Both hardware and software (algorithm) contribute to this demonstration. Two types of scaling are defined based on the solution time.

   - Strong Scalability: It is defined as how the solution time varies with the number of processors for a fixed total problem size. Strong scaling means the problem is solved in 1/N time (compared to serial) with N processors.
   - Weak Scalability: It is defined as how the solution time varies with the number of processors for a fixed problem size per processor. Weak scaling means an N times larger problem is solved in the same time as the original problem given N processors.

3. FLOPS: It refers to the number of floating point operations taking place in an algorithm per second. A powerful processor and a faster algorithm contribute to higher FLOPS.

5.6 Parallel Performance of Skyline Solver

In this section, the parallel performance of the skyline solver is studied. The solver speedup is recorded on a shared memory architecture. Its performance is compared with the widely used linear system solver MUMPS.

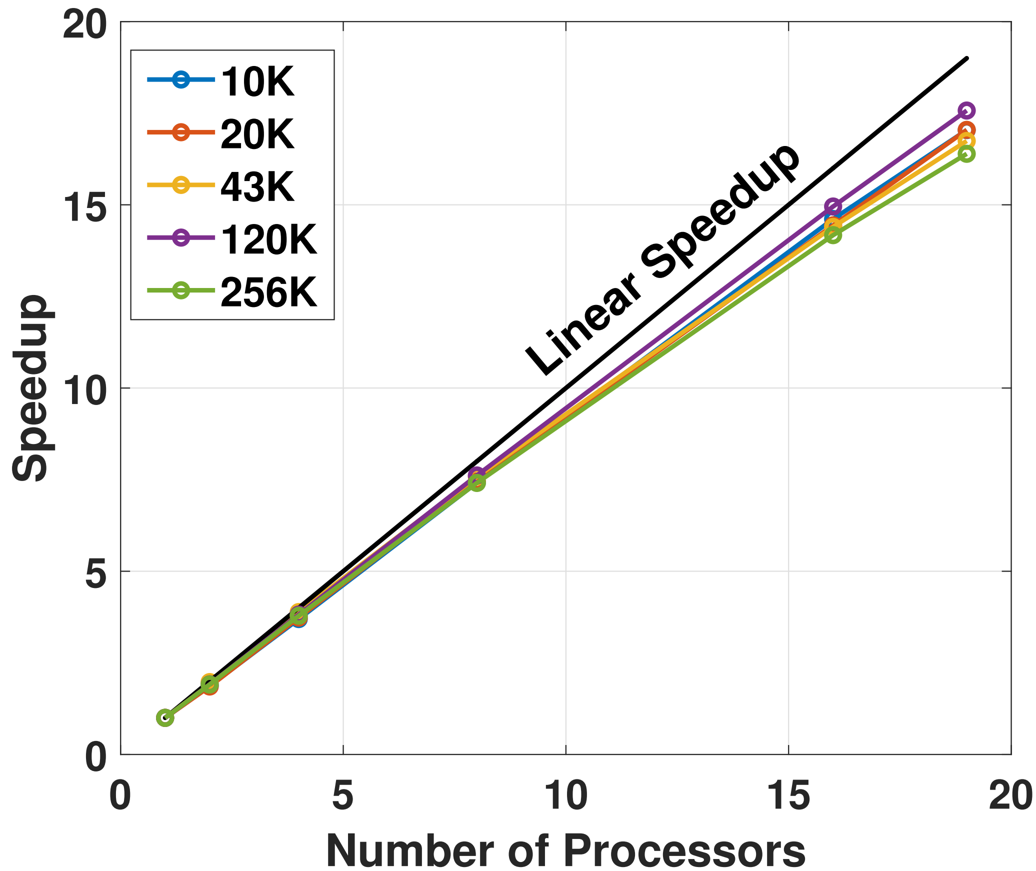

Figure 5.7: Speedup of the parallel skyline solver on a single node of 20 processors.

The speedup performance of the skyline solver was recorded using the 3D cantilevered beam test case with constant tip force, mentioned earlier in Chapter 4. This elementary test case allows to easily vary the mesh sizes, hence chosen for this study. Figure 5.7 shows the speedup with the number of shared memory processors for various mesh sizes ranging from 10K to 250K degrees of freedom. Regardless of size, a speedup of up to 17 is obtained over 19 processors, which accounts for

90% efficiency. Of 20 processors available on each node, one is usually dedicated to system management. Thus, using 19 provides the best speedup for computation.

Even though the parallel skyline solver achieves 90% speedup efficiency for a range of problem sizes, the solver does fail to achieve linear speedup for certain problem types. These limitations are dependent on the structure of the matrix solved. For a typical finite element problem, the matrix structure resembles a skyline shown in Figure 5.8(a). Consider the matrix obtained from the finite element in time formulation shown in Figure 5.8(b). The structure of this matrix still resembles a skyline but with a larger bandwidth resulting from periodic boundary conditions. Even though the matrices shown in Figure 5.8 are of similar sizes, the parallel skyline solver does not perform at the same efficiency. Figure 5.9 shows the speedup for both these matrices versus the number of processors. The speedup increases till 12 processors for the FET matrix, and after that the speedup remains constant with increasing processors. The high bandwidth results in high memory storage of a column which results in cache losses, resulting in decrease of speedup. Note that this behavior is dependent on the cache size of the architecture used. Hence a definitive problem size cannot be determined as to when the solver performance begins to degrade.

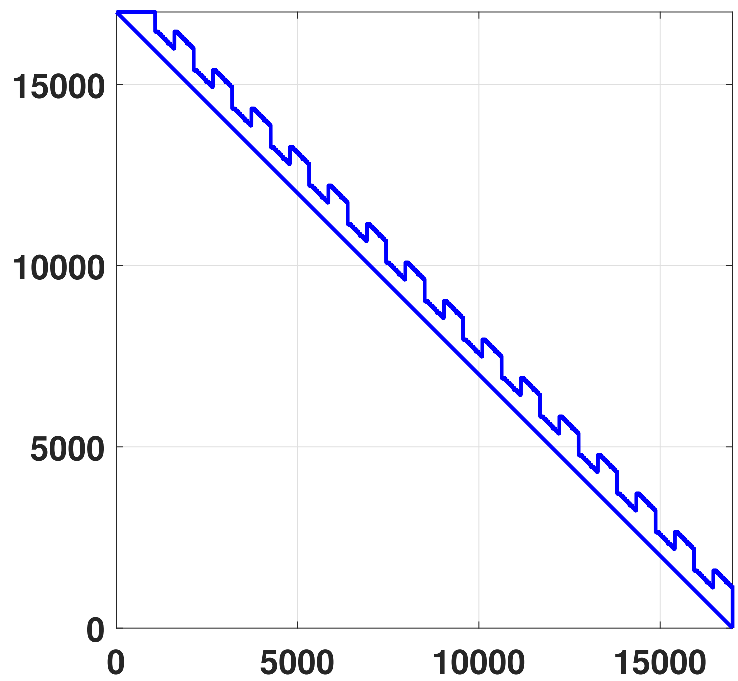

(a) FEM skyline

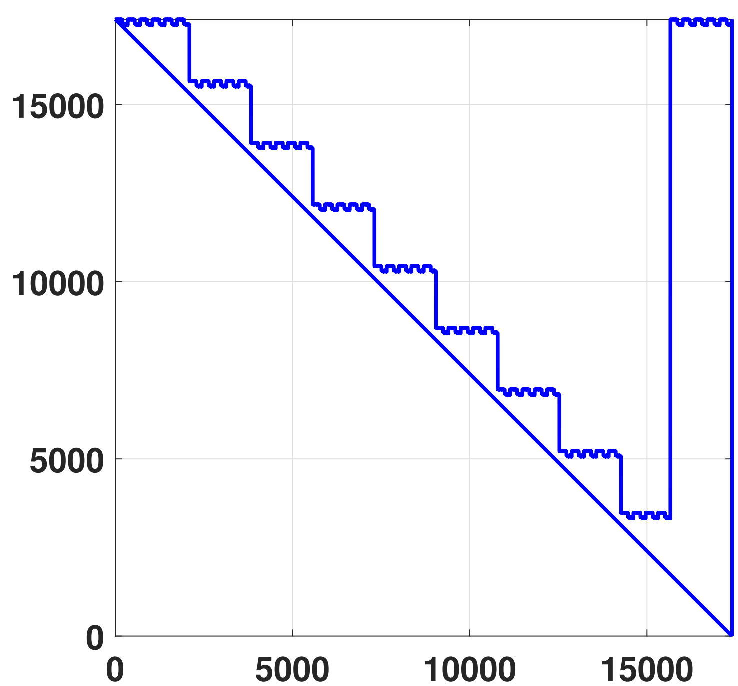

(b) FET skyline

Figure 5.8: Comparison of matrix skylines obtained from 3D FEM and 3D FET formulation.

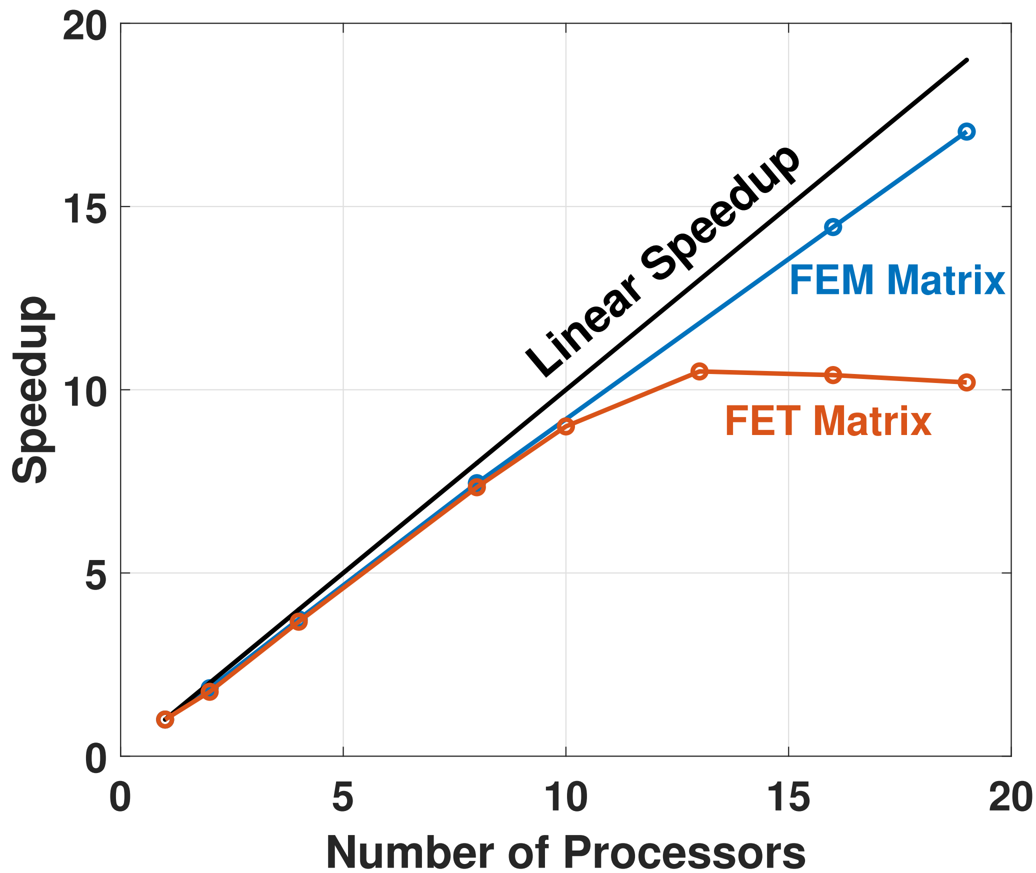

Figure 5.9: Speedup of the parallel skyline solver on matrices obtained from FEM and FET formulation versus number of processors.

There are several open source sparse direct solvers available to solve large systems of finite element equations. A widely used solver is the MUMPS (Multifrontal Massively Parallel sparse direct Solver) (References 123, 124). It implements the multifrontal method in parallel using MPI-OpenMP, and uses BLAS and ScaLAPACK kernels for dense matrix computations. The performance of the solver developed here is compared against MUMPS on a local desktop with a maximum of 16 processors and similar specifications as Deepthought2.

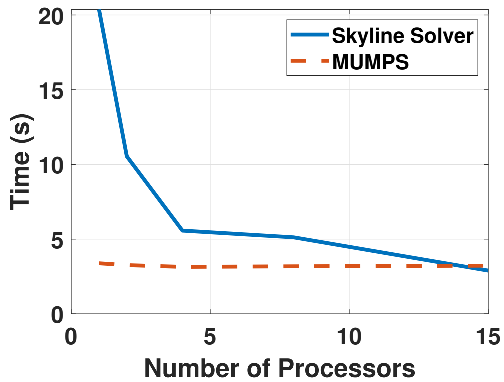

(a) N = 5K

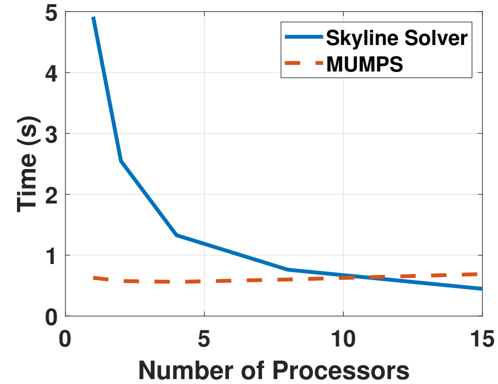

(b) N = 17K

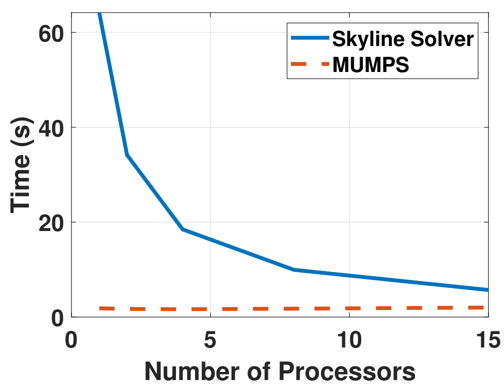

(c) N = 43K

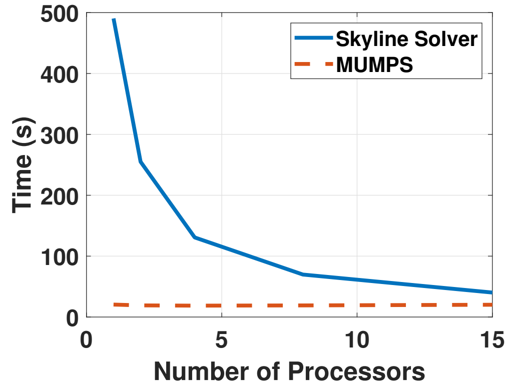

(d) N = 120K

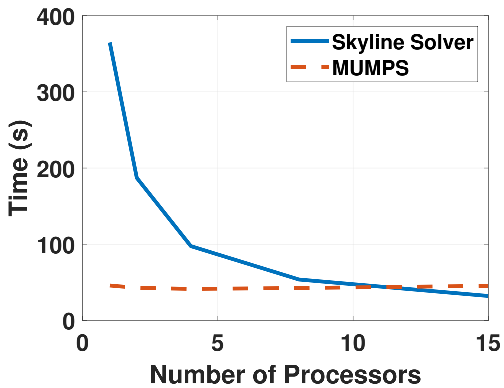

(e) N = 450K

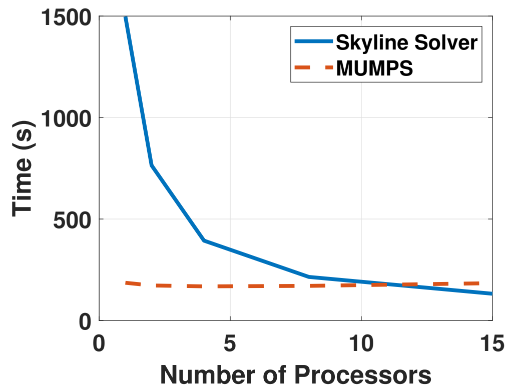

(f) N = 1800K

Figure 5.10: Performance comparison of solution time versus number of processors between skyline solver and MUMPS for various problem sizes.

Figure 5.10 shows the variation of solution time versus the number of shared-memory processors for various problem sizes. As expected, the solution time reduces for skyline solver with the number of processors, whereas it is constant for the MUMPS solver. This is observed regardless of the problem size. Thus, MUMPS is significantly faster in serial mode or when using a low number of processors. But as the number of processors increase, the parallel skyline solver appears to surpass it. The speedup characteristics for both solvers with number of processors is shown in Figure 5.11.

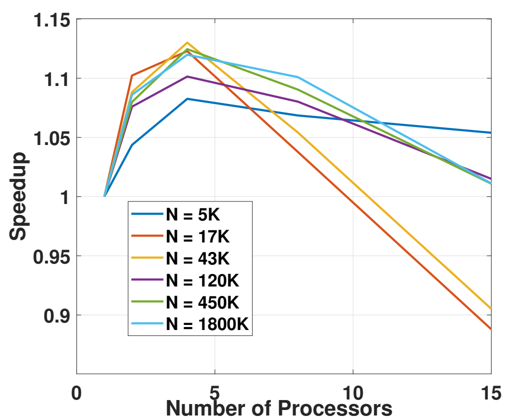

(a) MUMPS

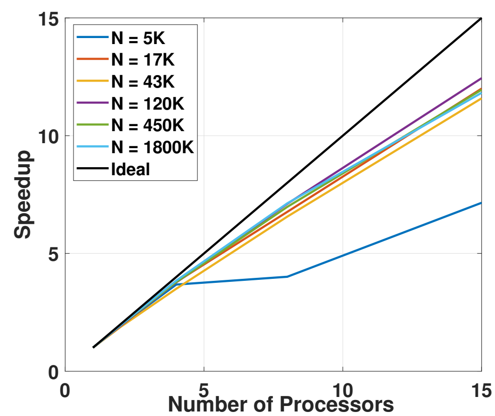

(b) Skyline Solver

Figure 5.11: Speedup of skyline solver and MUMPS solver versus number of processors for various problem sizes.

Direct solvers allow for the computation of the number of floating point operations. The number of floating point operations involved in the LDL^T factorization of the skyline solver is given by Eq. 5.2,

$$\sum_{j=1}^{N} 1 + h_j(h_j - 1) \tag{5.2}$$

where h_j is the height of column j in the skyline given by Eq. 3.16 in Chapter 3. MUMPS also reports the number of operations performed using its multifrontal method. Figure 5.12 shows that the floating point operations per second (FLOPS) for both solvers with number of processors for various problem sizes. Regardless of problem size, a maximum of 3 times higher FLOPS is achieved with skyline solver as compared to that of MUMPS.

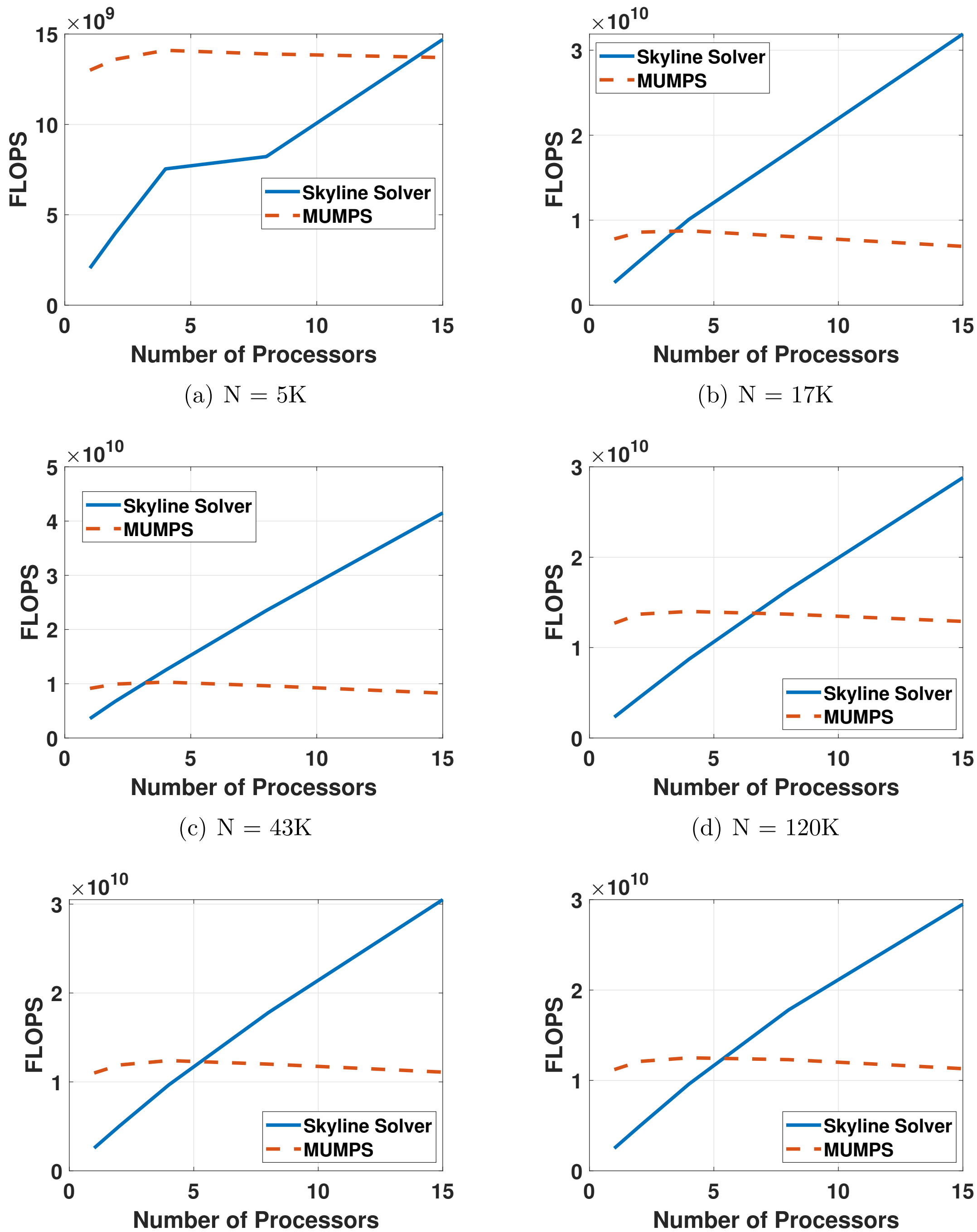

(a) N = 5K
(b) N = 17K
(c) N = 43K
(d) N = 120K
(e) N = 450K
(f) N = 1800K

Figure 5.12: Performance comparison of FLOPS versus number of processors between skyline solver and MUMPS for various problem sizes.

5.7 Convergence of MHB

The time histories of flap, lag, and torsional deformations at the tip in forward flight with fixed control inputs and $\Delta\psi = 1°$ are shown in Figure 5.13. As expected, time marching requires many rotor revolutions before periodicity is attained, particularly in lag, which has little to no aerodynamic damping. The flap and torsion modes converge in 10 revolutions, whereas lag reaches 5% accuracy in 10, 0.5% accuracy in 20 iterations. The same level of accuracy in modified harmonic balance requires 25-30 iterations.

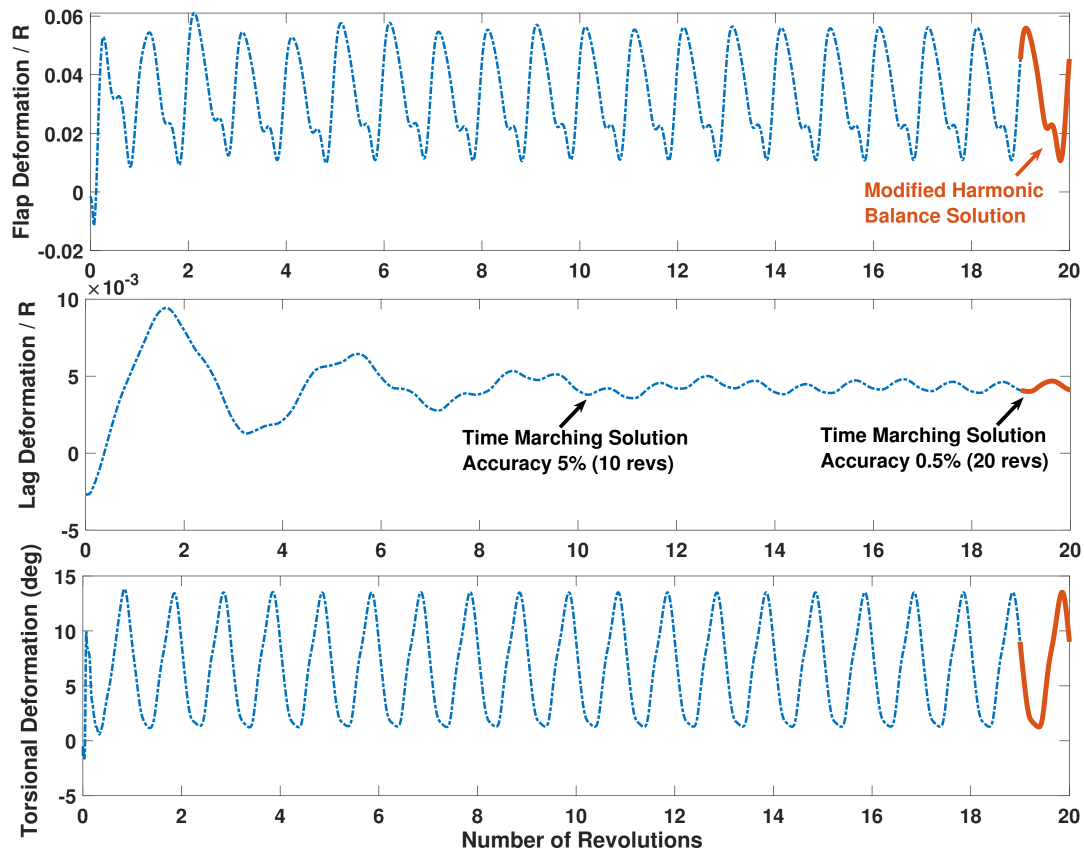

Figure 5.13: Time-history of flap, lag and torsional deformation at tip of UH-60A-like rotor in forward flight.

Figure 5.14 shows the convergence of harmonics with the iteration number. The error plotted is the difference between modified harmonic balance and time marching solutions at the tip for the UH-60A rotor test case. A typical solution reaches 1%

accuracy in 10 iterations, 0.01% in 30, and 0.0001% in 40 iterations. What time marching achieves with small azimuth-step and large number of revolutions, the modified harmonic balance achieves directly, albeit with iterations.

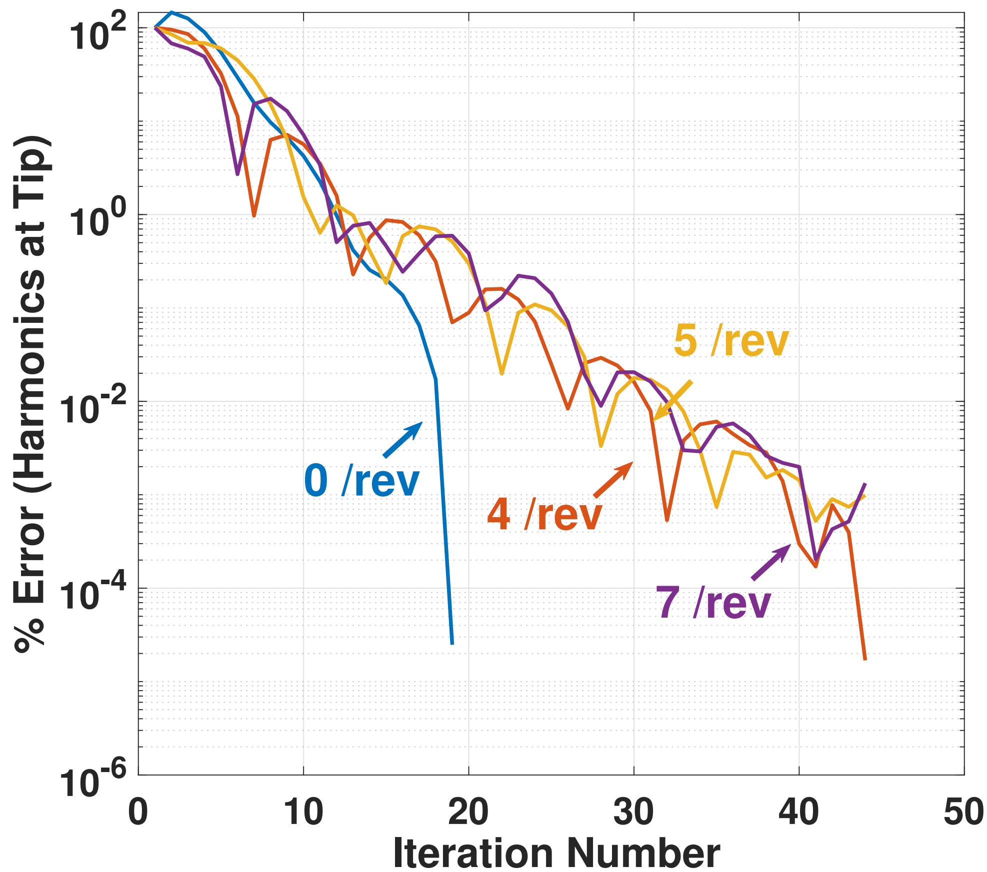

Figure 5.14: Convergence of harmonics in the solution at tip with iterations.

5.8 Parallel Performance of MHB

The parallel performance of the modified harmonic balance algorithm is characterized using three metrics: floating point operations per second (FLOPS), parallel speedup, and scalability with the number of harmonics and processors.

Figure 5.15 shows the variation of floating point operations per second (FLOPS) with the number of degrees of freedom for time marching and modified harmonic balance. The 3D cantilevered beam with sinusoidal varying tip force (see Chapter 4) is used as a test case for obtaining the FLOPS performance. A maximum of only 10 gigaFLOPS can be achieved using time marching. On the other hand, the modified harmonic balance reaches higher than 1 teraFLOPS. The key conclusion is that the modified harmonic balance will produce a gain of at least two orders of magnitude in FLOPS compared to time marching. Although this is not a fair comparison between the two algorithms, it does establish that the MHB is an inherently parallel algorithm that performs more computations at a lesser time.

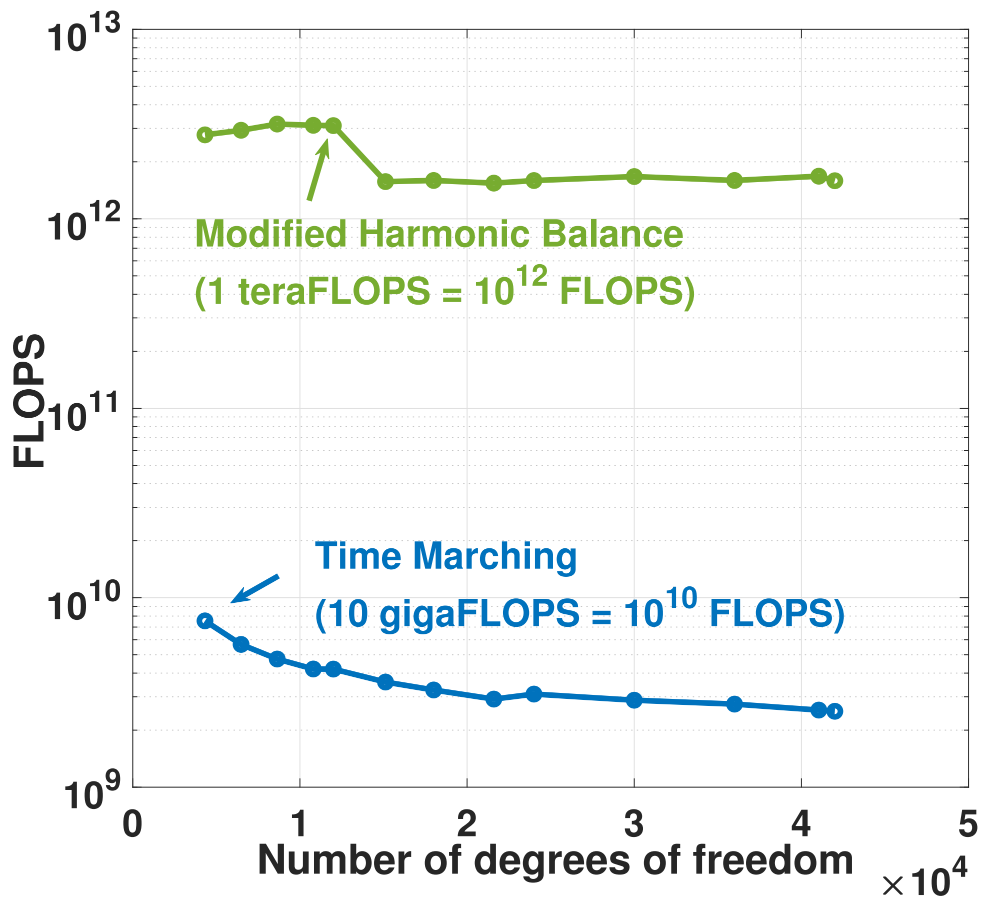

Figure 5.15: Variation of FLOPS versus the number of degrees of freedom for time marching and modified harmonic balance.

The solution times and speedup for the trim solution of UH-60A-like rotor test case are summarized in Table 5.1. The times for the time marching solution was obtained with $\Delta\psi = 5°$. The time marching solution on a single processor for a trim solution takes 100 minutes. The parallel skyline, but still with time marching, reduces it to 16 minutes, a speedup of around 6. Replacing time marching with the modified harmonic balance on a single processor with no parallelization produces a speedup of 10. When implemented in parallel (9 MPI tasks, 0 to 8 harmonics) with each using 10 shared memory processors internally, the time drops to 2 minutes, achieving a total speedup of 50. This massive speedup is a result of the combined effect of the parallel skyline and the inherent parallel nature of the modified harmonic balance.

Table 5.1: Solution times for serial and parallel time marching and modified harmonic balance for UH-60A-like rotor test case; parallel execution on combined shared and distributed memory architecture.

Solution Procedure	**Mode**	**Trim Solution**	**Speedup**
Time Marching	Serial	100 min	1
	Parallel	16 min	6
Modified Harmonic Balance	Serial	10 min	10
	Parallel	2 min	50

Table 5.2 provides the solution times and speedup for trim solution of TRAM test case. Because the TRAM test case has a larger problem size, the serial computational time for time marching takes 8 hours. The parallel skyline with time marching reduces it to 70 minutes, a speedup of around 7. Modified Harmonic Balance on a single processor solves the problem in 55 minutes, and the parallel version in 8 minutes. Overall the parallel modified harmonic balance yields a speedup of 70.

Table 5.2: Solution times for serial and parallel time marching and modified harmonic balance for the NASA TRAM test case; parallel execution on combined shared and distributed memory architecture.

Solution Procedure	**Mode**	**Trim Solution**	**Speedup**
Time Marching	Serial	8 hours	1
	Parallel	70 min	7
Modified Harmonic Balance	Serial	50 min	10
	Parallel	8 min	70

A total of $N+1$ MPI tasks are launched for obtaining solution with N harmonics $(0, 1, 2, ..., N)$. With each MPI task assigned with 10 shared memory processors, a total of $10 \times (N+1)$ processors (both MPI and OpenMP) are employed. The solution time for the trim solution remains almost constant with an increase in number of harmonics. Thus, a finer harmonic resolution is possible with no increase in solution time if more processors are available. Figure 5.16 shows the trim solution time versus number of harmonics and processors. For example, a total of 90 processors are used to solve for $0, 1, 2, ..., 8$ harmonics. This proves the weak scalability of the algorithm.

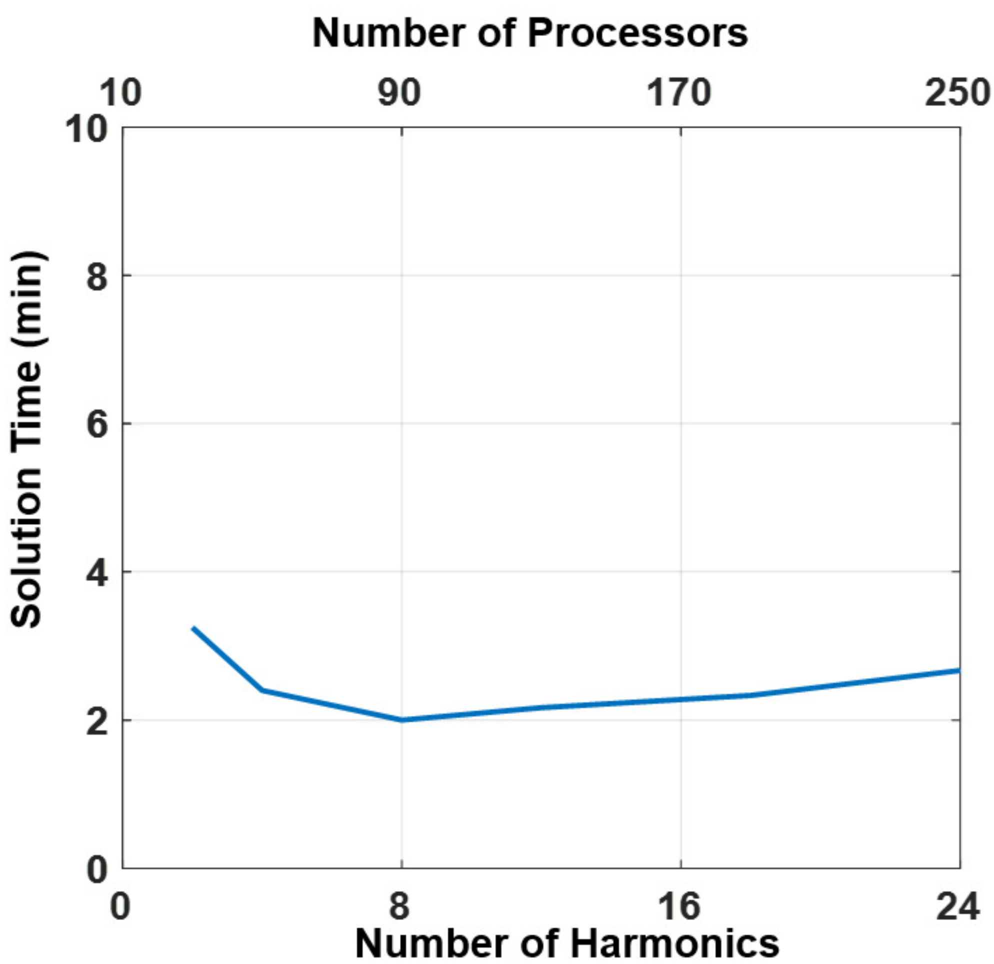

Figure 5.16: Trim solution time versus number of harmonics and processors; a total of $10 \times (N+1)$ processors are used to solve for $0, 1, 2, ..., N$ harmonics; solution time remains almost constant with increase in number of harmonics and processors.

5.9 Summary and Conclusions

The parallel performance of the skyline solver and modified harmonic balance algorithm was studied using different performance metrics. Idealized beam and real rotor test cases were used for this study. Based on the results obtained, the following conclusions are drawn.

1. Regardless of problem size, the parallel skyline solver provides a speedup of around 17 for 19 processors on a shared memory architecture. This makes it 90% efficient.

2. The matrix bandwidth does affect the performance of parallel skyline solver. A matrix with larger bandwidth such as that of FET matrices can only be speeded ten times with 19 processors. The drop in speedup is due to the cache losses occurring due to high bandwidth (high memory).

3. The parallel skyline solver performs better than the widely used open-source solver MUMPS. The solution time reduces for skyline solver with number of processors, whereas it is constant for the MUMPS solver. Thus, MUMPS is significantly faster in serial mode. But as the number of processors increases, the parallel skyline solver appears to surpass it. Regardless of problem size, a maximum of 3 times higher FLOPS is achieved with skyline solver compared to MUMPS.

4. The modified harmonic balance is verified to converge to the same time marching solution. The error drops to 1% with 10 iterations, 0.01% with 20, and 0.0001% with 40 iterations. This level of accuracy and convergence was observed for both idealized and practical rotor problems.

5. For the UH-60A rotor trim solution test case, a 50 times speedup is achieved using the parallel MHB method compared to the serial time marching method.

This brings the solution time from 100 minutes to 2 minutes. For the TRAM trim solution test case, a 70 times speedup is achieved. This brings the solution time from 9 hours to 8 minutes.

6. The MHB method exhibits weak scalability with number of processors and harmonics. The solution time for the trim solution remains almost constant with an increase in number of harmonics. Thus, a finer harmonic resolution is possible with no increase in solution time if more processors are available.

7. Peak performance of 1 teraFLOPS was recorded for the parallel modified harmonic balance algorithm on a model problem with structures alone.

Chapter 6: Three-Dimensional Coaxial Models

The establishment of new parallel X3D allows for expanding the scope of modeling advanced rotor configurations. In this work, the coaxial rotor is that selected configuration. This chapter deals with the development of three-dimensional coaxial models. Two open access models are developed; one is called the Metaltail – a hingeless conceptual design, and the other is an artificially made-up articulated coaxial with two UH-60A-like rotors.

6.1 The Metaltail

Metaltail was the name given to a notional coaxial tail-sitter proprotor aircraft designed by the University of Maryland as a part of the 2018 Vertical Flight Society Graduate Design Competition [125]. The rotor is henceforth referred to as the Metaltail rotor or just Metaltail. Cheng Chi of the 2018 design team first built this model. It is an open-source research rotor therefore adopted by the U.S. Army / DoD rotorcraft simulation software CREATE^{TM}–AV Helios [126] development team as an example case. Figure 6.1 shows the computer-aided design (CAD) model of the coaxial rotor. Table 1 lists the important rotor parameters.

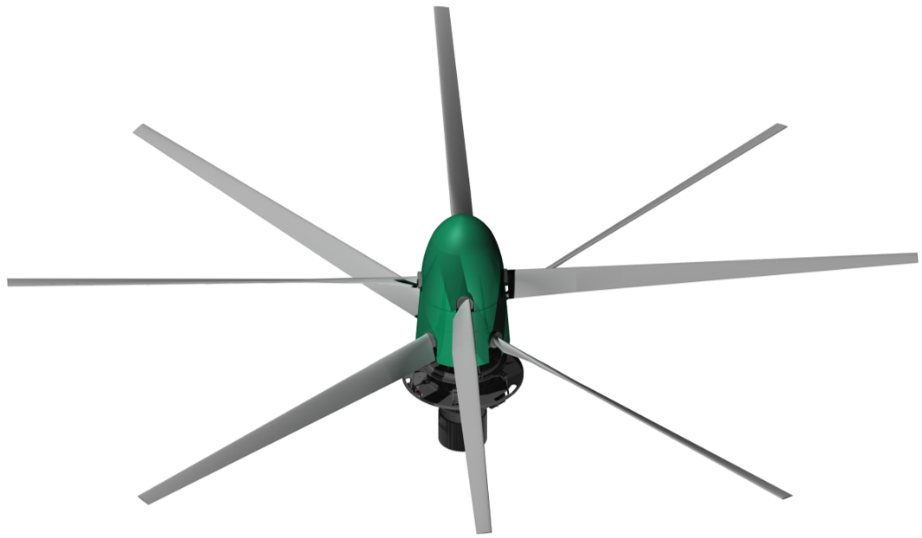

Figure 6.1: CAD model of Metaltail coaxial rotor.

Table 6.1: Properties of each Metaltail rotor

Property	Value
Radius	1.5 m (4.9 ft)
Number of Blades	4
Pre-cone	1.5°
Solidity, σ	0.0637
Rotor Separation, z/D	0.07
Rotor speed	1408 RPM (147 rad/s)

Staruk et al. [127] built the preliminary mesh and structural analysis model for this rotor; however, that model encountered convergence problems when coupled with Helios CFD. In order to dissect the problem, a new model was built ground-up and re-meshed. The following sections describe the creation of this new model step by step.

6.2 CAD Model

Figure 6.2 shows the CAD model for the upper rotor depicting attachment of blade root to hub through bearing housing. The blade consists of surface and internal structure. The structural dynamics model will contain a single blade, but with all details of its internals structure. Figure 6.3 shows the CAD model of individual parts of one Metaltail blade. It consists of the following parts – the blade, pitch horn, pitch link, inner cuff, outer cuff, thrust bearing, and journal bearing. The connectivity between each of these parts is described using the structural analysis representation below.

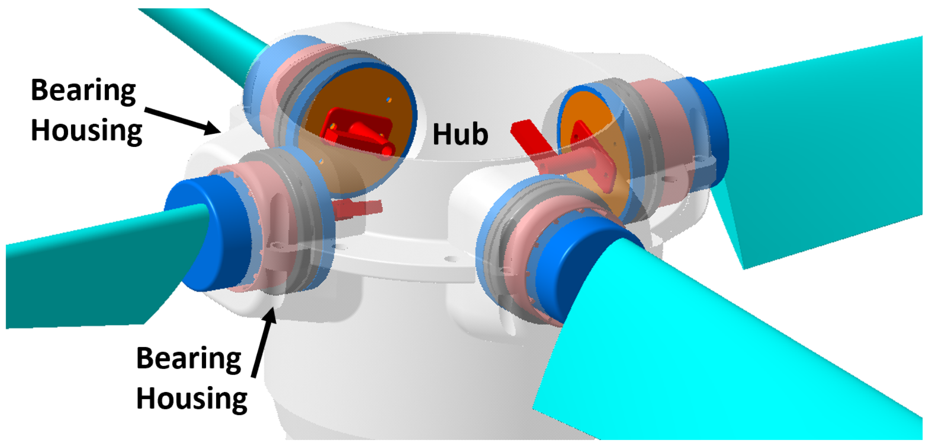

Figure 6.2: Attachment of Metaltail rotor blade root to hub through bearing housing.

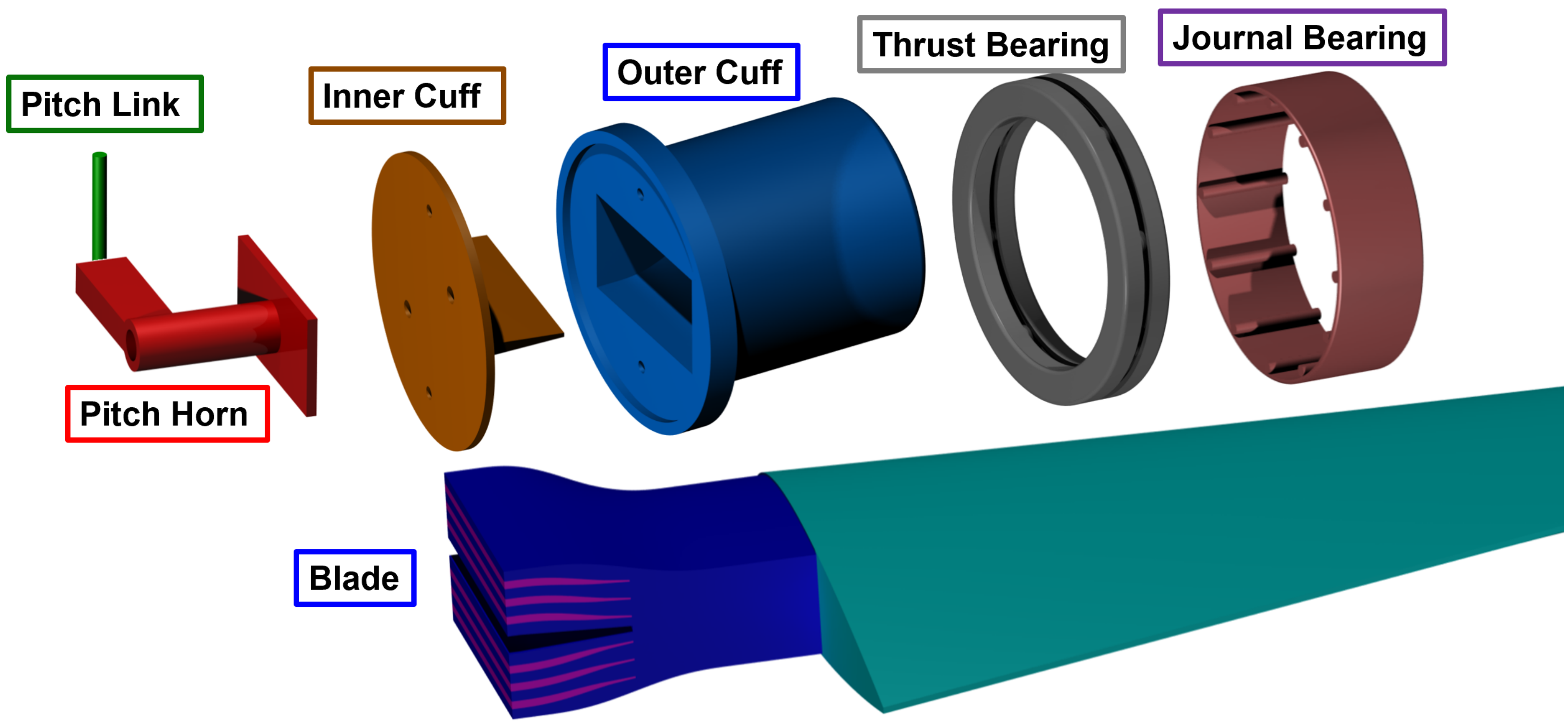

Figure 6.3: CAD model of the Metaltail rotor blade showing five flexible components and two bearings.

6.3 Structural Analysis Representation

The structural analysis representation assigns which parts are to be modeled using 3D finite elements and which parts are to be simply modeled as joints. It then defines the type and geometry of joint connections and assigns joint properties.

The Metaltail blade has five flexible parts: the blade, pitch horn, pitch link, inner cuff, outer cuff, and inner cuff. The bearings, fittings between the flexible parts, and hub connections are modeled as joints. Figure 6.2 showed the attachment of the blade root to the hub. The blade root is sandwiched by the bearing housing from top and bottom. The bearing housing connects the thrust and journal bearing to the hub. The pitch horn is located at the root of each inner sleeve and connected to the upper swashplate (not shown in Figure 6.2) with a pitch link.

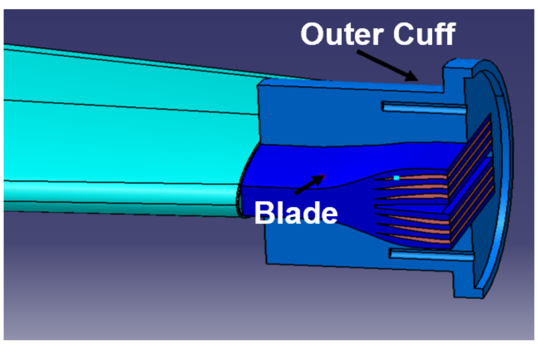

(a) Blade and outer cuff

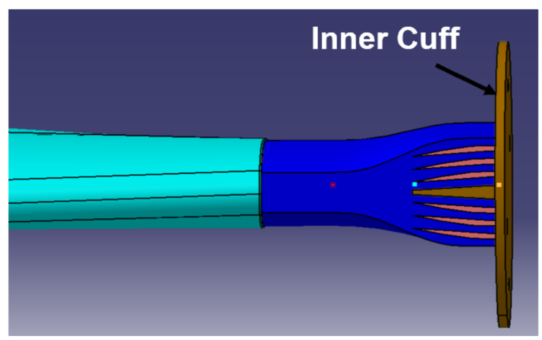

(b) Inner cuff and blade

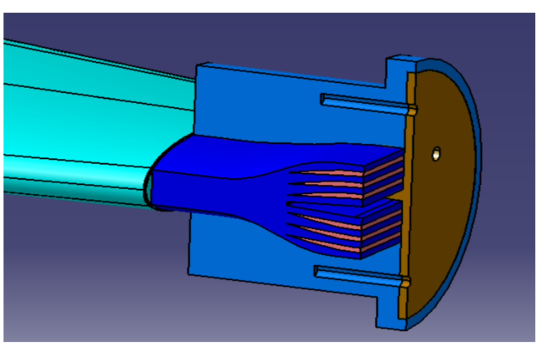

(c) Inner and outer cuff

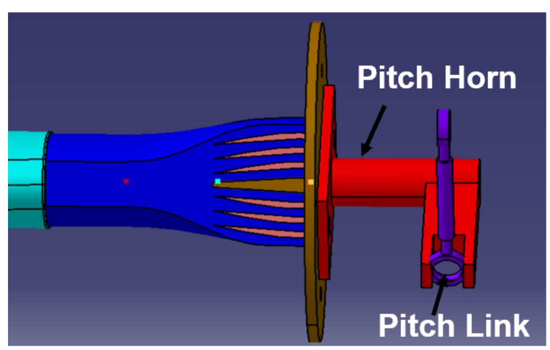

(d) Pitch link, pitch horn and blade

Figure 6.4: Physical connections between components of Metaltail; (a) blade and outer cuff connection; (b) inner cuff and blade connection; (c) inner and outer cuff connection; and (d) pitch link, pitch horn and blade connections.

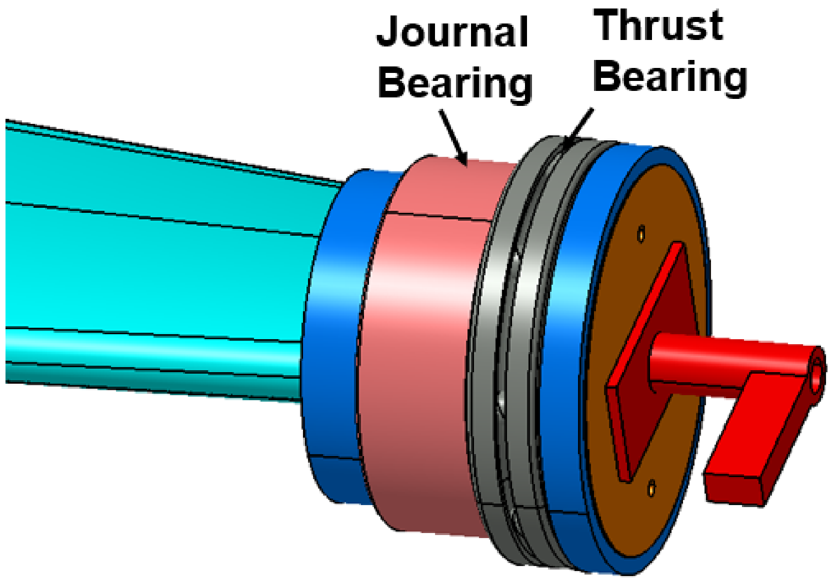

(a) Attachment of two bearings

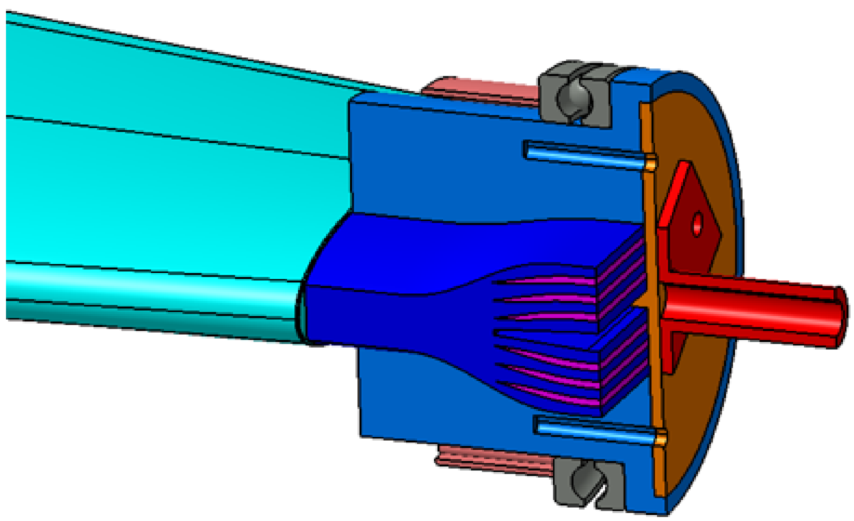

(b) Attachment of inner and outer cuff to blade

Figure 6.5: Cut away view of blade root showing attachment of (a) thrust and journal bearing; (b) inner and outer cuff to blade.

The bolts between the inner cuff and the outer cuff, the thrust and journal bearings, and pitch link connections to the pitch horn and hub are modeled as joints. The exposed root of the blade mates into the inner surfaces of the outer cuff, and the inner cuff locks into the open slot of the blade as shown in Figure 6.4. So, the connections between the blade and both the cuffs are modeled as rigid joints. The outer cuff is connected to the rotor hub through two bearings as shown in Figure 6.5(a). The thrust bearing transfers only axial force to the hub. The journal bearing transfers thrust, in- and out-of-plane shears, and the flapping and lead-lag moments. The inner cuff is connected to a pitch horn, which is then connected to a pitch link on the leading edge side of the blade. The torsion moment is transferred via inner cuff to the pitch link connection to the hub. The blade cross section consists of a tungsten leading edge weight, a solid uni-axial carbon-fiber D-spar, a machinable foam aft core, and a uni-axial carbon fiber trailing edge block, all wrapped in a ±45° carbon fiber skin. This is shown in Figure 6.6.

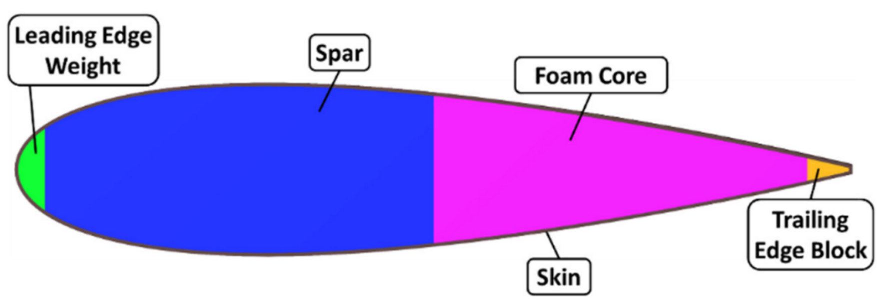

Figure 6.6: CAD model of the Metaltail blade cross-section at the root.

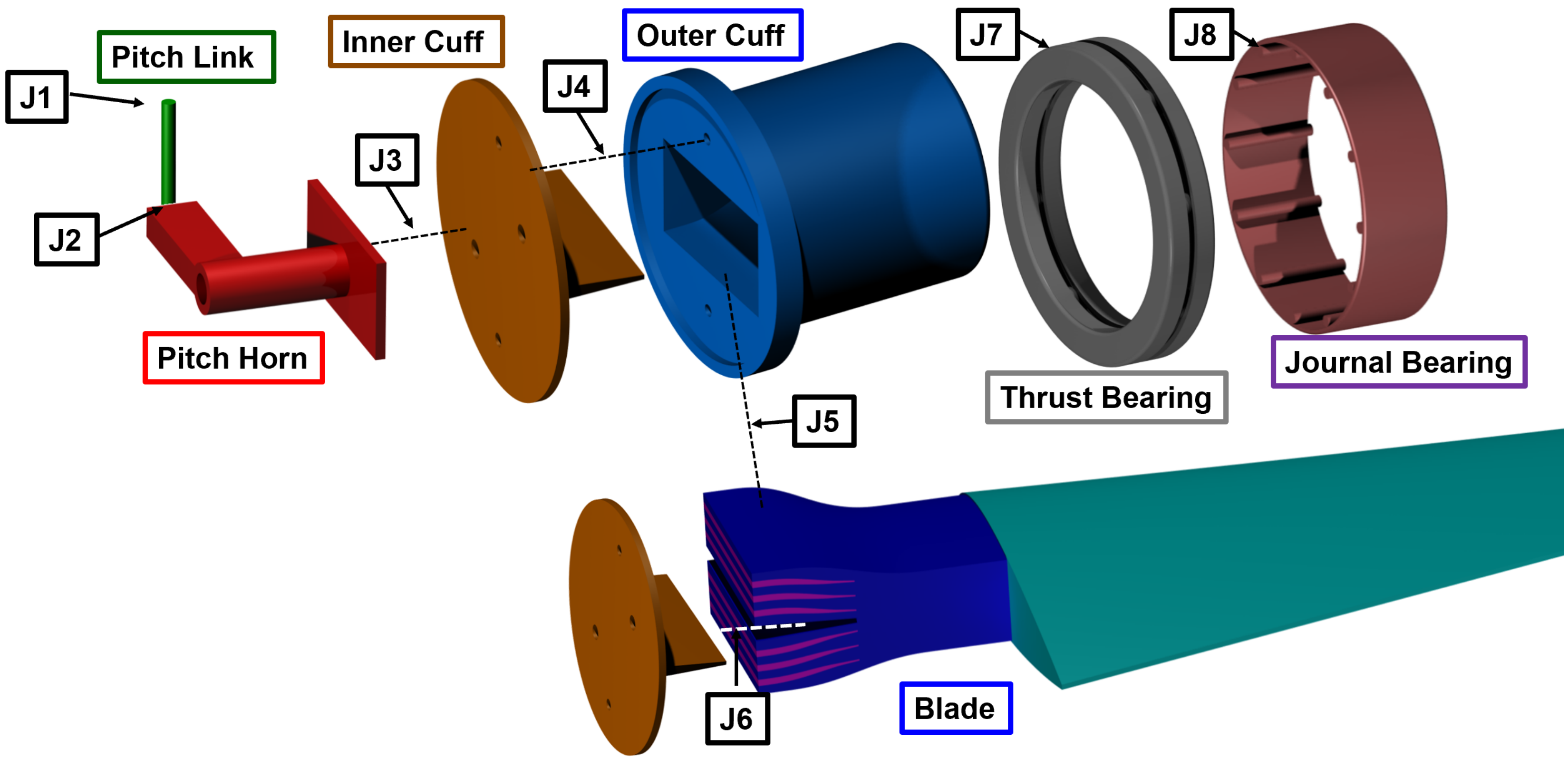

Figure 6.7: Joints in the Metaltail model; eight joints J1 – J8 are modeled for various purposes.

In total, the model has 13 parts, 5 of which are flexible parts and 8 are joints. These are shown in Figure 6.7 and listed in Table 6.2. Figure 6.8 shows the load flow diagram. This is the final structural analysis representation of the Metaltail. Each part has two ID numbers, one is the part number (P#), and another is the type number (F# for flex parts, J# for joint parts). The five flexible parts are meshed using brick finite elements. The eight joint parts are assigned kinematic constraints using Euler angles. Three joints are connected to the hub. These serve as load sensors, whose motion in corresponding directions yield the root loads. The root loads are then transferred to hub loads for studying rotor vibration. The identifier -1 (in Table 6.2) sets zero displacement boundary condition (in the rotating frame). Here, it is the hub. Vertical motion commanded to the joint (P1/J1) provides pitch control for trim solution.

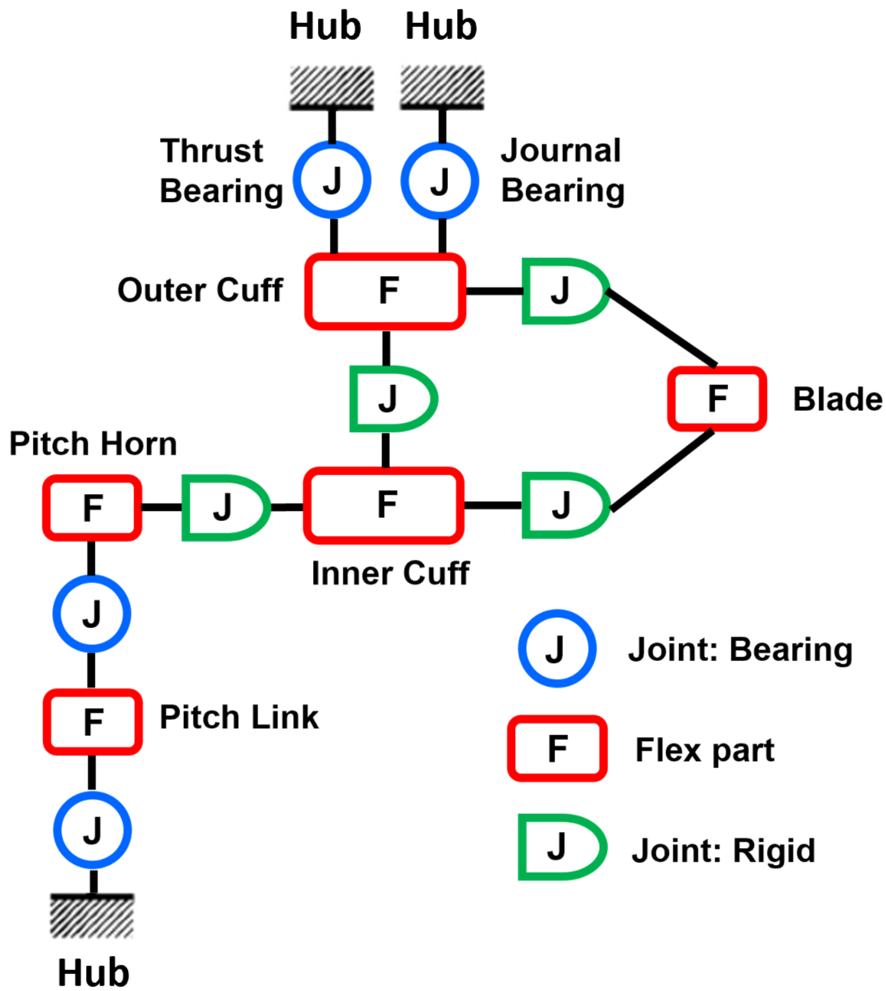

Figure 6.8: The load flow diagram is the final structural analysis representation of the Metaltail blade.

The hub is rigid, so the upper and lower rotors are independent with no dynamic interactions. The analysis is carried out using a single blade in each rotor. There are three connections to the hub for each rotor blade, as seen in Figure 6.8. Hence for the coaxial model, there are a total of six connections to the hub, three from each rotor.

6.4 Structural Analysis Model

Once the part types are assigned, the individual flexible parts are meshed in Cubit. Part meshes are independent. The meshes are generated using 27-node

Table 6.2: List of parts in the Metaltail blade structural model, including connections with -1 indicating a connection to the hub.

Part No.	Flexible/Joint No.	Name	Type	Connections
P1	J1	jPlinkHub	Joint	-1, P2
P2	F1	Pitch Link	Flex	P1, P3
P3	J2	jPlinkPhorn	Joint	P2, P4
P4	F2	Pitch Horn	Flex	P3, P5
P5	J3	jPhornIcuff	Joint	P4, P6
P6	F3	Inner Cuff	Flex	P5, P7, P11
P7	J4	jIcuffOcuff	Joint	P6, P8
P8	F4	Outer Cuff	Flex	P7, P10, P12, P13
P9	F5	Blade	Flex	P10, P11
P10	J5	jOcuffBlade	Joint	P8, P9
P11	J6	jIcuffBlade	Joint	P6, P9
P12	J7	jThrustBearing	Joint	-1, P8
P13	J8	jJournalBearing	Joint	-1, P8

isoparametric hexahedral brick elements. A detailed description of meshing rotor blades can be found in Reference [45]. The meshes and joints are assembled to create the final structural analysis model of the blade as shown in Figure 6.9. It consists of 1316 bricks with a total of 31,735 degrees of freedom.

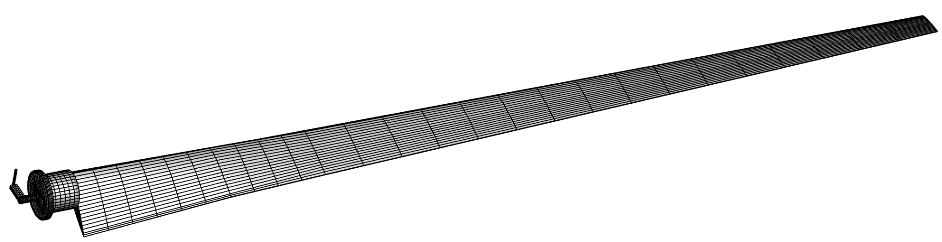

Figure 6.9: Assembled structural mesh is the final structural analysis model of the Metaltail blade.

Each part mesh is assigned three features: blocks (B), sidesets (SS), and nodesets (NS). These are also generated in Cubit. They are used by the solver for important tasks. Blocks assign materials for flexible parts, sidesets identify aerodynamic surface nodes, and nodesets are the finite element nodes to which joints connect. Figure 6.10 shows the different set of nodesets created for joint connections between components. The same is listed in Table 6.3. Figure 6.11

shows the nodesets along the span and can be used to extract 1D-like properties and sidesets for aerodynamic surfaces. A total of 10 sidesets are created for this model.

Table 6.3: Description of nodesets of Metaltail.

Component	Nodeset	Description
Pitch Link	NS401	Connects to hub
Pitch Link	NS402	Connects to pitch horn
Pitch Horn	NS401	Connects to inner cuff
Pitch Horn	NS402	Connects to pitch link
Inner Cuff	NS401	Connects to pitch horn
Inner Cuff	NS402	Connects to pitch outer cuff
Inner Cuff	NS403	Connects to blade
Outer Cuff	NS401	Connects to inner cuff
Outer Cuff	NS402	Connects to blade
Outer Cuff	NS403	Connects to thrust bearing
Outer Cuff	NS404	Connects to journal bearing
Blade	NS401	Connects to outer cuff
Blade	NS402	Connects to inner cuff
Blade	NS403	For tip loading

The meshes and joints are input to the solver through *SAM.input* file. This file can be made manually or automatically using the Python-based utility samBuilder [45]. The *SAM.input* is a FORTRAN namelist consisting of mesh positions and orientations, material properties, joint properties, and joint connections.

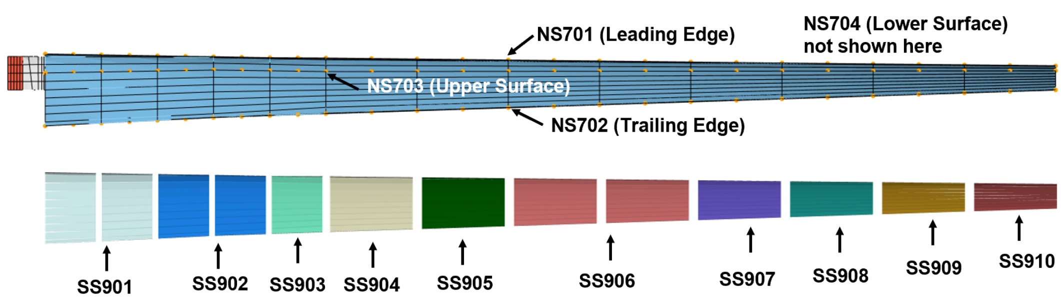

Figure 6.11: Depiction of nodesets along the blade span and sidesets for aerodynamic surfaces of Metaltail.

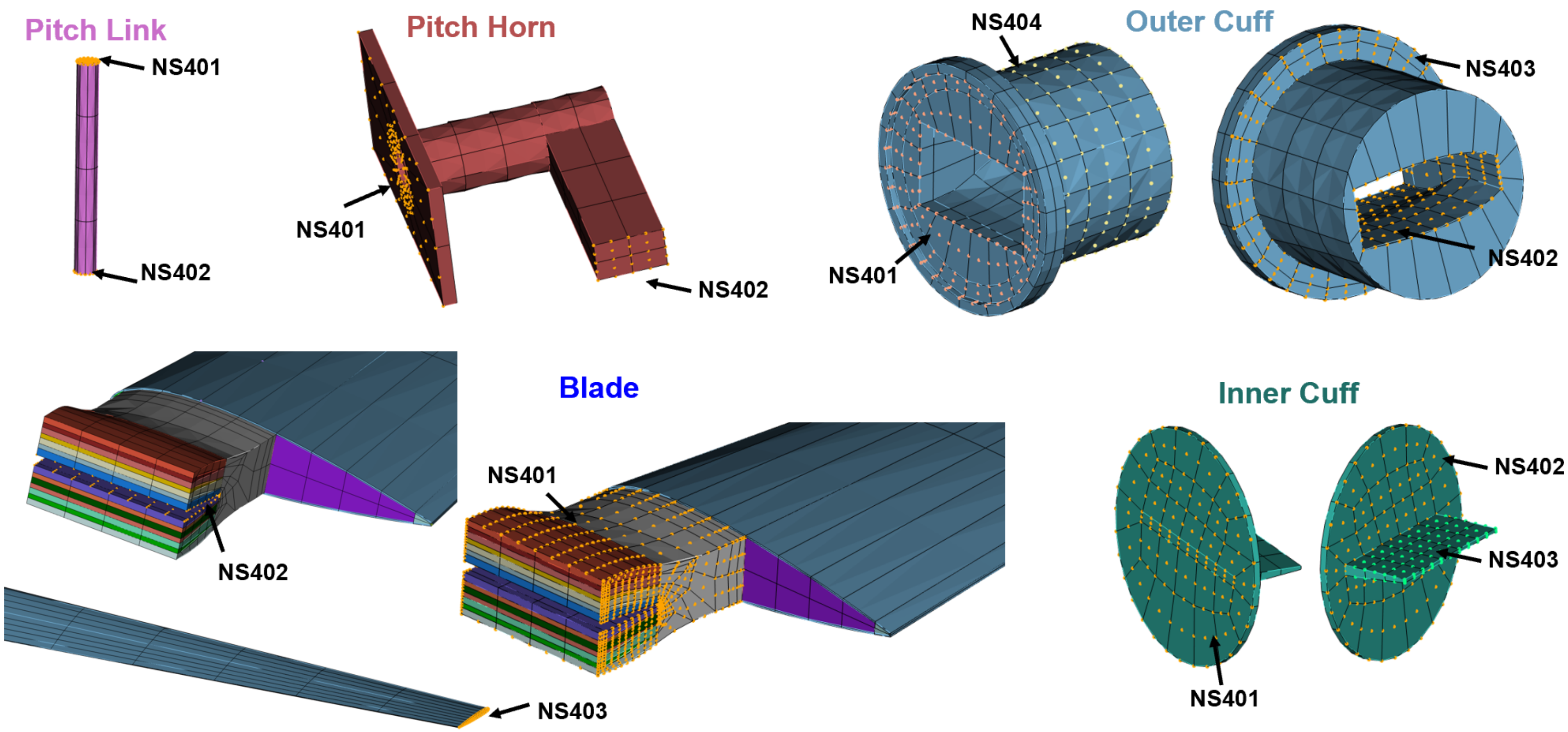

Figure 6.10: Different set of nodesets created for joint connections between components of Metaltail.

6.5 Material Properties

The material properties of the Metaltail blade are listed in Tables 6.4 and 6.5. The first table lists the material properties of flexible parts F1 to F4. All the parts F1 to F4 are made of an isotropic material, Titanium-6AL-4V. The second table lists the materials for the blade (F5). The blade consists of different parts (Figure 6.6), each made with different material.

Table 6.4: Material properties of Metaltail flexible parts (F1 to F4).

Properties	F1	F2	F3	F4
Component	Pitch Link	Pitch Horn	Inner Cuff	Outer Cuff
Material	Ti-6Al-4V	Ti-6Al-4V	Ti-6Al-4V	Ti-6Al-4V
Type	Isotropic	Isotropic	Isotropic	Isotropic
E, GPa	113.8	113.8	113.8	113.8
ν_{12}	0.342	0.342	0.342	0.342
ρ, kg/m^3	4430	4430	4430	4430

Table 6.5: Material properties of Metaltail blade (flex component F5).

Properties	Leading Edge	Spar	Foam	Trailing Edge	Skin
Material	Tungsten	T300 Graphite	Rohacell 71	T300 Graphite	IM7CF ($\pm 45°$)
Type	Isotropic	Ortho-Iso	Isotropic	Ortho-Iso	Ortho-Iso
E_1, GPa	330	131	0.092	131	68.47
E_2, GPa		9.3		9.3	64.54
ν_{12}	0.32	0.28	0.18	0.28	0.058
G_{12}, GPa		5.86		5.86	4.07
ρ, kg/m^3	17000	1600	75	1600	1600

6.6 Aerodynamic Model

The aerodynamic model of the blade is input through the *AER.input* file. It is a FORTRAN namelist of airfoil names and lifting line properties, no different from any beam-based comprehensive analysis. The Metaltail blade consists of two airfoils; NACA2420 at the root and SC1095 at the tip. The transition between the root airfoil and the tip airfoil occurs at 30% R. The blade is highly twisted at a nominal rate of $-56°$ per span. The chord and twist distribution are shown in Figures 6.12 and 6.13 respectively. The high twist of the blade makes it less representative of an edgewise coaxial rotor. Nevertheless, the high twist along with the intricate hub provides many of the complications desired in a test problem and also loosely represents the challenges involved in modeling a modern coaxial rotor.

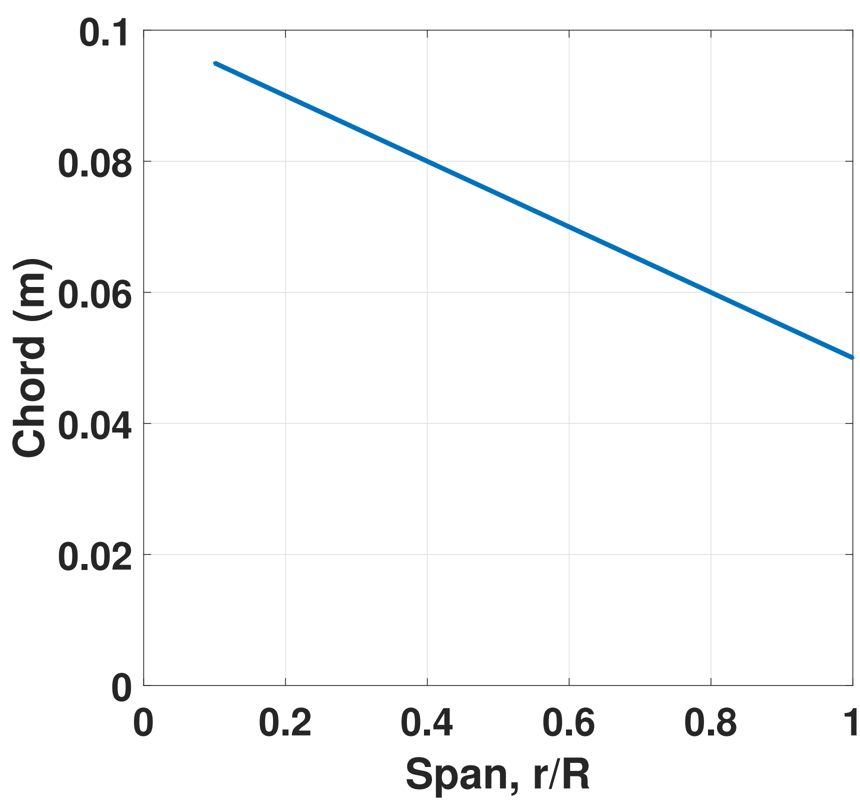

Figure 6.12: Span-wise chord distribution of Metaltail blade.

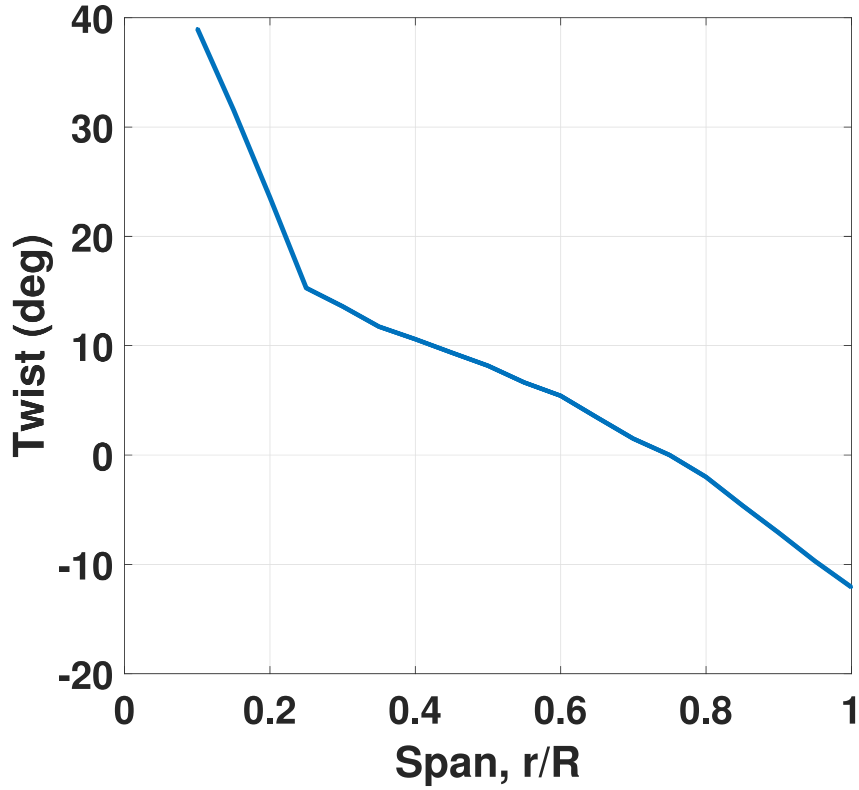

Figure 6.13: Span-wise twist distribution of Metaltail blade.

The blades for both rotors are meshed and assembled together as shown in the Figure 6.14. Naturally it consists of twice the number of degrees of freedom as the single rotor model. For X3D purposes, the input parameters for both rotors are identical except the direction of rotation. The upper rotor rotates in counter clockwise direction (+1) and lower rotor in clockwise direction (-1). The direction of rotation, rotor-rotor separation distance, and other top-level parameters are specified in the system definition (*SDN*.input) file.

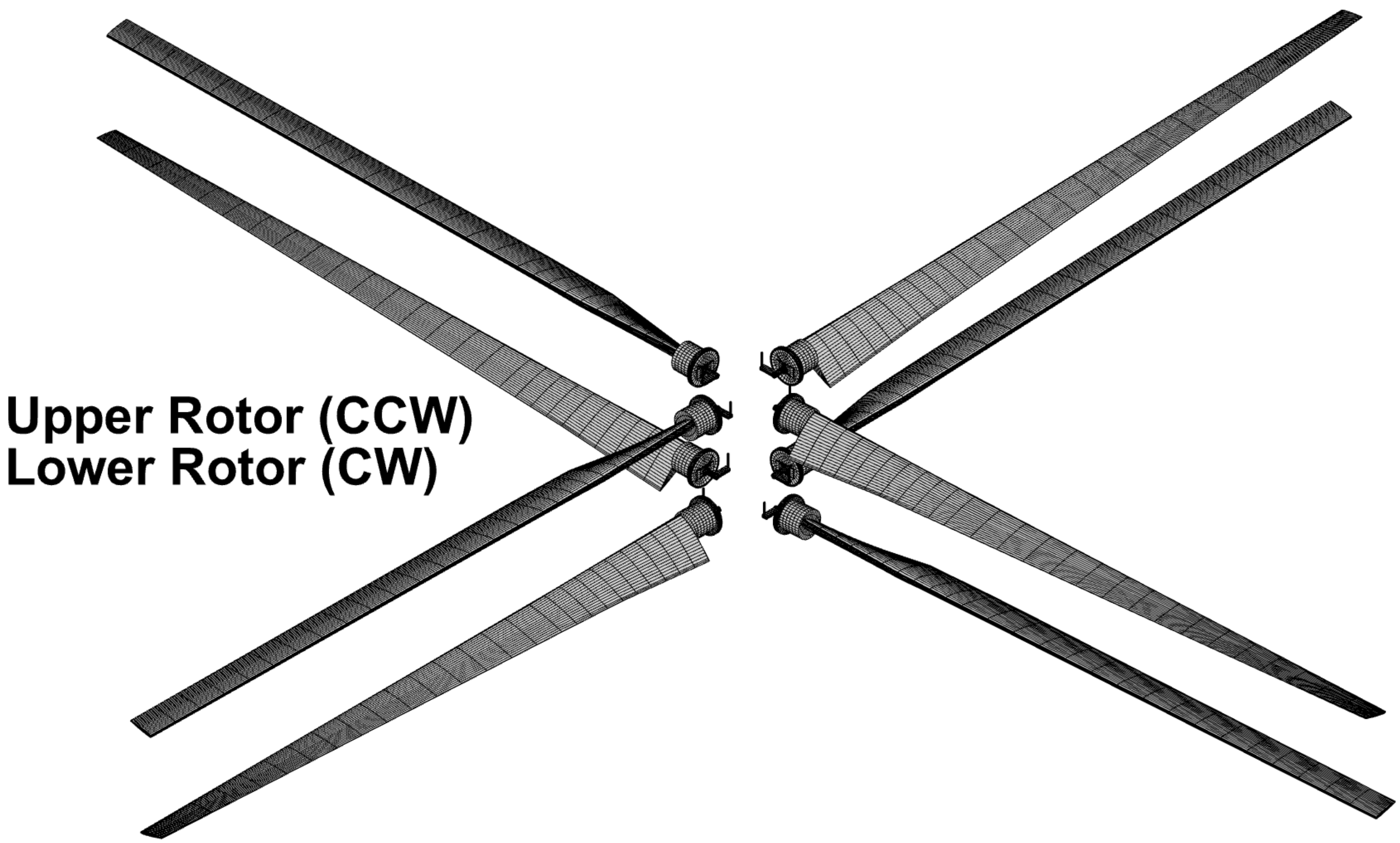

Figure 6.14: Assembled structural mesh of coaxial Metaltail.

Once the development of Metaltail model was completed, the first step was to perform the simple sanity checks. The load path was verified with loads (forces and moments) applied at the tip. It checked the loads were transferred to the hub through the correct load path.

6.7 Rotor Frequencies

The rotor frequencies are shown in Figure 9. At the nominal rotor speed of 1408 RPM, the frequencies clear all the integer harmonics. The flap and lag modes are coupled due to the high twist. The first flap-lag frequency is 1.3 /rev. The first torsion is 5.22 /rev. The high first flap frequency is not unusual for modern coaxial rotors. The first six natural frequencies are listed at the operating rotor speed in Table 6.6.

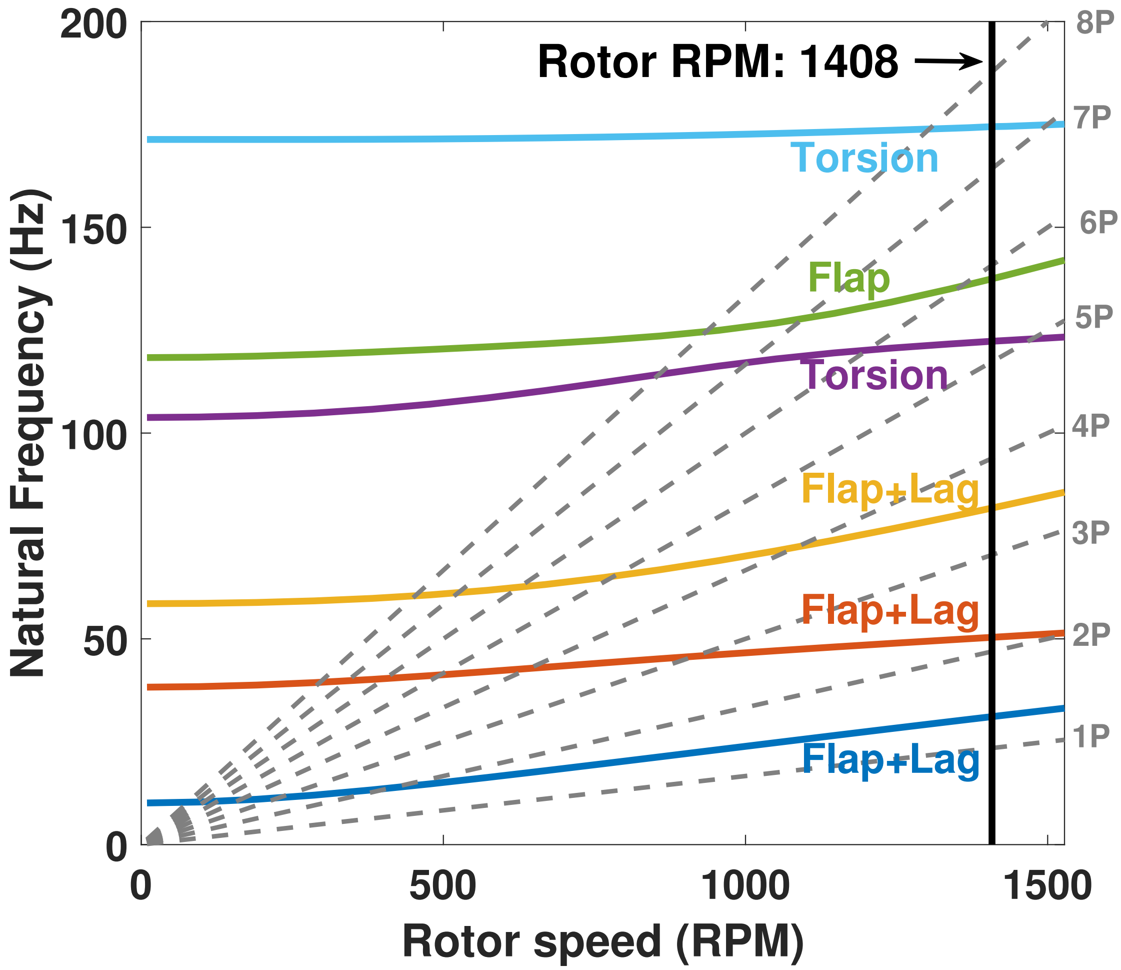

Figure 6.15: Rotating frequencies of the Metaltail blade.

Table 6.6: First six blade frequencies in vacuum at 1408 RPM.

Mode	Freq (/rev)
1st Flap/Lag	1.33
2nd Flap/Lag	2.15
3rd Flap/Lag	3.48
1st Torsion	5.22
4th Flap	5.85
2nd Torsion	7.43

6.8 Airloads

Airloads are predicted in edgewise flight at advance ratio $\mu = 0.1$, forward shaft tilt of $\alpha = -2°$, and blade loading $C_T/\sigma = 0.08$. The trim targets are thrust and zero hub moments. The advance ratio and trim targets are chosen to allow for qualitative comparison with the TRAM test data.

Predictions are shown for two inflow models: linear and free-wake. The free-wake model employs a fully rolled up single tip vortex with filament strengths of 70% maximum bound circulation occuring outboard of 50% R.

Figures 6.16 and 6.17 show the normal force predictions in the time and frequency domain at two radial stations: $72\%R$ and $90\%R$. The linear inflow model can only capture the gross 1/rev characteristics of the airloads, which are too coarse a representation to be used for good airloads prediction. The free-wake model predicts higher harmonics with the characteristics of vortex loadings in the first and fourth quadrant near the tip. The lift near tip has a significant 4/rev as shown in Figure 8.9(b). The proprotor roll up is a complex viscosity-driven phenomenon usually beyond the capabilities of lifting line models. The purpose here is only to verify the general trends.

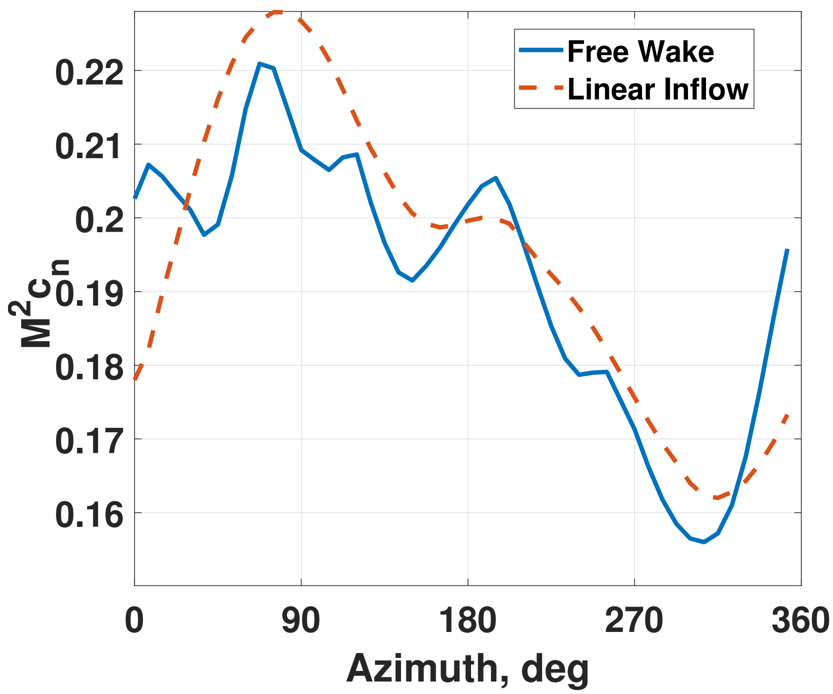

(a) Normal force at 72% radial location

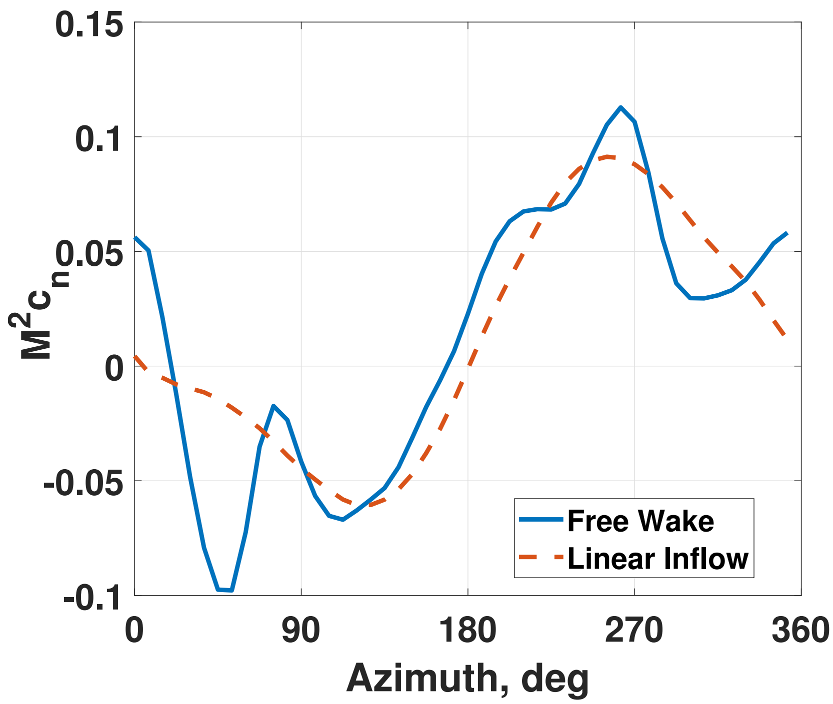

(b) Normal force at 90% radial location

Figure 6.16: Predictions of normal force with linear inflow and free-wake models at $\mu = 0.1$, $C_T/\sigma = 0.08$; (a) 72% R; (b) 90% R.

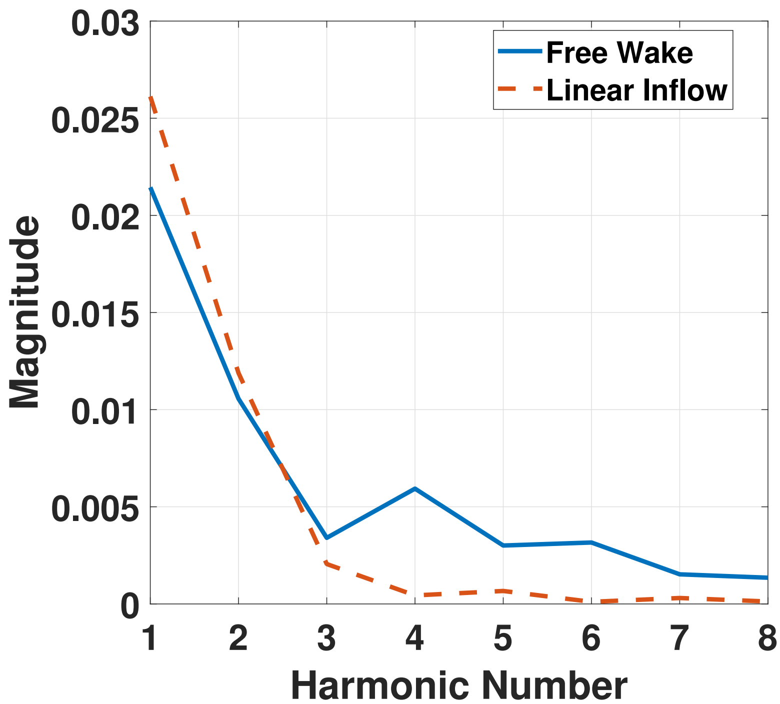

(a) Normal force harmonics at 72% radial location

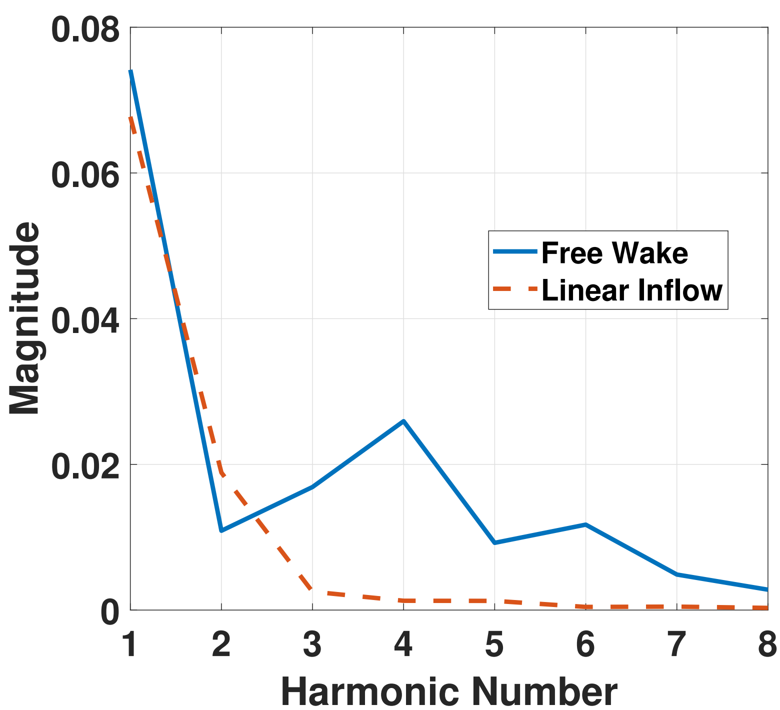

(b) Normal force harmonics at 90% radial location

Figure 6.17: Predicted normal force harmonics with linear inflow and free-wake at $\mu = 0.1$, $C_T/\sigma = 0.08$; (a) 72% R; (b) 90% R.

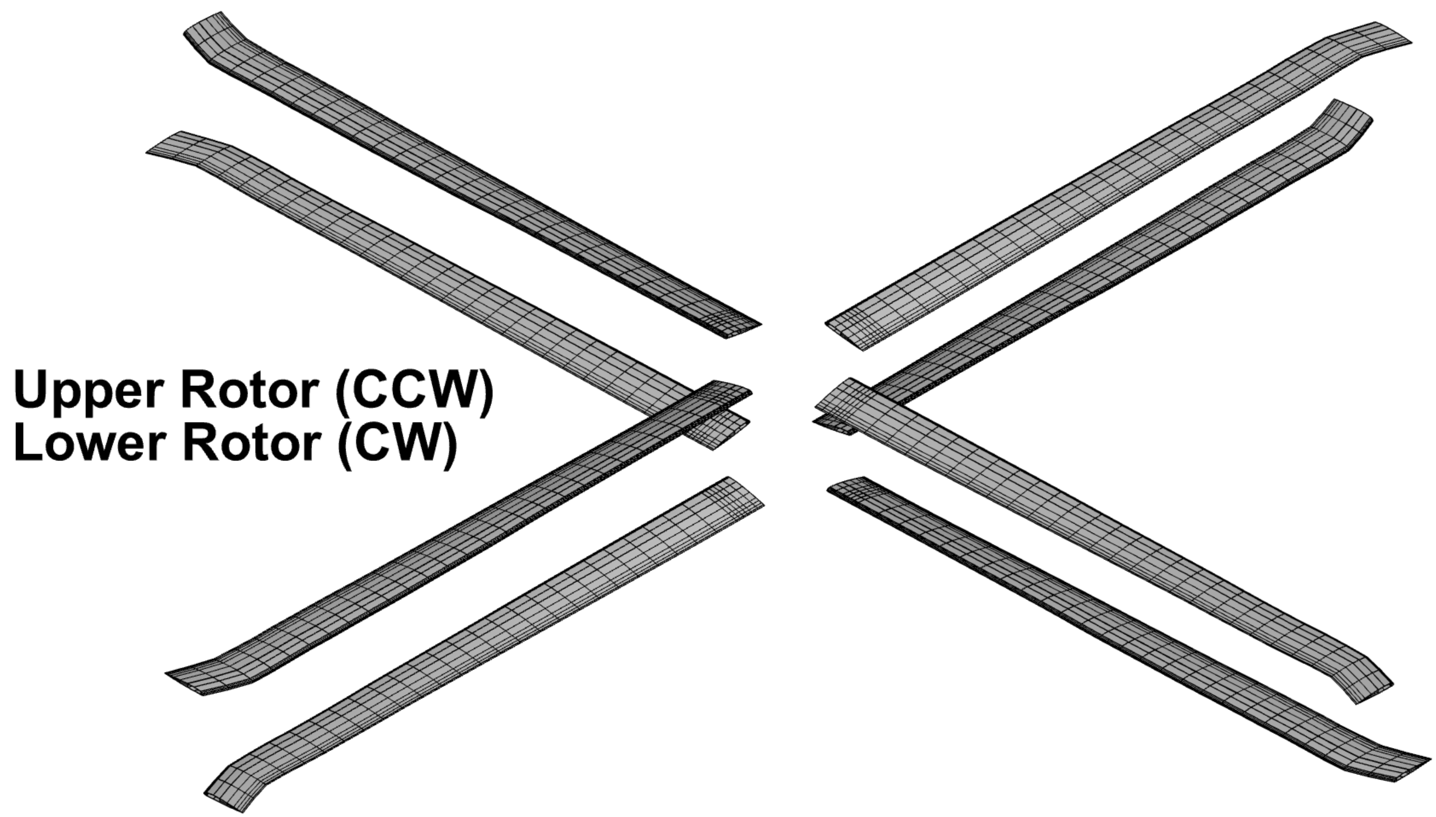

Figure 6.18: Assembled structural mesh of UH-60A-like coaxial rotor configuration.

6.9 UH-60A Coaxial Rotor

A notional coaxial configuration is developed using two UH-60A-like rotors stacked on top of each other. This model provides the benefit of being a realistic edgewise rotor with moderate twist, thereby useful for qualitative comparison with the aeromechanics predictions of Metaltail and S-97 Raider data. The inter-rotor separation is kept identical to Metaltail ($z/D = 0.07$). This coaxial rotor uses a representative model of an UH-60A rotor blade, which is identical to that studied in Chapter 4.

Figure 6.18 shows the assembled structural mesh for the coaxial Metaltail. Unlike Metaltail, this is an articulated rotor. Each blade connects to the hub through a single articulated joint. The upper and lower rotors are still kept independent with no dynamic interactions. The analysis is carried out using a single blade in each rotor.

6.10 Summary and Conclusions

Two notional 3D coaxial models were developed in preparation for coaxial aeromechanical analysis. One is the Metaltail – a hingeless coaxial rotor, and the other is the coaxial rotor built from articulated UH-60A-like rotors. The development of the 3D model for the Metaltail proprotor was described in detail, from CAD to the structural analysis model.

Chapter 7: The Coaxial X3D Solver

The X3D solver is expanded to model multiple rotors. Modifications were needed in both structural dynamics and aerodynamics modeling. The first section of this chapter describes these modifications. The aerodynamics is validated first with coaxial hover data to ensure interactions are correctly captured. Then the analysis is extended to forward flight. In the absence of measured airloads, the UH-60A coaxial rotor is studied with infinite separation to confirm they collapse to single rotor predictions.

7.1 Structural Dynamics

The structural dynamics module of X3D was modified to allow modeling of arbitrary number of rotors spinning in counter clockwise (CCW) or clockwise (CW) directions. X3D carries out the analysis in a right-handed CCW frame. To model CW rotating rotor, the calculations are performed as a CCW rotor, with the conditions, motions and loads changing signs appropriately. For example, the wake analysis is in the fixed frame, so blade motions into the wake and inflow out of the wake are adjusted appropriately. The transformation between the CCW and CW frames is given by Eq. 7.1.

$$\begin{Bmatrix} x \\ y \\ z \end{Bmatrix}^{CCW} = \begin{bmatrix} 1 & 0 & 0 \\ 0 & -1 & 0 \\ 0 & 0 & 1 \end{bmatrix} \begin{Bmatrix} x \\ y \\ z \end{Bmatrix}^{CW} \tag{7.1}$$

Consider two rotors, each rotating in opposite directions. Suppose both are

Table 7.1: Sign changes of velocities and loads between CCW and CW rotors.

Variables	CCW	CW
V_X	V_1	V_1
V_Y	V_2	$-V_2$
V_Z	V_3	V_3
F_X	H	H
F_Y	Y	$-Y$
F_Z	T	T
M_X	M_R	$-M_R$
M_Y	M_P	M_P
M_Z	Q	$-Q$

operated at identical conditions and control angles. In that case, the hub forces and moments for the rotor with CW rotation can be obtained from the CCW analysis by changing the signs according to the following table.

7.2 Aerodynamics

The aerodynamics of coaxial rotors were modeled using quasi-steady lifting line theory coupled with time accurate free-wake. The Maryland Free Wake (MFW) was updated to a new version [19] that can analyze variable and transient RPM (including stopped rotor) on multiple rotors even though that feature is not used in the present work. In addition, a rigid nonlinear near-wake model was added to X3D. The validation for this updated aerodynamics module is discussed in the later section.

7.3 Trim

The goal of an aircraft trim solver is to calculate the necessary inputs to achieve a desired equilibrium flight condition. The trim module in X3D was expanded to include multiple options for coaxial trim. The upper and lower rotor collectives (θ_0^U, θ_0^L) provide total thrust and torque balance. The cyclics can be solved with two options. In the first option, the lateral ($\theta_{1c}^U, \theta_{1c}^L$) and longitudinal ($\theta_{1s}^U, \theta_{1s}^L$) cyclics can be solved for specified roll and pitch moments on each rotor. The body pitch and roll angles are specified. This option is useful for fundamental understanding and research and is used in this work. In the second option, the lateral cyclic is kept same for both upper and lower rotors ($\theta_{1c}^U = \theta_{1c}^L = \theta_{1c}$) and this value along with the two longitudinal ($\theta_{1s}^U, \theta_{1s}^L$) cyclics are solved for a specified lift offset and net roll and pitch moments. The body pitch and roll angles are specified. The second option is similar to the actual aircraft trim where the pitch and roll angles are found from propulsive force and side force balance. In total, there are 7 controls ($\theta_0^U, \theta_0^L, \theta_{1c}, \theta_{1s}^U, \theta_{1s}^L, \alpha_s$, and ϕ_s) for 6 equilibrium equations plus the lift offset.

7.4 Coaxial Hover

The data used to validate the coaxial aerodynamic analysis is from the U.S. Army model test conducted by Ramasamy 2015 [128]. The tests include a single rotor setup and a twin-rotor setup, shown in Figure 7.1. The twin rotors are independent; hence the inter-rotor separation could be varied. The system allowed for independent rotor measurements. The tests were carried out with a straight blade with the NACA 0012 airfoil and a special-purpose twisted blade with tilt rotor airfoils for both single and coaxial configurations. The tilt rotor airfoils are not available in the public domain, so the current validation uses only the straight blades. The validation cases include:

1. Single rotor thrust sweeps, with both three and six blades,
2. coaxial thrust sweep at constant inter-rotor separation, and
3. coaxial separation sweep, at two thrust settings.

The rotor is rigid, so no blade flexibility is modeled. Thus, this is a pure aerodynamic validation. Table 7.2 summarizes the parameters of the rotors. The

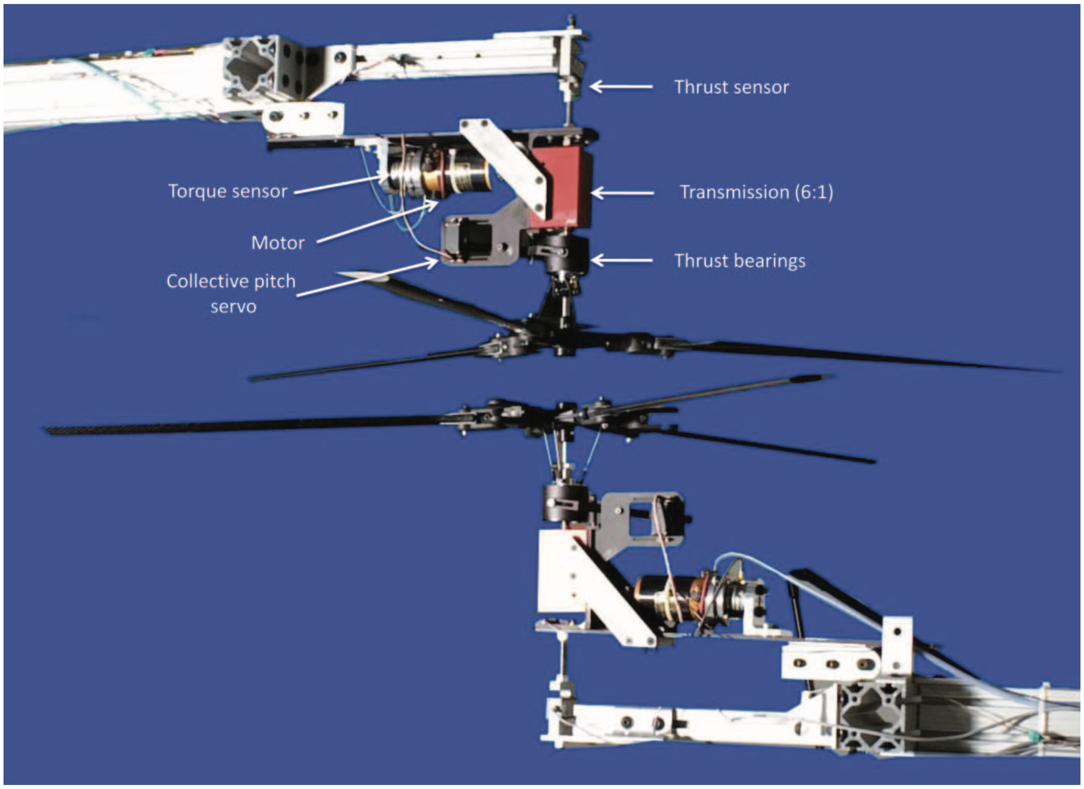

Figure 7.1: Coaxial rotor test setup of U.S. Army model test conducted by Ramasamy [128].

Table 7.2: Ramasamy rotor parameters.

Parameter	Value
Number of Blades	3 or 6
Radius, ft (m)	2.17 (0.66)
Chord, in (m)	2.29 (0.0647)
Root cutout	19.1%
RPM	1200
Rotor Separation, z/D	0.07
Re_{Tip}	$315,000$
M_{Tip}	0.25
Solidity, $N_b = 3$	0.0679
Solidity, $N_b = 6$	0.1359
Twist	0
Taper	1
Airfoil	NACA 0012

baseline rotor separation is 7% diameter (z/D = 0.07). The rotor speed is 1200 RPM. The test data includes thrust and torque for each rotor. For the single rotor, the thrust sweep was achieved by sweeping the collective. For the coaxial rotor, the thrust sweep was achieved by sweeping the upper rotor collective and setting the lower rotor collective to achieve zero torque ($Q_u + Q_l = 0$). For the inter-rotor separation sweeps, the total thrust ($T_u + T_l =$ constant) and zero torque ($Q_u + Q_l = 0$) were targeted using the upper and lower rotor collectives.

The analysis used a lifting-line model with airfoil lookup tables coupled with free-wake. The important features of this model are documented as follows.

1. The free-wake model used a single tip rolled-up vortex released from each blade and azimuthal discretization of 7.5°.

2. A nonlinear lifting-line model was used with prescribed near-wake geometry that extended 30° behind each blade.

3. The initial core size was set to 10% of chord-length.

4. The tip vortex strength was taken as 40% of the maximum bound circulation outboard of 50%R. The 40% value was chosen for no other reason but to obtain good agreement with single rotor ($N_b = 3$) test data.

5. The vortex diffusion constant in the Squire core growth model was set to $a = 0.05$.

6. The number of free-wake turns was set to 6, but for the inter-rotor separation sweeps, it was increased to 20 to ensure that even at the largest separation ($z/D = 1.5$), the upper wake would travel far enough downstream to reach the lower rotor.

7. The number of time marching revolutions for new transient free-wake was set to 20.

8. Reynolds number correction was used for airfoil drag according to Yamauchi and Johnson [129]. The tip Reynolds number (325,000) was low enough that the corrections were needed. The Reynolds number of the NACA 0012 airfoil tables was assumed to be $Re_{table} = 10$ million. The Reynolds number corrections are:

$$c_l(\alpha) = K c_{l_{table}}(\overline{\alpha}) \ ; \qquad c_d(\alpha) = \frac{c_{d_{table}}(\alpha)}{K} \ ; \qquad \overline{\alpha} = \alpha_z + \frac{(\alpha - \alpha_z)}{K} \tag{7.2}$$

where c_l is the resulting coefficient of lift, α is the angle of attack, K is the correction factor, $c_{l_{table}}$ is the coefficient of lift from the table, c_d is the resulting coefficient of drag, $c_{d_{table}}$ is the coefficient of drag from the table, and α_z is the angle of attack for zero lift. The correction factor is given as:

$$K = \left(\frac{Re}{Re_{table}}\right)^n \tag{7.3}$$

where Re and Re_{table} are the blade and table Reynolds numbers, respectively, and n is an adjustable constant, between 1/8 to 1/5 (turbulent flat plate limit). In the present work only the drag correction was used with $n = 1/8$.

The first validation case is the performance of a single rotor. Figure 7.2 shows the predictions and measurement of thrust and power coefficients for a single rotor with 3 and 6 blades. Figure 7.3 shows the corresponding Figure of Merit versus thrust coefficient. The X3D predictions show good agreement with the test data for both cases. Due to higher solidity, the six-bladed rotor has a higher profile power than a three-bladed rotor. As a result, the Figure of Merit of the three-bladed rotor is higher than that of the six-bladed rotor for a given thrust. The induced power for both rotors have similar trends as it is independent of the number of blades. However, the blade loading (C_T/σ) for a three-bladed rotor is higher than the six-bladed rotor, which results in early occurrence of blade stall for the same thrust C_T. An early stall is seen as a quick rise in the power profile of the three-bladed rotor at higher thrust (Figure 7.2). Figures 7.4 and 7.5 show the free-wake geometry of single rotor with three and six blades respectively.

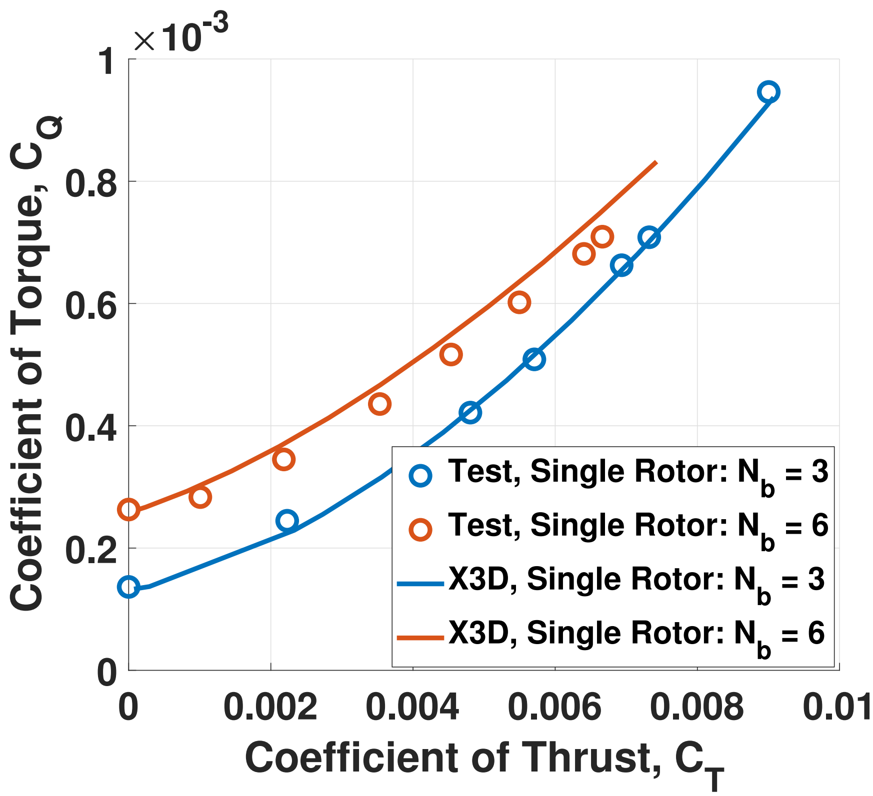

Figure 7.2: Performance (power vs thrust) of single rotor with 3 and 6 blades in hover; predictions compared with measurements.

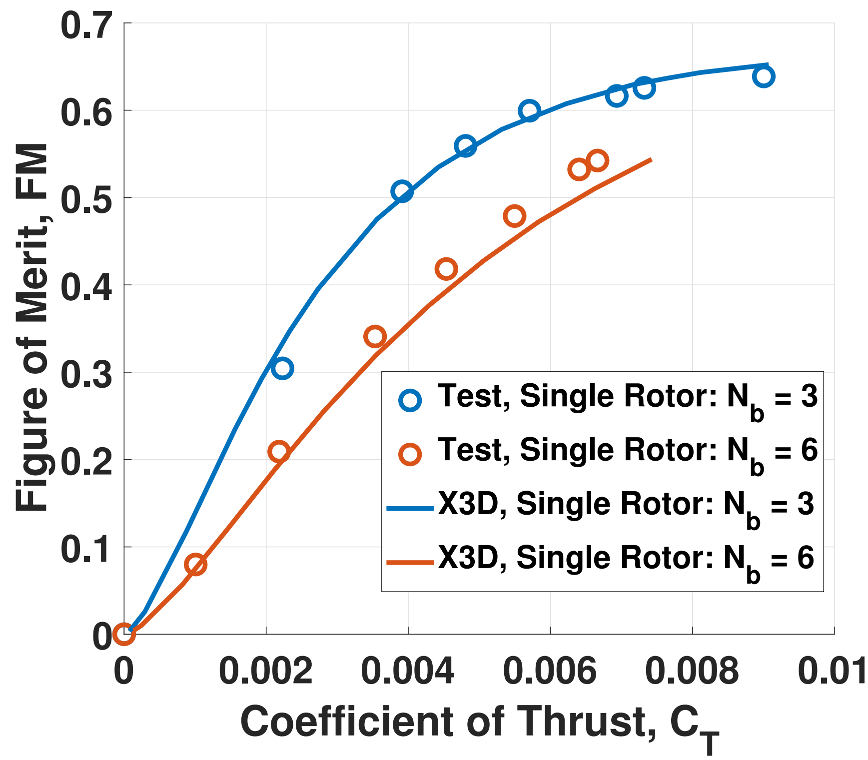

Figure 7.3: Performance (Figure of Merit vs thrust) of single rotor with 3 and 6 blades in hover; predictions compared with measurements.

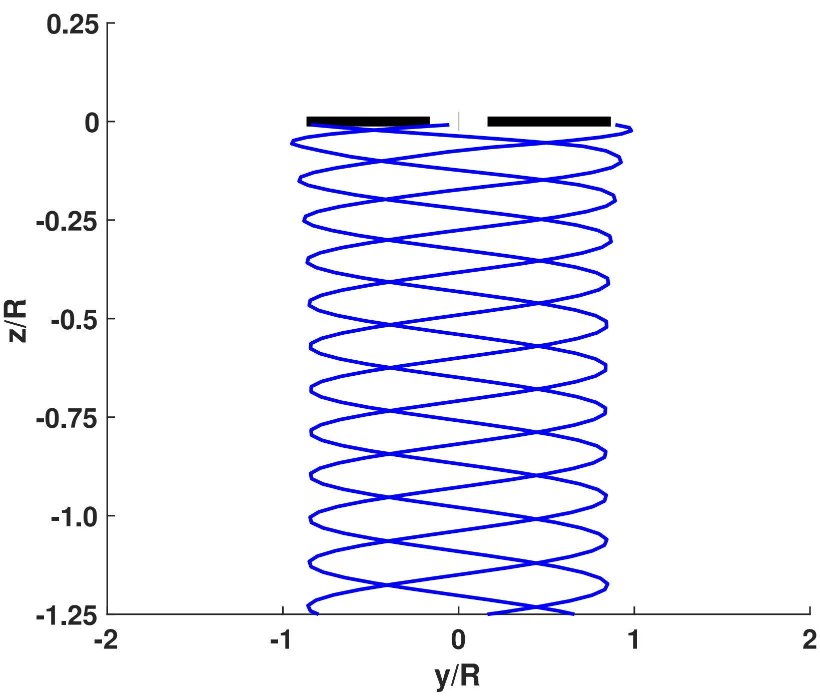

Figure 7.4: Free-wake geometry of single rotor wake with 3 blades, at $C_T = 0.005$.

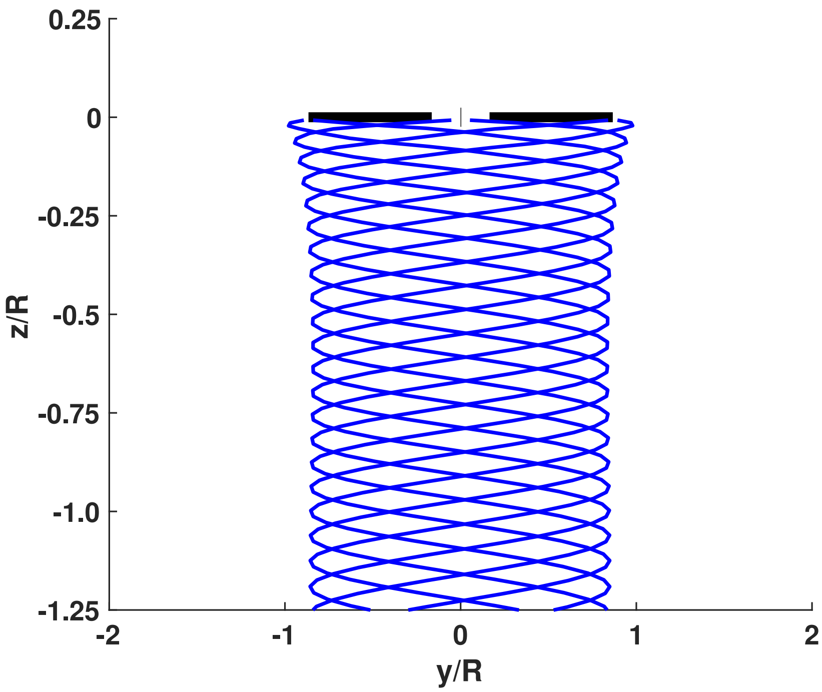

Figure 7.5: Free-wake geometry of single rotor wake with 6 blades, at $C_T = 0.005$

The coaxial rotor validation follows the single rotor validation. For the coaxial rotor, first a thrust sweep was conducted at the inter-rotor separation of $z/D = 0.07$. Figures 7.6 - 7.10 correspond to the results obtained from this sweep.

The performance of upper and lower rotors of a coaxial configuration is compared with the single rotor configuration in Figure 7.6. Figure 7.6(a) shows power versus thrust, and Figure 7.6(b) shows the same data as Figure of Merit versus thrust. The single rotor data is the same as shown in the previous section. Between upper and lower rotors, the analysis shows better agreement with the latter test data. At low thrust, the analysis matches well with the test data for both rotors, but with the increase in thrust, the power grows slightly more quickly in the analysis than in the data. The analysis predicts correctly that the lower rotor should be less efficient than the upper and that both should be worse than a single rotor. This comparison shows that a rotor is more efficient in isolation than in a coaxial system for the same thrust.

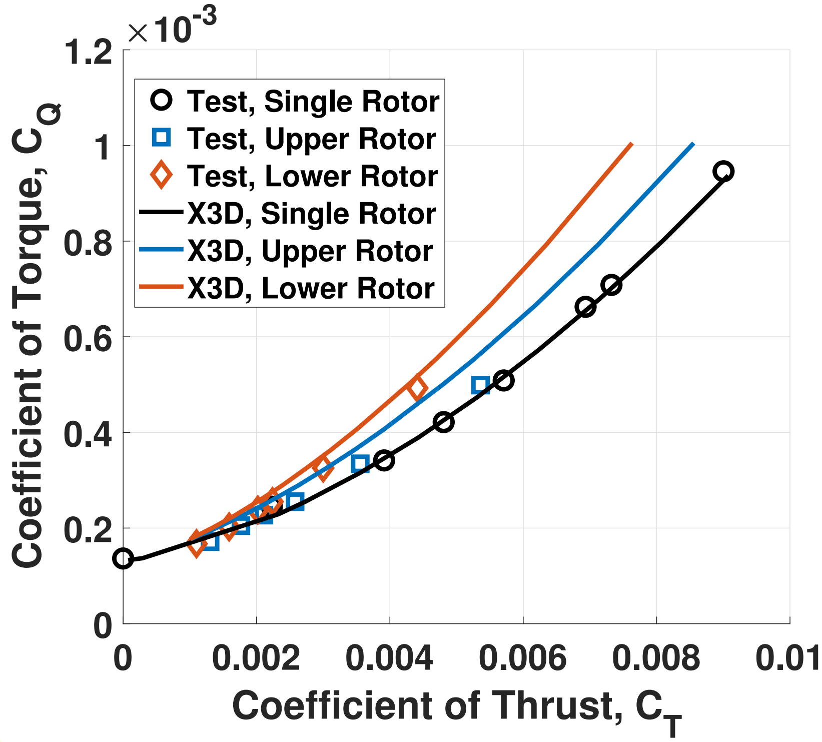

(a)

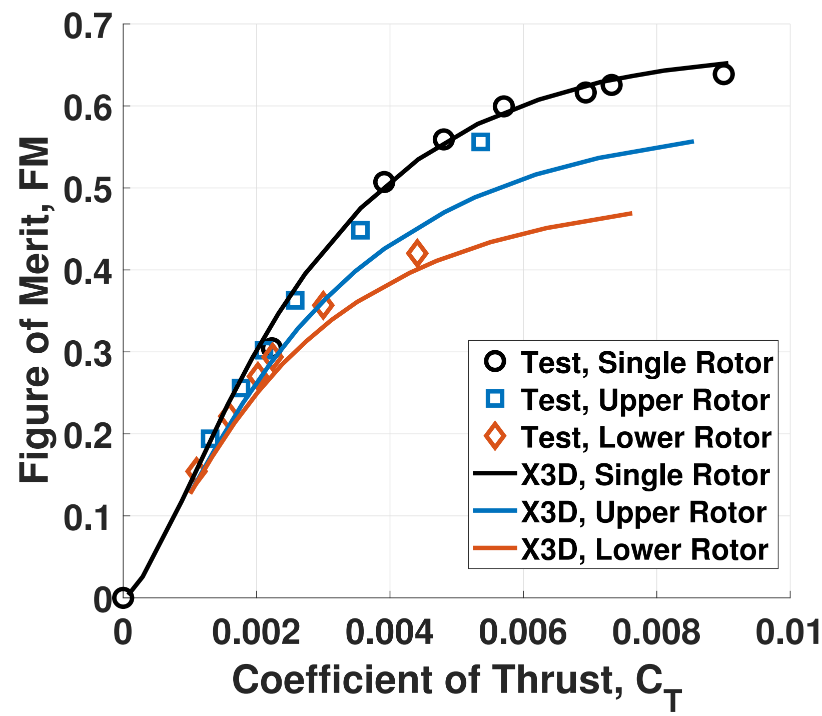

(b)

Figure 7.6: Performance comparison of single rotor and individual rotors within coaxial system ($z/D = 0.07$); all at 1200 RPM.

Figure 7.7 shows a comparison of a coaxial rotor, each rotor with three blades, and an isolated single rotor with six blades. This comparison ensures that the total number of blades remains the same. Thus the skin friction losses and profile power stay the same, and differences can be attributed primarily to induced power due to interference. Figure 7.7(a) shows power versus thrust variation. The analysis slightly over-predicts the power for single and coaxial rotor cases at higher thrust conditions. The results of this comparison show that the coaxial rotor is more efficient than the isolated rotor. The improved efficiency of the coaxial rotor stems from two effects. The primary benefit is from inter-rotor separation - the upper wake contracts before reaching the lower rotor; therefore, the lower rotor effectively provides additional disk area. This benefit is dependent on wake contraction and, hence the inter-rotor separation. A secondary effect is the swirl recovery of each rotor counteracts the other and reduces net momentum loss due to swirl. Momentum theory predicts a 9% reduction in power for a fully contracted upper wake compared to the single rotor. The test data shows a 6% benefit, and the predictions show a 4-5% benefit in power compared to the single rotor.

Figure 7.7(b) shows Figure of Merit (FM) versus thrust variation. The FM for multi rotors is defined using ideal power of a single rotor of same projected area. This is the proper definition as it captures the interference effects between the rotors.

$$FM = \frac{P_{Ideal}}{P_{Measured}} = \frac{\frac{T^{3/2}}{\sqrt{2\rho A}}}{P_{Measured}} = \frac{\frac{{C_T}^{3/2}}{\sqrt{2}}}{C_{P_{Measured}}} \tag{7.4}$$

In the above equation, T is thrust, P is power, ρ is density, A is projected area, and C_T and C_P are the coefficients of thrust and power, respectively. The projected area A for coaxial rotors remains the same as the single rotor.

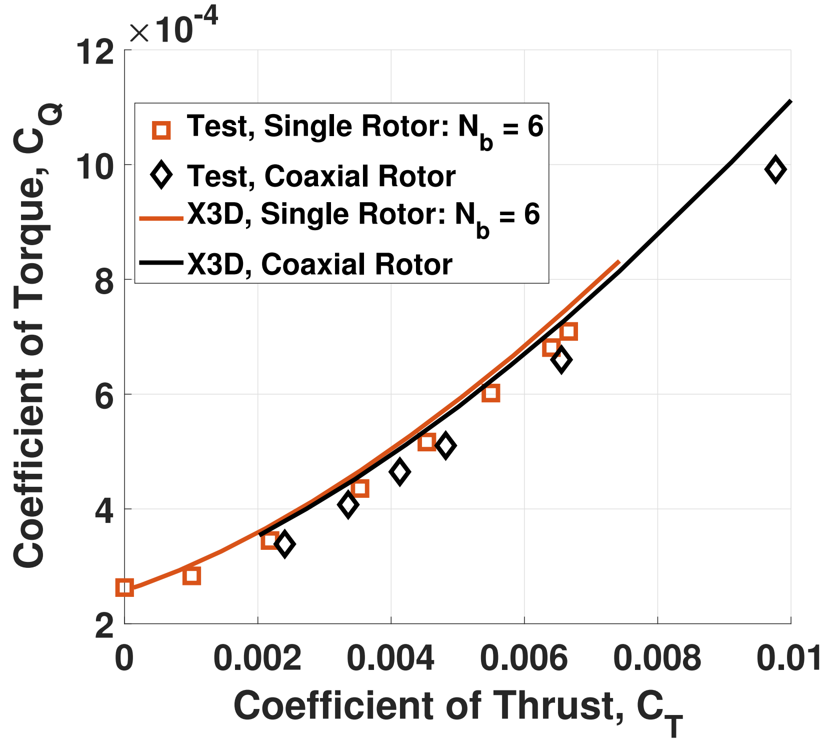

(a)

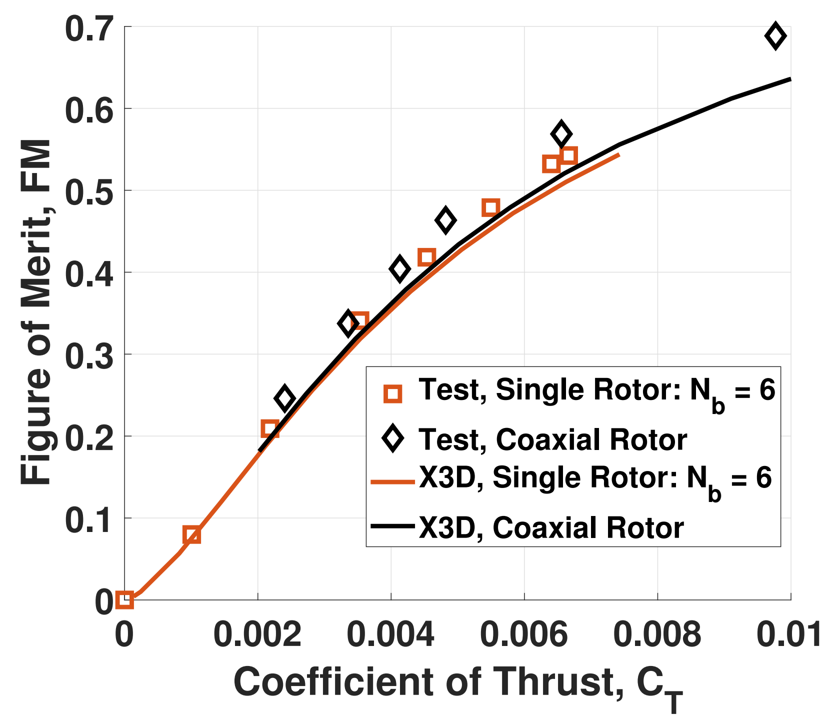

(b)

Figure 7.7: Performance comparison of six-bladed single rotor and coaxial rotor ($z/D = 0.07$); all at 1200 RPM.

The thrust sharing between the rotors is shown in Figure 7.8, plotted versus total system thrust. The results in Figure 7.8(a) suggest that the individual thrust of both rotors increases linearly with increasing system thrust, and the upper rotor thrust has a higher rate of increase than the lower rotor thrust. This implies that with increasing system thrust, the aerodynamic efficiency of the upper rotor increases relative to that of the lower rotor. With increasing thrust, the tip vortices convect down faster, so more of the lower rotor is within the radial boundary of the upper rotor wake. Also, with increasing thrust, the strength of the vortices increases; this leads to higher levels of downwash for points located inside the radial boundary of the upper rotor wake; and upwash for points located outside the radial boundary of the upper rotor wake. As a result of both these reasons, the efficiency of the upper rotor increases relative to that of the lower rotor with increasing system thrust. Figure 7.8(b) shows the torque balance. The rotors are trimmed to the same torque, only the magnitude is over predicted. This results in an under prediction of the Figure of Merit especially at higher thrust levels as seen in Figure 7.8(d). Figure 7.8(c) shows that the upper and lower rotors produce about 55% and 45% of the total thrust, respectively. The ratio is insensitive to thrust level across the sweep.

Figures 7.9 and 7.10 show the free-wake geometry of the coaxial wake for two rotor separation distances: $z/D = 0.07$ and $z/D = 1.5$ respectively. As mentioned earlier, more free-wake turns were used for the larger separation case to ensure the wake of the upper rotor is fully developed to interact with the lower rotor.

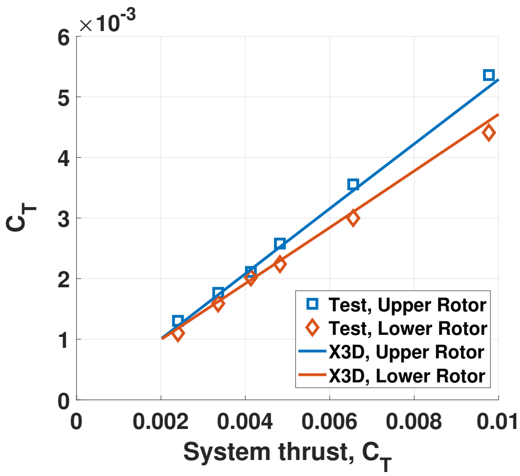

(a) Coefficient of Thrust

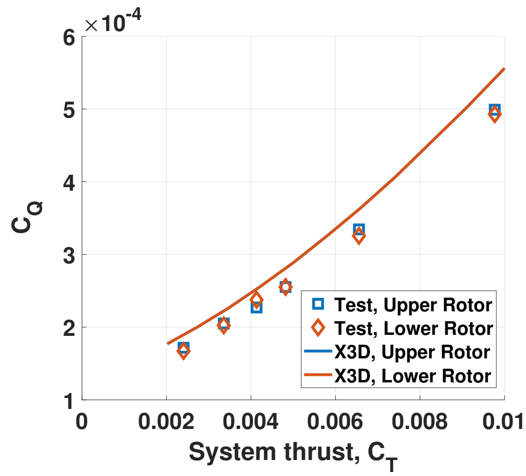

(b) Coefficient of Torque

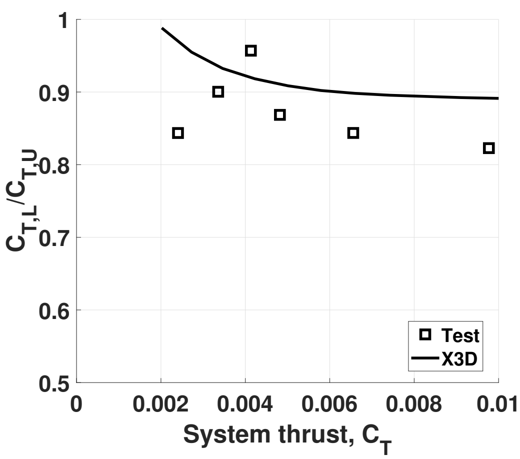

(c) Thrust Sharing

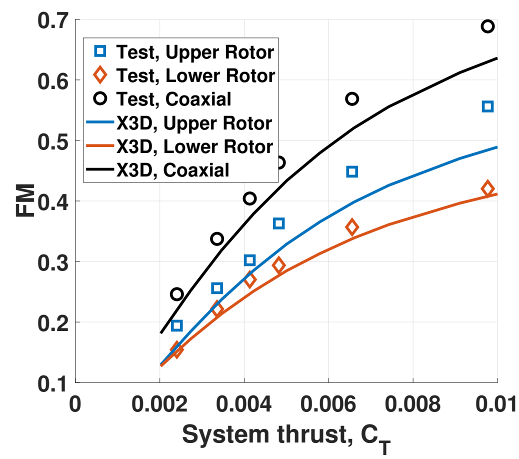

(d) Figure of Merit

Figure 7.8: Performance of coaxial rotor over thrust sweep, at 1200 RPM, $z/D = 0.07$.

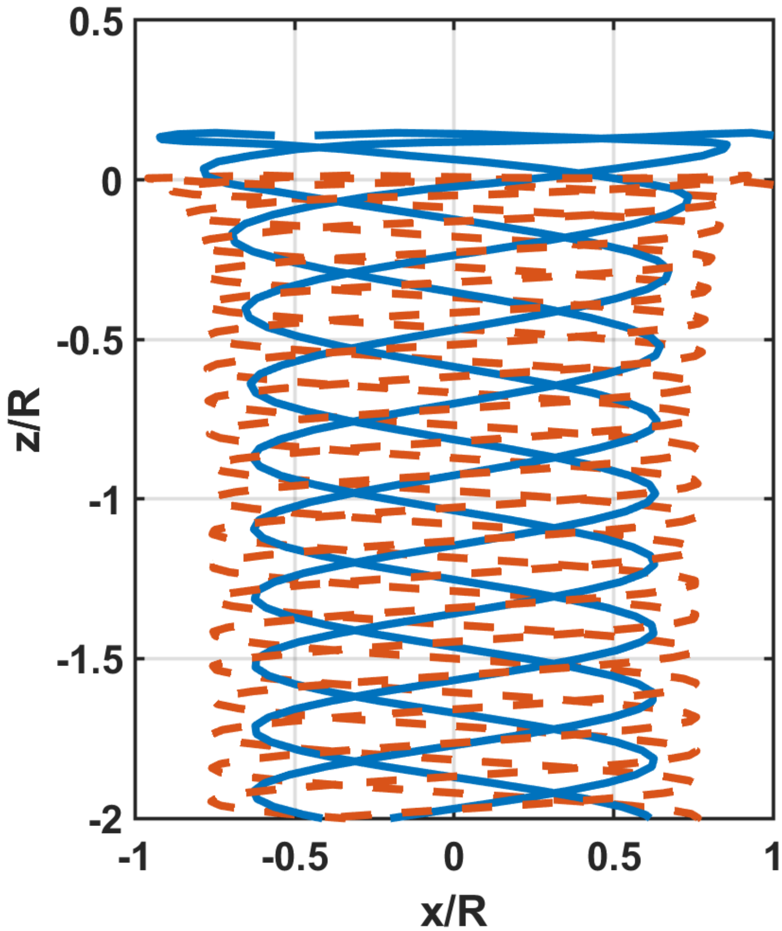

Figure 7.9: Free-wake geometry of coaxial wake in hover at 1200 RPM; rotors are separated at a distance of $z/D = 0.07$; each rotor blade has single tip vortex.

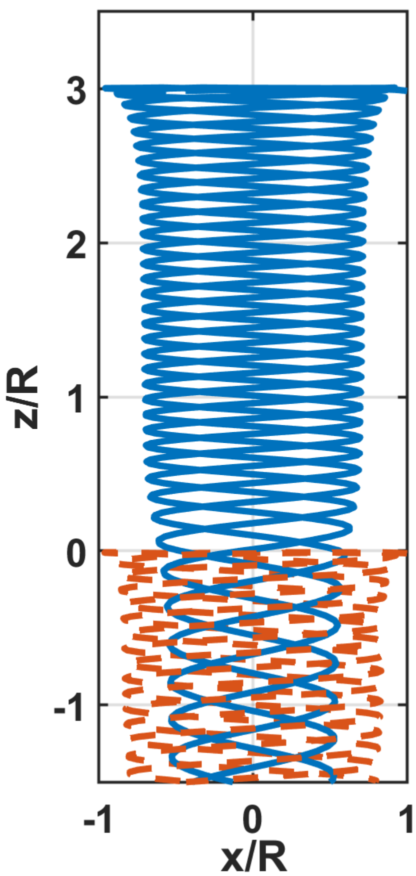

Figure 7.10: Free-wake geometry of coaxial wake in hover at 1200 RPM; rotors are separated at a distance of $z/D = 1.5$; each rotor blade has single tip vortex.

Next, a sweep of inter-rotor separation is performed for the validation study. This sweep is more vital as it is beyond the predictive capability of momentum theory and tests the accuracy of the free-wake model. The sweep is conducted over a range of separation distances from $z/D = 0.05$ to $z/D = 1.5$, for two total thrust conditions: $C_T = 0.007$ and $C_T = 0.014$. The upper and lower collectives are trimmed to achieve the required total thrust C_T and torque balance C_Q. Figure 7.11 shows the thrust and power sharing at the low thrust level $C_T = 0.007$ plotted versus the inter-rotor separation, z/D. The predictions show good agreement with the test for all separation distances. With increasing separation, the lower rotor produces a lower thrust until the wake of the upper rotor is fully developed. Thereafter the thrust sharing is constant. As the rotors get closer, the upper rotor thrust decreases due to the influence of the lower rotor, as seen in Figure 7.11(a). Figure 7.11(b) shows the torque balance, where both rotors are trimmed to identical torque. Figure 7.11(c) shows the thrust sharing fraction, depicting that as the separation increases the thrust share stabilizes around $T^L/T^U \approx= 0.75$ for rotor separation $z/D \geq 0.5$. This behavior suggests that by then, the upper rotor wake is already fully contracted. Similar to the thrust sweep, power is over predicted, which results in an under prediction in Figure of Merit in Figure 7.11(d).

A similar sweep is also carried out at a higher thrust level, $C_T = 0.014$, shown in Figure 7.12. The trends are similar as earlier. The thrust sharing in Figure 7.12(a) shows good agreement with the test data. Again, the sharing begins nearly equal, and as the inter-rotor separation increases, the upper rotor provides more thrust. The torque balance matches well across the sweep, as shown in Figure 7.12(b). Having matched the thrust and torque well, the Figure of Merit prediction (Figure 7.12(d)) also matches very well. At higher thrust condition, the thrust sharing is predicted to level out at a smaller inter-rotor separation $z/D = 0.35$ as seen in Figure 7.12(c). This is because the wake contracts faster with higher thrust. However, this is not

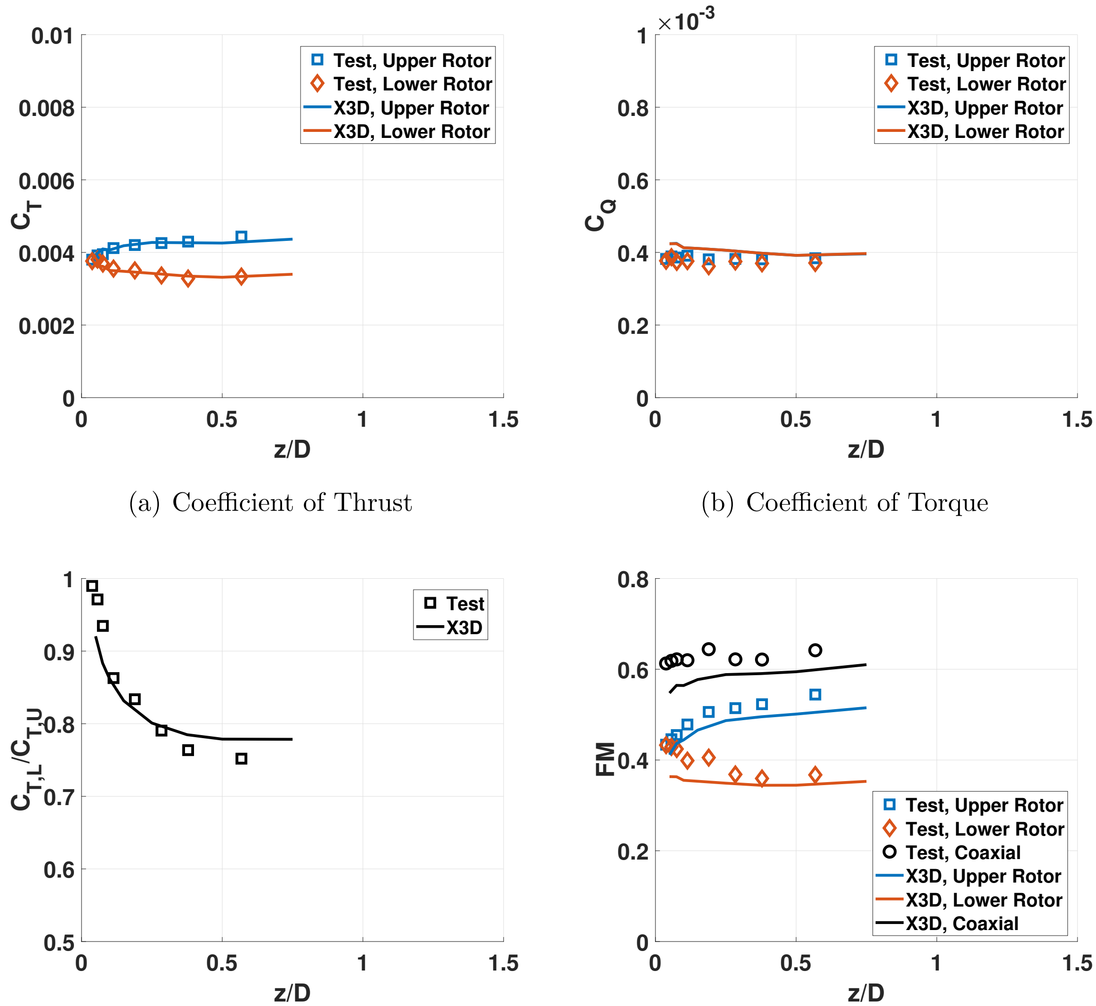

(a) Coefficient of Thrust

(b) Coefficient of Torque

(c) Thrust Sharing

(d) Figure of Merit

Figure 7.11: Performance of coaxial rotor over separation sweep, at 1200 RPM with total $C_T = 0.007$.

seen in the test data. The predictions show that the thrust sharing stabilizes around $T^L/T^U \approx= 0.75$, while the test data shows slightly higher $T^L/T^U \approx= 0.8$.

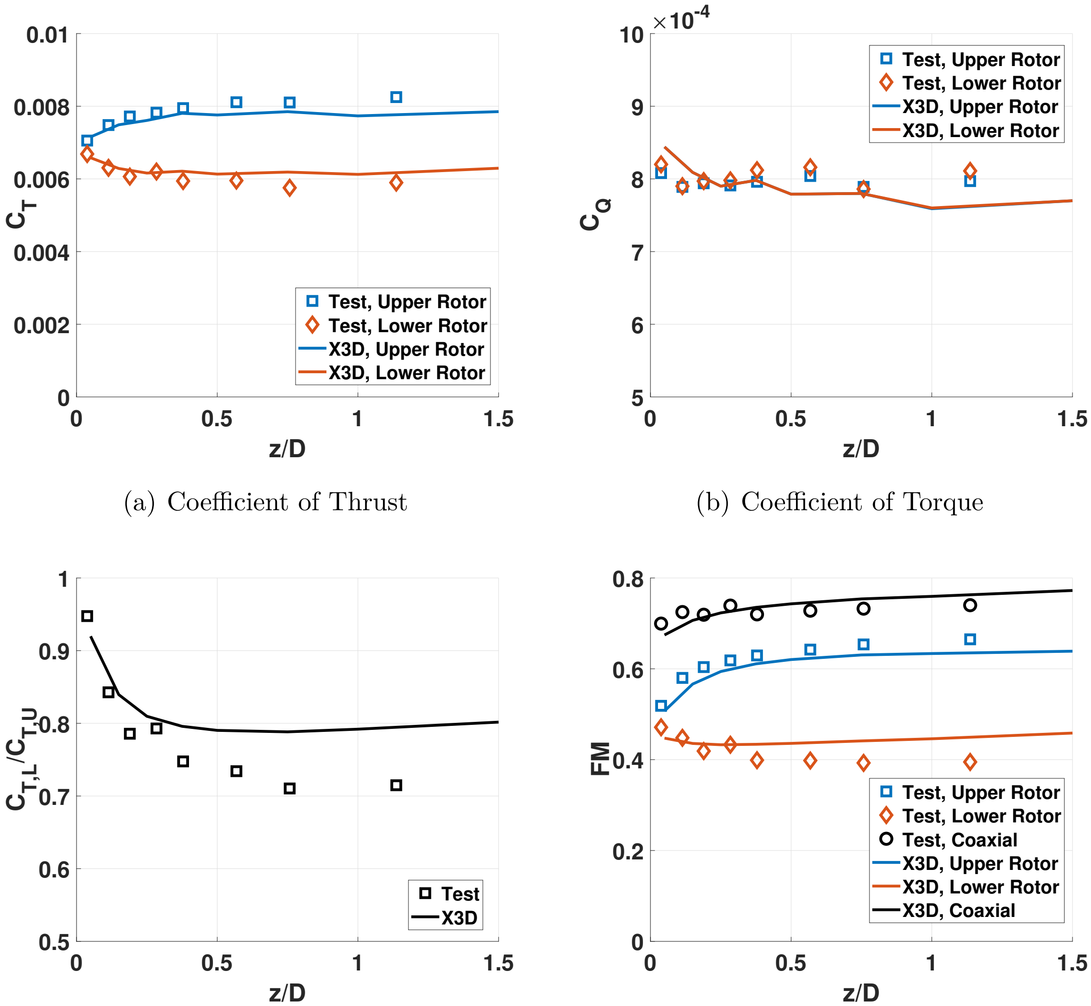

(a) Coefficient of Thrust

(b) Coefficient of Torque

(c) Thrust Sharing

(d) Figure of Merit

Figure 7.12: Performance of coaxial rotor over separation sweep, at 1200 RPM with total $C_T = 0.014$.

7.5 UH-60A-like Coaxial in Forward Flight

In the absence of measured coaxial airloads, the notional coaxial UH-60A-like rotor model is used for validation. This validation is more of a sanity check that verifies the working of coaxial-related refinements made in the X3D solver. The validation is performed on the limiting case of infinite separation between the rotors. There are no rotor-rotor interactions at this separation, and both rotors are expected to behave as isolated single rotor helicopters. Predictions of normal force are compared with the flight-test data from UH-60A Airloads Program transition flight C8513. The conditions are: $\mu = 0.15, \alpha = -3.75°, C_T/\sigma = 0.076$. This is the same condition studied earlier in Chapter 4.

The free-wake model utilizes a fully rolled-up single-tip vortex model with no inboard wake. Figure 7.13 shows the measured and predicted normal forces and its harmonics content at different radial stations along the azimuth. This is the same data as shown earlier in Chapter 4. The upper and lower rotors yield the same results when plotted in their local azimuth. This is the expected result with no side slip. This verification ensures that the coaxial-related modifications in X3D are functioning as intended.

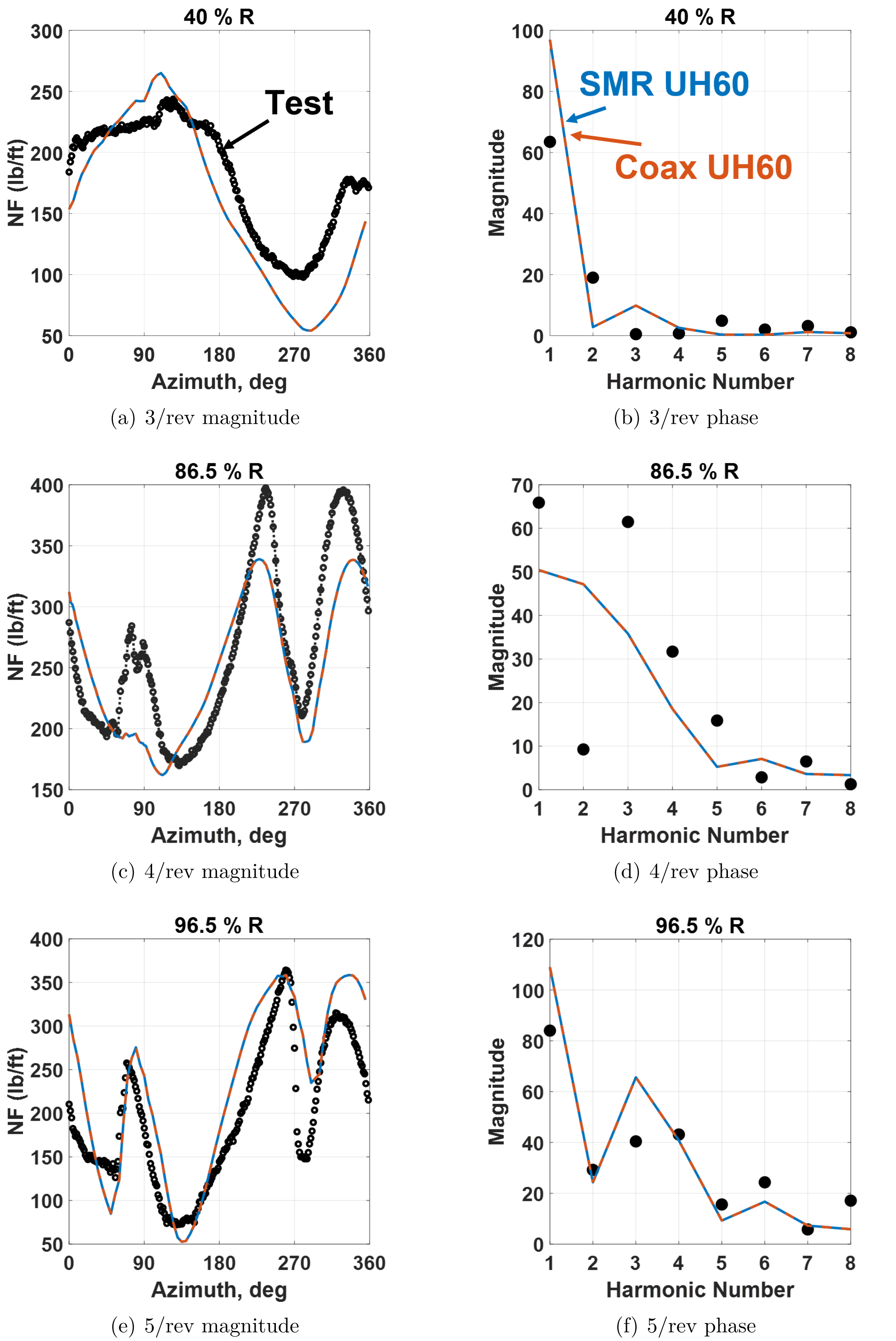

(a) 3/rev magnitude

(b) 3/rev phase

(c) 4/rev magnitude

(d) 4/rev phase

(e) 5/rev magnitude

(f) 5/rev phase

Figure 7.13: Normal force and its harmonics distribution along azimuth at different radial stations; predictions of single and coaxial rotor compared with flight test data.

7.6 Summary and Conclusions

The parallel X3D solver was extended for coaxial rotors. Modifications were performed to structural dynamics, aerodynamics, and trim modules. The new solver was validated with hover performance data obtained from U.S. Army Model test, and forward flight data of the UH-60A coaxial rotor with the limiting case of infinite separation between the rotors. Based on the results obtained, the following conclusions are drawn.

1. For the same thrust, momentum theory predicts a 9% reduction in coaxial hover power for a fully contracted upper rotor wake compared to the single rotor. The rotor separation needed to achieve this is far beyond $z/D = 0.07$ used in actual aircraft. Thus, momentum theory is useless and free-wake is needed to get meaningful results.

2. The lifting-line free-wake model captures the correct trends observed in test data. The test data shows a 6% benefit, and the free-wake predictions show a 4-5% benefit in coaxial hover power compared to the single rotor.

3. For constant separation ($z/D = 0.07$), with increasing system thrust, both predictions and test data show that the aerodynamic efficiency of the upper rotor increases relative to that of the lower rotor. The individual thrust of both rotors increases linearly with increasing system thrust, and the upper rotor thrust has a higher rate of increase than the lower rotor. The upper and lower rotor produces approximately 55% and 45% of the total system thrust, respectively. This ratio is insensitive to the thrust level across the sweep.

4. With increasing separation between the rotors of a coaxial system, the lower rotor produces a lower thrust until the wake of the upper rotor is fully developed. Thereafter the thrust sharing is constant. As the rotors get closer, the upper

rotor thrust decreases due to the influence of the lower rotor. Both predictions and test data captured this behavior and was found to be independent of the total system thrust.

5. At low system thrust ($C_T = 0.007$), both predictions and test data showed that the thrust sharing fraction stabilizes around $T^L/T^U \approx= 0.75$ for rotor separation $z/D \geq 0.5$.

6. At higher thrust ($C_T = 0.014$), the thrust sharing is predicted to level out with $T^L/T^U \approx= 0.75$ at a smaller inter-rotor separation $z/D = 0.35$. However, the test data showed that the level out to be slightly higher $T^L/T^U \approx= 0.8$.

7. The upper and lower rotors of the UH-60A coaxial rotor yield the same blade airloads in forward flight when the rotors are infinitely separated. This is expected as there are no rotor-rotor interactions at that separation.

Chapter 8: Understanding Coaxial Aeromechanics in Forward Flight

This chapter studies the coaxial aeromechanics in forward flight to gain fundamental insight. Both Metaltail and UH-60A coaxial models are used for this study, with the former being the primary focus. The analysis is performed at a low-speed flight condition for which qualitative data is available for the Sikorsky S-97 Raider aircraft for comparison [84–86]. Predictors of rotor performance, blade airloads, root loads, 4/rev vibratory hub loads, and three-dimensional stresses are studied. The effect of inter-rotor phase is examined on vibratory hub loads.

8.1 Test Conditions

The predictions are obtained for edgewise flight at advance ratio $\mu = 0.1$, forward shaft tilt $\alpha = -2°$, and blade loading $C_T/\sigma = 0.08$. The choice of low-speed flight allows for qualitative comparison with the S-97 Raider data published recently in References 84–86. The trim targets are specified thrust, zero torque, and specified hub roll and pitch moments. The hub pitch moments of each rotor are set to zero and hub roll moments are set to satisfy a specified lift offset. Two lift offset (LO) conditions are used: 0% R and 10% R. Predictions for performance and vibratory loads are obtained for a range of advance ratios.

All results are obtained with free-wake based lifting-line aerodynamics. The free-wake model employs a fully rolled-up single tip vortex with filament strength of 40% maximum bound circulation occurring outboard of 50% R. These are the same parameters used earlier for the coaxial hover validation.

8.2 Rotor Performance

Predictions of rotor lift to equivalent drag ratio, L/D_e, with advance ratio for multiple lift offsets are shown in Figure 8.1. The rotor L/D_e is defined as

$$L/D_e = \frac{C_L}{C_P/\mu + C_X} \tag{8.1}$$

where $C_L = C_L^U + C_L^L$ is the total lift, $C_X = C_X^U + C_X^L$ is the total propulsive force, and C_P is the sum of absolute torques $|C_Q^U| + |C_Q^L|$. The Metaltail rotor has a very low L/D_e, typical of a proprotor in helicopter mode. This is due to the highly twisted blades. The rotor L/D_e increases with advance ratio till around $\mu = 0.3$. An increase in lift offset helps increase the cruise performance up to about 15% R. Beyond that, it degrades the performance.

Figure 8.2 shows the control angles for both upper and lower rotors for LO = 0% R and 10% R. The collectives more or less follow the power curve trend. The lower rotor has a higher collective than the upper. Because of the high flap frequency, the roll moment is primarily affected by the longitudinal cyclic θ_{1s}. An increase in specified lift offset leads to a greater longitudinal cyclic requirement to provide the necessary roll moment.

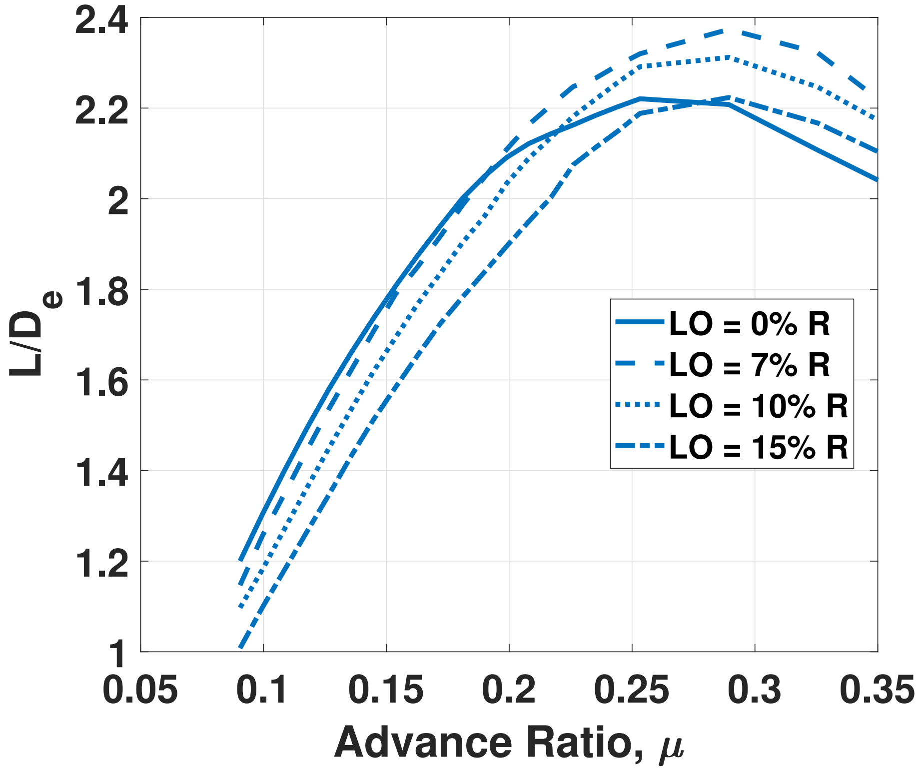

Figure 8.1: Metaltail rotor lift to equivalent drag ratio (L/D_e) versus advance ratio (μ) for multiple lift offsets.

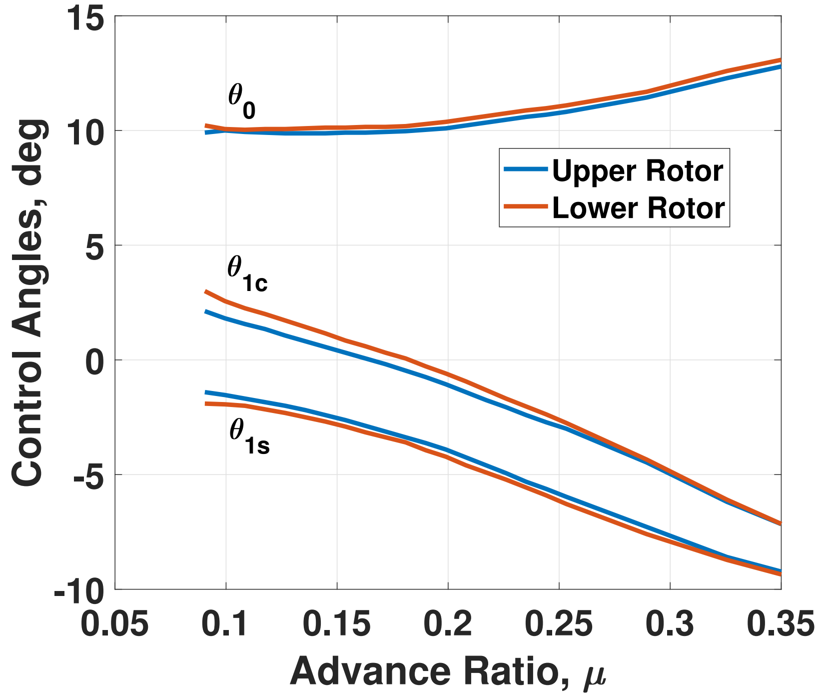

(a) LO = 0% R

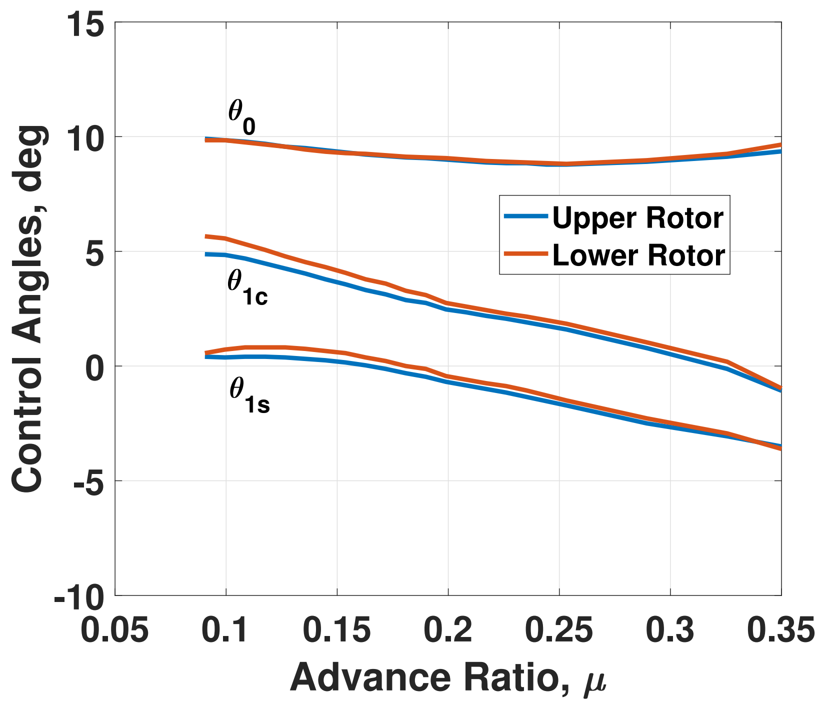

(b) LO = 10% R

Figure 8.2: Control angles ($\theta_0, \theta_{1c}, \theta_{1s}$) for upper and lower rotor versus advance ratio with; (a) LO = 0% R; (b) LO = 10% R.

8.3 Airloads

Figure 8.3 shows the normal force predictions versus azimuth at 72%R and 90%R for upper and lower rotors with zero lift offset. Note that the azimuth axes correspond to the local azimuth of each rotor. Figure 8.4 shows the corresponding harmonics. The lower rotor has higher harmonics 3,4,5 /revs but primarily the 4/rev. This is attributed to the upper rotor wake impinging on the lower rotor. At low-speed, this interaction is significant and can be observed as a magnified impulse in the first quadrant of the lower rotor. The 8/rev blade passage spikes are not noticeable.

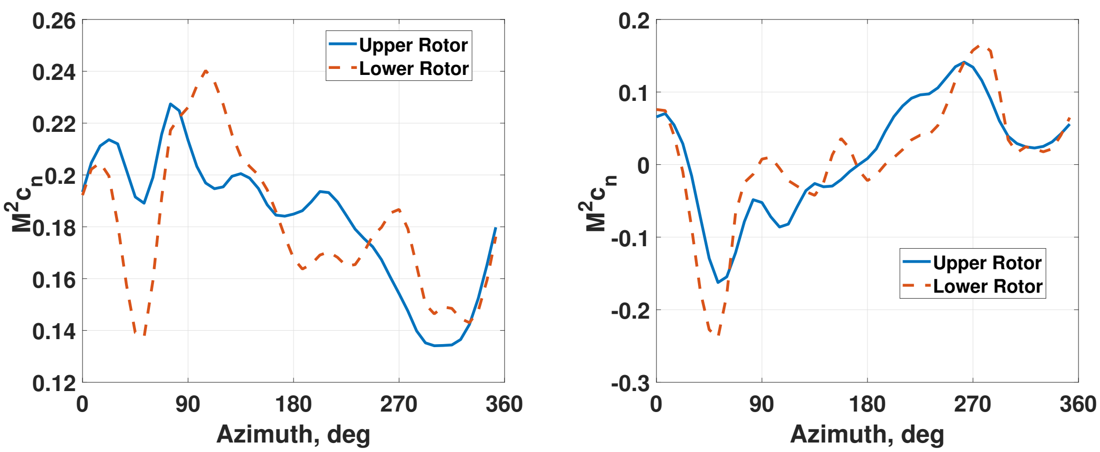

(a) Normal force at 72% R

(b) Normal force at 90% R

Figure 8.3: Predictions of normal force for Metaltail with LO = 0% R; (a) 72% R; (b) 90% R.

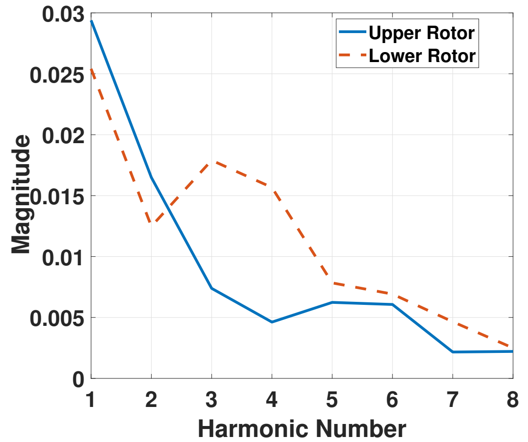

(a) Normal force harmonics at 72% R

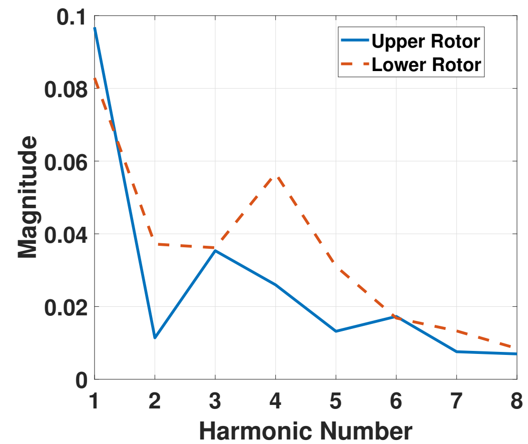

(b) Normal force harmonics at 90% R

Figure 8.4: Predictions of normal force harmonics for Metaltail with LO = 0% R; (a) 72% R; (b) 90% R.

Figures 8.5 and 8.6 show the same airloads and its harmonics but now with LO = 10% R. With lift offset, the blade lift increases on the advancing side and decreases on the retreating side. Similar to the zero lift offset case, the lower rotor again experiences higher harmonics due to the upper rotor wake impinging on the lower rotor.

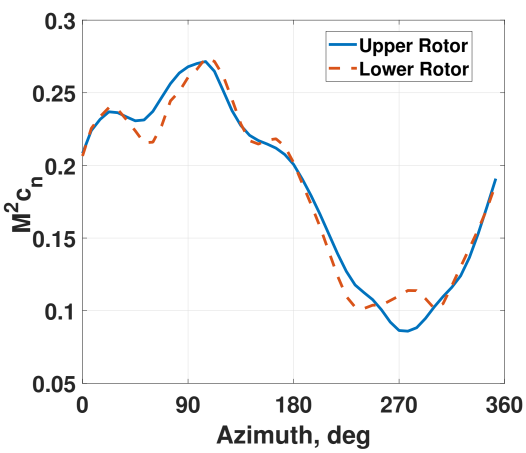

(a) Normal force at 72% R

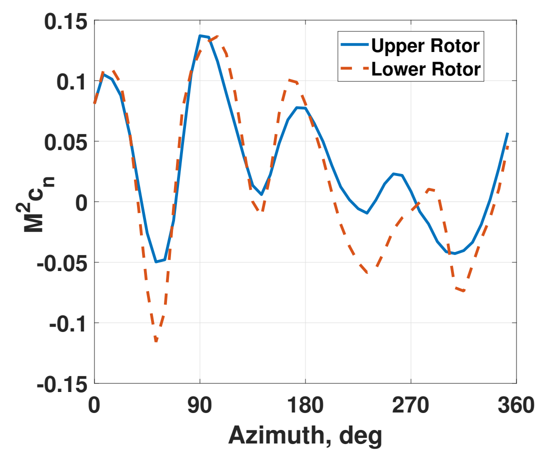

(b) Normal force at 90% R

Figure 8.5: Predictions of normal force for Metaltail with LO = 10% R; (a) 72% R; (b) 90% R.

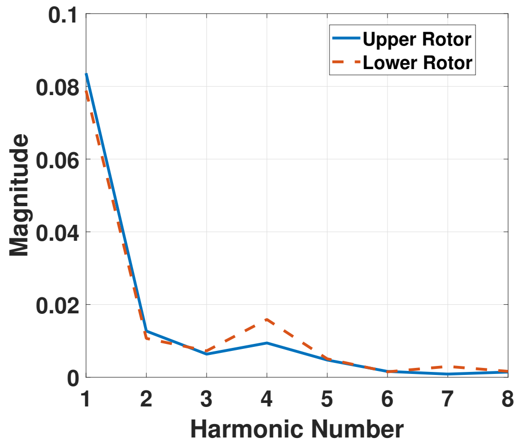

(a) Normal force harmonics at 72% R

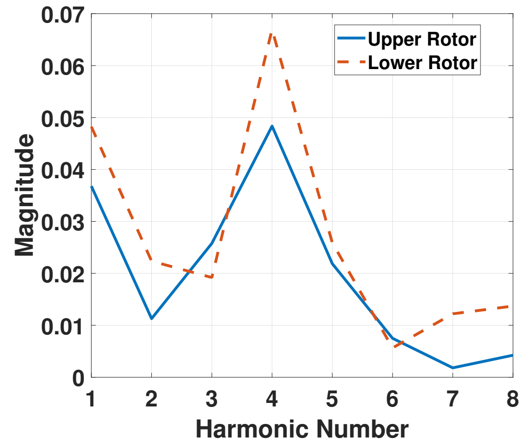

(b) Normal force harmonics at 90% R

Figure 8.6: Predictions of normal force harmonics for Metaltail with LO = 10% R; (a) 72% R; (b) 90% R.

Figure 8.7 shows the free-wake geometry. It can be seen that the wake at transition flight speed involves noticeable interferences of upper rotor wake on the rear part of lower rotor.

Zhao et al. [84, 85] discuss the low-speed forward flight predictions of the S-97 Raider using CFD/CA analysis. It is mentioned that the inter-rotor interactions in a coaxial system result in a dominant 3/rev contribution in the lift of the lower rotor blade near the tip. Figure 8.8 shows the snapshot of the S-97 blade tip airloads at transition flight condition from Reference 84. However, this dominant 3/rev is not observed for Metaltail. A dominant 4/rev is seen instead. This difference was investigated as discussed below.

The complexity of proprotor roll-up makes a coaxial wake even more complicated. The single rotor Metaltail showed 4/rev in the blade lift distribution earlier (Figure 8.9). In the coaxial Metaltail, this effect is amplified. The high twist in Metaltail is the cause of this phenomenon and hence the deviation from the S-97 data.

To investigate this further, the coaxial UH-60A-like rotor was used. It is more

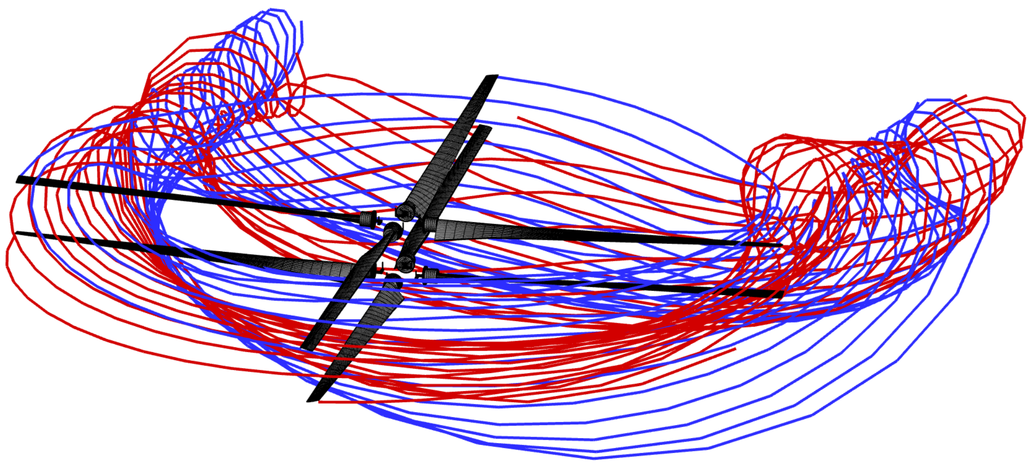

(a) Isometric View

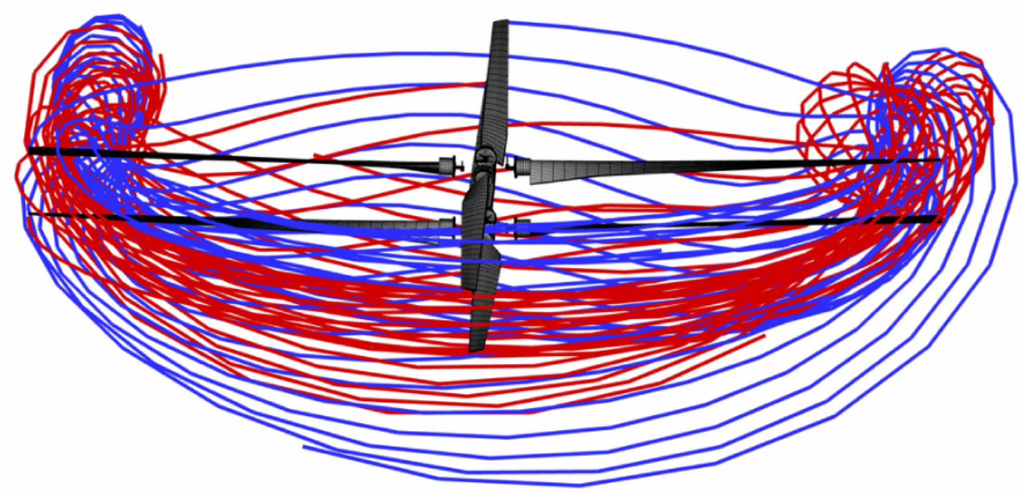

(b) Front View

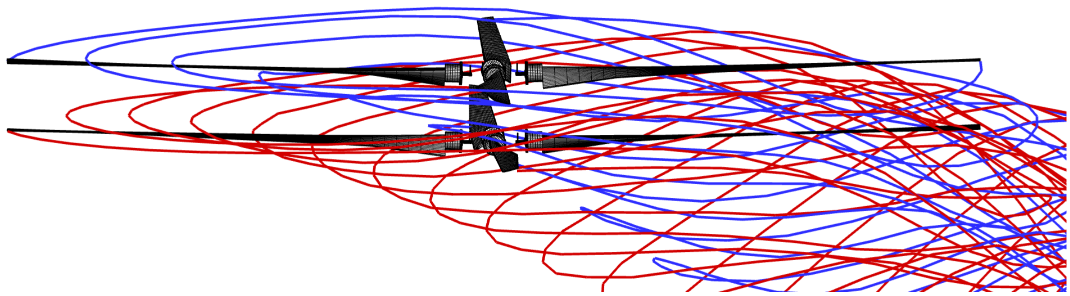

(c) Side View

Figure 8.7: Free-wake geometry for Metaltail at low-speed flight ($\mu = 0.1$) in (a) isometric, (b) front view, and (c) side view.

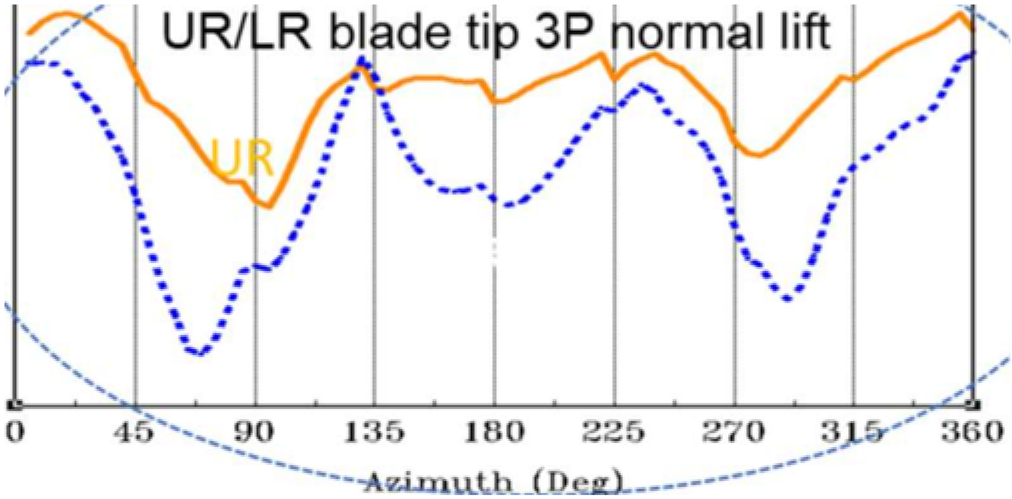

Figure 8.8: Snapshot of the S-97 blade airloads at tip at transition flight condition from the Reference 84.

likely to have a twist similar to S-97. Because UH-60A is an articulated rotor, the coaxial configuration was analyzed at zero lift offset. Figures 8.10 and 8.11 show the airloads near blade tip in the time and frequency domain respectively. A dominant 3/rev is indeed observed in the lower rotor, which is similar to the behavior reported for S-97 Raider in Reference [84]. Thus, it can be concluded that twist indeed is the source of difference.

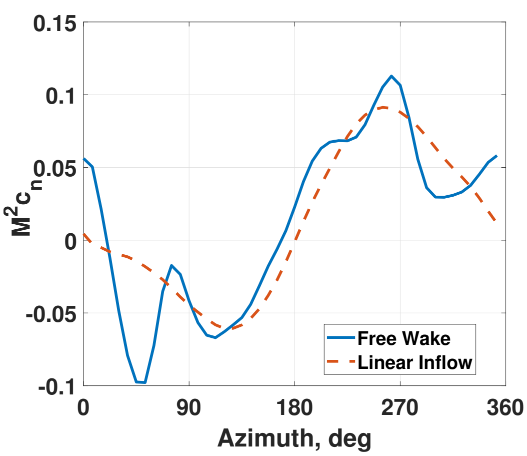

(a) Normal force at 90% R

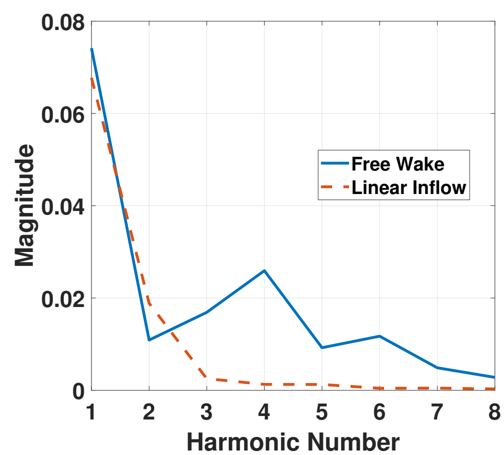

(b) Normal force harmonics at 90% R

Figure 8.9: Predictions of normal force and harmonics for single rotor Metaltail at r = 90% R for $\mu = 0.1$, $C_T/\sigma = 0.08$.

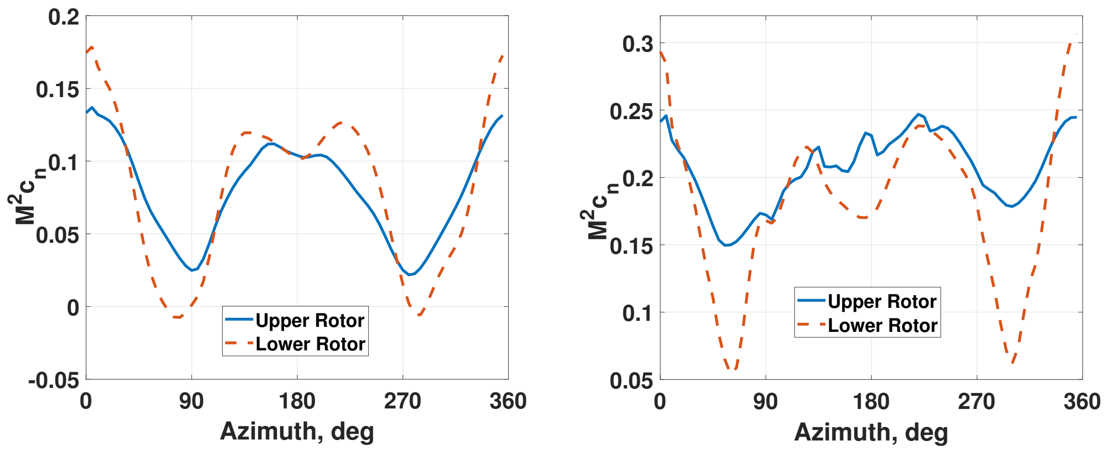

(a) Normal force at 72% R

(b) Normal force at 90% R

Figure 8.10: Predictions of normal force for UH-60A coaxial rotor with LO = 0% R; (a) 72% R; (b) 90% R.

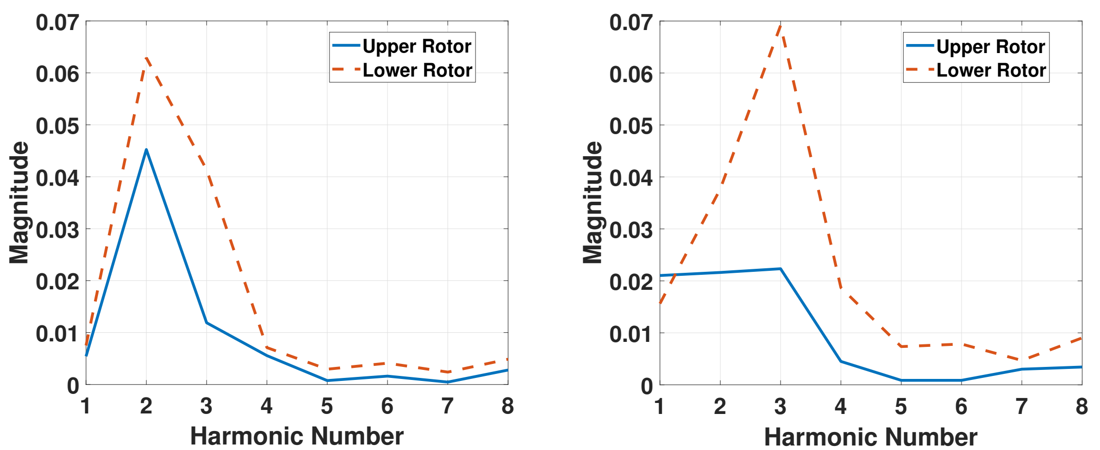

(a) Normal force at 72% R

(b) Normal force at 90% R

Figure 8.11: Predictions of normal force harmonics for UH-60A coaxial rotor with LO = 0% R; (a) 72% R; (b) 90% R.

Figures 8.12 and 8.13 show the span wise distribution of 3/rev and 4/rev normal force harmonics for Metaltail with LO = 0% R and LO = 10% R respectively. The airloads are concentrated at the tip in both cases. The 4/rev harmonics are higher than 3/rev, and the contributions of upper and lower rotors are comparable. Figure 8.14 shows the snapshot of span wise distribution of 3/rev normal force harmonics for S-97 rotor from Reference 85. In this case, the lower rotor harmonics are significantly higher than the upper rotor. As expected, this behavior is visible in UH-60A coaxial rotor shown in Figure 8.15. For UH-60A coaxial rotor, the 3/rev contributions are significantly higher than the 4/rev, and the lower rotor shows higher contributions over the upper rotor.

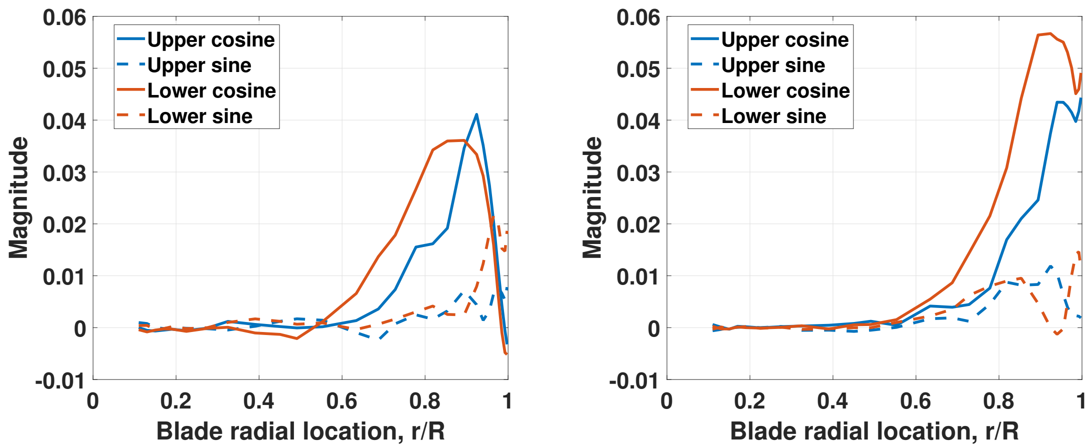

(a) 3/rev Harmonics

(b) 4/rev Harmonics

Figure 8.12: Span wise distribution of 3/rev and 4/rev normal force harmonics for Metaltail with LO = 0% R.

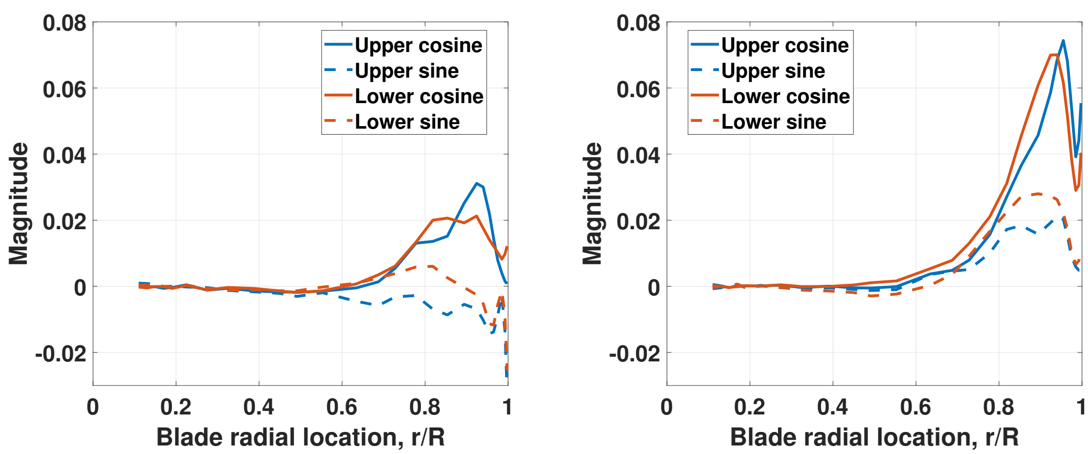

(a) 3/rev Harmonics

(b) 4/rev Harmonics

Figure 8.13: Span wise distribution of 3/rev and 4/rev normal force harmonics for Metaltail with LO = 10% R.

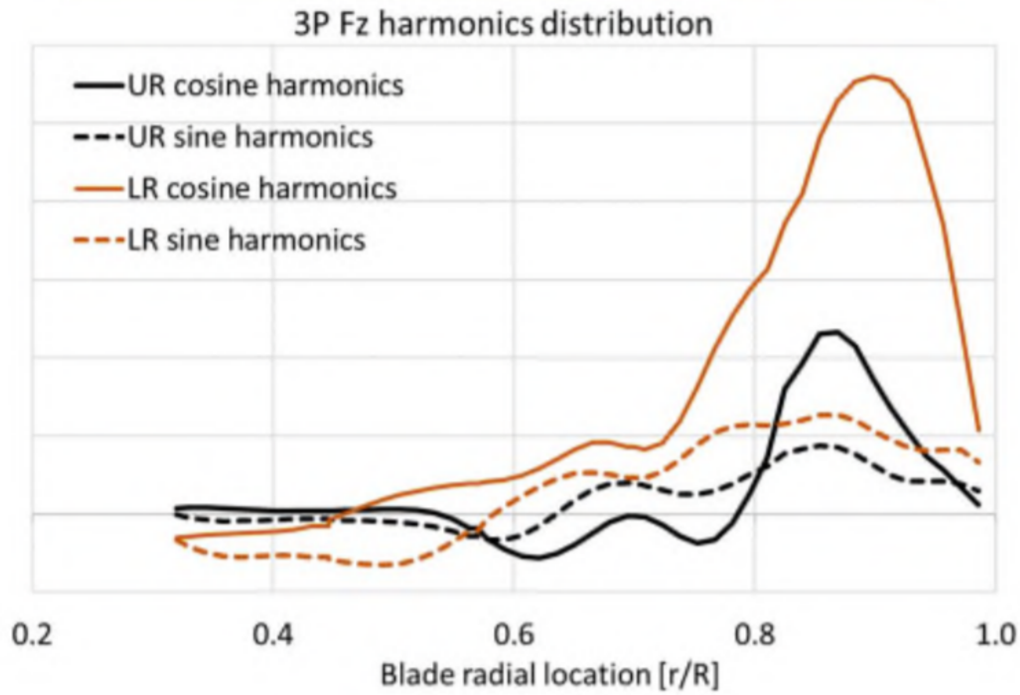

Figure 8.14: Snapshot of the span wise distribution of 3/rev normal force harmonics for S-97 rotor from Reference 85.

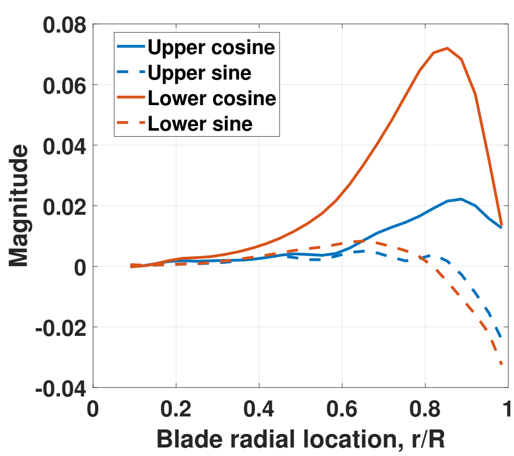

(a) 3/rev Harmonics

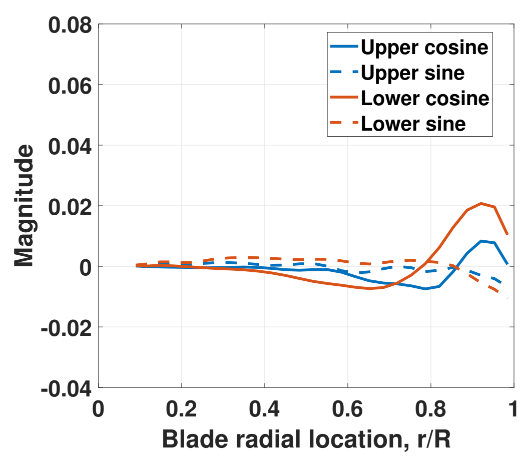

(b) 4/rev Harmonics

Figure 8.15: Span wise distribution of 3/rev and 4/rev normal force harmonics for UH-60A coaxial rotor with LO = 0% R.

8.4 Blade Root Loads

Figures 8.16 and 8.17 show the predicted upper and lower rotor bending moments in flap, lag and torsion at blade root with LO = 0%R and 10% R respectively. These are obtained using the joint sensors associated with the Metaltail load path mentioned in Chapter 6.

The flap bending moment for LO = 0% R in Figure 8.16(c) has a close to zero 1/rev signal, whereas the Figure 8.17(c) for LO = 10% R shows a dominant 1/rev signal, which is required to satisfy the steady hub roll moment. The lag bending moment for both lift offset cases shows a dominant 2/rev contribution. The torsional moment has contributions from higher harmonics 5, 6 /rev as the first torsion frequency is close to 5/rev.

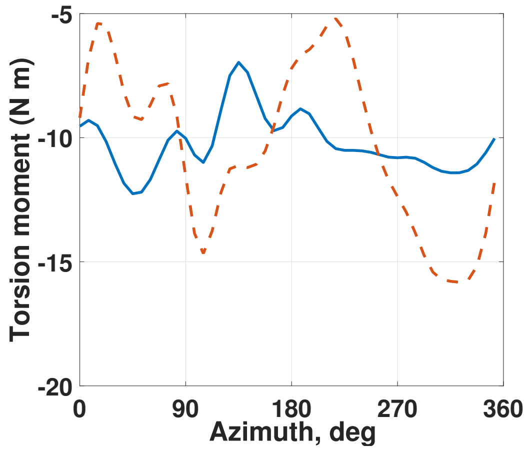

(a) Torsion Moment

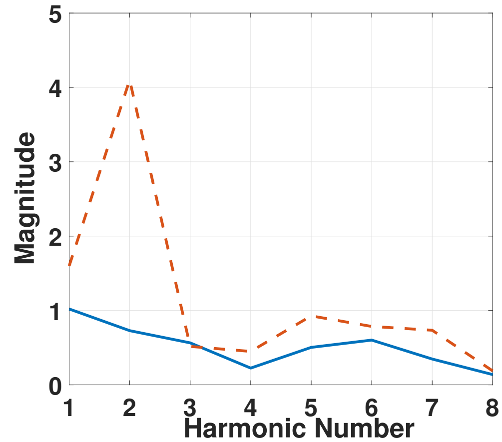

(b) Torsion Moment Harmonics

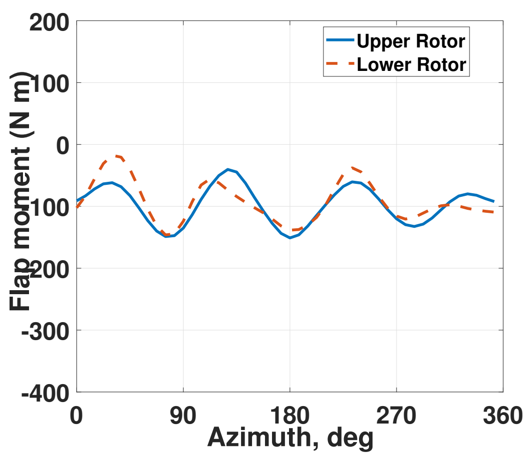

(c) Flap Moment

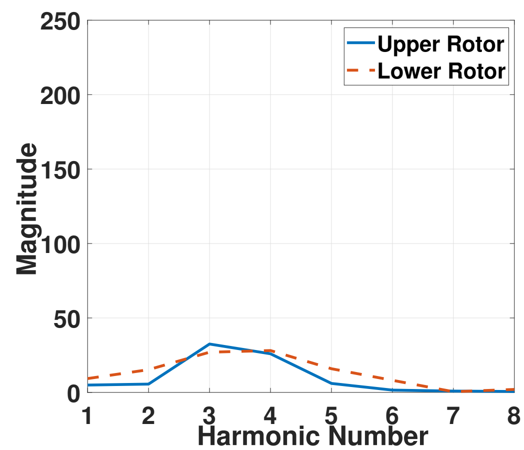

(d) Flap Moment Harmonics

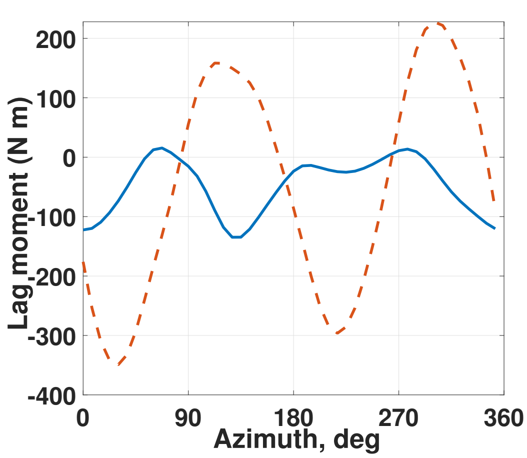

(e) Lag Moment

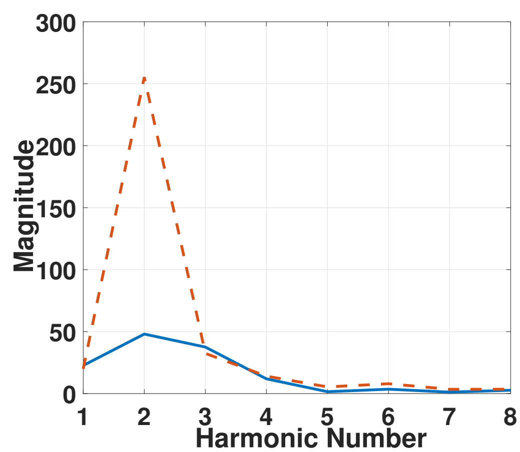

(f) Lag Moment Harmonics

Figure 8.16: Root torsion, flap and lag bending moments for Metaltail at $\mu = 0.1$ with LO = 0% R.

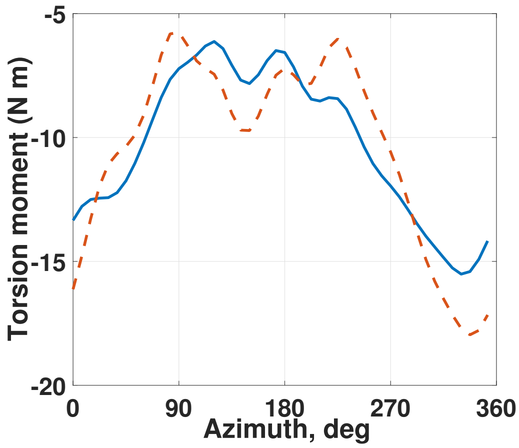

(a) Torsion Moment

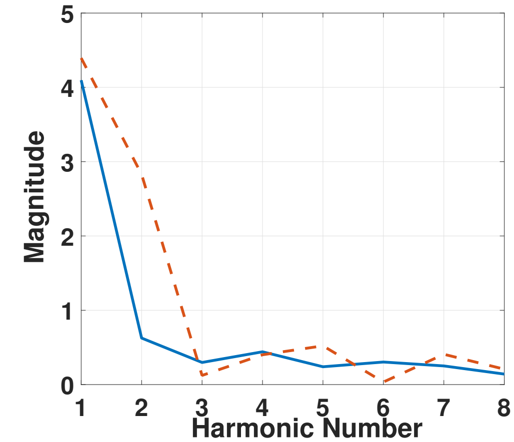

(b) Torsion Moment Harmonics

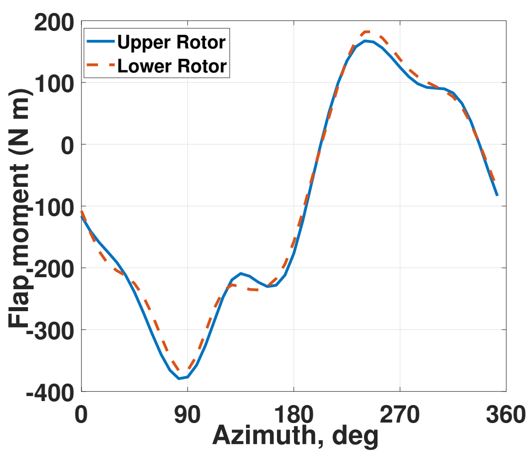

(c) Flap Moment

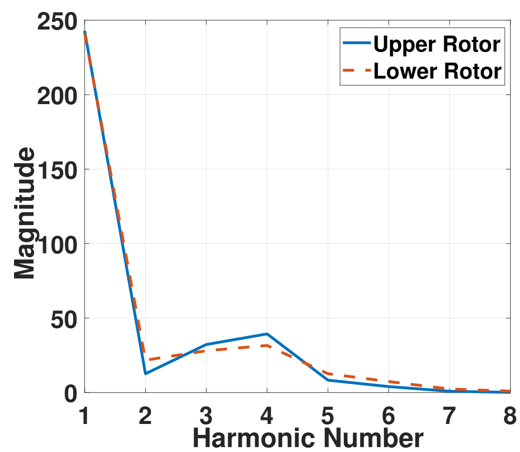

(d) Flap Moment Harmonics

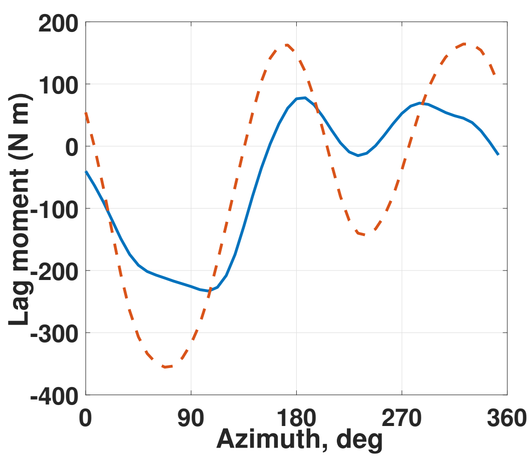

(e) Lag Moment

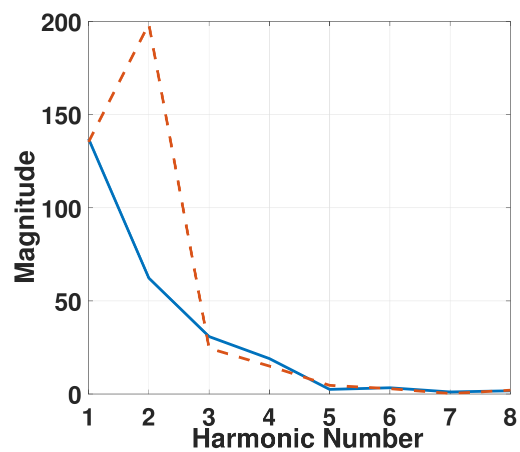

(f) Lag Moment Harmonics

Figure 8.17: Root torsion, flap and lag bending moments for Metaltail at $\mu = 0.1$ with LO = 10% R.

8.5 Hub Loads

Figures 8.18 and 8.19 show the predicted upper and lower rotor hub loads with LO = 0% R and 10% R respectively. F_X, F_Y, and F_Z correspond to the longitudinal, lateral, and vertical hub forces respectively. M_X, M_Y, and M_Z correspond to the rolling, pitching, and yawing hub moments respectively. The hub loads of both rotors are dominated by 4/rev as there are 4 blades in each rotor. The total coaxial hub loads are obtained as a sum of upper and lower rotors.

The contributions from upper and lower rotors cancel each other in the time domain for lateral shear F_Y, rolling moment M_X, and torque M_Z. A non-zero lift offset will produce a non-zero roll moment for upper and lower rotor. The total contribution is zero. The remaining two forces F_X, F_Z, and pitching moment M_Y of each rotor add. The pitching moment for each rotor is zero, so the total is also zero.

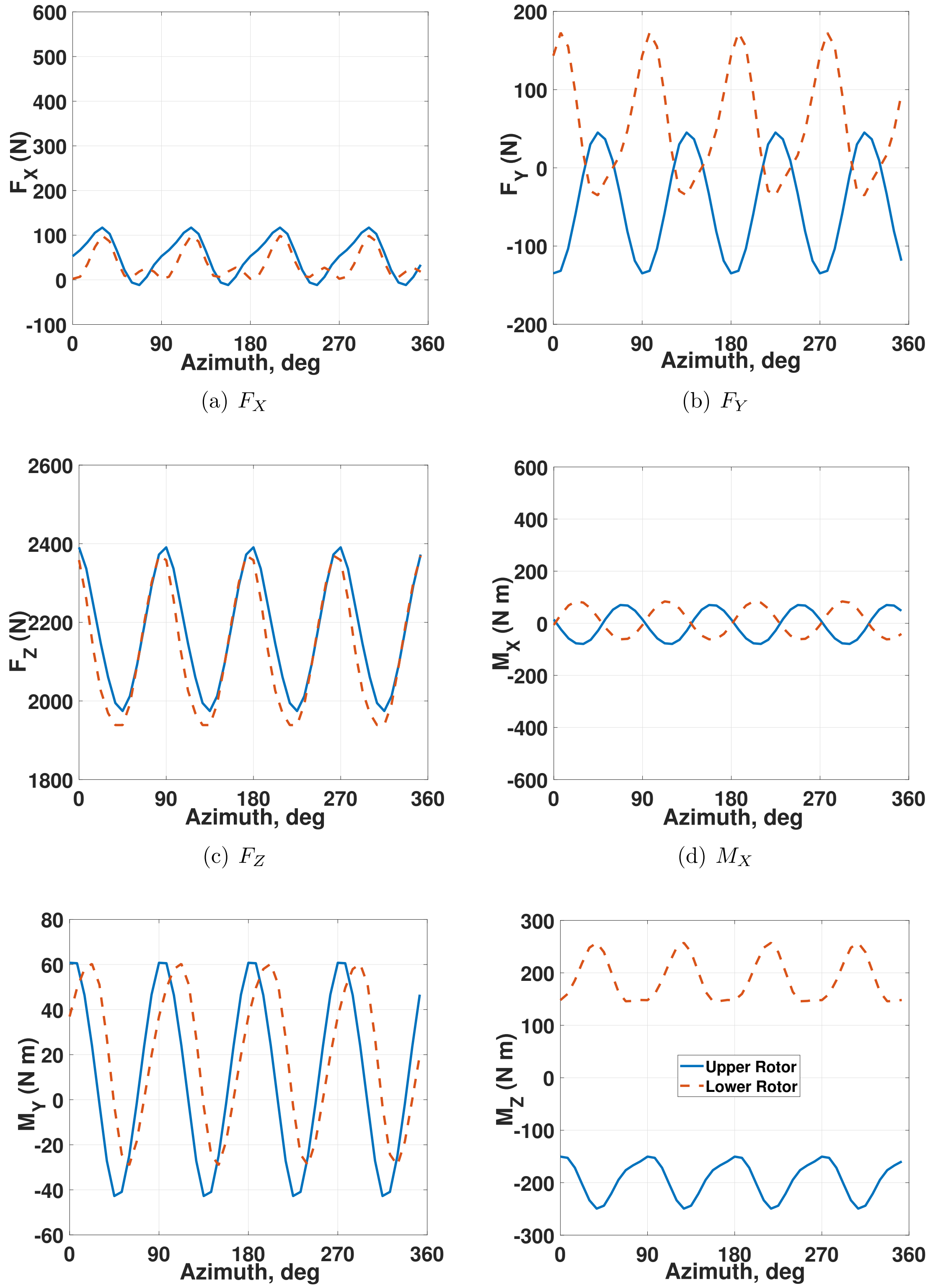

(a) F_X

(b) F_Y

(c) F_Z

(d) M_X

(e) M_Y

(f) M_Z

Figure 8.18: Hub forces and moments for Metaltail at $\mu = 0.1$ with LO = 0% R.

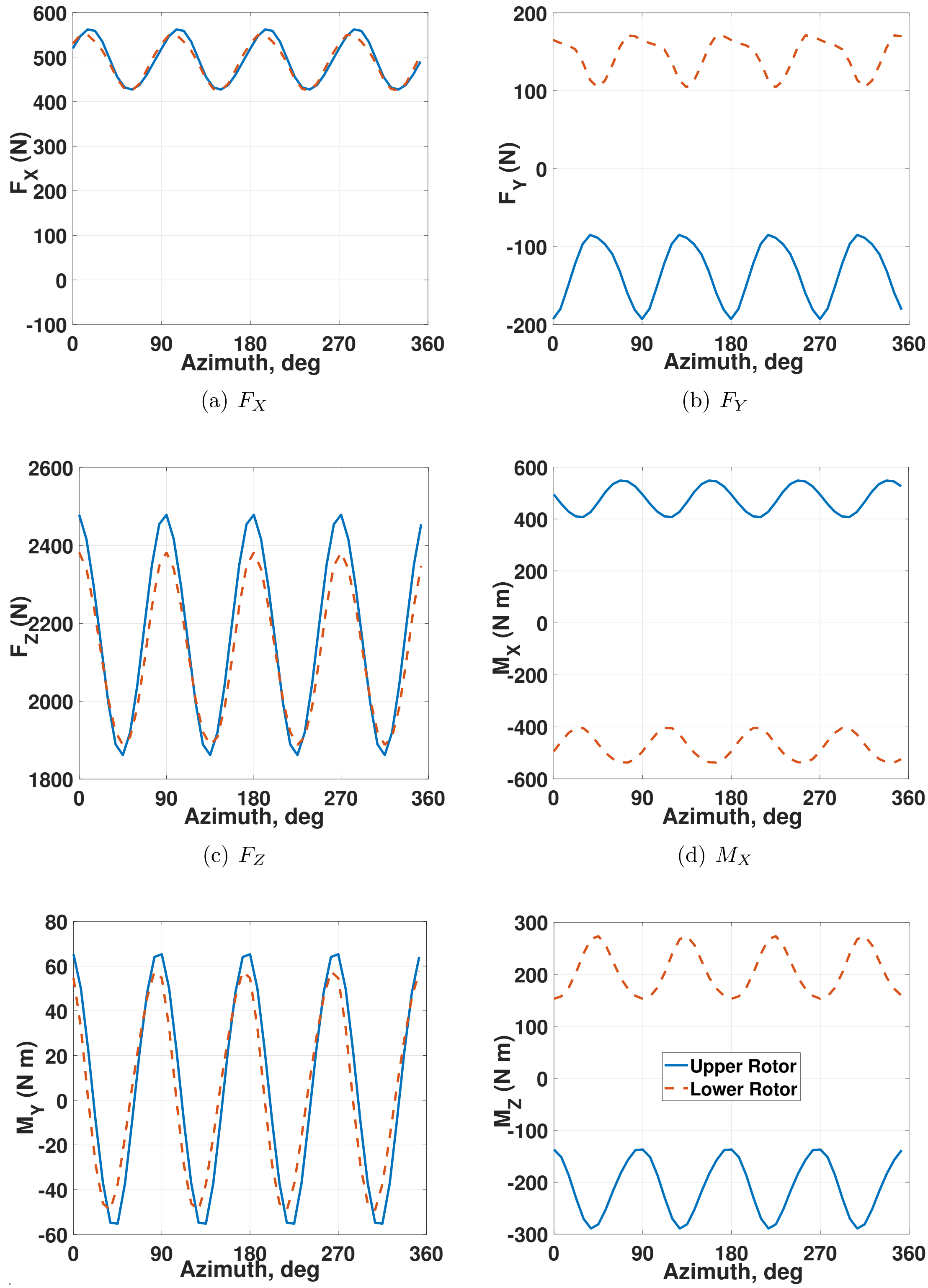

(a) F_X (b) F_Y

(c) F_Z (d) M_X

(e) M_Y (f) M_Z

Figure 8.19: Hub forces and moments for Metaltail at $\mu = 0.1$ with LO = 10% R.

8.6 Vibratory Hub Loads

Main rotor vibratory loads is characterized by pN_b /rev harmonics for identical blades, where p is an integer. Here $N_b = 4$ and 4/rev is the dominant harmonic.

Figure 8.20 shows the predicted 4/rev vibratory harmonics of roll M_X, pitch M_Y, resultant $\sqrt{M_X^2 + M_Y^2}$, and thrust F_Z for upper, lower, and total as a function of advance ratio. The lift offset is zero. As expected, the roll moment for upper and lower rotors cancel (Figure 8.20(a)), while the pitch moment add (Figure 8.20(b)). The resultant moment $\sqrt{M_X^2 + M_Y^2}$ then takes the form of pitch moment (Figure 8.20(c)). The thrust for upper and lower rotors add (Figure 8.20(d)). The maximum hub moment is observed at the transition speed of $\mu = 0.1 - 0.15$. The 4/rev hub thrust decreases with the advance ratio. Similar observations can be made for LO = 10% R as shown in Figure 8.21. The vibratory harmonics of LO = 0% R and LO = 10% R are compared in Figure 8.22. A higher lift offset shows higher vibration at lower speeds. This increase in vibration is not significant but noticeable.

Figures 8.23 and 8.24 show the snapshot of predicted 4/rev rotor hub loads and flight test data of S-97 at low-speed flight from Reference 84. Overall, the trends for $\sqrt{M_X^2 + M_Y^2}$ shown in Figure 8.20(c) are similar to S-97. No consistent trend was observed between the contributions of upper and lower rotors to the total 4/rev harmonics. This is because the upper and lower rotors of Metaltail show a similar magnitude of harmonic content in airloads distribution, as discussed earlier. However, comparing the S-97 with the UH-60A coaxial rotor (Figure 8.25) reveals that the trends are much more similar.

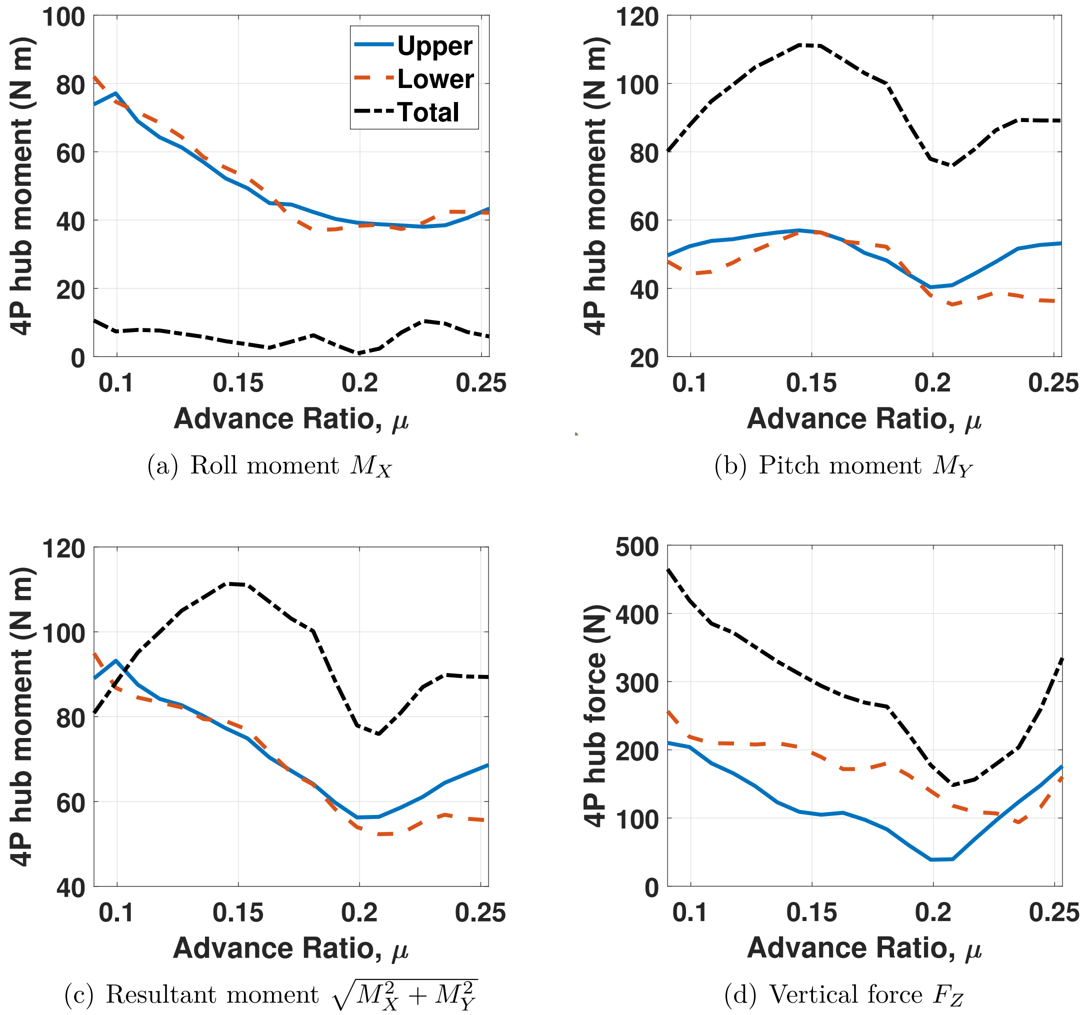

(a) Roll moment M_X

(b) Pitch moment M_Y

(c) Resultant moment $\sqrt{M_X^2 + M_Y^2}$

(d) Vertical force F_Z

Figure 8.20: Predicted 4/rev vibratory harmonics of hub loads for Metaltail at low-speed flight with LO = 0% R.

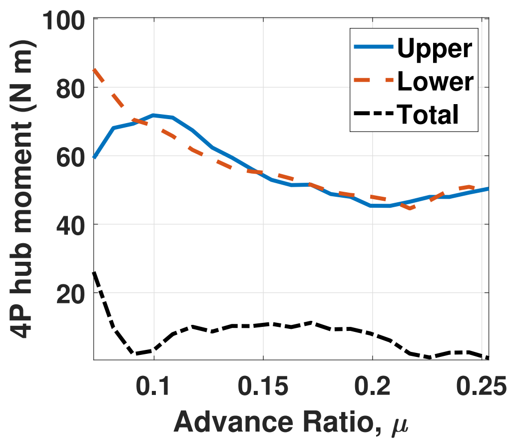

(a) Roll moment M_X

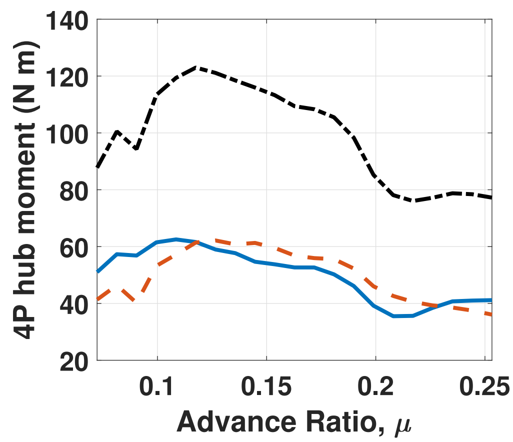

(b) Pitch moment M_Y

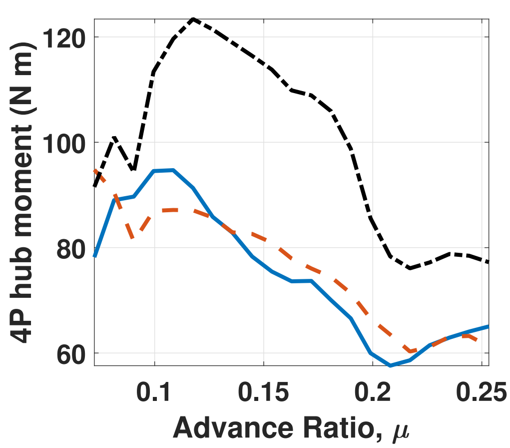

(c) Resultant moment $\sqrt{M_X^2 + M_Y^2}$

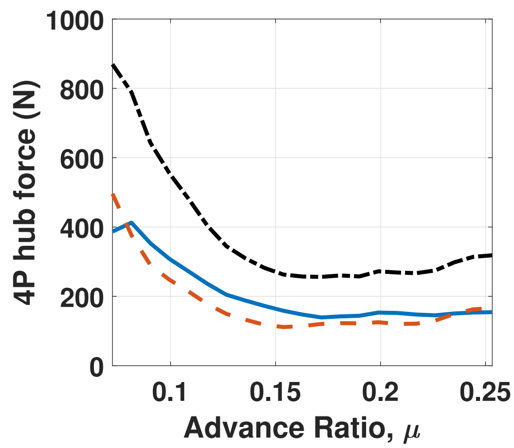

(d) Vertical force F_Z

Figure 8.21: Predicted 4/rev vibratory harmonics of hub loads for Metaltail at low-speed flight with LO = 10% R.

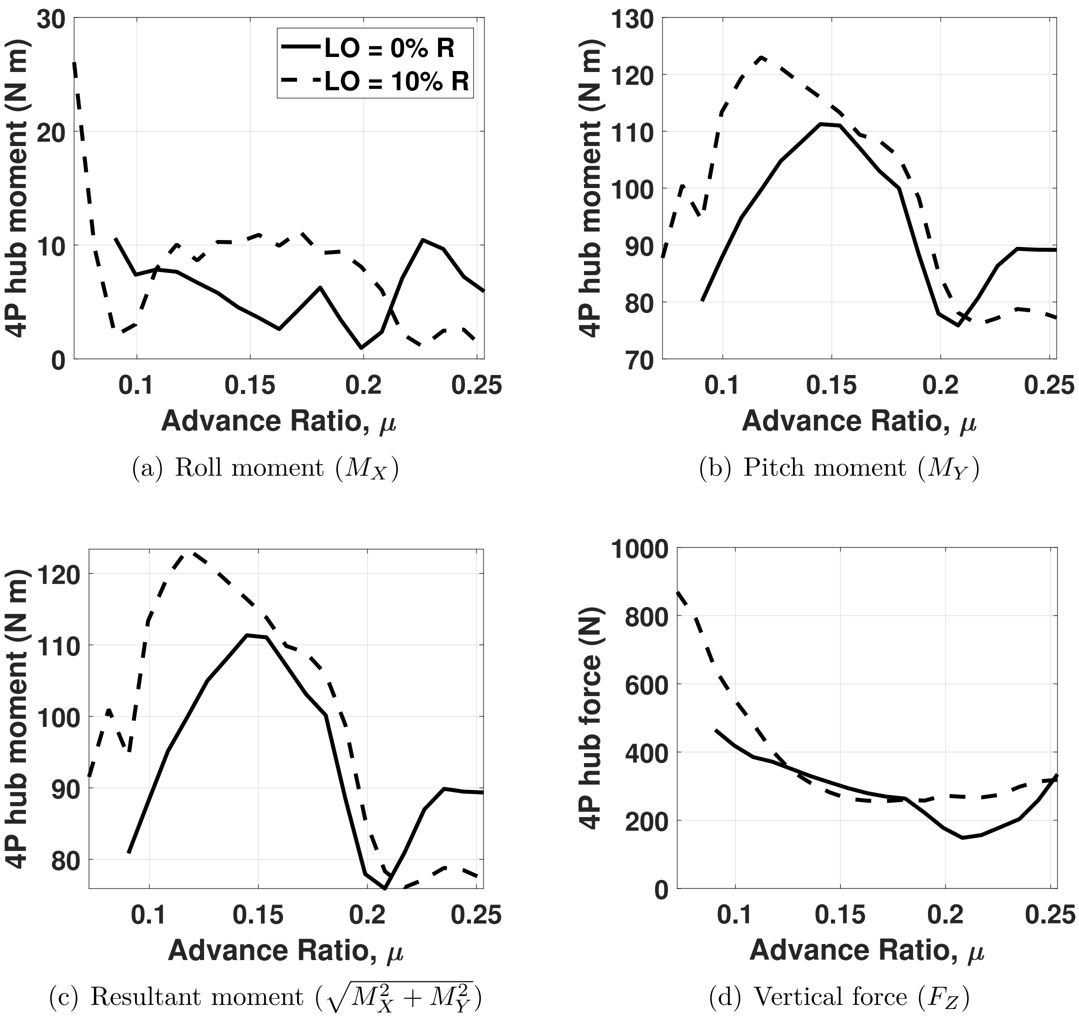

(a) Roll moment (M_X)

(b) Pitch moment (M_Y)

(c) Resultant moment ($\sqrt{M_X^2 + M_Y^2}$)

(d) Vertical force (F_Z)

Figure 8.22: Comparison of 4/rev vibratory harmonics of hub loads for Metaltail with LO = 0% R and LO = 10% R.

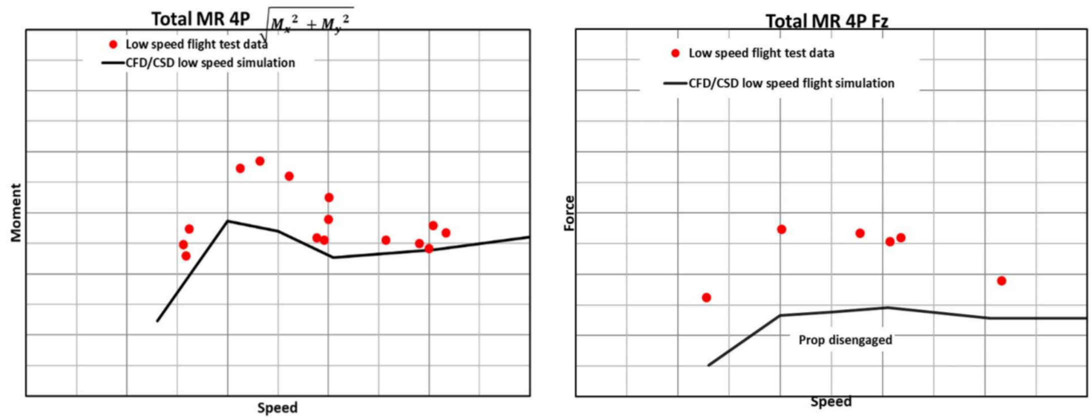

Figure 8.23: Snapshot of CFD/CA predicted 4/rev rotor hub loads and flight test data at low-speed transition flight for S-97 rotor from Reference 84 (left plot: hub resultant moment; right plot: hub vertical force).

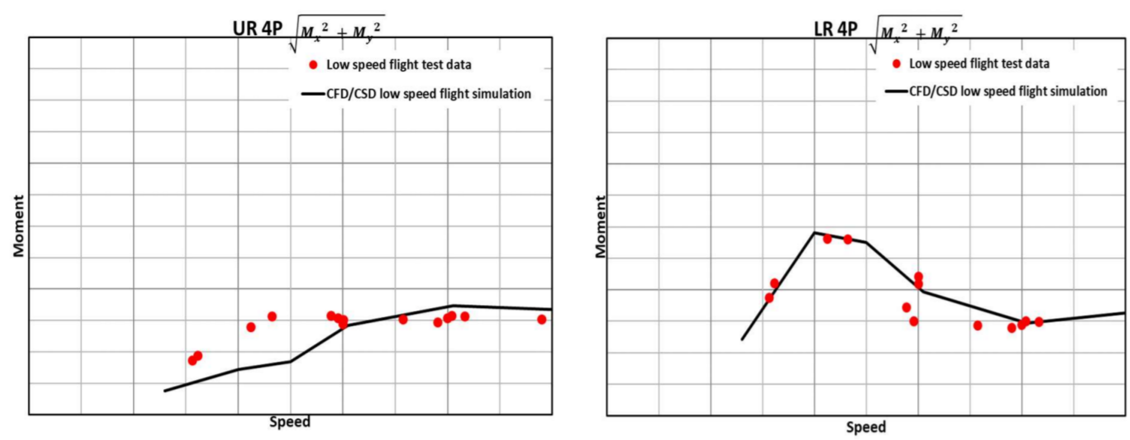

Figure 8.24: Snapshot of CFD/CA predicted 4/rev rotor hub loads and flight test data at low-speed transition flight for S-97 rotor from Reference 84 (left plot: upper rotor; right plot: lower rotor).

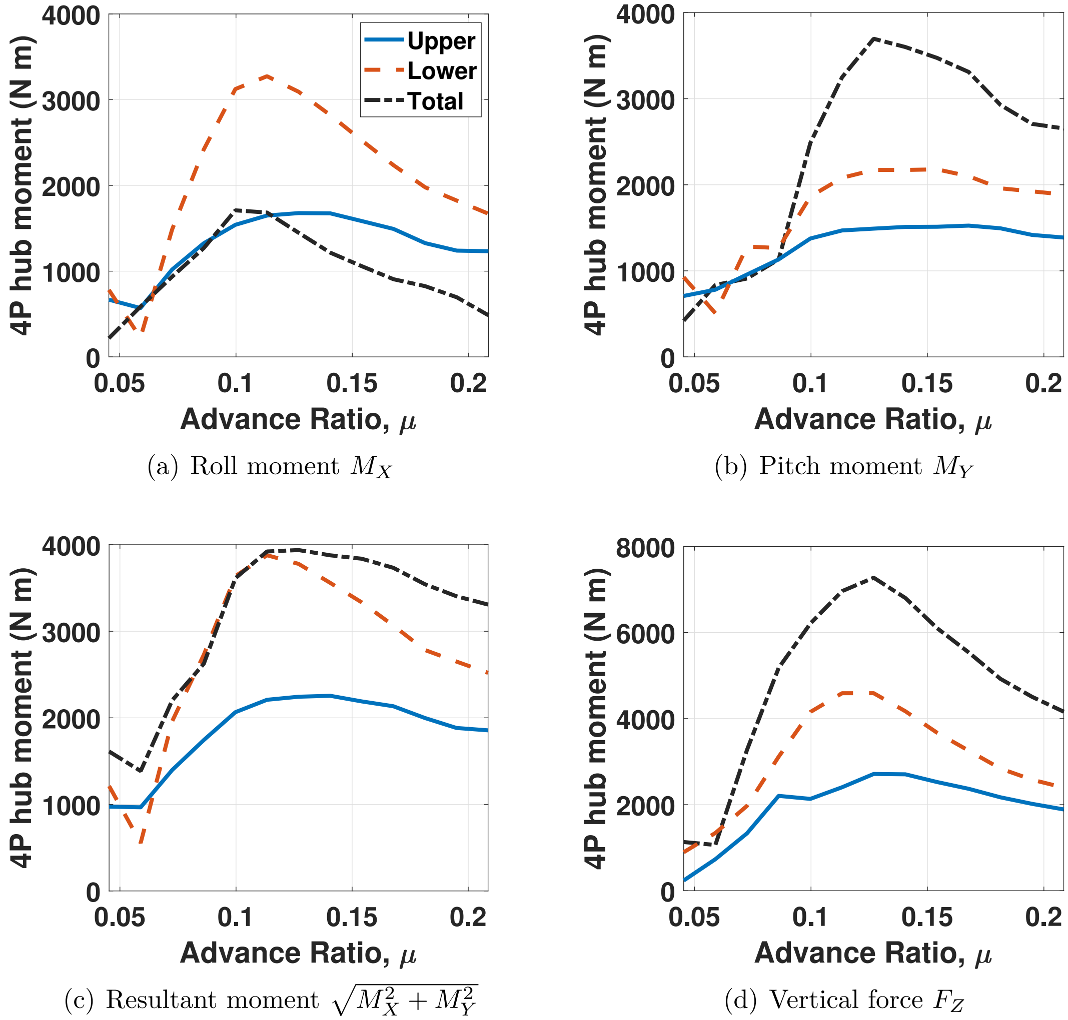

(a) Roll moment M_X

(b) Pitch moment M_Y

(c) Resultant moment $\sqrt{M_X^2 + M_Y^2}$

(d) Vertical force F_Z

Figure 8.25: Predicted 4/rev vibratory harmonics of hub loads for UH-60A coaxial rotor at low-speed flight with LO = 0% R.

8.7 Effect of Inter-Rotor Phase

Inter-rotor phase (ϕ) is defined as the angle between the blades of upper and lower rotor in their initial configuration i.e., when the rotor blade is at $\psi = 0°$ (aligned with the tail line). Figure 8.26 shows the coaxial rotor arrangement at $\psi = 0°$ for $\phi = 0°$ and $45°$. The rotor phasing changes the magnitude of 4/rev vibratory hub loads. It selectively cancels or adds the components. At $\phi = 0°$, the roll moments cancel and pitch moments add. However at $\phi = 45°$, the roll moments add up and pitch moments cancel. At intermediate angles, the total moments are a combination. Apart from the geometric interactions, there are wake interactions that change hub loads on each rotor.

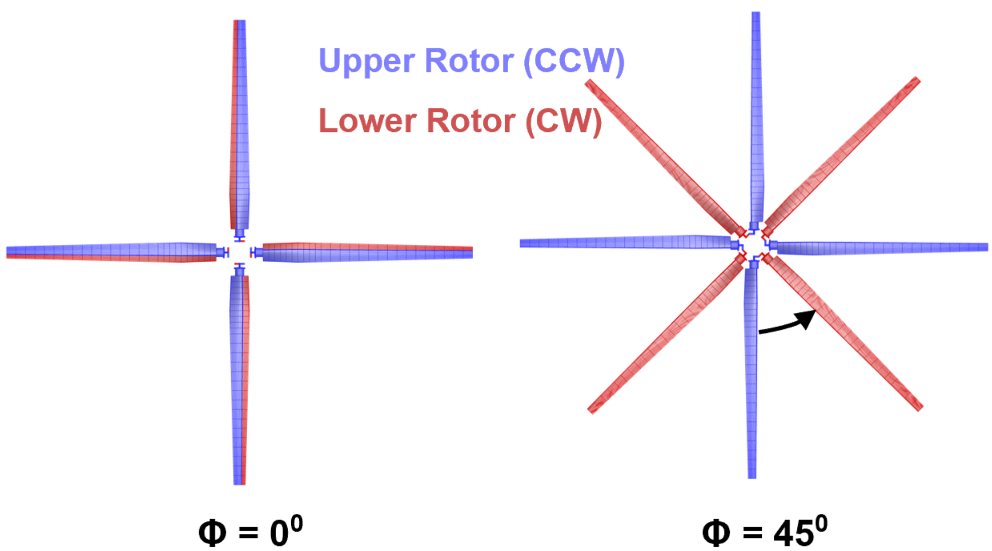

Figure 8.26: Coaxial rotor arrangement at $\psi = 0°$ for inter-rotor phase angles, $\phi = 0°$ and $45°$.

The geometric interaction provides the baseline of how rotor phasing changes the total hub moments. The hub moment from the upper and lower rotor can be broken down into its harmonic components. For a coaxial system with 4 blades on each rotor, the hub loads for rolling and pitching moment can be expressed as shown in Eqs. 8.2 - 8.5. Only integer multiples of 4/rev harmonics are included. The hub loads for upper and lower rotors are assumed to be similar for simplicity – meaning no inter-rotor interactions are considered. The lower rotor hub loads with the effect of inter-rotor phase are given in Eqs. 8.6 and 8.7. The total rotor hub loads is then calculated as the sum of upper and lower rotor loads as given in Eqs. 8.8 and 8.9. It is seen that the total rotor loads is dependent on the rotor-to-rotor phase angle, ϕ, and the harmonic content of the original wave form.

$$M_X^U = \sum^k (A_{4kc}\cos(4k\psi) + A_{4ks}\sin(4k\psi)) \tag{8.2}$$

$$M_Y^U = \sum^k (A_{4kc}\cos(4k\psi) + A_{4ks}\sin(4k\psi)) \tag{8.3}$$

$$M_X^L = \sum^k (-A_{4kc}\cos(4k(\psi)) - A_{4ks}\sin(4k(\psi))) \tag{8.4}$$

$$M_Y^L = \sum^k (A_{4kc}\cos(4k(\psi)) + A_{4ks}\sin(4k(\psi))) \tag{8.5}$$

$$M_X^L(\phi) = \sum^k (-A_{4kc}\cos(4k(\psi+\phi)) - A_{4ks}\sin(4k(\psi+\phi))) \tag{8.6}$$

$$M_Y^L(\phi) = \sum^k (A_{4kc}\cos(4k(\psi+\phi)) + A_{4ks}\sin(4k(\psi+\phi))) \tag{8.7}$$

$$M_X^U + M_X^L = \sum^k 2\sin(2k\phi)(A_{4kc}\sin(4k\psi+2k\phi) - A_{4ks}\cos(4k\psi+2k\phi)) \tag{8.8}$$

$$M_Y^U + M_Y^L = \sum^k 2\cos(2k\phi)(A_{4kc}\cos(4k\psi+2k\phi) + A_{4ks}\sin(4k\psi+2k\phi)) \tag{8.9}$$

Consider some sample values. Let the hub loads comprise of 0, 4, 8, and 12 harmonics. Let the coefficients be an arbitrary set: $A_{0c} = 10.0$, $A_{4c} = 1$, $A_{4s} = 0$, $A_{8c} = 0.0$, $A_{8s} = 0.05$, $A_{12c} = 0.0$, $A_{12s} = 0.02$. Figure 8.27 shows the variation of magnitude of 0, 4, 8 and 12 /rev harmonics of total hub rolling moment as a function of inter-rotor phase angle. Clearly, the 0/rev content is zero irrespective of inter-rotor phase. The higher harmonics (4, 8, and 12/rev) vary with inter-rotor phase. The

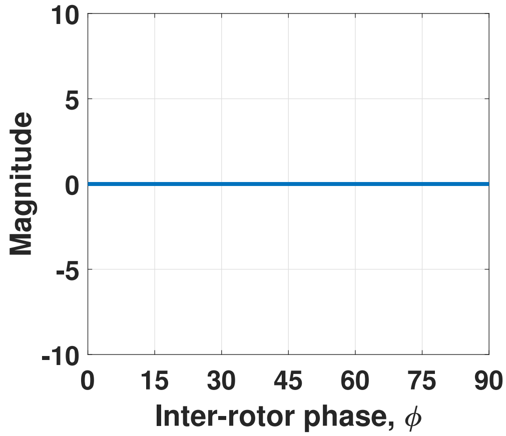

(a) 0/rev

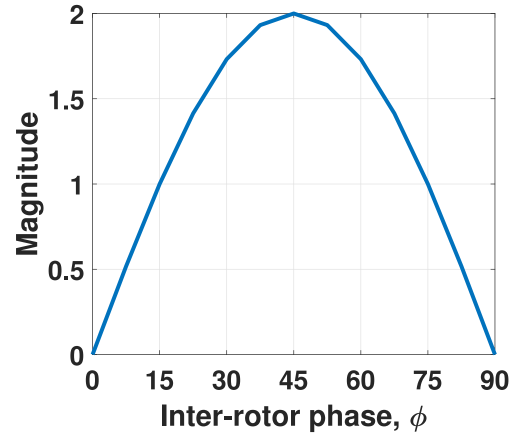

(b) 4/rev

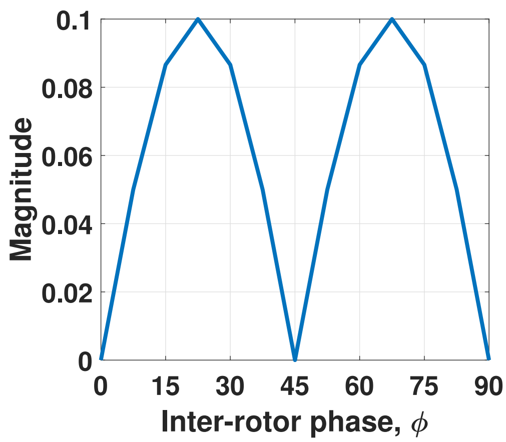

(c) 8/rev

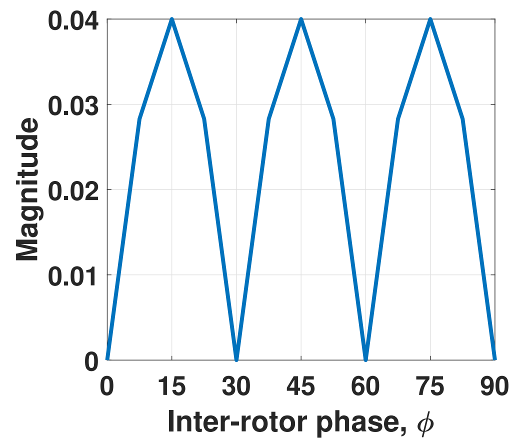

(d) 12/rev

Figure 8.27: Variation of magnitude of 0, 4, 8 and 12 /rev harmonics of total theoretical hub rolling moment of a coaxial rotor with inter-rotor phase angle.

4/rev (first blade passage) roll moment is maximum at one phase $\phi = 45°$. The 8/rev (second blade passage) is maximum at two phases $\phi = 22.5°$, and $67.5°$. The 12/rev (third blade passage) is maximum at three phases $\phi = 15°$, $45°$, and $75°$. Similar analysis for the pitching hub moment is seen in Figure 8.28. Here, the 0/rev pitching moment is non-zero and constant. The 4/rev pitch moment is minimum at $\phi = 45°$. The 8/rev pitch moment is minimum at $\phi = 22.5°$, and $67.5°$. The 12/rev pitch moment is minimum at $\phi = 15°, 45°, 75°$. Therefore, the minimum hub pitch occurs at the same inter-rotor phase as the maximum hub roll.

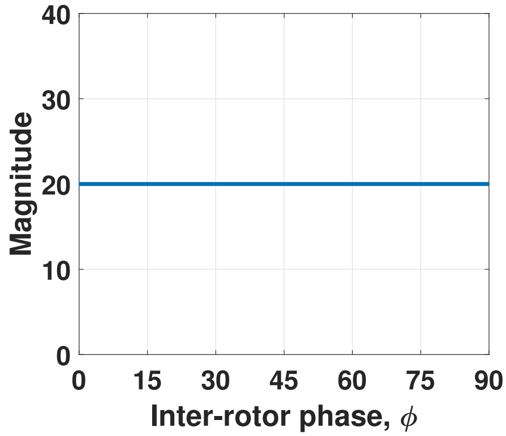

(a) 0/rev

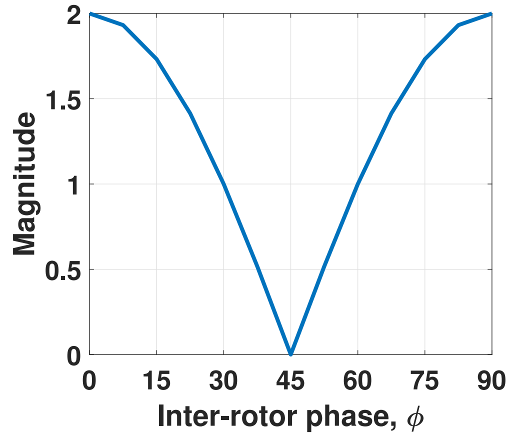

(b) 4/rev

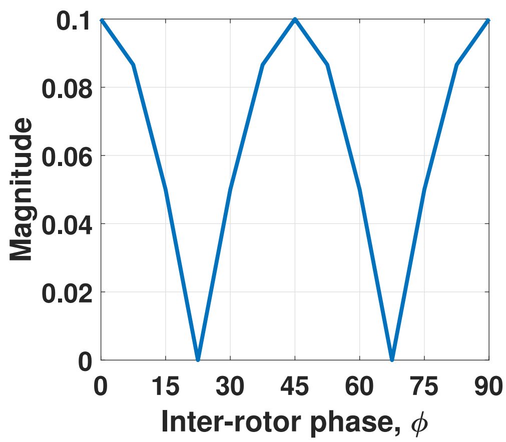

(c) 8/rev

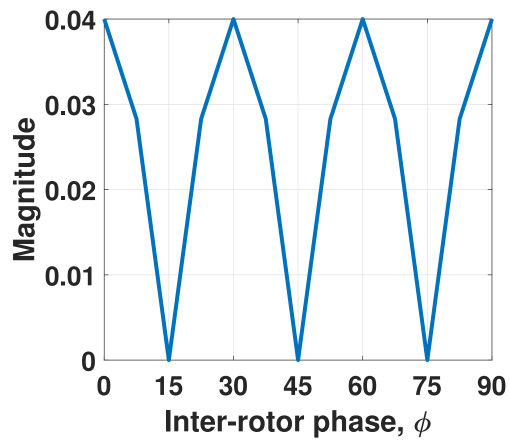

(d) 12/rev

Figure 8.28: Variation of magnitude of 0, 4, 8 and 12 /rev harmonics of total theoretical hub pitching moment of a coaxial rotor with inter-rotor phase angle.

Let us now replace the arbitrary coefficients with actual calculations. The hub loads for Metaltail with different inter-rotor phase angles are shown in Figure 8.29. These include the inter-rotor interactions from the wake. The total rolling moment (4/rev harmonics) is maximum at $\phi = 45°$ and minimum at $\phi = 0°$. The total pitching moment (4/rev harmonics) is maximum at $\phi = 0°$ and minimum at $\phi = 45°$. The results are consistent with the made-up case shown before.

It is important to look at the variation of 4/rev vibratory harmonics as a function of advance ratio for different inter-rotor phase angles. Figure 8.30 shows the total 4/rev vibratory harmonics of roll M_X, pitch M_Y, resultant $\sqrt{M_X^2 + M_Y^2}$, and vertical force F_Z for different phase angles as a function of advance ratio. This is obtained deliberately using a uniform inflow model so the interaction is only geometric. Note that, the results shown in Figure 8.30 do not signify any physical meaning as the interactions of a coaxial system are not captured using the uniform inflow model. The expected trends are captured – the net roll moment is zero for $\phi = 0°$, and the net pitch moment is zero for $\phi = 45°$. The effect of inter-rotor wake interactions is shown next.

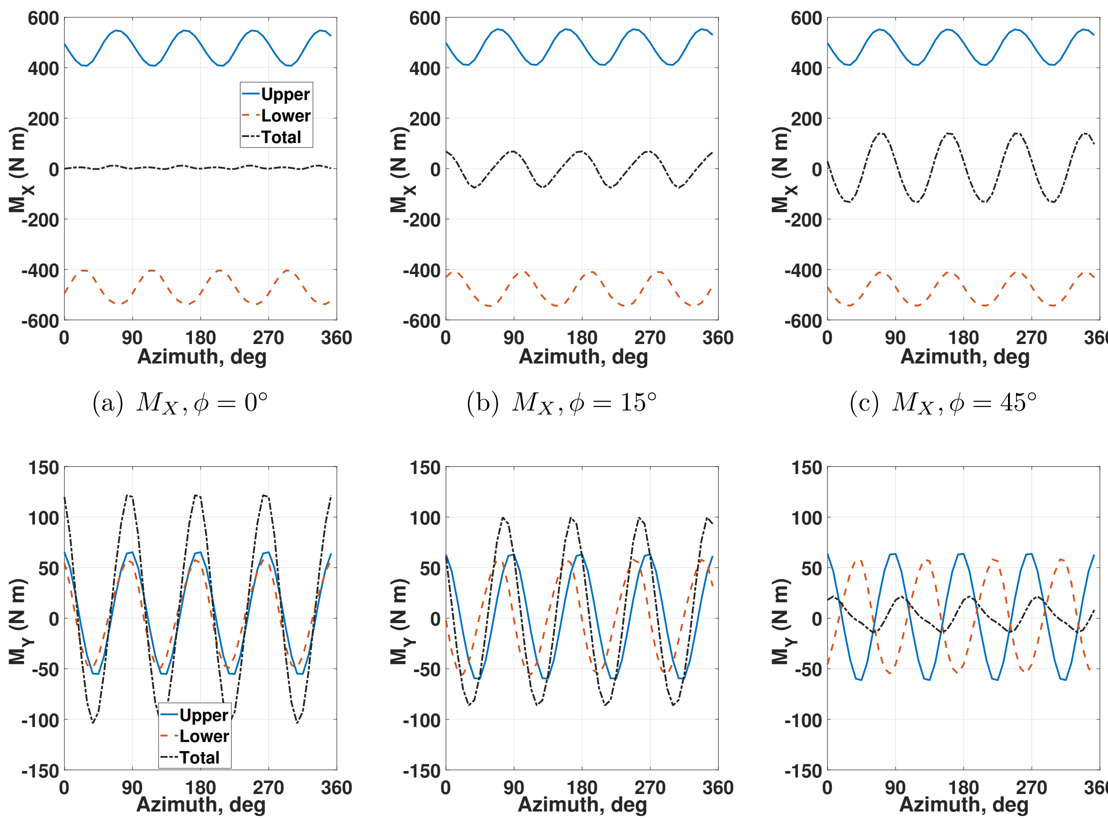

(a) $M_X, \phi = 0°$ (b) $M_X, \phi = 15°$ (c) $M_X, \phi = 45°$

(d) $M_Y, \phi = 0°$ (e) $M_Y, \phi = 15°$ (f) $M_Y, \phi = 45°$

Figure 8.29: Rolling and pitching hub moments for Metaltail with different inter-rotor phase angles.

Figures 8.31 and 8.32 show the effect of wake on total coaxial rotor 4/rev vibratory harmonics of roll M_X, pitch M_Y, resultant $\sqrt{M_X^2 + M_Y^2}$, and vertical force F_Z for different phase angles as a function of advance ratio with LO = 0% R and

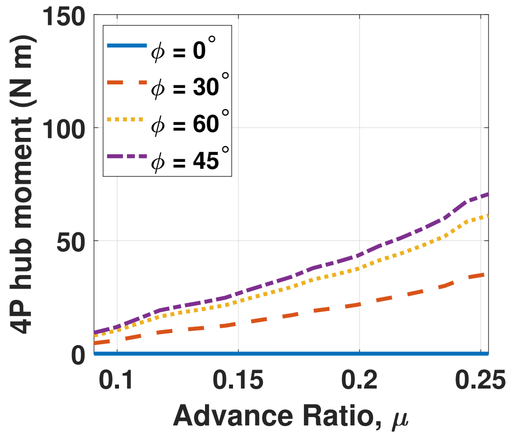

(a) Roll moment M_X

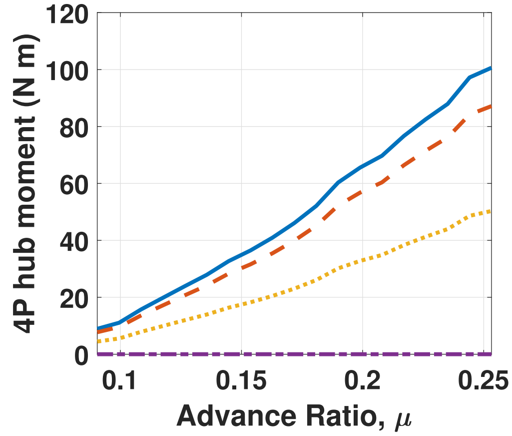

(b) Pitch moment M_Y

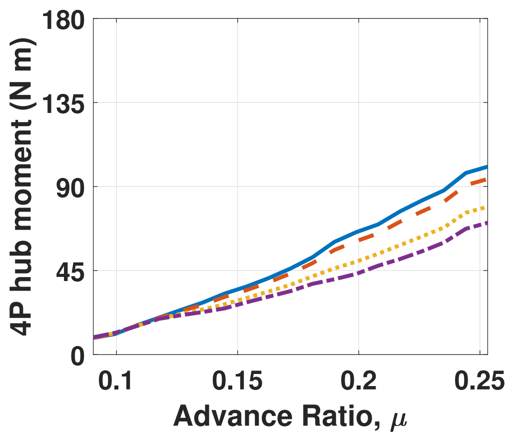

(c) Resultant moment $\sqrt{M_X^2 + M_Y^2}$

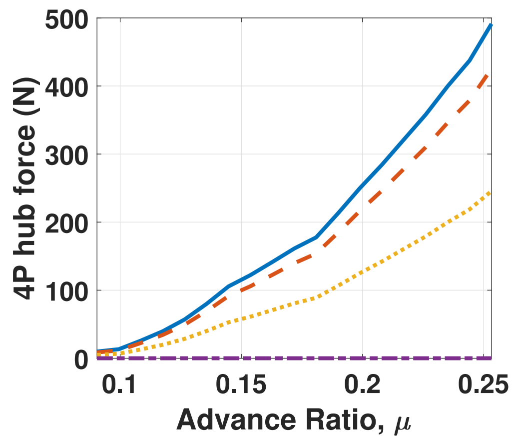

(d) Vertical force F_Z

Figure 8.30: Total 4/rev vibratory harmonics of Metaltail with a uniform inflow model for different phase angles at low-speeds with LO = 0% R.

LO = 10% R respectively. The predictions take into account the effects of wake interactions. The results for $\phi = 0°$ are identical to the ones shown in Figures 8.20 and 8.21. Both the lift offset cases show similar trends and observations. The phase $\phi = 0°$ provides the lowest 4/rev vibratory moment. However, the phase $\phi = 45°$ provides the lowest 4/rev vibratory vertical force. The intermediate phase angles do not show the extreme contributions for either force or moment and are in-between the lowest and highest vibratory harmonics. The choice of ϕ depends on whether vertical force or moments create more fuselage vibration. In general, the

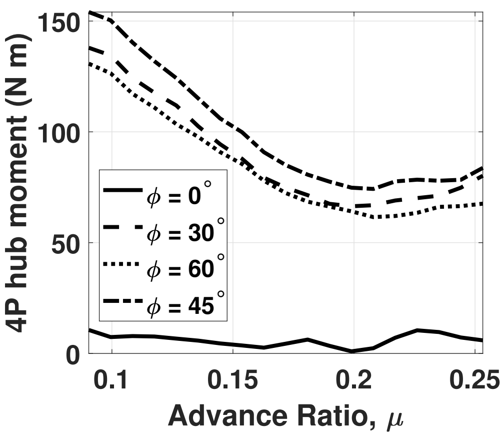

(a) Roll moment M_X

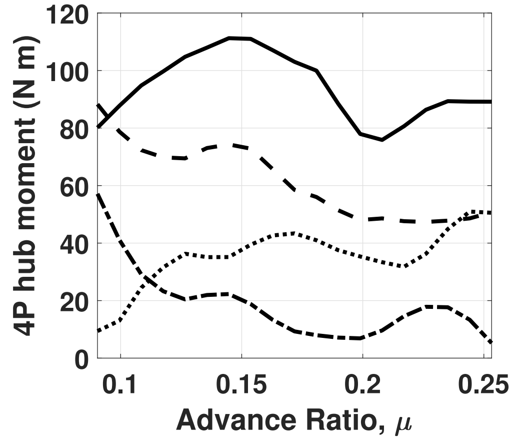

(b) Pitch moment M_Y

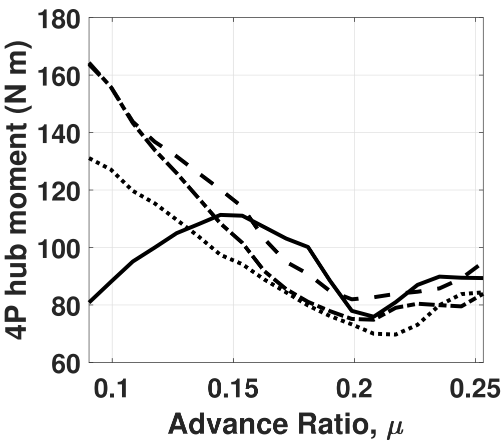

(c) Resultant moment $\sqrt{M_X^2 + M_Y^2}$

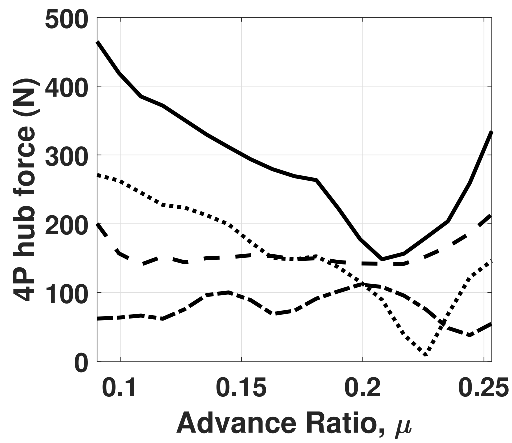

(d) Vertical force F_Z

Figure 8.31: Total 4/rev vibratory harmonics of Metaltail with free-wake interactions for different phase angles at low-speeds with LO = 0% R.

choice of $\phi = 45°$ seems to provide a higher drop in vertical force compared to hub moments. The key conclusion is that the effect of wake interactions dominates over the effect of geometric influence. The geometric influence alone captures neither the magnitude nor trend of vibratory hub loads. Bringing in the wake interactions flips the geometric influence trend and increases vibratory magnitude by up to 5 times.

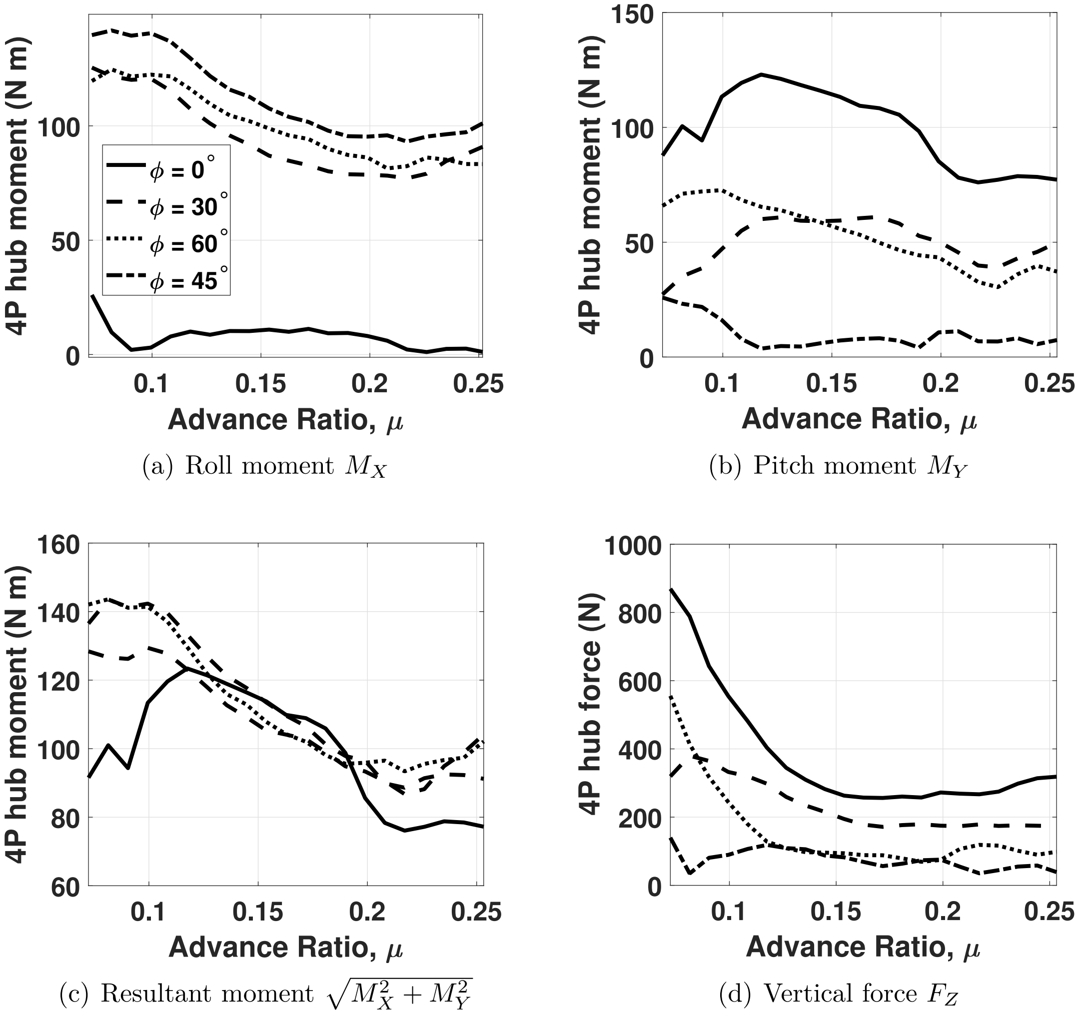

(a) Roll moment M_X

(b) Pitch moment M_Y

(c) Resultant moment $\sqrt{M_X^2 + M_Y^2}$

(d) Vertical force F_Z

Figure 8.32: Total 4/rev vibratory harmonics of Metaltail with free-wake interactions for different phase angles at low-speeds with LO = 10% R.

8.8 Three-Dimensional Stresses

The benefit to full 3D FEA-based structural modeling is the ability to predict stresses and strains throughout the rotor, including the hub components. The plots shown here provide only a sample of the results generated for axial/bending stress, but a wealth of data is available for different stresses and strains.

Figures 8.33 and 8.34 show the axial/bending stresses (σ_{11}) for Metaltail with LO = 0% R and 10% R respectively. The highest stresses occur near the advancing and retreating sides. For LO = 0% R, the negative blade lift on the advancing side causes downward bending and higher positive lift on the retreating side causes upward bending. Hence the blades of both rotors are closest at $\psi = 90°$ and farthest at $\psi = 270°$. With LO = 10% R, the advancing side produces more positive lift compared to retreating side to produce the individual rotor roll moment. Hence the blades of both rotors are closest at $\psi = 270°$ and farthest at $\psi = 90°$.

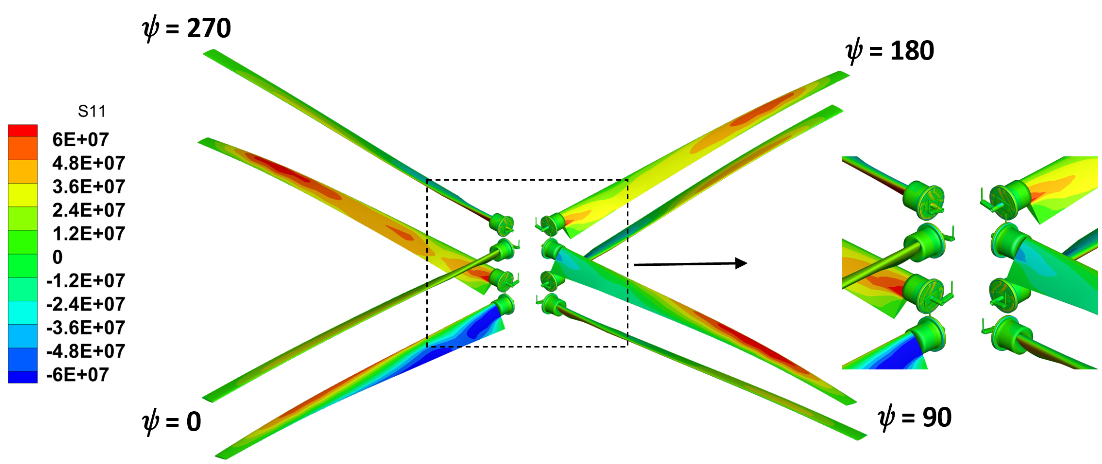

Figure 8.33: Axial/bending stress distribution for Metaltail with LO = 0% R.

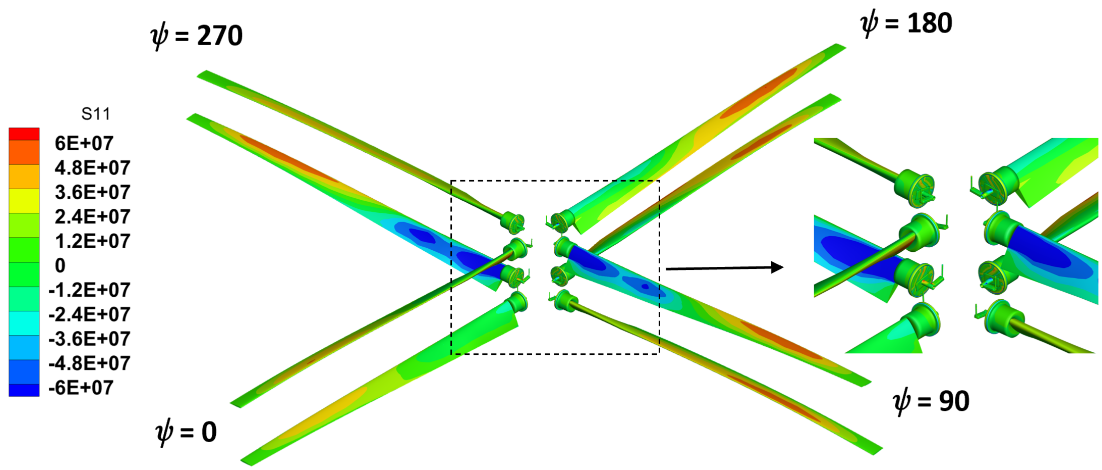

Figure 8.34: Axial/bending stress distribution for Metaltail with LO = 10% R.

Figures 8.35 and 8.36 show the cross-sectional axial/bending stresses within the blade at $\psi = 90°$ and 270° for LO = 0% R. Figures 8.37 and 8.38 show the same stresses with LO = 10% R. Examination of cross section reveals that the blade spar takes most of the bending stress, but there appears to be some stress carried by the leading edge weight. The stress distribution along the span follows the blade bending. This is determined by the lift and the centrifugal force. The pre-cone in the blade results a downward bending due to centrifugal force, even without aerodynamics. Consider the case with LO = 10% R. At $\psi = 90°$, shown in Figure 8.37, the positive lift at the tip causes a upward bending of the blade. This is seen as a compression on the top and extension on the bottom near the root. Outboard, the moment due to lift force decreases and the centrifugal force dominates. These effects oppose each other but the net effect is an extension on the top and compression on the bottom surface. Similar observations can be obtained with other cases.

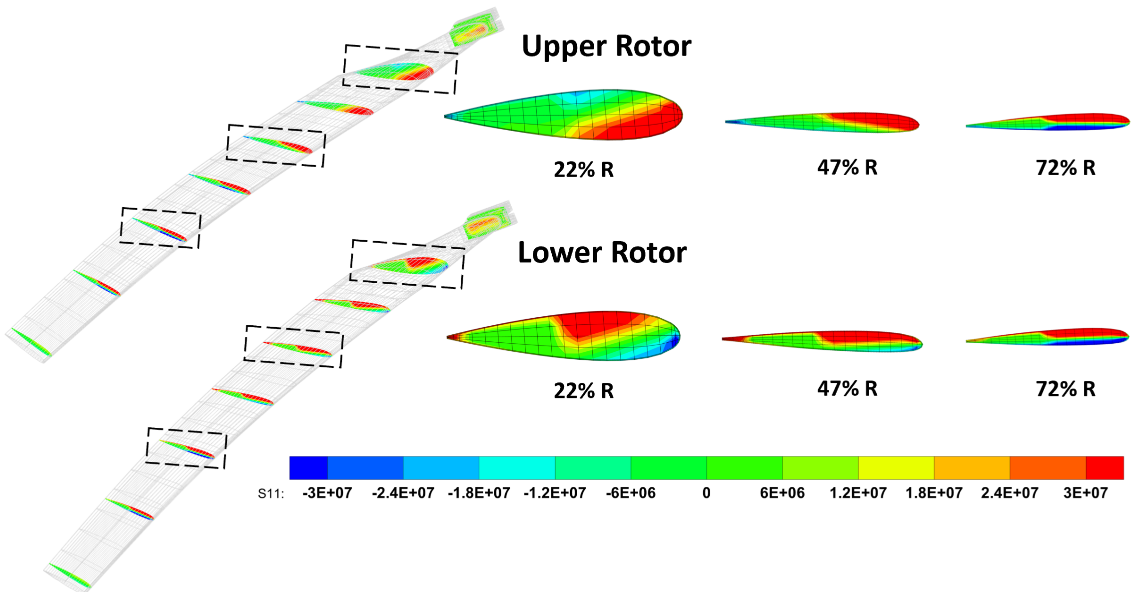

Figure 8.35: Blade axial/bending stress distribution at $\psi = 90°$ with LO = 0% R. (scale adjusted)

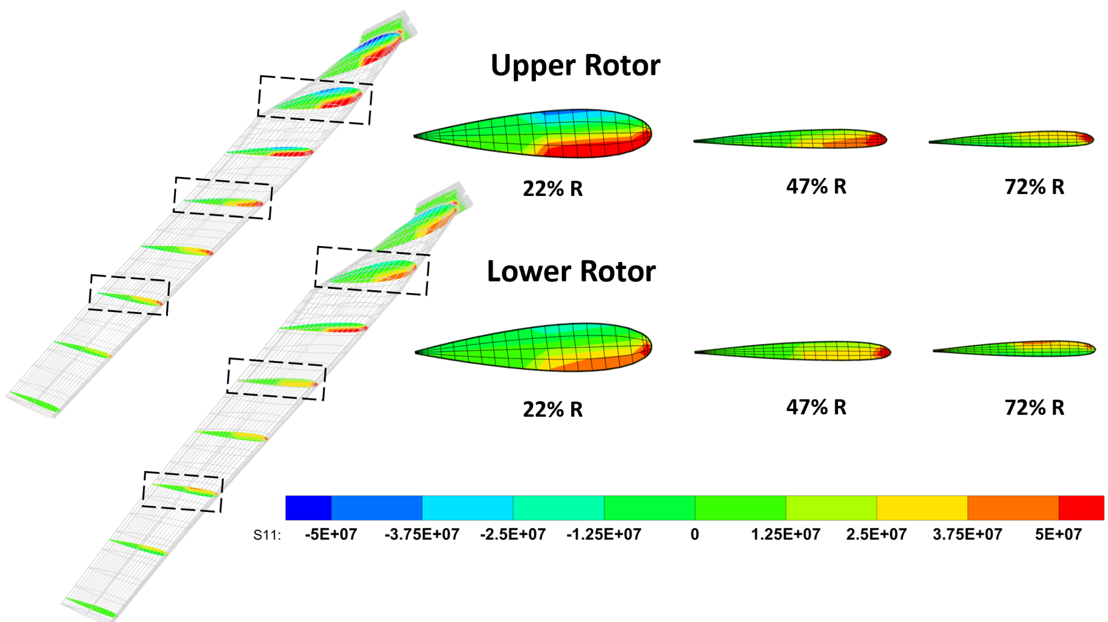

Figure 8.36: Blade axial/bending stress distribution at $\psi = 270°$ with LO = 0% R. (scale adjusted)

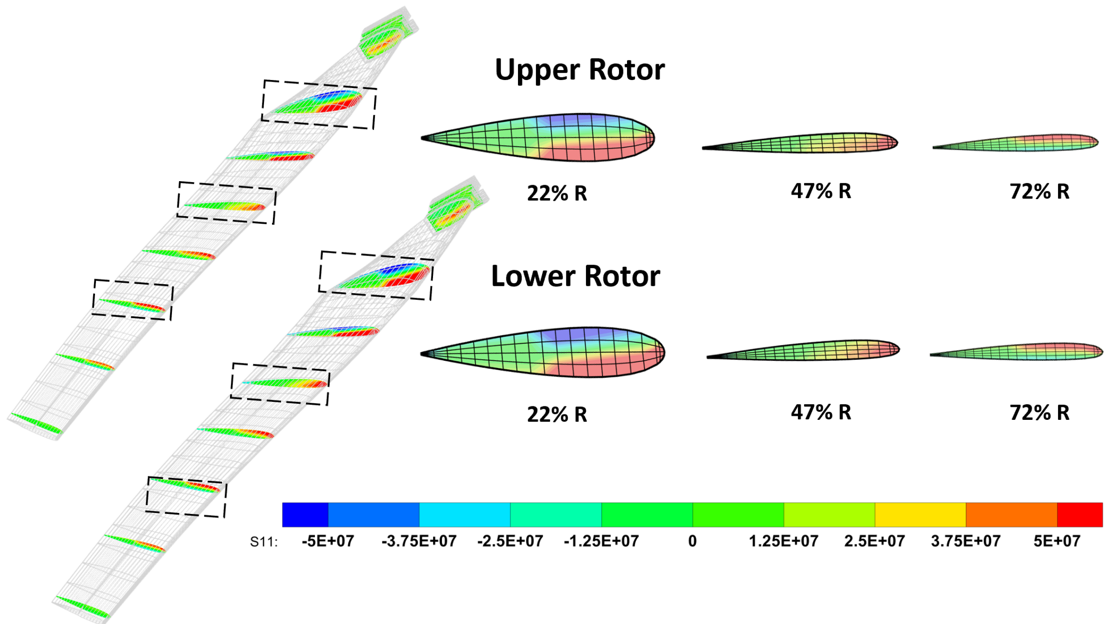

Figure 8.37: Blade axial/bending stress distribution at $\psi = 90°$ with LO = 10% R. (scale adjusted)

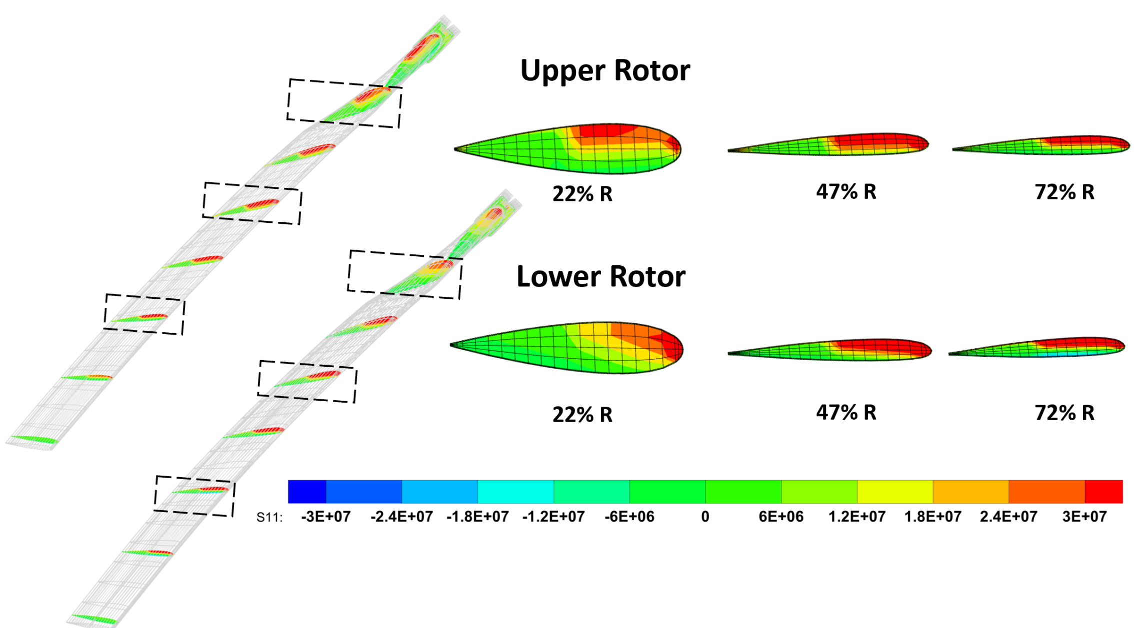

Figure 8.38: Blade axial/bending stress distribution at $\psi = 270°$ with LO = 10% R. (scale adjusted)

Figures 8.39 and 8.40 show the axial stresses at blade root connections to hub at different azimuths for LO = 0% R and 10% R. The lower rotor has a higher stress than the upper rotor. The connection to the outer cuff shows high stress concentrations, as the stress from the blade spar is transferred. Otherwise,it is generally lightly stressed. The inner cuff also shows some stress concentrations near the outer edge.

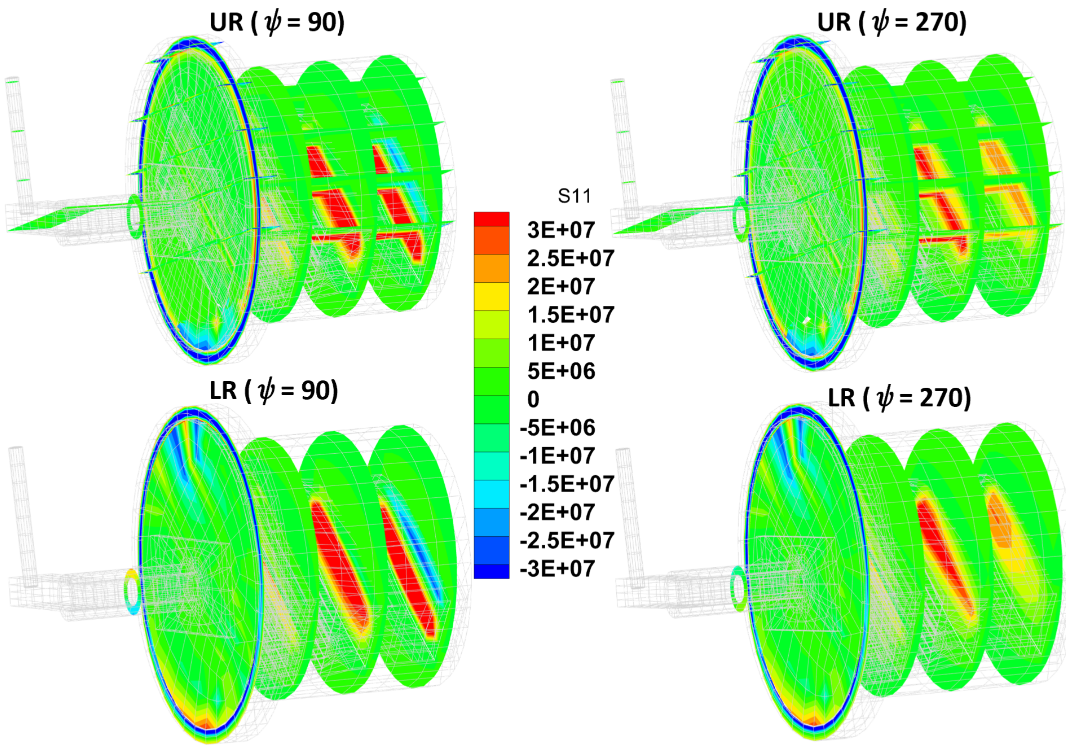

Figure 8.39: Axial/bending stress distribution near blade root at $\psi = 90°$ and $270°$ with LO = 0% R.

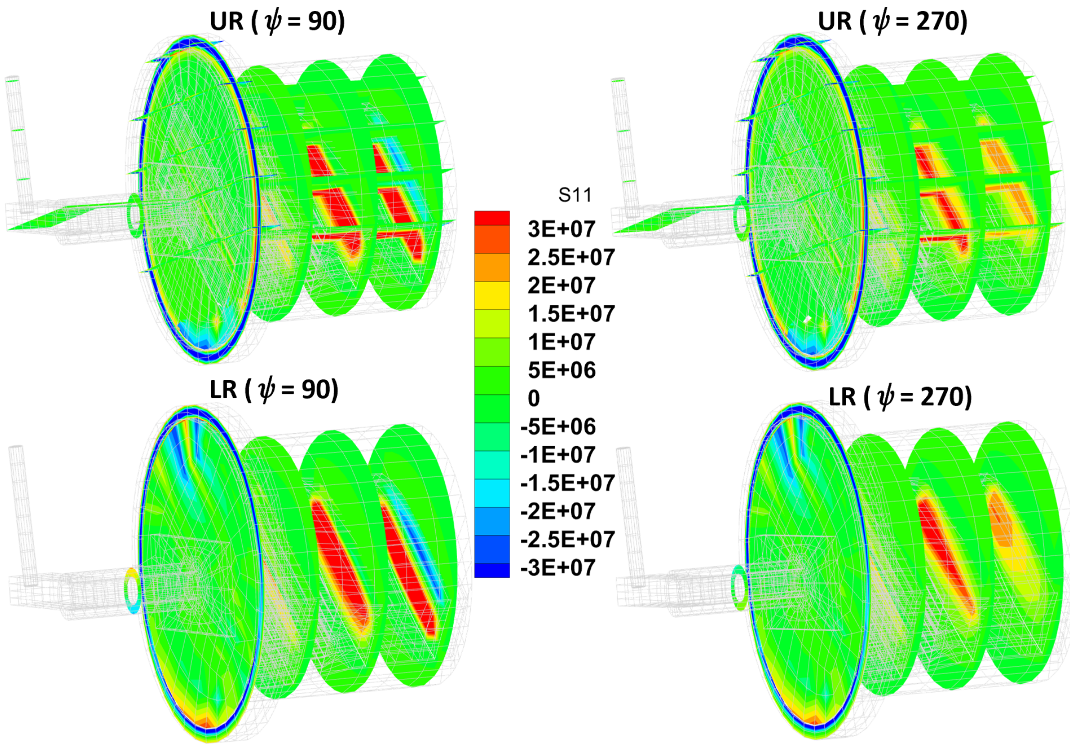

Figure 8.40: Axial/bending stress distribution near blade root at $\psi = 90°$ and $270°$ with LO = 10% R.

8.9 Computational Cost

The periodic rotor solution was obtained using the modified harmonic balance (MHB) algorithm with rotor solution consisting of eight harmonics and executed on a hybrid distributed – shared memory architecture with 90 processors. The 6 degrees of freedom trim solution for a coaxial rotor requires around 50 minutes of wall clock time. The free-wake model is also parallelized with shared memory OpenMP processors, with the number of processors equal to the number of tip trailers (8 in our case). The free-wake computations for each trim iteration require 1 minute wall clock time for ten wake turns and 20 revolutions in time with 7.5 degree time-step.

8.10 Summary and Conclusions

The X3D solver was used to perform aeromechanical analysis of coaxial rotors. Metaltail was used as the test example. The UH-60A coaxial rotor was also studied for certain parameters. Predictions of performance, airloads, hub loads, 4/rev vibratory harmonics, and 3D stress fields generated with free-wake lifting line aerodynamics were discussed, and qualitatively compared with test data from Sikorsky S-97 Raider aircraft. Although the intended goal was capability demonstration, some key conclusions are drawn from the analysis:

1. It is possible to use 3D structures to model a coaxial rotor and obtain aeroelastic stresses and strains from first principles. This was effectively demonstrated on two notional coaxial model test cases. One is the Metaltail, a hingeless coaxial proprotor aircraft, and two is the articulated coaxial rotor built from two UH-60A-like rotors.

2. The lower rotor of a coaxial helicopter sees higher harmonics in blade lift distribution. The rear part of the lower rotor (first quadrant) sees magnified impulses. This is due to the upper rotor wake impinging on the lower rotor.

3. The higher harmonic content observed in the lower rotor is dependent on the blade twist; a 3/rev is observed in a edgewise rotor (UH-60A coaxial rotor) and 4/rev for a highly twisted proprotor (Metaltail).

4. The trends obtained for the total main rotor vibratory loads of coaxial Metaltail are similar with the data published for S-97 Raider. For the range of speeds studied ($\mu \leq 0.25$), the peak vibration for hub moments was observed at the transition speed ($\mu = 0.1 - 0.15$), and the 4/rev vertical force decreased with increasing advance ratio.

5. There is no clear trend observed between the contributions of upper rotor and lower rotor to the total 4/rev vibratory harmonics. This is because the upper and lower rotors of Metaltail show similar magnitude of harmonic content in airloads distribution. For the UH-60A coaxial rotor, the lower rotor showed higher contributions to 4/rev vibratory harmonics at low-speeds. This behavior is similar to S-97 because the lower rotor had higher harmonic content in the airloads distribution.

6. Increase in lift offset increases the 4/rev vibratory loads at low-speed flight, thereby increasing the rotor vibration.

7. The effect of inter-rotor phase on 4/rev vibratory harmonics showed that $\phi = 0°$ provides lowest hub moments and $\phi = 45°$ provides lowest vertical hub force. An ideal choice of inter-rotor phase angle for lowering vibratory loads depends on which loading (vertical force or moment) ultimately creates vibration at the fuselage. In general, the choice of $\phi = 45°$ seems to provide a higher drop in vertical force compared to hub moments.

8. The effect of wake interactions dominates over the effect of geometric influence. The geometric influence alone could neither capture the magnitude nor trend of vibratory hub loads. Bringing in the wake interactions flips the geometric influence trend and increases vibratory magnitude by up to 5 times.

9. The examination of 3D stress fields revealed that the advancing and retreating sides showed higher stress concentrations over the rotor azimuth. Some stress concentrations at the hub were observed, with the lower rotor showing slightly higher stresses than the upper rotor of Metaltail.

Chapter 9: Summary and Conclusions

This chapter summarizes the work performed, including key conclusions, contributions, and recommendations for future research.

9.1 Summary

The principal barrier of computational time for rotorcraft trim solution using high-fidelity three-dimensional (3D) structures on real rotor problems was overcome with parallel and scalable algorithms. These algorithms were devised by leveraging the modern supercomputer architecture. The resulting parallel X3D solver was used to investigate advanced coaxial rotors using a notional hingeless rotor test case, Metaltail. This investigation included rotor performance, blade airloads, hub loads, and three-dimensional stresses.

The technical approach consisted of first studying existing algorithms for periodic rotor dynamics — time marching, finite element in time (FET), and harmonic balance. The feasibility of these algorithms was studied for large-scale rotor structures, and drawbacks were identified. Modifications were then performed on the harmonic balance method to obtain a Modified Harmonic Balance (MHB) method. A parallel algorithm for skyline solver was devised on shared memory to obtain faster solutions to large linear system of equations. The MHB method was implemented on a hybrid distributed-shared memory architecture. Next, these developed algorithms were integrated into the X3D solver to obtain a new parallel X3D.

The new parallel X3D was verified and validated in hover and forward flight conditions for both idealized and real rotor test cases. A total of four test cases were studied. The first was a uniform idealized beam, which was analyzed for tip loading. The second was the Frank Harris rotor. The third was the UH-60A Black Hawk single main rotor model validated at low-speed flight with flight-test counter 8513 data from the UH-60A Airloads Program. The last test case was the NASA Tilt-Rotor Aeroacoustic Model (TRAM), validated at low-speed forward flight with DNW tunnel test data. Predictions of tip displacements, normal and chord forces, and stress distributions were studied.

Next, the parallel performance of the solvers was measured for the test cases mentioned above. The performance of the parallel skyline solver was compared with commercially available solvers like MUMPS. The performance of the MHB algorithm was compared with the time marching algorithm for speedup and the number of floating-point operations per second (FLOPS). Lastly, the algorithm's scalability was studied with the increase in the number of harmonics and processors.

The new parallel X3D solver allowed for modeling advanced rotor configurations. In this work, the coaxial rotor was the selected configuration. Two open access models were developed; 1) a notional hingeless coaxial rotor, and 2) a notional articulated UH-60A-like coaxial rotor. The aerodynamics, structural dynamics, and trim modules of X3D were expanded for coaxial modeling. The coaxial aerodynamics was validated with hover performance data from the U.S. Army model test. Inter-rotor separation sweeps were carried out to validate the inter-rotor interactions.

The coaxial solver was then used to study rotor aeromechanics in forward flight. Both Metaltail and UH-60A coaxial models were studied. The UH-60A analysis allowed qualitative comparison with the Sikorsky S-97 Raider data as the twists are likely similar. Predictions of performance, airloads, hub loads, and three-dimensional dynamic stresses were studied. The effect of the inter-rotor phase was investigated for the reduction of vibratory hub loads. Based on all of these studies, the following key conclusions are drawn.

9.2 Key Conclusions

The key conclusions are listed in the order they were drawn, not in order of importance. They are all equally important.

1. Time marching methods carry both the transient and the forced response as part of the total solution. As a result, they are not efficient for rotor applications, where the modes are lightly damped and up to 20 revolutions are necessary for transients to die. This makes large-scale applications very expensive.

2. Parallel and scalable extraction of periodic dynamics is possible for large-scale rotor dynamic models. However, the current algorithms will not be able to carry out such tasks efficiently in tolerable time. Of the two widely used algorithms, the finite element in time is infeasible due to its overwhelming matrix size, and harmonic balance is unscalable due to skyline breakdown of matrix. However, modifications to the harmonic balance are possible that circumvent these problems.

3. A Modified Harmonic Balance (MHB) formulated in the complex domain can retain the original size and skyline. The kernel of the algorithm then becomes a parallel solver for the skyline. This can be devised on a shared memory architecture deliberately designed for speed. The parallel skyline is then unleashed on each harmonic, and the harmonics are solved independently on distributed memory.

4. The modified harmonic balance is verified to converge to the same time marching solution. The error drops to 1% with 10 iterations, 0.01% with 20, and 0.0001%

with 40 iterations. This level of accuracy and convergence is demonstrated on both idealized and practical rotor problems.

5. The solver was validated on the UH-60A-like rotor in a wake-dominated low-speed transition flight and showed consistent levels of accuracy with time marching for airloads, sectional deformations, and 3D blade stresses. Similar observations were found for the NASA TRAM test case.

6. The performance results of the parallel MHB method show a 50 times speedup compared to time marching in serial and at least 8 times speedup compared to time marching in parallel for the UH-60A rotor test case. The speedup progression for the trim solution is as follows: between time marching in serial to time marching in parallel, there is a speedup of 6. Between time marching in serial to modified harmonic balance in serial, there is a speedup of 10. Thus, the modified harmonic balance in parallel provides a net speedup of 50 from time marching in serial. Similar performance analysis for the NASA TRAM test case demonstrated 70 times overall speedup for the parallel MHB method from time marching in serial.

7. The MHB method exhibits weak scalability with processors as well as with harmonics. Peak performance of 1 teraFLOPS was recorded for a model problem with structures alone.

8. The open-source surrogate models provide useful templates for 3D modeling of production rotors from CAD to stresses and strains. The development of the 3D model for the Metaltail proprotor was described in detail, including its flex part connections, joint modeling, and structural mesh.

9. For the same thrust, momentum theory predicts a 9% reduction in coaxial hover power for a fully contracted upper rotor wake compared to the single

rotor. The rotor separation needed to achieve this is far beyond $z/D = 0.07$ used in actual aircraft. Thus, momentum theory is useless and free-wake is needed to get meaningful results.

10. The lifting-line free-wake model captures the correct trends observed in test data. The test data shows a 6% benefit, and the free-wake predictions show a 4-5% benefit in coaxial hover power compared to the single rotor.

11. For constant separation ($z/D = 0.07$), with increasing system thrust, both predictions and test data show that the aerodynamic efficiency of the upper rotor increases relative to that of the lower rotor. The individual thrust of both rotors increases linearly with increasing system thrust, and the upper rotor thrust has a higher rate of increase than the lower rotor. The upper and lower rotor produces approximately 55% and 45% of the total system thrust, respectively. This ratio is insensitive to the thrust level across the sweep.

12. In hover, with increasing separation between the rotor of a coaxial system, the lower rotor produces a lower thrust until the wake of the upper rotor is fully developed. Thereafter the thrust sharing is constant. As the rotors get closer, the upper rotor thrust decreases due to the influence of the lower rotor. Both predictions and test data captured this behavior and was found to be independent of the total system thrust.

13. At low system thrust ($C_T = 0.007$), both predictions and test data showed that the thrust sharing fraction stabilizes around $T^L/T^U \approx= 0.75$ for rotor separation $z/D \geq 0.5$.

14. At higher thrust ($C_T = 0.014$), the thrust sharing is predicted to level out with $T^L/T^U \approx= 0.75$ at a smaller inter-rotor separation $z/D = 0.35$. However, the test data showed that the level out to be slightly higher $T^L/T^U \approx= 0.8$.

15. It is possible to use 3D structures to model a coaxial rotor and obtain aeroelastic stresses and strains from the first principles. This was effectively demonstrated on two notional coaxial model test cases. One is the Metaltail, a hingeless coaxial proprotor aircraft, and two is the articulated coaxial rotor built from UH-60A-like rotors.

16. The lower rotor of a coaxial helicopter sees higher harmonics in blade lift distribution at low speeds. The rear part of the lower rotor (first quadrant) sees magnified impulses. This is due to the upper rotor wake impinging on the lower rotor.

17. The higher harmonic content observed in the lower rotor is dependent on the blade twist; a 3/rev is observed in a moderately twisted rotor (UH-60A coaxial rotor) and 4/rev for a highly twisted proprotor (Metaltail).

18. The trends obtained for the total main rotor vibratory loads of coaxial Metaltail are similar with the data published for S-97 Raider. For the range of speeds studied ($\mu \leq 0.25$), the peak vibration for hub moments was observed at the transition speed ($\mu = 0.1 - 0.15$), and the 4/rev vertical force decreased with increasing advance ratio.

19. Increase in lift offset increases the 4/rev vibratory loads at low-speed flight, thereby increasing the rotor vibration.

20. The effect of inter-rotor phase on 4/rev vibratory harmonics showed that $\phi = 0°$ provides lowest hub moments and $\phi = 45°$ provides lowest vertical hub force. An ideal choice of inter-rotor phase angle for lowering vibratory loads depends on which loading (vertical force or moment) ultimately creates vibration at the fuselage. In general, the choice of $\phi = 45°$ seems to provide a higher drop in vertical force compared to hub moments.

21. The effect of wake interactions dominates over the effect of geometric influence. The geometric influence alone could neither capture the magnitude nor trend of vibratory hub loads. Bringing in the wake interactions flips the geometric influence trend and increases vibratory magnitude by up to 5 times.

22. The examination of 3D stress fields revealed that the advancing and retreating sides showed higher stress concentrations over the rotor azimuth. Some stress concentrations at the hub were observed, with the lower rotor showing slightly higher stresses than the upper rotor of Metaltail.

9.3 Contributions

There are four principal contributions of this thesis. These are listed below.

1. A parallel and scalable algorithm for periodic solution of large-scale three-dimensional finite element analysis.

2. A new parallel X3D software that can be executed on shared memory systems such as desktops or on supercomputer clusters to make use of both distributed and shared memory architecture.

3. A three-dimensional model of a notional hingeless coaxial rotor, Metaltail that can serve as an open-source test case for academia, industry, government/Helios joint action. It can provide a template for X3D modeling of real rotors from CAD to stresses and strains.

4. The new parallel X3D expanded and validated for coaxial aeromechanics. A new Maryland Free Wake is integrated into the solver that can capture wake interactions of variable speed multi-rotor systems.

9.4 Future Work

The research demonstrated that full 3D FEA for rotors is practical for design. This capability opens many future opportunities.

1. **Parallel in space and time** – Chapter 1 mentioned that the path to exascale computing could be through parallelization in space and time. This dissertation achieved the parallel in time. A contemporary effort by Lumba [54, 55] has achieved parallel in space. The ultimate goal is to combine the two. Figure 9.1 shows a schematic of this vision. A parallel in space algorithm uses spatial partitions which are assigned to MPI tasks (seen as concentric rings). A parallel in time uses a hybrid MPI-OpenMP approach with harmonics distributed across MPI tasks. The combination of both will involve each MPI spatial partition to be solved for its harmonics using the parallel in time hybrid approach. Hence, the overall implementation is still a hybrid MPI-OpenMP approach, but with higher (hundreds to thousands) number of processors.

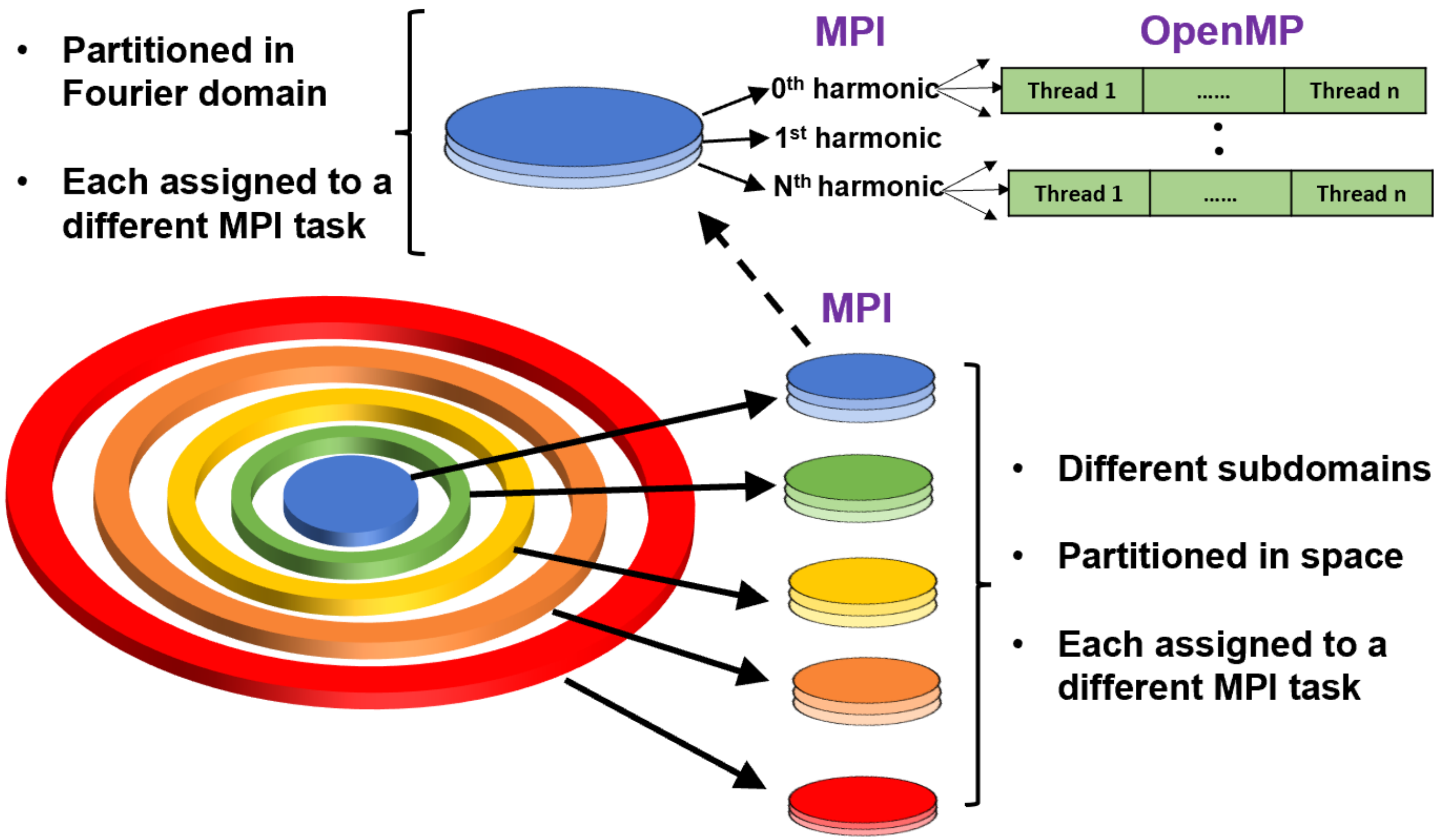

Figure 9.1: Schematics of implementation of parallel in space and time capabilities for 3D rotor structures.

2. **Refined Fluid-Structure CFD/CSD Interface** – The new parallel X3D should be coupled to CFD. It should begin with a 1D lifting-line interface (Level I) but eventually an exact 3D interface (Level III) between the CFD surface mesh and the 3D structural mesh is required. A 3D interface will require reformulation and fine-grained data exchange.

3. **Model the S-97 Raider** – The current work used Metaltail as a test case for demonstrating 3D capability for coaxial rotors. However, the high twist of its blades makes it representative of the S-97 coaxial rotor. It is desired that UMD teams with Sikorsky to build the 3D model for the S-97 Raider.

4. **Coaxial Wind Tunnel Tests** – There is no test data for coaxial rotor airloads. There is no test data for blade strains. More tests in the near future are needed to fill these gaps.

Bibliography

[1] Leishman, J. G., *The Helicopter: Thinking Forward, Looking Back*, College Park Press, 2007.

[2] Johnson, W., "A History of Rotorcraft Comprehensive Analyses," Tech. Rep. NASA/TP–2012–216012, April 2012.

[3] Johnson, W., and Datta, A., "Requirements for Next Generation Comprehensive Analysis of Rotorcraft," American Helicopter Society Specialist's Conference on Aeromechanics, San Francisco, CA, January 23–25, 2008.

[4] Datta, A., "X3D – A 3D Solid Finite Element Multibody Dynamic Analysis for Rotorcraft," American Helicopter Society Technical Meeting on Aeromechanics Design for Vertical Lift, San Francisco, CA, January 20-22, 2016.

[5] Johnson, W., "Milestones in Rotorcraft Aeromechanics," Tech. Rep. NASA/TP–2011-215971, May 2011.

[6] Glauert, H., "The Theory of the Autogyro," *The Journal of the Royal Aeronautical Society*, Vol. 31, No. 198, June 1927, pp. 483–508.

[7] Gustafson, F. B., and Gessow, A., "Effect of Rotor Tip Speed on Helicopter Rotor Performance and Maximum Forward Speed," Tech. Rep. NACA ARR L6A16, 1946.

[8] Piziali, R., and DuWaldt, F., "Computation of Rotary Wing Harmonic Airloads and Comparison with Experimental Results," 18th Annual National Forum of the American Helicopter Society, Washington, DC,, 1962.

[9] Landgrebe, A., "An Analytical Method for Predicting Rotor Wake Geometry," *Journal of the American Helicopter Society*, Vol. 14, No. 4, 1969, pp. 20–32.

[10] Landgrebe, A., "The Wake Geometry of a Hovering Rotor and its Influence on Rotor Performance," *Journal of the American Helicopter Society*, Vol. 17, No. 4, 1972, pp. 3–15.

[11] Egolf, T., and Landgrebe, A., "Helicopter Rotor Wake Geometry and its influence in Forward Flight, Vol. 1 - Generalized Wake Geometry and Wake Effects in Rotor Airloads and Performance," Tech. Rep. NASA CR-3726, 1983.

[12] Scully, M. P., “A Method of Computing Helicopter Vortex Wake Distortion,” Tech. Rep. ASRL TR 138-1, MIT, 1967.

[13] Scully, M. P., “Computation of Helicopter Rotor Wake Geometry and Its Influence on Rotor Harmonic Airloads,” Tech. Rep. ASRL TR 178-1, MIT, 1975.

[14] Miller, W. O., and Bliss, D. B., “Direct Periodic Solutions of Rotor Free Wake Calculations,” *Journal of the American Helicopter Society*, Vol. 38, No. 2, April 1993, pp. 53–60.

[15] Johnson, W., “A General Free Wake Geometry Calculation For Wings and Rotors,” 51st Annual Forum of the American Helicopter Society, Fort Worth, Texas, May 9-11, 1995.

[16] Bagai, A., and Leishman, J. G., “Rotor Free-Wake Modeling Using a Pseudo-Implicit Technique - Including Comparisons with Experimental Data,” *Journal of the American Helicopter Society*, Vol. 40, No. 3, July 1995, pp. 29–41.

[17] Bhagwat, M., and Leishman, J. G., “Stability, Consistency and Convergence of Numerical Algorithms for Time-Marching Free-Vortex Wake Analyses,” *Journal of the American Helicopter Society*, Vol. 46, No. 1, January 2001, pp. 59–71.

[18] Bhagwat, M., and Leishman, J. G., “Rotor Aerodynamics During Maneuvering Flight Using a Time-Accurate Free-Vortex Wake,” *Journal of the American Helicopter Society*, Vol. 48, No. 3, July 2003, pp. 143–158.

[19] Shastry, A., and Datta, A., “Predicting Wake and Structural Loads in RPM Controlled Multirotor Aircraft,” Vertical Flight Society Transformative Vertical Flight Technical Meeting, San Jose, California, January 21-23, 2020.

[20] Mangler, K. W., and Squire, H. B., “Calculation of the Induced Velocity Field of a Rotor,” Tech. Rep. Royal Aircraft Establishment, Report Aero 2247, September 1948.

[21] Joglekar, M., and Loewy, R., “An Actuator-Disk Analysis of Helicopter Wake Geometry and the Corresponding Blade Response,” Tech. Rep. USAAVLABS, Technical Report 69-66, December 1970.

[22] Pitt, D., and Peters, D., “Rotor Dynamic Inflow Derivatives and Time Constants from Various Inflow Models,” 9th European Rotorcraft Forum, Stresa, Italy, September 13-15, 1983.

[23] Peters, D., and He, C. J., “Finite State Induced Flow Models Part II: ThreeDimensional Rotor Disk,” *Journal of Aircraft*, Vol. 32, No. 2, 1995, pp. 323–333.

[24] Leishman, J. G., and Beddoes, T. S., “A Semi-Empirical Model for Dynamic Stall,” *Journal of the American Helicopter Society*, Vol. 34, No. 3, July 1989, pp. 3–17. https://doi.org/10.4050/JAHS.34.3.3.

[25] Leishman, J. G., and Beddoes, T. S., “Modeling Sweep Effects on Dynamic Stall,” *Journal of the American Helicopter Society*, Vol. 34, No. 3, July 1989, pp. 18–29. https://doi.org/10.4050/JAHS.34.3.18.

[26] Petot, D., “Differential Equation Modeling of Dynamic Stall,” Tech. Rep. La Recherche Aerospatiale, Number 1989-5, 1989.

[27] Truong, V. K., “A 2-D Dynamic Stall Model Based on a Hopf Bifurcation,” 19th European Rotorcraft Forum, Marseilles, France, September, 1998.

[28] Strawn, R. C., Caradonna, F. X., and Duque, E. P. N., “30 Years of Rotorcraft Computational Fluid Dynamics Research and Development,” *Journal of the American Helicopter Society*, Vol. 51, No. 1, January 2006, pp. 5–21. https://doi.org/10.4050/1.3092875.

[29] Datta, A., Nixon, M., and Chopra, I., “Review of Rotor Loads Prediction with the Emergence of Rotorcraft CFD,” *Journal of the American Helicopter Society*, Vol. 52, No. 4, October 2007, pp. 287–317. https://doi.org/10.4050/JAHS.52.287.

[30] Houbolt, J., and Brooks, G., “Differential Equations of Motion for Combined Flapwise Bending, Chordwise Bending, and Torsion of Twisted Nonuniform Rotor Blades,” Tech. Rep. NACA-TN-3905, March 1957.

[31] Hodges, D., and Dowell, E., “Nonlinear Equations of Motion for the Elastic Bending and Torsion of Twisted Nonuniform Rotor Blades,” Tech. Rep. NACA-TN-D7818, March 1974.

[32] Hodges, D., Ormiston, R., and Peters, D., “On the Nonlinear Deformation Geometry of Euler–Bernoulli Beams,” Tech. Rep. NASA-TP-1566, March 1980.

[33] Kvaternik, R., and Kirshna, R., “Nonlinear Curvature Expressions for Combined Flapwise Bending, Chordwise Bending, Torsion, and Extension of Twisted Rotor Blades,” Tech. Rep. NASA-TM-X-73997, March 1976.

[34] Rosen, A., and Friedmann, P., “Nonlinear Equations of Equilibrium for Elastic Helicopter or Wind Turbine Blades Undergoing Moderate Deformation,” Tech. Rep. NASA CR-159478, March 1978.

[35] Johnson, W., “Aeroelastic Analysis for Rotorcraft in Flight or in a Wind Tunnel,” Tech. Rep. NASA-TN-D-8515, March 1977.

[36] Bauchau, O., and Hong, C., “Nonlinear Composite Beam Theory,” *Journal of Applied Mechanics*, Vol. 55, No. 1, March 1988, pp. 156–163. https://doi.org/10.1115/1.3173622.

[37] Smith, E., and Chopra, I., “Aeroelastic Response, Loads, and Stability of a Composite Rotor in Forward Flight,” *AIAA Journal*, Vol. 31, No. 7, July 1993, pp. 1265–1273. https://doi.org/10.2514/3.49066.

[38] Bauchau, O., and Kang, N., "A Multibody Formulation for Helicopter Structural Dynamic Analysis," *Journal of American Helicopter Society*, Vol. 38, No. 2, April 1993, pp. 3–14. https://doi.org/10.4050/JAHS.38.2.3.

[39] Hodges, D. H., *Nonlinear Composite Beam Theory*, American Institute of Aeronautics, 2006.

[40] Johnson, W., and Datta, A., "An Assessment of the State-of-the-art in Multidisciplinary Aeromechanical Analyses," American Helicopter Society Specialist's Conference on Aeromechanics, San Francisco, CA, January 23–25, 2008.

[41] Post, D., Atwood, C., Newmeyer, K., and Landsber, S., "The Computational Research and Engineering Acquisition Tools and Environments (CREATE) Program," *Computing in Science and Engineering*, Vol. 18, No. 1, 2016, pp. 10–13. https://doi.org/10.1109/MCSE.2016.2.

[42] Datta, A., and Johnson, W., "Three-Dimensional Finite Element Formulation and Scalable Domain Decomposition for High Fidelity Rotor Dynamic Analysis," *Journal of the American Helicopter Society*, Vol. 56, No. 2, April 2011, pp. 1–14. https://doi.org/10.4050/JAHS.56.022003.

[43] Datta, A., and Johnson, W., "Integrated Aeromechanics with ThreeDimensional Solid-Multibody Structures," 70th Annual Forum of the Vertical Flight Society, Montreal, Quebec, May 20-22, 2014.

[44] Staruk, W., Chopra, I., and Datta, A., "Three-Dimensional CAD-Based Structural Modeling for Next Generation Rotor Dynamic Analysis," 70th Annual Forum of the American Helicopter Society, Montréal, Quebec, May 20-22, 2014.

[45] Staruk, W., "CAD-Based Modeling of Advanced Rotary Wing Structures for Integrated 3-D Aeromechanics Analysis," Ph.D. thesis, Department of Aerospace Engineering, University of Maryland, 2017.

[46] Staruk, W., Datta, A., Chopra, I., and Jayaraman, B., "An Integrated Three-Dimensional Aeromechanics Analysis of the NASA Tilt Rotor Aeroacoustic Model," *Journal of American Helicopter Society*, Vol. 63, No. 3, July 2018, pp. 1–12. https://doi.org/10.4050/JAHS.63.032002.

[47] Ward, E., Chopra, I., and Datta, A., "Rotation Frequency-Driven Extension-Torsion Coupled Self-Twisting Rotor Blades," *Journal of Aircraft*, Vol. 55, No. 5, September 2018, pp. 1–13. https://doi.org/10.2514/1.C034617.

[48] Ward, E., "Aeromechanical Behavior of Twist-Morphing, High-Speed, Slowed RPM Rotors," Ph.D. thesis, Department of Aerospace Engineering, University of Maryland, 2017.

[49] Patil, M., and Datta, A., "A Scalable Time-Parallel Solution of Periodic Rotor Dynamics in X3D," *Journal of the American Helicopter Society*, Vol. 66, No. 4, October 2021, pp. 1–16.

[50] Patil, M., and Datta, A., "A Scalable Time-Parallel Solution of Periodic Rotor Dynamics in X3D," 76th Annual Forum of the Vertical Flight Society, Virtual, October 6-8, 2020.

[51] Patil, M., and Datta, A., "Time-Parallel Scalable Solution of Periodic Rotor Dynamics for Large-Scale 3D Structures," AIAA Scitech 2021 Forum, AIAA Paper 2021-1079, Virtual, January, 2021. https://doi.org/10.2514/6.2021-1079.

[52] Patil, M., and Datta, A., "Three-Dimensional Aeromechanical Analysis of Lift-Offset Coaxial Rotors," AIAA Scitech 2022 Forum, AIAA Paper 2022-0928, San Diego, CA, January, 2022. https://doi.org/10.2514/6.2022-0928.

[53] Patil, M., Arias, P., Baeder, J., and Datta, A., "An Integrated Three-Dimensional Aeromechanical Analysis of Lift Offset Coaxial Rotors," 78th Annual Forum of the Vertical Flight Society, Fort Worth, Texas, May 10-12, 2022.

[54] Lumba, R. T., and Datta, A., "Scalable Mesh Partitioning for Large-Scale 3D Finite Element Multibody Structures," 76th Annual Forum of the Vertical Flight Society, Virtual, October 6-8, 2020.

[55] Lumba, R. T., and Datta, A., "Scalable Domain Decomposition for Large-Scale Multibody-3D Finite Element Structures," AIAA Scitech 2021 Forum, AIAA Paper 2021-1078, Virtual, January, 2021. https://doi.org/10.2514/6.2021-1078.

[56] Lumba, R. T., and Datta, A., "Development of a Parallel 3D FEA Multibody Solver and Partitioner for Rotorcraft," AIAA Scitech 2022 Forum, AIAA Paper 2022-2410, San Diego, CA, January, 2022. https://doi.org/10.2514/6.2022-2410.

[57] Chi, C., Datta, A., and Panda, B., "Vacuum and Hover Test of a Double Anhedral Tip Composite Rotor," Aeromechanics for Advanced Vertical Flight Technical Meeting, Transformative Vertical Flight, San Jose, California, January 2022.

[58] Lumba, R., Chi, C., Datta, A., Perez, W. K. N. P., and Cummings, H., "Structural Design and Aeromechanical Analysis of Unconventional Blades for Future Mars Rotorcraft," Aeromechanics for Advanced Vertical Flight Technical Meeting, Transformative Vertical Flight, San Jose, California, January 2022.

[59] Chi, C., Lumba, R., Jung, Y. S., and Datta, A., "Aeromechanical Analysis of a Next-Generation Mars Hexacopter Rotor," *Journal of Aircraft*, Vol. 63, No. 3, May 2022, pp. 1–15. https://doi.org/10.2514/1.C036739.

[60] Blatov, Vladislav, A., and Proserpio, D. M., "Periodic-Graph Approaches in Crystal Structure Prediction," *Modern methods of crystal structure prediction*, Vol. 1, January 2011, pp. 1–28.

[61] Aprille, T., and Trick, T., “Steady-state Analysis of Nonlinear Circuits with Periodic Inputs,” *Proceedings of the IEEE*, Vol. 60, No. 1, January 1972, pp. 108–114. https://doi.org/10.1109/PROC.1972.8563.

[62] Meyer, K. R., “Periodic Solutions of the N-body Problem,” *Journal of Differential Equations*, Vol. 39, No. 1, January 1981, pp. 2–38. https://doi.org/10.1016/0022-0396(81)90081-4.

[63] Panda, B., and Chopra, I., “Flap-Lag-Torsion Stability in Forward Flight,” *Journal of the American Helicopter Society*, Vol. 30, No. 4, October 1985, pp. 30–39. https://doi.org/10.4050/JAHS.30.30.

[64] Argyris, J., and Scharpf, D., “Finite Elements in Time and Space,” *Nuclear Engineering and Design*, Vol. 10, No. 4, December 1969, pp. 456–464. https://doi.org/10.1016/0029-5493(69)90081-8.

[65] Borri, M., “Helicopter Rotor Dynamics by Finite Element Time Approximation,” *Computers and Mathematics with Applications*, Vol. 12, No. 1, January 1986, pp. 149–160. https://doi.org/10.1016/0898-1221(86)90092-1.

[66] Peters, D., and Hou, L. J., “hp-version Finite Elements for the Space-Time Domain,” *Computational Mechanics*, Vol. 3, No. 2, March 1988, pp. 73–88. https://doi.org/10.1007/BF00317056.

[67] Panda, B., and Chopra, I., “Dynamics of Composite Rotor Blades in Forward Flight,” *VERTICA*, Vol. 11, No. 1, November-December 1987, pp. 187–210.

[68] Dull, A. L., and Chopra, I., “Aeroelastic Stability of Bearingless Rotors in Forward Flight,” *Journal of the American Helicopter Society*, Vol. 33, No. 4, October 1988, pp. 38–46. https://doi.org/10.4050/JAHS.33.38.

[69] Choi, S., Datta, A., and Alonso, J. J., “Prediction of Helicopter Rotor Loads using Time-Spectral Computational Fluid Dynamics and an Exact Fluid-Structure Interface,” *Journal of the American Helicopter Society*, Vol. 56, No. 4, October 2011, pp. 1–15. https://doi.org/10.4050/JAHS.56.042001.

[70] Mcmullen, M., Jameson, A., and Alonso, J. J., “Demonstration of Non-linear Frequency Domain Methods,” *Journal of Aircraft*, Vol. 44, No. 7, July 2006, pp. 1428–1435. https://doi.org/10.2514/1.15127.

[71] Ekici, K., Hall, K. C., and Dowell, E. H., “Computationally Fast Harmonic Balance Methods for Unsteady Aerodynamic Predictions of Helicopter Rotors,” *Journal of Computational Physics*, Vol. 227, No. 12, June 2008, pp. 6206–6225. https://doi.org/10.1016/j.jcp.2008.02.028.

[72] Peters, D. A., and Ormiston, R. A., “Flapping Response Characteristics of Hingeless Rotor Blades by a Generalized Harmonic Balance Method,” Tech. Rep. NASA TN D-7856, February 1975.

[73] Lions, J., Maday, Y., and Turinici, G., "A Parareal in Time Discretization of PDEs," *Comptes Rendus de l'Académie des Sciences, Série I.*, Vol. 332, No. 7, April 2001, pp. 661–668. https://doi.org/10.1016/S0764-4442(00)01793-6.

[74] Adel, B., Boudin, L., and Kaber, S., "Parallel in Time Algorithms with Reduction Methods for Solving Chemical Kinetics," *Communications in Applied Mathematics and Computational Science*, Vol. 5, No. 2, January 2011, pp. 241–263. https://doi.org/10.2140/camcos.2010.5.241.

[75] Gurrala, G., Sreekanth, A. D. P., Simunovic, S., and Starke, M., "Parareal in Time for Dynamics Simulations of Power Systems," *IEEE Transactions on Power Systems*, Vol. 31, No. 3, May 2016, pp. 1820–1830. https://doi.org/10.1109/TPWRS.2015.2434833.

[76] Cheney, M. C., "The ABC Helicopter," *Journal of AircraftJournal of the American Helicopter Society*, Vol. 14, No. 4, October 1969, pp. 10–19. https://doi.org/10.4050/JAHS.14.4.10.

[77] Arents, D. N., "An Assessment of The Hover Performance of The XH-59A Advancing Blade Concept Demonstration Helicopter," Tech. Rep. ADA042063, May 1977.

[78] Ruddell, A. J., "XH-59A ABC Technology Demonstrator Altitude Expansion and Operational Tests," Tech. Rep. ADA111114, December 1981.

[79] Blackwell, R., and Millott, T., "Dynamics Design Characteristics of the Sikorsky X2 Technology Demonstrator Aircraft," 64th Annual Forum of the American Helicopter Society, 2008.

[80] Bagai, A., "Aerodynamic Design of the X2 Technology Demonstrator Main Rotor Blade," 64th Annual Forum of the American Helicopter Society, 2008.

[81] Walsh, D., Weiner, S., Arifian, K., Bagai, A., Lawrence, T., and Blackwell, R., "Development Testing of the Sikorsky X2 Technology Demonstrator," 65th Annual Forum of the American Helicopter Society, Grapevine, Texas, May 27-29, 2009.

[82] Walsh, D., Weiner, S., Arifian, K., Lawrence, T., Wilson, M., Millot, T., and Blackwell, R., "High Air-speed Testing of the Sikorsky X2 Technology Demonstrator," 67th Annual Forum of the American Helicopter Society, Virginia Beach, VA, May 3-5, 2011.

[83] Lorber, P. F., Law, G. K., O'Neil, J. J., Matalanis, C., and Bowles, P., "Overview of S-97 RaiderTM Scale Model Tests," 72nd Annual Forum of the American Helicopter Society, West Palm Beach, Florida, May 17-19, 2016.

[84] Zhao, J., Brigley, M., and Modarres, R., "S-97 RAIDER Rotor Low Speed Vibratory Loads Analysis using CFD-CSD," AIAA Scitech 2019 Forum, AIAA

Paper 2019-0860, San Diego, CA, January, 2019. https://doi.org/10.2514/6.2019-0860.

[85] Zhao, J., Xin, H., Modarres, R., and Brigley, M., "Methodology Correlation for Coaxial Rotor and Blade Load Prediction," 76th Annual Forum of the Vertical Flight Society, Virtual, October 6-8, 2020.

[86] Zhao, J., , Tuozzo, N., Brigley, M., Modarres, R., Monico, M., and Makinen, S., "CFD-CSD Support for Rotor Design Improvement to Reduce Vibrations," 77th Annual Forum of the Vertical Flight Society, Virtual, May 10-12, 2021.

[87] Colemann, C. P., "A Survey of Theoretical and Experimental Coaxial Rotor Aerodynamic Research," Tech. Rep. NASA TP-3675, March 1997.

[88] Escobar, D., Chopra, I., and Datta, A., "High-Fidelity Aeromechanical Analysis of Coaxial Mars Helicopter," *Journal of Aircraft*, Vol. 58, No. 3, March 2021, pp. 1–15. https://doi.org/10.2514/1.C035895.

[89] Leishman, J. G., "Principles of Helicopter Aerodynamics," New York: Cambridge University Press, 2006.

[90] Ananthan, S., and Leishman, G. J., "An Optimum Coaxial Rotor System for Axial Flight," *Journal of the American Helicopter Society*, Vol. 53, No. 4, October 2008, pp. 366–381. https://doi.org/10.4050/JAHS.53.366.

[91] Bagai, A., and Lesihman, J. G., "Free-Wake Analysis of Tandem, Tilt-Rotor and Coaxial Rotor Configurations," *Journal of American Helicopter Society*, Vol. 41, No. 3, July 1996, pp. 196–207.

[92] Brown, R. E., "Rotor Wake Modeling for Flight Dynamic Simulation of Helicopters," *AIAA Journal*, Vol. 38, No. 1, January 2000, pp. 57–63. https://doi.org/10.2514/2.922.

[93] Lim, J., McAlister, K. W., and Johnson, W., "Hover Performance Correlation for Full-Scale and Model-Scale Coaxial Rotors," *Journal of American Helicopter Society*, Vol. 54, No. 3, July 2009, pp. 1–14. https://doi.org/10.4050/JAHS.54.032005.

[94] Syal, M., and Leishman, G. J., "Aerodynamic Optimization Study of a Coaxial Rotor in Hovering Flight," *Journal of the American Helicopter Society*, Vol. 57, No. 4, October 2012, pp. 1–15. https://doi.org/10.4050/JAHS.57.042003.

[95] Singh, P., and Friedmann, P. P., "Application of Vortex Methods to Coaxial Rotor Wake and Load Calculations in Hover," *Journal of Aircraft*, Vol. 55, No. 1, September 2017, pp. 373–381. https://doi.org/10.2514/1.C034520.

[96] Singh, P., and Friedmann, P. P., "Aeromechanics and Aeroelastic Stability of Coaxial Rotors," *Journal of Aircraft*, Vol. 58, No. 6, August 2021. https://doi.org/10.2514/1.C036291.

[97] Ruzicka, G. C., and Strawn, R. C., "Computational Fluid Dynamics Analysis of a Coaxial Rotor Using Overset Grids," American Helicopter Society Specialist's Conference on Aeromechanics, San Francisco, CA, January 23-25, 2008.

[98] Lakshminarayan, V. K., and Baeder, J., "High-Resolution Computational Investigation of Trimmed Coaxial Rotor Aerodynamics in Hover," *Journal of American Helicopter Society*, Vol. 54, No. 4, October 2009, pp. 1–21. https://doi.org/10.4050/JAHS.54.042008.

[99] Juhasz, O., Syal, M., Celi, R., Khromov, V., Rand, O., Ruzicka, G. C., and Strawn, R. C., "Comparison of Three Coaxial Aerodynamic Prediction Methods Including Validation with Model Test Data," *Journal of American Helicopter Society*, Vol. 59, No. 3, July 2014, p. 14. https://doi.org/10.4050/JAHS.59.032006.

[100] Harrington, R. D., "Full-scale-tunnel Investigation of the Static-thrust Performance of a Coaxial Helicopter Rotor," Tech. Rep. NACA-TN-2318, March 1951.

[101] Reed, E., and Egolf, T. A., "Coaxial Rotor Wake and Prop Induction Impact on a Horizontal Tail Using HPCMP CREATE™-AV Helios," 53rd AIAA Aerospace Sciences Meeting, AIAA Paper 2015-0554, 2015. https://doi.org/10.2514/6.2015-0554.

[102] Bowles, P. O., Matalanis, C., Battisti, M., Min, B., Wake, B. E., Tuozzo, N., and Lorber, P. F., "Full-Configuration CFD Analysis of the S-97 RAIDER," 75th Annual Forum of the Vertical Flight Society, Philadelphia, PA, May 2019.

[103] Johnson, W., "Influence of Lift Offset on Rotorcraft Performance," Tech. Rep. NASA/TP–2009-215404, November 2009.

[104] Johnson, W., Moodie, A. M., and Yeo, H., "Design and Performance of LiftOffset Rotorcraft for Short-Haul Missions," American Helicopter Society Future Vertical Lift Aircraft Design Conference, AHS International, San Francisco, CA, January 2012.

[105] Yeo, H., and Johnson, W., "Investigation of Maximum Blade Loading Capability of Lift-Offset Rotors," *Journal of the American Helicopter Society*, Vol. 59, No. 1, January 2014, pp. 1–12. https://doi.org/10.4050/JAHS.59.012005.

[106] Schmaus, J., and Chopra, I., "Aeromechanics of Rigid Coaxial Rotor Models for Wind-Tunnel Testing," *Journal of Aircraft*, Vol. 54, No. 4, July 2017, pp. 1486–1497. https://doi.org/10.2514/1.C034157.

[107] Schmaus, J., "Aeromechanics of a High Speed Coaxial Helicopter Rotor," Ph.D. thesis, Department of Aerospace Engineering, University of Maryland, 2017.

[108] Feil, R., Rauleder, J., Cameron, C., Karpatne, A., and Sirohi, J., "Aeromechanics Analysis of a High-Advance-Ratio Lift-Offset Coaxial Rotor System," *Journal of Aircraft*, Vol. 56, No. 1, January 2019, pp. 166–178. https://doi.org/10.2514/1.C034748.

[109] Feil, R., and Hajek, M., "Aeromechanics of a Coaxial Ultralight Rotorcraft During Turn, Climb, and Descent Flight," *Journal of Aircraft*, Vol. 58, No. 1, July 2020. https://doi.org/10.2514/1.C035684.

[110] Escobar, D., "Fundamental Understanding of Helicopter Aeromechanics on Mars Through Chamber Testing and High-Fidelity Analysis," Ph.D. thesis, Department of Aerospace Engineering, University of Maryland, 2020.

[111] Singh, R., and Kang, H., "Computational Investigation of Transient Loads and Blade Deformations on Coaxial Rotor Systems," AIAA Aviation Forum, 33rd AIAA Applied Aerodynamics Conference, AIAA Paper 2015-2884, Dallas, Texas, June 22-26, 2015. https://doi.org/10.2514/6.2015-2884.

[112] Singh, R., Kang, H., Bhagwat, M., Cameron, C., and Sirohi, J., "Computational and Experimental Study of Coaxial Rotor Steady and Vibratory Loads," AIAA Scitech 2016 Forum, AIAA Paper 2016-1787, San Diego, CA, January, 2016. https://doi.org/10.2514/6.2016-1787.

[113] Passe, B., Sridharan, A., and Baeder, J., "Computational Investigation of Coaxial Rotor Interactional Aerodynamics in Steady Forward Flight," AIAA Aviation Forum, 33rd AIAA Applied Aerodynamics Conference, AIAA Paper 2015-2883, Dallas, Texas, June 22-26, 2015. https://doi.org/10.2514/6.2015-2883.

[114] Passe, B., Sridharan, A., Baeder, J., and Singh, R., "Identification of Rotor-Fuselage Aerodynamic Interactions in a Compound Coaxial Helicopter using CFD-CSD Coupling," AHS Technical Conference on Aeromechanics Design for Transformative Vertical Flight, American Helicopter Society, San Francisco, CA, January 20-22, 2016.

[115] Klimchenko, V., and Baeder, J. D., "CFD/CSD Study of Interactional Aerodynamics of a Coaxial Compound Helicopter in High-Speed Forward Flight," AIAA SciTech 2020 Forum, AIAA Paper 2020-0304, Orlando, Florida, January, 2020. https://doi.org/10.2514/6.2020-0304.

[116] Bathe, K., "Finite Element Procedures in Engineering Analysis," Tech. Rep. Prentice-Hall, Inc., NJ 1982.

[117] Zienkiewicz, O. C., and Taylor, R. L., "The Finite Element Method for Solid and Structural Mechanics," Tech. Rep. Elsevier Butterworth-Heinemann, Sixth Edition, Oxford, UK 2006.

[118] Datta, A., "X3D Version 1.0 Theory Manual," Tech. rep., September 2017.

[119] Hall, K. C., Ekici, K., Thomas, J. P., and Dowell, E. H., "Harmonic balance methods applied to computational fluid dynamics problems," *International Journal of Computational Fluid Dynamics*, Vol. 27, No. 2, January 2013, pp. 52–67. https://doi.org/10.4050/JAHS.52.287.

[120] Harris, F. D., "Technical Notes: The Rotor Blade Flap Bending Problem—An Analytical Test Case," *Journal of American Helicopter Society*, Vol. 37, No. 4, October 1992, pp. 64–67. https://doi.org/10.4050/JAHS.37.64.

[121] Acree, C. W., Martin, P., and Romander, E., "Impact of Airfoils on Aerodynamic Optimization of Heavy Lift Rotorcraf," AHS Vertical Lift Aircraft Design, San Francisco, CA, January 18-20, 2006.

[122] Johnson, W., "Calculation of Tilt Rotor Aeroacoustic Model (TRAM DNW) Performance, Airloads, and Structural Loads," American Helicopter Society Aeromechanics Specialists' Meeting, Atlanta, GA, November 13-15, 2000.

[123] Amestoy, P. R., Duff, I. S., Koster, J., and L'Excellent, J. Y., "A Fully Asynchronous Multifrontal Solver Using Distributed Dynamic Scheduling," *SIAM Journal on Matrix Analysis and Applications*, Vol. 27, No. 1, 2001, pp. 15–41. https://doi.org/10.1137/S0895479899358194.

[124] Amestoy, P. R., Buttari, A., L'Excellent, J. Y., and Mary, T., "Performance and Scalability of the Block Low-rank Multifrontal Factorization on Multicore Architectures," *ACM Transactions on Mathematical Software*, Vol. 45, No. 1, 2019, pp. 1–26. https://doi.org/10.1145/3242094.

[125] Tsai, F., O'Reilly, C., Klimchenko, V., Solomon, E., Philips, B., Costenoble, A., Chi, C., Govindarajan, B., Nagaraj, V. T., and Chopra, I., "Metaltail: A Reconfigurable VTOL Aircraft,," Tech. rep., Winning submission to the 35th Annual VFS Student Design Competition, University of Maryland, 2018.

[126] Strawn, R., "High-Performance Computing for Rotorcraft Modeling and Simulation," *Computing in Science and Engineering*, Vol. 12, No. 5, September–October 2010, pp. 27–35. https://doi.org/10.1109/MCSE.2010.110.

[127] Staruk, W., Jayaraman, B., Sitaraman, J., and Datta, A., "Integrated 3-D Structural Dynamics Using the Helios v9 Rotorcraft Analysis Framework," AIAA Scitech 2019 Forum, AIAA Paper 2019-0842, San Diego, CA, January, 2019. https://doi.org/10.2514/6.2019-0842.

[128] Ramasamy, M., "Hover Performance Measurements Toward Understanding Aerodynamic Interference in Coaxial, Tandem, and Tilt Rotors," *Journal of American Helicopter Society*, Vol. 60, No. 3, July 2015, pp. 1–17. https://doi.org/10.4050/JAHS.60.032005.

[129] Yamauchi, G., and Johnson, W., "Trends of Reynolds Number Effects on TwoDimensional Airfoil Characteristics for Helicopter Rotor Analyses," Tech. Rep. NASA-TM-84363, April 1983.